Dissertation

submitted to the

Combined Faculties of the Natural Sciences and Mathematics

of the Ruperto-Carola-University of Heidelberg, Germany

for the degree of

Doctor of Natural Sciences

Put forward by

M.Sc. Stepan Dobrodey

born in: Wladiwostok, Russia

Oral examination: 30.10.2019

Charge-exchange studies of bare and hydrogen-like low-Z ions in the X-ray and extreme-ultraviolet ranges inside an electron beam ion trap

Untersuchungen von Ladungsaustausch nackter und wasserstoff-artiger Ionen kleiner Kernladungszahl in den Röntgen- und extremen Ultraviolett-Bereichen innerhalb einer Elektronenstrahl-Ionenfalle:

In der vorliegenden Arbeit wurde eine kryogene Elektronenstrahl-Ionenfalle für das Ladungsbrüten seltener, kurzlebiger, radioaktiver Isotope an der ARIEL Einrichtung am TRIUMF für zukünftige Untersuchungen astrophysikalischer Prozesse entworfen und gebaut. Diese wurde bei einem maximal erreichten Elektronen-Strahlstrom von $1\,\mathrm{A}$ charakterisiert. Des Weiteren wurden Ladungsaustausch-Prozesse, die relevant für die Schnittstelle von heißen Plasmen und kalter Gase in astrophysikalischen Umgebungen ist, ausgiebig analysiert. In diesen Experimenten wurden ursprünglich wasserstoff-artige und nackte Schwefel-, Argon- und Sauerstoff-Ionen, nach Einfang von Elektronen aus neutralen Gas-Teilchen in hoch angeregte Zustände und anschließenden radiativen Relaxation durch Emission von Röntgen-Photonen untersucht. Dabei wurde eine mögliche Erklärung für die kürzlich beobachtete Emissionslinie bei $3.5\,\mathrm{keV}$ in Galaxienhaufen, mit einem vorgeschlagenen Ursprung im Zerfall steriler Neutrinos, in Form von Ladungsaustausch induzierter K-Schalen-Emission von wasserstoff-artigem Schwefel gegeben. Zusätzlich wurden Messungen von extrem ultravioletten L-Schalen-Übergängen nach Ladungsaustausch von hoch geladenem Sauerstoff in einem Bereich von $8\,\mathrm{nm}$ und $20\,\mathrm{nm}$ unter Verwendung eines Extrem-Ultraviolett-Gitterspektrometers präsentiert. Die Ergebnisse wurden mit verschiedenen Ladungsaustausch-Modellen, die größtenteils auf der Multikanal Landau-Zener Methode basieren, verglichen. Signifikante Unstimmigkeiten wurden sowohl zwischen diversen Experimenten und Modellen, als auch zwischen den Modellen untereinander festgestellt und ausgiebig diskutiert.

Charge-exchange studies of bare and hydrogen-like low-Z ions in the X-ray and extreme-ultraviolet ranges inside an electron beam ion trap:

In this work, a cryogenic electron beam ion trap (EBIT) for charge breeding of rare, short-lived isotopes at the ARIEL facility at TRIUMF was designed and assembled for future investigations of astrophysical processes. It was characterized at a maximum electron-beam current of $1\,\mathrm{A}$. Furthermore, charge-exchange (CX) processes, which are relevant for the interface between hot plasmas and cold gases in astrophysical environments, were extensively studied. In these experiments, hydrogen-like and bare sulfur, argon, and oxygen ions capturing electrons from various neutral gas targets into highly-excited states with subsequent radiative relaxation via emission of X-rays were investigated. Thereby, a possible explanation for the recently observed emission line at $3.5\,\mathrm{keV}$ in galaxy clusters, with a proposed origin in the decay of sterile neutrinos, was given, in the form of CX induced K-shell emission from hydrogen-like sulfur. Additionally, measurements of extreme-ultraviolet L-shell transitions following CX into highly ionized oxygen in the range between $8\,\mathrm{nm}$ and $20\,\mathrm{nm}$, utilizing a grating spectrometer, is presented. The results are compared with different CX models, mainly based on the multichannel Landau-Zener approach. Significant discrepancies between various experiments and models, as well as the models among each other, were ascertained and are extensively discussed.

Contents

1 Introduction

> Mit der Theorie […] mit den Atomen mit mehr als einem Elektron ist es momentan ein großer Jammer![1]

<div align="right">

Wolfgang Pauli, 1923[2]

</div>

In ancient China 240 BC, a celestial apparition of a "broom star" was reported in the *Records of the Grand Historian* [159, 147]. This descriptive term with several others like "sweeping star", "long star" or "candle-flame star" [127] implies the presence of a tail of this celestial object nowadays classified as a comet. It was the first of the hitherto 25 sightings of *Halley's comet*, named after the English astronomer Edmond Halley, who determined the periodicity of this object in 1705. As an explanation for this phenomenon, a broad spectrum of theories over several centuries ranging from meteorological phenomena, exhalations from Earth, to optical illusions caused by reflections of sunlight was suggested [147]. A comet, derived from the ancient Greek term *komētēs* ("wearing long hair"), is a celestial body that is formed in the outermost, colder regions of the solar system within the Kuiper belt or the Oort cloud. Due to the condensation of hydrogenic and carbonic compounds in these regions, it consists mainly of water, carbon monoxide, carbon dioxide, and formaldehyde molecules [14]. At large distances from the sun, the direct detection of comets is challenging due to the small size of the nucleus in the order of typically kilometers. Moreover, the surface of the nucleus consists of dense crystalline ice with a mixture of organic compounds reducing the albedo to $\sim 4\,\%$ [106]. The interior of a comet is typically less solid. At a distance of ~ 5 astronomical units, a comet interacts with the solar wind and solar radiation leading to the formation of a coma by sublimation of ice and dust particles. Evaporation and outpouring of volatile material cause the formation of a dust tail and the ionization of those particles a gas tail, following magnetic field lines and typically pointing in a slightly different direction than the dust tail.

Since the discovery of Halley's comet, hundreds of other comets have been observed and studied with earthbound telescopes. Not only comets are the subject of interest for astronomical observations. With telescopes in the radio-frequency domain, galaxy clusters and clouds of hydrogen were found. With visible-light telescopes, star constellations, planets, and small celestial bodies were observed. However, the universe is hot and

---

[1] Engl.: The theory […] with atoms having more than one electron, it is currently such a great misery!
[2] Letter from Pauli to Sommerfeld, 1923 [88].

dominated by high-energetic X-ray emission, since most of the matter is present in form of highly ionized plasmas [66], where the majority of bound electrons compared to the neutral matter are removed. Such hot environments prevail in active galactic nuclei, neutron stars, binary systems, supernova remnants, and the solar corona. The observation of these objects is impossible on the Earth's surface since the emitted X-ray radiation is absorbed by the atmosphere, and thus, space technology was required. With the launch of rockets in 1949 and satellites equipped with instruments for the detection of X-ray photons [120, 178] beginning from 1977, the X-ray astronomy was founded in order to unveil the hot and violent universe.

X-rays are mainly produced by the interaction of ions with high-energetic electrons. One contribution is the Bremsstrahlung, where an electron is deflected by the electric field of the nucleus losing its kinetic energy by emission of X-rays with a continuous flux distribution as a function of the photon energy. The second mechanism is the excitation of atomic transitions, leading to discrete and characteristic emission lines. This X-ray energy is determined by the energetic difference of the initial excited and the final atomic state.

Besides the imaging of these hot sources to locate their position in the cosmos, spectroscopic investigations allow for the determination of the physical properties of astrophysical plasmas. The position of spectral lines or transition energies provides information about the elemental composition and corresponding charge state. From the intensity ratio of specific spectral lines, the ion density and temperature can be determined. With these parameters, atomic processes and physical conditions in hot astrophysical plasmas can be investigated.

However, it was surprisingly found that X-ray emission is not exclusively restricted to hot objects. In 1996 the comet C/Hyakutake 1996 B2, which passed by the Earth at a distance of 0.109 astronomical units was investigated by Lisse et al. [115] with the German Röntgen X-ray Satellite (ROSAT) and by Mumma et al. [125] with the Extreme Ultraviolet Explorer (EUVE). With an average daytime surface temperature of 200 K [65], a comet is comparably cold, and thus, X-ray emission was not expected in the beginning. Nonetheless, X-ray and extreme ultraviolet (EUV) emission from a volume surrounding the comet was observed with the ROSAT satellite, equipped with X-ray and EUV cameras [41], see figure 1.1.

The X-ray image (a)) was acquired with the High-Resolution Imager (HRI) in a photon energy range of $0.1-2.0$ keV and the EUV image (b)) with the Wide-Field Camera (WFC) in a range of $0.09-0.2$ keV. The subfigure c) shows an optical image superimposed with the X-ray and the EUV emission represented by white/black and yellow contour lines, respectively.

Several explanations for the unexpected soft X-ray emission were proposed, including thermal Bremsstrahlung [115], magnetic-field-line reconnection [128], Fermi acceleration
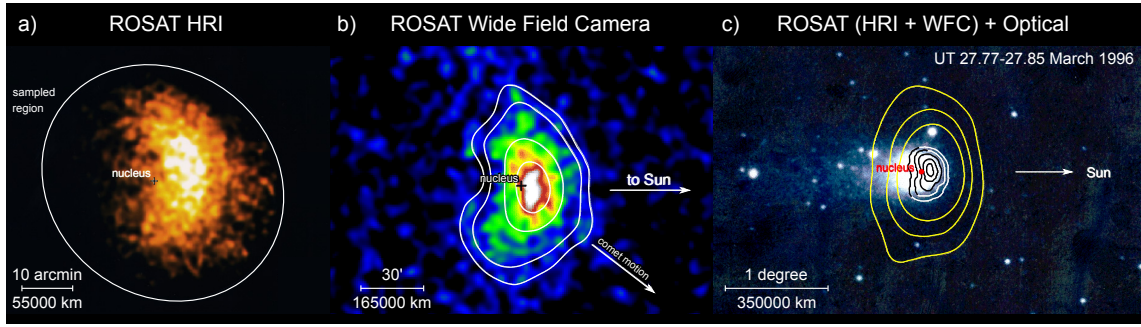
Figure 1.1: Images from the comet C/Hyakutake 1996 B2 taken simultaneously on March, 27th, 1996 by the X-ray satellite ROSAT. **a)** X-ray image acquired with the High-Resolution Imager. **b)** Extreme Ultraviolet image obtained with the Wide Field Camera. **c)** Overlay of an optical image with EUV and X-ray emission, shown as yellow and black/white contour lines, respectively. The nucleus of the comet is marked in each image. The sun is located on the right-hand side, and the motion of the comet inclined by 45 %. Adapted from Ref. [1, 115, 131] and modified.

[81, 82], X-ray scattering from small dust particles [125], and charge transfer mechanisms between the solar wind ions and the neutral gas surrounding the comet [49, 125]. The latter approach was confirmed by Ref. [103] where the first cometary emission spectrum in a wavelength range between 8 nm and 70 nm of the comet Hyakutake, was obtained by EUVE equipped with a grating spectrometer. The dominant process was determined to be charge exchange (CX), where a loosely bound electron of the neutral target is captured into an excited state of highly charged $O^{4+} \ldots O^{6+}$, C^{4+} and He^+ projectile ions of the solar wind, with subsequent deexcitation and emission of a photon, reducing the charge of the initial ion by one after the interaction.

Subsequent to the discovery of X-rays emitted from the comet Hyakutake, charge exchange emission from other comets was observed [134, 102, 114].

In order to interpret the astrophysical observations, theoretical models have been developed for the charge-exchange process. Since the cross-sections for electron-capture are not well known, laboratory measurements became crucial for benchmarking the theory. In the field of plasma physics already in the late 1970s, total charge exchange cross-sections for some elements in various charge states were measured utilizing accelerators and gas targets [138]. However, the knowledge about the total CX cross-sections, solely, is not sufficient in order to understand astrophysical spectra. Therefore, systematic spectroscopic measurements are required for the investigation of cometary X-rays in the laboratory.

One of the first experiments mimicking the cometary CX process is presented in Ref. [22] where an electron beam ion trap (EBIT), equipped with a high-resolution micro-calorimeter as an X-ray detector, was utilized for production and storage of highly charged ions interacting with a beam of neutral gas. In figure 1.2, the cometary emission spectrum of
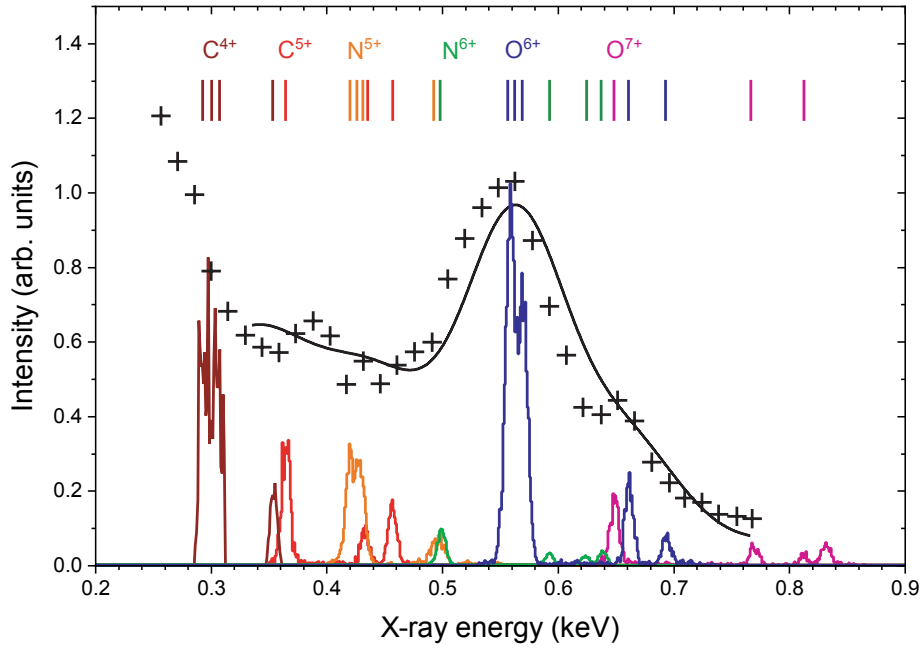
Figure 1.2: X-ray spectrum of the comet Linear C/1999 S4 obtained by the Chandra X-ray space telescope. The intensity as a function of the photon energy. The crosses represent the observation and the solid line the best fit utilizing the charge exchange induced X-ray emission from EBIT measurements of C^{6+}, C^{5+}, N^{6+}, N^{7+}, O^{7+} and O^{8+} interacting with neutral CO_2. Adapted from Ref. [22] and modified.

Linear C/1999 S4 and the laboratory-simulated spectrum using the EBIT is illustrated. In these measurements highly charged carbon, nitrogen and oxygen ions, produced in the EBIT interacted with a beam of neutral CO_2. The resulting charge-exchange induced X-ray emission is plotted as a function of the photon energy. The black crosses indicate the observation of the Chandra X-ray space telescope, the solid black line the best fit utilizing the single emission lines of C^{4+}, C^{5+}, N^{6+}, N^{7+}, O^{7+} and O^{8+}, illustrated with color traces, after charge exchange with the target gas inside the EBIT. The simulation indicates a high abundance of hydrogen-like oxygen and carbon in the solar wind from 14 July 2000, followed by fully ionized carbon and hydrogen-like oxygen. This measurement has also shown that charge exchange emission could be utilized as a diagnostic tool to determine the composition of coronal mass ejection.

Further works were performed on the studies of cometary X-rays in laboratories utilizing ion sources and gas targets where the highly charged ions interact with neutral gas [36]. Here, mainly *L*-shell transitions from principal quantum number states $n = 3, 4, 5$ to $n = 2$ of highly ionized oxygen and carbon ions induced by charge exchange were investigated in the extreme-ultraviolet domain between $6\,\text{nm}$ and $30\,\text{nm}$.

The discovery of CX from comets has attracted particular attention in the astrophysical

community and gave rise to a number of publications concerning the interaction of the solar wind with the Martian exosphere [101, 57], with Jupiter [171, 40], with the "dark side of the moon" [174] and with the atmosphere of the Earth [73]. Outside the solar system, a possible observation of charge exchange in the outer rims of the Cygnus Loop supernova remnant (SNR) was reported in Ref. [99]. An enhanced emission feature at $\sim 0.7\,\text{keV}$ in the spectrum of the SNR was proposed to have an origin in K-shell transitions from principal quantum number states $n = 3, 4, 5, \ldots$ to the ground state $n = 1$ of helium-like oxygen O^{6+}, but other possible sources are not excluded hitherto.

In 2014 the detection of an unidentified line-like emission feature at $\sim 3.5\,\text{keV}$ in the Perseus galaxy cluster and independent observations in other galaxy clusters with X-ray space telescopes was reported. This feature was proposed to have an origin in a decaying dark matter particle candidate, the sterile neutrino [39, 42, 170] since this line could not be assigned to an atomic transition in standard wavelength databases. An explanation for this emission line was given in Ref. [83], where a fully-ionized sulfur ion captures an electron from atomic hydrogen into a high Rydberg state n. A direct radiative relaxation from $n \geq 7$ to the ground state $n = 1$ leads to emission of an X-ray photon with an energy of $\sim 3.47\,\text{keV}$. These transitions are often missing in standard wavelength catalogs. The fact that high-energetic states can be efficiently populated by charge exchange was not considered in the model utilized in Ref. [39, 42, 170]. Since the hot galactic plasmas contain significant amounts of hydrogen-like and fully-stripped sulfur ions [126] interacting with clouds of atomic hydrogen, the CX process has to be considered in astrophysical modeling. In this work, the scenario of CX between fully-stripped sulfur with neutral gas [83, 149] is investigated and strongly supported. This measurement demonstrates the necessity of laboratory X-ray measurements in order to explain anomalous X-ray emission in observed astrophysical spectra of hot objects outside the solar system.

Besides the astrophysical motivation for investigation of the CX process, it is fundamentally crucial to understand the atomic processes of ion-atom collisions. For the charge exchange process, a broad spectrum of theoretical models exists, ranging from straightforward classical approaches, like the classical over-the-barrier (COB) model [142], numerical quantum-mechanical two-state methods like Landau-Zener [179, 107] or multichannel Landau-Zener (MCLZ) to more sophisticated quantum mechanical molecular orbital close-coupling (QMOCC) calculations. The most established model in the astrophysical community for simulation of CX spectra is the MCLZ approach. To generate reliable synthetic CX spectra a full knowledge of the principal quantum number state n, angular momentum l and spin s of the captured electron, and the radiative transition rates of all possible decay channels to the ground state is required. For non-bare projectiles, the calculated cross-section for CX is resolved in n and l of the captured electron, but the reliability with systems containing more than one electron is limited. For bare ion

collisions resulting in a hydrogen-like system after CX, only *n*-resolved cross-sections can be calculated with MCLZ [53], and an *l*-distribution must be applied. Depending on the collision velocity between projectile and target different angular momentum distributions are applicable. To benchmark these approaches and theories, systematic spectroscopic laboratory measurements are necessary.

In addition to the charge exchange process, other various atomic processes in highly ionized plasmas are present in hot astrophysical environments, including interaction with high-energetic photons and free electrons. In hotter environments present in stars located at the asymptotic giant branch of the Hertzsprung-Russel diagram, or in supernova explosions and neutron star mergers, heavy elements of the periodic table are formed by slow or rapid neutron capture, denoted as the s-process and the r-process, respectively. In order to understand the relevant processes in astrophysical plasmas, various laboratory experiments have been performed in storage rings [180], in electron beam ion traps [26, 15], and other facilities.

In this work, an electron beam ion trap acting as a charge breeder at the rare-isotope facility at TRIUMF was developed, assembled and characterized. It will provide highly charged, rare, short-lived isotopes in a specific charge state for the investigation of the stellar nucleosynthesis, in particular, the r-process and the s-process, among others.

Furthermore, systematic charge exchange measurements in the X-ray range of fully ionized ions interacting with different neutral target gases were performed utilizing the FLASH electron beam ion trap, equipped with photon detectors in the EUV and X-ray regime. To benchmark the models, the spectra of Ar^{18+} colliding with various neutrals are compared to different theoretical approaches, including a cascade model for the reconstruction of the angular momentum distribution of the captured electrons, developed within the scope of this thesis. Moreover, CX measurements of fully ionized sulfur interacting with neutral CS_2 were conducted in order to investigate the proposed explanation of Ref. [83] for the origin of the 3.5 keV dark matter line. Additionally, an in-situ charge exchange experiment in the EUV range in an electron beam ion trap is presented. Here, the CX interaction of O^{8+}, O^{7+}, and O^{6+} with neutral O_2 was investigated with a grating spectrometer in a wavelength range of $8-20$ nm.

This thesis is structured as follows. In the second chapter, the theoretical fundamentals relevant for the description of charge exchange and atomic processes in an electron beam ion trap, in general, are provided. In the third chapter, the single components and the function principle of an EBIT are briefly described with the focus on the CANREB-EBIS, which was developed and characterized within the scope of this work. In the fourth chapter, the experimental setup, the data acquisition, and the charge exchange measurements of highly charged argon, sulfur, and oxygen are presented with subsequent analysis and interpretation. The last chapter is dedicated to the summary of the experimentally obtained

results and comparison to theoretical models, a discussion of the interpretation and an outlook with regards to future experiments and space missions investigating the process of charge exchange.

2 Theoretical fundamentals

In this chapter, a brief description of the theoretical fundamentals relevant to this work will be provided. Since ionic systems with one electron, hereafter denoted as hydrogen-like, or H-like systems are investigated in the measurements, the starting point will be the quantum-mechanical description of the hydrogen atom followed by the expansion of the approach to multi-electron systems. In the third part, explanations of atomic processes in plasmas with a focus on the process of charge exchange, which is the central component of this thesis, will be provided.

2.1 Fundamentals of quantum mechanics

2.1.1 The hydrogen atom

The simplest atomic system is atomic hydrogen composed of an electron in a Coulomb potential V of a proton described by

$$V = -\frac{Ze^2}{4\pi\epsilon_0|\vec{r}|} \tag{2.1}$$

with atomic number $Z = 1$, elementary charge e, the permittivity of free space ϵ_0 and the distance r between the proton and the electron. According to N. Bohr [37], the energy level of a bound electron in the shell n can be calculated to

$$E_n = -R_y \frac{Z^2}{n^2}, \quad R_y = \frac{m_e e^4}{8h^2\epsilon_0^2}, \quad n = 1, 2, 3, ...N \tag{2.2}$$

with electron mass m_e, Planck constant h, the principal quantum number n, and Rydberg energy $R_y = hcR_\infty \approx 13.6\,\mathrm{eV}$ where R_∞ is the Rydberg constant. The Schrödinger equation [144, 145, 146]

$$\widehat{\mathrm{H}}\Psi(\vec{r}, t) = i\hbar\frac{\partial}{\partial t}\Psi(\vec{r}, t) \tag{2.3}$$

for this system has an analytical solution where the eigenvalues of the Hamilton operator

$$\widehat{\mathrm{H}} = -\frac{\hbar}{2m_e}\Delta_r + V(\vec{r}, t) \tag{2.4}$$

are equivalent to equation 2.2. The major difference to the approach in 2.2 is the consideration of wave functions $\Psi(\vec{r}, t)$. By separation of $\Psi(\vec{r}, t)$ into a radial part $R_{nl}(r)$ and an angular part $Y_{lm}(\Theta, \Phi)$ the solution of the Schrödinger equation is given by

$$\Psi(\vec{r}, t) = R_{nl}(r) Y_{lm}(\Theta, \Phi) \tag{2.5}$$

with the spherical harmonics Y_{lm} and

$$R_{nl} = D_{nl} \exp\left(-\frac{Zr}{na_0}\right)\left(\frac{2Zr}{na_0}\right)^l L_{n+l}^{2l+1}\left(\frac{2Zr}{na_0}\right) \tag{2.6}$$

with Laguerre polynomials L_{n+l}^{2l+1}, a normalization constant D_{nl}, and a constant a_0 which can be interpreted as the classical Bohr radius for the ground state. The wave functions describe electron probability densities instead of discrete orbits. For high principal quantum numbers n the system is in a so-called Rydberg state which approaches a classical orbital according to the correspondence principle. The energy levels are n^2-fold degenerated, and the system is fully described by the principal quantum number $n = 1, 2, 3, \ldots, N$, the angular quantum number $l = 0, 1, 2, \ldots n - 1$ and the magnetic quantum number $m = -l, -l + 1, \ldots, l - 1, +l$.

In first-order approximation, the theory provides accurate values for the energy levels, but within the frame of the theory of special relativity, this approach is not Lorentz-invariant. In 1928 P. Dirac presented a covariant formulation of the Schrödinger equation. Here the relativistic energy-momentum relation

$$E^2 = \vec{p}^2 c^2 + m_0^2 c^4 \tag{2.7}$$

has to be satisfied. The most straightforward approach is an introduction of a Hamilton operator

$$\widehat{H} = c\vec{\alpha}\vec{p} + \beta m c^2 \tag{2.8}$$

where $\vec{\alpha}$ and β are 4×4 matrices that fulfill the relation $\vec{\alpha}^2 = \mathbb{1}$ and $\beta^2 = \mathbb{1}$. The eigenvalues of the Hamilton operator are given by

$$E = \pm\sqrt{c^2\vec{p} + m_0 c^4}, \tag{2.9}$$

where the negative solution of the energy describes the anti-particles. By consideration of the Coulomb potential, the complete Dirac equation can be written as

$$E\Psi = \left(c\vec{\alpha}\vec{p} + \beta m_e c^2 - \frac{Z\alpha}{|\vec{r}|}\right)\Psi. \tag{2.10}$$

with the Sommerfeld's fine-structure constant $\alpha = e^2/4\pi\epsilon_0 ch$. An expansion of those eigenvalues in terms of $Z\alpha$ leads to

$$E_{nj} = m_0 c^2 \left[1 - \frac{(Z\alpha)^2}{2n^2} - \frac{(Z\alpha)^4}{2n^3} \left(\frac{1}{j+1/2} - \frac{3}{4n} \right) + \dots \right] \tag{2.11}$$

with the total angular momentum $j = l \pm \frac{1}{2}$. The first term describes the rest energy of the electron, the second term the binding energy in the Coulomb potential and the third term can be interpreted as the relativistic increase of the mass and the interaction between the spin and the angular momentum of the electron. Due to this spin, a magnetic moment $\vec{\mu}_S$ is induced which can interact with external magnetic fields or magnetic moments of other electrons. The interaction of $\vec{\mu}_S$ with the induced magnetic moment due to the motion of the electron in the Coulomb potential of the nucleus is denoted as the spin-orbit coupling (LS-coupling) where the non-relativistic energy levels are split. The splitting is termed as the fine structure which scales with a factor $\frac{(Z\alpha)^2}{n}$ concerning the binding energy. The interaction of the spin and the angular momentum with the nuclear spin leads to a splitting which is called hyperfine structure, which is smaller by a factor of 2000 than the fine-structure splitting.

By including the interactions with the quantized electromagnetic field more effects which shift the energy levels manifest, referred to as quantum-electrodynamics (QED). In the first-order approximation, only interactions with one single virtual photon are considered leading to two effects: the self-energy and the vacuum polarization. The self-energy is denoted as the interaction between an electron with itself by emission and subsequent absorption of a virtual photon where the trajectory of the electron is slightly perturbed. The vacuum polarization is a short-termed creation and annihilation of electron-positron pairs leading to a slight deviation from the Coulomb interaction resulting in a cancellation of the degeneracy of the $2s_{1/2}$ and the $2p_{1/2}$ state which was experimentally shown in 1947 by Lamb and Retherford [105]. This effects scale with a factor of $Z\alpha^2/n^3$.

2.1.2 Multi-electron systems

For systems containing more than one electron, the interaction between the electrons among each other has to be considered. Therefore an analytical solution of the Schrödinger equation can not be provided in general. In the non-relativistic case, the Hamiltonian for an N-electron system is given by

$$\widehat{H}_{\text{Tot}} = \sum_{i=1}^{N} \left(\frac{\widehat{p}^2}{2m_e} + V(\vec{r}_i) \right) + \sum_{i<j} \frac{e^2}{|\vec{r}_i - \vec{r}_j|} \tag{2.12}$$

with total number N of electrons, the momentum operator $\widehat{p}$, electron mass m_e, charge e and position vector $\vec{r}_i$ of the i-th electron. The corresponding Schrödinger equation can be solved by a Hartree-Fock approximation [87, 69]. The approach is an assignment of a wave function to each electron with a modified nuclear potential by the remaining electrons. The total wave function $|\Psi(1, \ldots, N)\rangle$ of the system can be written as a product of the single-electron wave functions $\psi(i)$, by the satisfaction of the Pauli principle which prohibits two electrons from populating the same quantum state. Thus the wave function can be represented by a slater determinant

$$|\Psi(1, \ldots, N)\rangle = \frac{1}{\sqrt{N!}} \begin{vmatrix} \psi_1(1) & \psi_2(1) & \cdots & \psi_N(1) \\ \psi_1(2) & \psi_2(2) & \cdots & \psi_N(2) \\ \vdots & \vdots & \ddots & \vdots \\ \psi_1(N) & \psi_2(N) & \cdots & \psi_N(N) \end{vmatrix}. \tag{2.13}$$

The solution of the Schrödinger equation is obtained by a numerical method, where the single wave functions are iteratively varied in order to minimize the energy of the system. In each iteration the nuclear potential is adjusted for the wave functions $\psi(i)$, considering the screening effects. The relative uncertainty of this approach is in the order of $0.5\,\%$. For a relativistic treatment of the system, the Hamiltonian has to be modified. The Dirac-Coulomb-Breit operator

$$\widehat{H}_{\mathrm{DCB}} = \sum_{i=1}^{N} \widehat{H}_{\mathrm{Dirac}} + \sum_{i<j} \frac{e^2}{r_{ij}} - \sum_{i<j} \widehat{B}_{ij} \tag{2.14}$$

is a composition of the Dirac-Hamilton operator $\widehat{H}_{\mathrm{Dirac}}$, Coulomb repulsion $\frac{e^2}{r_{ij}}$ of two electrons and the Breit operator $\widehat{B}_{ij}$. The latter two operators are represented by

$$\widehat{H}_{\mathrm{Dirac}} = \left(c\alpha \times \left(\widehat{p} - \frac{e}{c}\vec{A} \right) + \beta mc^2 + e\Phi \right) \tag{2.15}$$

$$\widehat{B}_{ij} = \frac{e^2}{2r_{ij}} \left(\vec{\alpha}_i\vec{\alpha}_j + \frac{(\vec{\alpha}_i r_{ij})(\vec{\alpha}_j r_{ij})}{|\vec{r}_{ij}|^2} \right), \tag{2.16}$$

respectively. The Dirac operator describes the coupling to an electrical field with a vector potential $\vec{A}$, a scalar potential $e\Phi$ and the Dirac matrices $\vec{\alpha}$ and β, described in equation 2.8. The magnetic interaction between the electrons and the retardation of the magnetic and electric potentials are considered by the Breit operator in the first-order approximation in αZ. Second-order quantum electrodynamical (QED) effects like vacuum polarization where an electron interacts via a virtual photon with a virtual electron-positron pair, are disregarded.

Modern theoretical many-body QED approaches utilize perturbational and variational

calculus to determine the properties of many-electron systems. The method relevant for this work is the configuration interaction method (CI), where the total wave function is composed of a linear combination

$$\Psi_{\text{Tot}} = \sum_{i=1}^{n} c_i \Phi_i \tag{2.17}$$

of n states with the electron configurations Φ, which is a combination of single-electron wave functions, in analogy to the Slater determinant in equation 2.13, and the mixing coefficients c_i. By variation of the mixing coefficients with predetermined Φ_i, the total energy of the many-body system is minimized. This method is applied by the flexible atomic code (FAC) [85] utilized in this work. Other approaches like the Multi-Configuration-Hartree-Fock (MCHF), Multi-Configuration-Dirac-Fock (MCDF) or perturbation theoretical methods like the Relativistic Many-Body Perturbation Theory (RMBPT) [121] are not discussed within the frame of this thesis.

2.2 Fundamentals of plasma physics

2.2.1 Highly charged ions

Atoms, where most of the electrons with regard to their atomic number are detached, are denoted as highly charged ions (HCI). Like a neutral atom, it is a system consisting of a nucleus with a specific charge and one or multiple bound electrons. A particular case of an HCI is a fully ionized atom, where all electrons are removed, and only the nucleus remains. One of the established notations for the specification of the charge state is the spectroscopic notation, where the ionization state of the ion is given by the symbol of the regarded element followed by a Roman numeral, where I represents the neutral. An argon atom with the atomic number $Z = 18$ and one remaining electron, for example, is denoted as Ar XVIII. The charge state can also be described by an isoelectronic notation of the number of the remaining electrons N to the corresponding neutral element with N electrons. In the case of Ar XVIII, it can be termed as hydrogen-like. Another notation of the charge state is the symbol of the element with the superscripted Arabic number of removed electrons or remaining positive charges with a following plus sign. For the example of hydrogen-like argon, it is Ar^{17+}. Analogous to neutral atomic systems the electronic shell of HCIs can interact with photons, free electrons or loosely bound electrons of neutral systems. The latter interaction is denoted as charge exchange and is the main subject of this thesis. In the following sections, these interactions will be briefly described.

2.3 Atomic processes in plasmas

2.3.1 Excitation

An ion can be excited to a higher energetic state by the addition of energy into the system. Thereby a bound electron is elevated into a higher energetic level if the added energy is sufficient to induce this transition.

2.3.1.1 Electron-impact excitation

In the case of energy transfer by a free electron to the ionic system, the process is designated as electron-impact excitation of the form

$$A + e^-_{\text{kin}} \rightarrow A^* + e^-_{\text{kin}'}, \tag{2.18}$$

where A represents the ion and e^-_{kin} a free electron with a specific kinetic energy. After the collision the ionic system is in an excited state A^*. The cross-section σ_{EIE} for this process is given by the Bethe approximation [140]

$$\sigma_{\text{EIE}} = \frac{8\pi}{\sqrt{3}} \frac{1}{E_{\text{kin}}} \frac{I_{\text{H}}}{E_j - E_i} f_{ij} g a_0^2 \tag{2.19}$$

with the kinetic energy of the free electron E_{kin}, the threshold ionization energy of atomic hydrogen I_{H}, the classical Bohr radius a_0, Gaunt factor g, and the corresponding oscillator strength f_{ij} of the transition from an initial level j to the final level i with energies E_j and E_i, respectively. The Gaunt factor is a quantum-mechanical correction for the classical absorption cross-section and describes the probability of the transition of an incident electron to an energetic state $E_{\text{kin}'}$ as a function of the initial kinetic energy E_{kin}.

2.3.1.2 Photoexcitation

If a photon transfers the energy for the excitation with energy $h\nu$, the process is denoted as photoexcitation with the corresponding reaction equation

$$A + h\nu \rightarrow A^*. \tag{2.20}$$
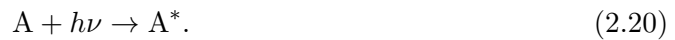
In contrast to electron-impact excitation, the photoexcitation is a resonant process that only occurs if the energy of the incident photon matches the energy difference of the initial and excited state. This process can be considered as an interaction of the electronic shell with a radiation field. On the other hand, a transition from an excited state to an energetically lower state can occur by the emission of one or multiple photons. This process

is given by

$$A^* \rightarrow A + nh\nu_n \tag{2.21}$$

with an integer number n of photons with energy $h\nu$. Since no laser-spectroscopic measurements are performed and the energy spectral densities of the radiation field in the plasma are comparably low, this process will not be discussed further.

2.3.1.3 Ion-Ion collisions

In general energy transfer by inelastic ion-ion collision is possible, but due to strong Coulomb repulsion, the bound electron experience a small energy change and thus only energetically adjacent states can be populated [172]. For higher collision energies above 10 keV, ion-ion collisions become essential. In Ref. [172], the cross-section for this process is derived analogously to the Bethe approximation for electron-impact excitation, modified with certain scaling relations. Since the collision energies investigated in this work are comparably small, this process will be neglected.

2.3.2 Ionization

The primary mechanism for the production of highly charged ions in the following experiments is electron-impact ionization, where an initially neutral atom interacts with free electrons with a specific kinetic energy. The loosely bound electrons of the system are subsequently detached by impact with the free electrons until their kinetic energy does not suffice to exceed the ionization potential. The reaction mechanism is described by

$$A^{q+} + e^- \rightarrow A^{(q+1)+} + 2e^- \tag{2.22}$$

with an ion A in charge state q. The cross-section for this process as a function of the kinetic energy E_{kin} of the free electron is given by the semi-empirical Lotz formula [116]

$$\sigma_{EII} = \sum_{i=1}^{N} a_i k_i \frac{\ln\left(E_{kin}/E_B\right)}{E_{kin}E_B} \left\{ 1 - b_i \exp\left[-c_i \left(\frac{E_{kin}}{E_B} - 1 \right) \right] \right\} \tag{2.23}$$

with the binding energy $E_B \leq E_{kin}$ of the released electron and the number k_i of electrons in the subshell i. The parameters a_i, b_i and c_i depend on the element and have to be determined experimentally. For $E_{kin} < E_B$ no ionization can occur. For $E_{kin} = E_B$ the cross-section is zero and achieves a maximum at $E_{kin} \approx 2.3 E_B$. For high collision energies $E_{kin} \gg E_B$ equation 2.23 can be simplified to

$$\sigma_{EII} \approx \frac{\ln E_{kin}}{E_B}. \tag{2.24}$$

Furthermore, a bound electron can be detached by absorption of a photon with sufficient energy according to

$$A^{q+} + h\nu \rightarrow A^{(q+1)+} + e^- \tag{2.25}$$

with a photon energy $h\nu \geq E_B$. This process is denoted as photoionization.

2.3.2.1 Auger-Meitner decay

The detachment of an electron by interaction with a photon can also occur resonantly via an autoionizing state. This process is denoted as Auger-Meitner decay and is illustrated schematically in figure 2.1. In the first step an inner-shell electron can be excited to a higher energetic level by absorption of the photon resulting in a doubly excited state as shown in panel 1) of the Auger decay in the figure. Relaxation to the ground state can proceed non-radiatively by transfer of the energy to an excited electron, releasing it into the continuum (panel 2)).

2.3.3 Recombination of ions with electrons

The time inverse processes to the corresponding ionization mechanisms discussed in the previous section, ceasing with a free electron into the continuum, are indicated as recombination processes. In general, the reaction is given by

$$A^{q+} + e^- \rightarrow A^{(q-1)+} + h\nu. \tag{2.26}$$

2.3.3.1 Radiative recombination

A capture of a free electron into a bound state of an ion is denoted as radiative recombination (RR), which is the time-inverse process of photoionization (compare RR panel of figure 2.1). Here a free electron with kinetic energy E_{kin} recombines into a bound state by emission of a photon with an energy corresponding to the sum of the kinetic energy and the binding energy of the captured electron with

$$h\nu = E_{kin} + E_B. \tag{2.27}$$

The cross-section of this non-resonant process is given by a modified Kramers formula [100]

$$\sigma_{RR} = \frac{8\pi}{3\sqrt{3}} \frac{\alpha^5}{n^3} \frac{Z_{Eff}^4}{E_{kin}E_\gamma}, \tag{2.28}$$

where n represents the principal quantum number of the state in which the electron is captured, Z_{Eff} the effective charge and E_γ the photon energy.
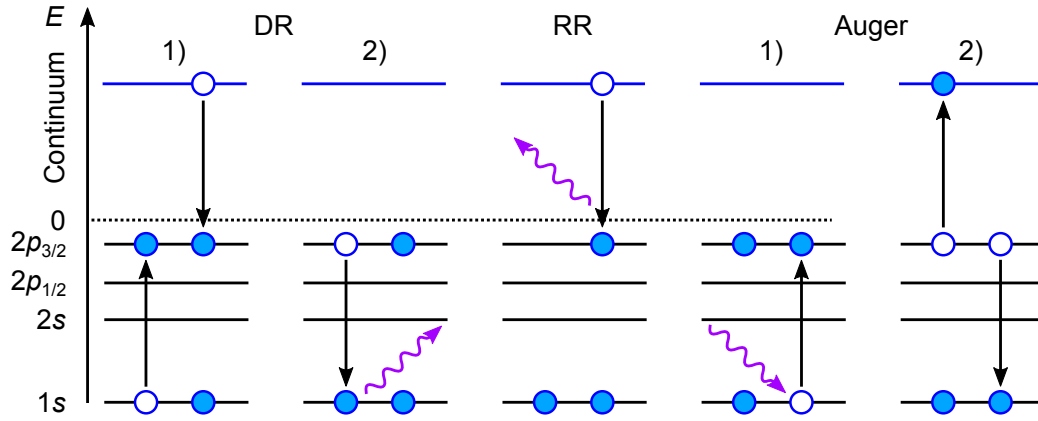
Figure 2.1: Schematic illustration of the process of dielectronic recombination (DR), radiative recombination (RR) and Auger decay.

2.3.3.2 Resonant recombination

Electron capture can also occur resonantly. Here a free electron with kinetic energy E_{kin} recombines into a bound state by simultaneous excitation of one or several inner-shell electrons as illustrated in the first step of the DR panel in figure 2.1). The first-order recombination process, where one inner-shell electron is excited, is denoted as dielectronic recombination, according to the scheme

$$\mathrm{A}^{q+} + e^- \rightarrow \mathrm{A}^{((q-1)+)**} \rightarrow \mathrm{A}^{(q-1)+} + h\nu \tag{2.29}$$
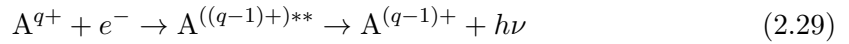
with an intermediate doubly excited state $\mathrm{A}^{((q-1)+)**}$. Here, the sum of the kinetic energy of the electron and the binding energy of the state, in which the electron is captured, has to match the energetic difference between the ground state and the excited state of the excited electron. By emission of a photon with a characteristic energy corresponding to the energetic difference between the excited and final state, the system stabilizes to the ground state.

Analogously to the Auger notation, the shell of the initial state of the excited electron is termed first, followed by the shell of its final state and at last the shell in which the free electron recombines. For example, a free electron is captured into the L-shell by excitation of a K-shell electron into the L-shell. This specific resonant capture process is denoted as K-LL dielectronic recombination. Processes of higher orders like trielectronic recombination have been investigated in other works [30, 29, 28, 27] and will not be discussed further.

2.3.4 Charge exchange

Charge exchange (hereafter denoted as CX) is a semi-resonant atomic process where a highly charged ion interacts with a neutral molecule or atom in proximity, leading to a transfer of one or more loosely bound electrons of the neutral target to an excited state of the highly charged projectile followed by radiative stabilization to the ground state. This process can be described as

$$A^{q+} + B \rightarrow A^{(q-n)+*} + B^{n+} \rightarrow A^{(q-n)+} + B^{n+} + mh\nu, \qquad (2.30)$$
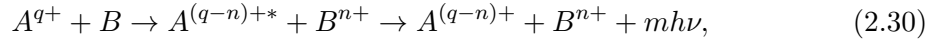
where A is the atomic number of the projectile ion with charge q, B the atomic number of the neutral target and n the number of captured electrons.

During the CX process, the highly charged projectile approaches the neutral target leading to a superposition of their electrostatic potentials and thus to a distortion of the energy levels. At certain internuclear distances R_n of the donor and the projectile, the energy levels overlap, and the system forms a quasi-molecule. At this so-called "curve crossings", the electron of the donor may be transferred non-radiatively to the projectile [173]. Curve crossings occur at different internuclear distances R_n leading to a possible capture of the electron into different energy states. Preferably those energy levels of the HCI are populated which match approximately the binding energy of the loosely bound electron of the donor resulting in a capture into a high Rydberg state peaked around a principal quantum number n_{CX}. The distribution of the angular momentum states and spin states strongly depends on the species of the projectile, the donor, the relative collision velocity between both and the number of transferred electrons [95].

In case that the donor has more than one electron, multi-electron capture is also possible introducing additional processes and interactions like auto-ionization, true double capture, correlated double capture, interatomic auger decay, et cetera increasing the complexity of the describing model tremendously. Signatures of multi-electron capture have been observed by other groups [93, 9, 10], but only single-electron capture will be considered within the scope of this thesis.

The quasi-molecule dissociates due to a Coulomb explosion resulting in a highly charged ion with a reduced charge and an initially neutral with increased charge. CX between an HCI and an ion is also possible, but the cross-section for this process is small due to Coulomb repulsion and therefore will be neglected in this work.

The shape of the spectra resulting from charge exchange is highly sensitive to the quantum numbers of the state in which the electron is captured. The population of low angular momentum states predominantly leads to emission of photons with somewhat higher energy (compare to figure 2.2). Due to selection rules, an electron in the initial state np can decay directly to the ground state 1s. An electron in ns may decay to $(n-1)$p and
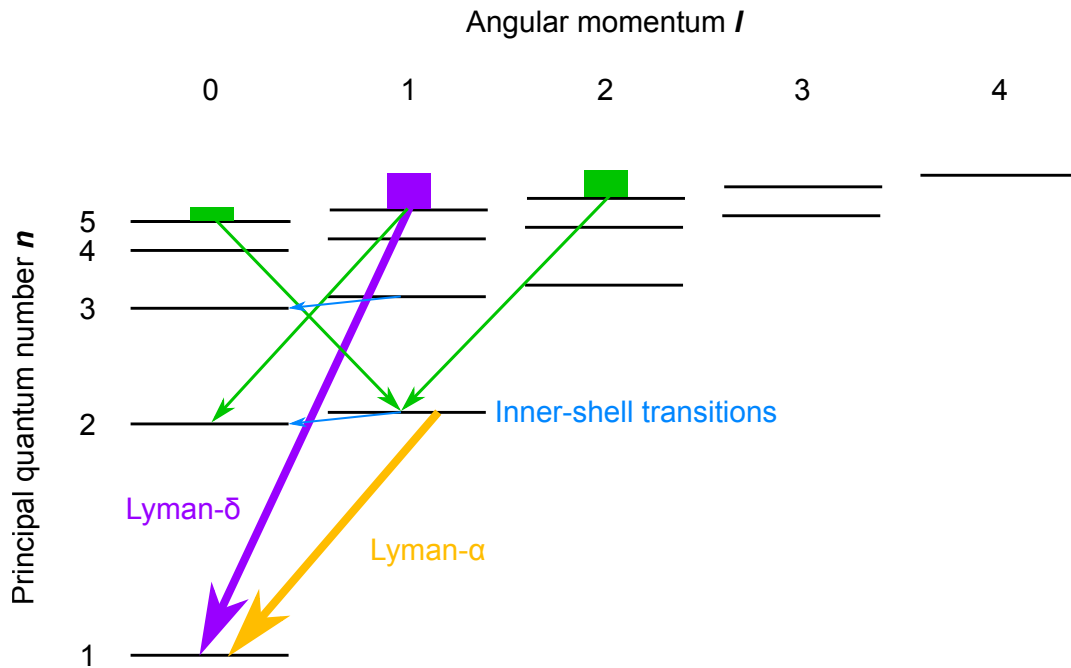
Figure 2.2: Electron capture in lower angular momentum states will lead to emission of photons with comparably higher energy.

subsequently to the ground state.

However, an electron in a high angular momentum state nl would reduce its angular momentum by radiative cascades with $\Delta n = -1$ and $\Delta l = -1$ to the ground state resulting in the emission of several comparably low energetic photons (compare to figure 2.3).

In order to understand the CX spectra of astronomical observations or laboratory measurements, detailed state-resolved models are required. In the following, a brief description of the most common theoretical models which are applied for different ranges of collision velocities between target and projectile will be given.

2.3.4.1 The classial over-the-barrier model (COB)

A simple approximation applicable for collision energies between the highly charged projectile and the neutral target in the range between $100 \, \text{eV/amu}$ and $10 \, \text{keV/amu}$ [36] is given by the classical over-the-barrier (COB) model [142]. The basic principle is that a highly charged projectile together with a neutral target in proximity form a joint electrostatic potential, where the captured electron can move freely inside this potential well leading to the formation of a quasi-molecule. The requirement for this process is that the height of the potential well between projectile and target is lower than the ionization energy of the target electron.

The joint potential V between the two nuclei with an internuclear distance R can be
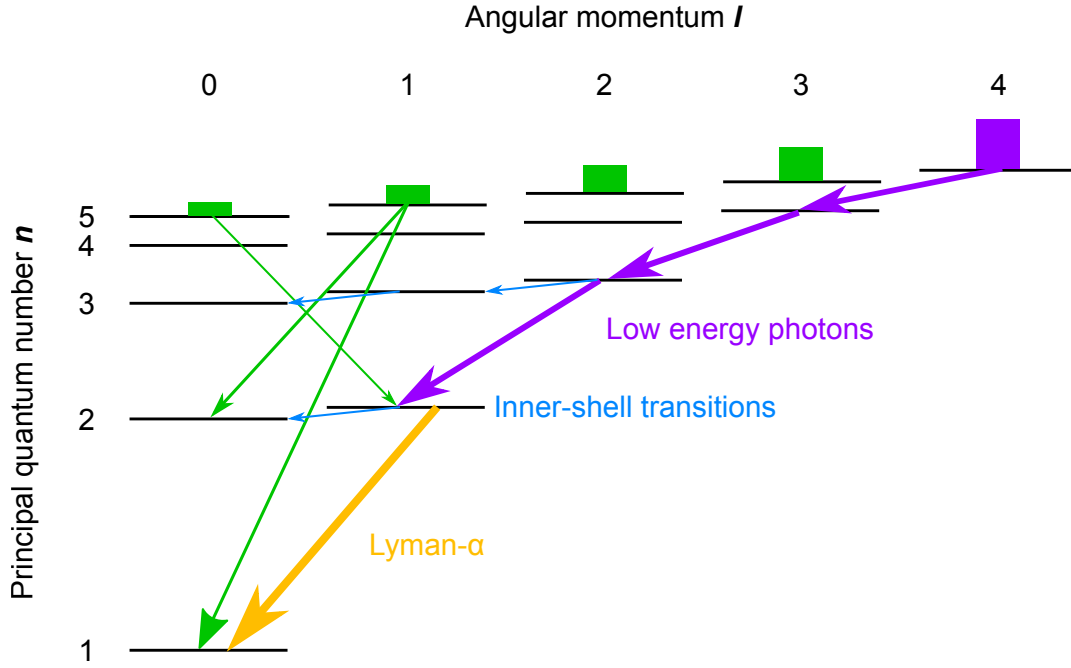
Angular momentum *l*

Figure 2.3: Electron capture into higher angular momentum states will lead to emission of several photons with comparably lower energy.

written as

$$V(r) = -\frac{q}{|R - r|} - \frac{1}{|r|} \quad \text{for} \quad 0 < |r| < |R|, \tag{2.31}$$

where r represents the distance to the target nucleus and q the charge of the projectile.

Calculating the zero-crossing of the first derivative of $V(r)$ provides both, the position r_0 of the top of the potential with

$$r_0 = \frac{R}{\sqrt{q} + 1} \tag{2.32}$$

and the height of the potential barrier V_{max} with

$$V_{\mathrm{max}} = -\frac{(\sqrt{q} + 1)^2}{R}. \tag{2.33}$$

The loosely bound electron of the neutral has at infinite distance $R = \infty$ a binding energy of I_{P}, which is increased due to the Stark shift caused by the approaching Coulomb potential of the projectile:

$$I(R) = I_{\mathrm{P}} - \frac{q}{R}. \tag{2.34}$$

The electron is transferred if $V_{\max}$ is lower than its binding energy:

$$-\frac{(\sqrt{q}+1)^2}{R} \leq I_\mathrm{P} - \frac{q}{R}. \tag{2.35}$$

Setting this condition leads to the internuclear separation R_CX, where the charge exchange occurs with

$$R_\mathrm{CX} = \frac{2\sqrt{q}+1}{-I_\mathrm{P}}. \tag{2.36}$$

After dissociation of the quasi-molecular state, the potential barrier increases with increasing distance of both collision partners and the initial binding energy of the captured electron at the barrier crossing is lowered due to the Stark shift. The charge of the projectile is reduced, and the charge of the target is increased by one, respectively:

$$I_\mathrm{f} = I_\mathrm{P}(R_\mathrm{CX}) + \frac{1}{R_\mathrm{CX}} = I_\mathrm{P} - \frac{q-1}{R_\mathrm{CX}}. \tag{2.37}$$

With a classical approximation of the energy levels $E_n = q/n^2$, the principal quantum number n_CX in which the electron is captured can be estimated to

$$n_\mathrm{CX} = \frac{q}{\sqrt{|I_\mathrm{f}|}} = \frac{q}{\sqrt{\left|-I_\mathrm{P}\left(1+\frac{q-1}{2\sqrt{q}+1}\right)\right|}} \tag{2.38}$$

with the argument inside the square root given in atomic units. The cross-section for this process can be determined geometrically from equation 2.36 with

$$\sigma = \pi R_\mathrm{CX}^2 = \pi \left(\frac{2\sqrt{q}+1}{-I_\mathrm{P}}\right)^2, \tag{2.39}$$

which is typically in the order of $10^{-15} - 10^{-14}\,\mathrm{cm}^2$. As an example, a collision between an Ar^{18+} ion and neutral argon is illustrated in figure 2.4. The initial ionization potential of the neutral is $I_\mathrm{P} = -15.76\,\mathrm{eV}$. At an internuclear distance of $R_\mathrm{CX} = 8.2\,\mathrm{a.u.}$, the electron is captured in a quasi-molecular state with a binding energy of $I_\mathrm{P} = -45.65\,\mathrm{eV}$. After transfer of the electron to the projectile and dissociation of the quasi-molecular state the final binding energy is $I_\mathrm{f} = -44.0\,\mathrm{eV}$ corresponding to a principal quantum number $n_\mathrm{CX} = 10$ according to equation 2.38, in which the electron is captured.

In figure 2.5, the calculated principal quantum number n_CX is plotted as a function of the charge state of the projectile for collisions with different targets.

The COB gives a reasonable estimate of the cross-section for CX and the most probable level n_CX for electron capture, but it does not provide an $n-$ or l-distribution. The incorporation of conservation of the angular momentum l of the captured electron to the COB model is given in Ref. [43]. This extension is based on the principle that an electron
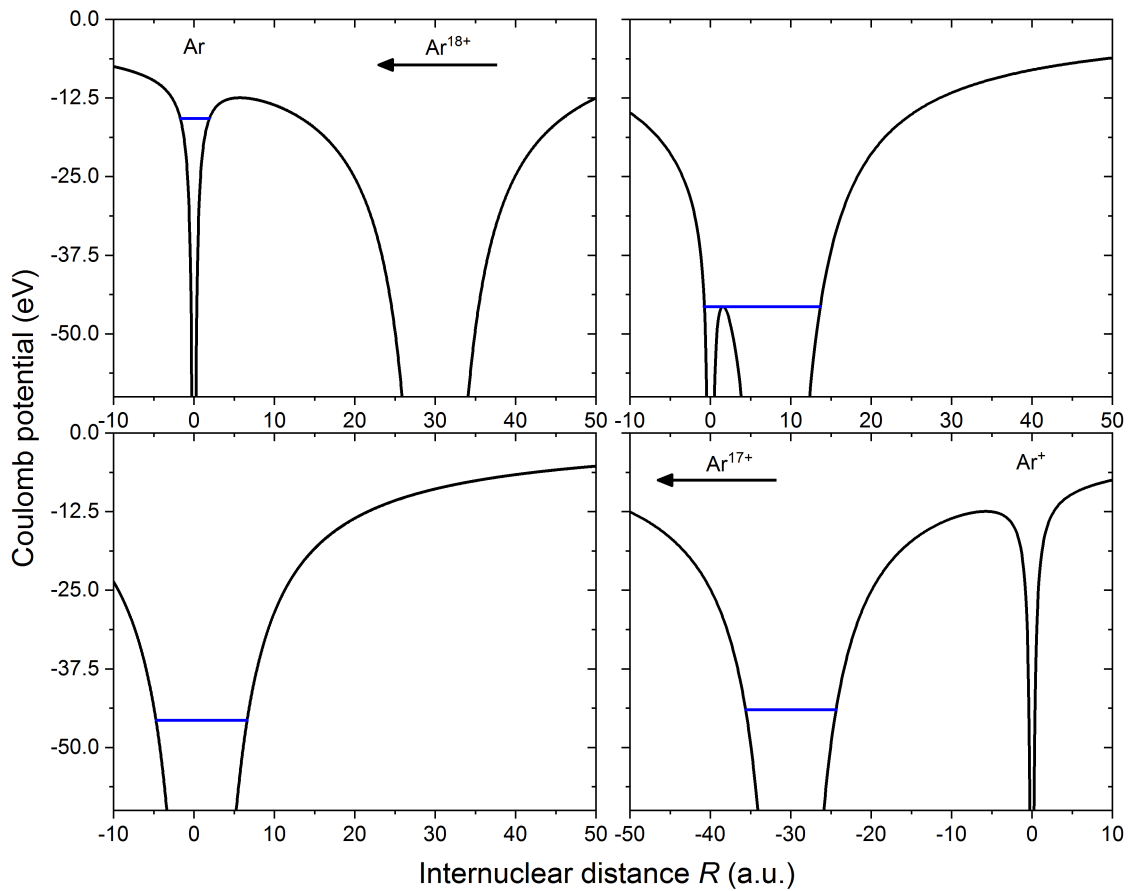
Figure 2.4: Top left: An Ar^{18+} is approaching a neutral argon atom at $R = 0$. **Top right:** At $R = R_{CX} = 8.2$ a.u. the potential barrier is lowered, and the electron of the neutral may be transferred. **Bottom left:** The system forms a quasi-molecular state where the binding energy of the shared electron does not change. **Bottom right:** Dissociation of the quasi-molecular state. The charge of the projectile is lowered, and the charge of the target increased by one, respectively. The binding energy of the captured electron in the final state is lowered due to the Stark shift caused by the charged target.
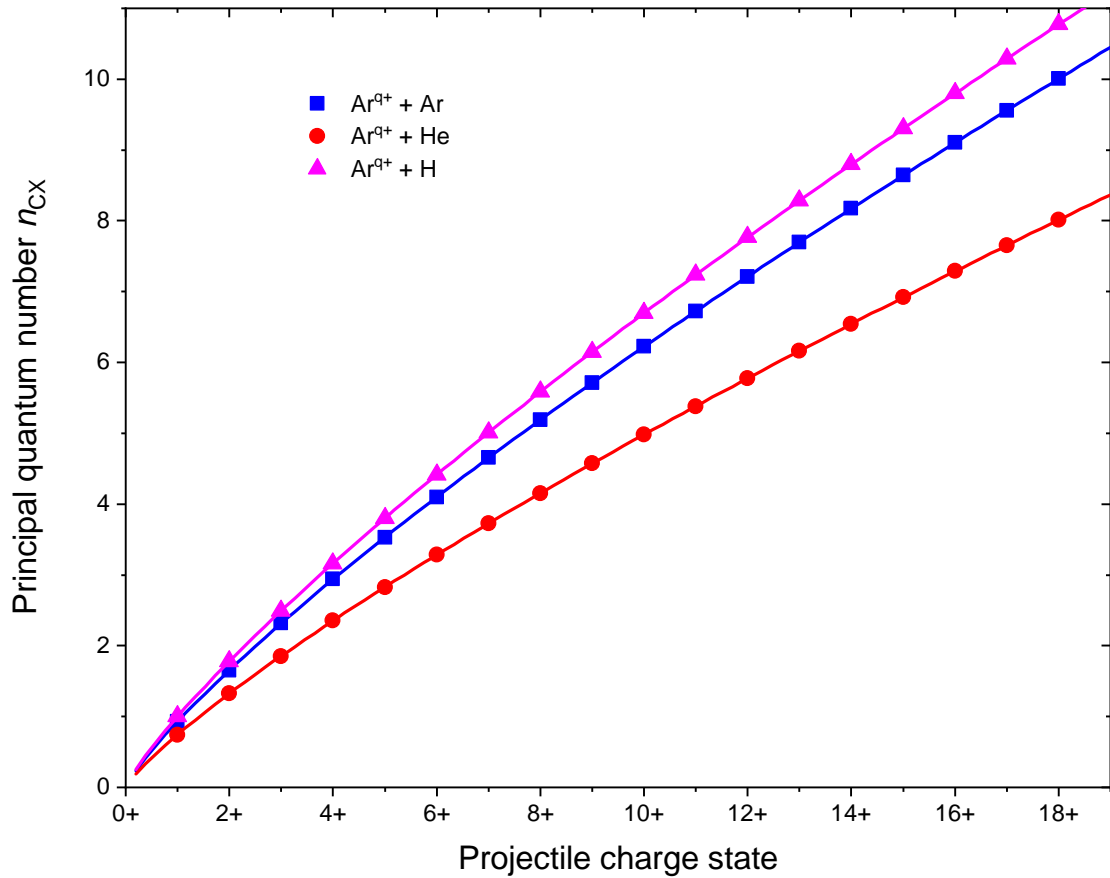
Figure 2.5: Most probably quantum number n_{CX} in which an electron is captured during CX as a function of the charge of the argon projectile for collisions with different targets, according to the classical over-the-barrier model.

of the target has an angular momentum in the order of bv with respect to the co-moving frame of the projectile, where b represents an impact parameter and v the relative velocity of the collision partners. The total CX cross-section σ_l is given by

$$\sigma_l = A2\pi \int_0^{R_{\mathrm{CX}}} W_l(b)b\mathrm{d}b \tag{2.40}$$

with a proportionality factor A and the probability distribution $W_l(b)$ as a function of the impact parameter b. The distribution $W_l(b)$ can be written as

$$W_l(b) = \Theta(l + 1 - bv)\Theta(bv - l), \tag{2.41}$$

where the step function Θ represents the conservation of the angular momentum.

Including the centrifugal potential of the captured electron with angular momentum l leads to a modified internuclear separation R'_{CX} where charge exchange occurs with

$$R'_{\mathrm{CX}}(n_{\mathrm{CX}}(l)) = \frac{2(q-1)}{-2|I_{\mathrm{P}}| + q^2/n_{\mathrm{CX}}(l)^2}. \tag{2.42}$$

The principal quantum number $n_{\mathrm{CX}}(l)$ as a function of the angular momentum l is given by

$$n_{\mathrm{CX}}(l) = q\sqrt{\frac{2\sqrt{q}+1}{2|I_{\mathrm{P}}|(q+2\sqrt{q})}} \times \sqrt{1 + \frac{(q-1)(q+\sqrt{q})^2|I_{\mathrm{P}}|l^2}{2q(2\sqrt{q}+1)^3}}. \tag{2.43}$$

Additionally, a proportionality factor A is introduced, which represents an angular momentum distribution with

$$A = \frac{2l + 1}{2l + 1 + n^2}. \tag{2.44}$$

The normalization of $W_l(b)$ leads to

$$W_l(b) = \frac{1}{\sqrt{\pi}\Delta l}\left[\exp\left(-\frac{l'-vb}{\Delta l}\right)^2 + \exp\left(-\frac{l'+vb}{\Delta l}\right)^2\right], \tag{2.45}$$

where $\Delta l = R_{\mathrm{CX}}\sqrt{2/(3\sqrt{\pi})\Delta E}$ represents the width of the l-distribution around $l' = l + 1/2$ with the uncertainty of the barrier height ΔE.

With equation 2.40, 2.44, and 2.45 the l-resolved cross-section σ_l can be calculated to

$$\sigma_l = \frac{2l+1}{2l+1+n^2}\frac{2\sqrt{\pi}}{\Delta l}\int_0^{R_{\mathrm{CX}}} b\mathrm{d}b\left[\exp\left(-\frac{l'-vb}{\Delta l}\right)^2 + \exp\left(-\frac{l'+vb}{\Delta l}\right)^2\right]. \tag{2.46}$$

The theoretical cross-sections, according to equation 2.46, are presented in figure 2.6 for a collision of O^{6+} and atomic hydrogen as a function of the relative collisional velocity.
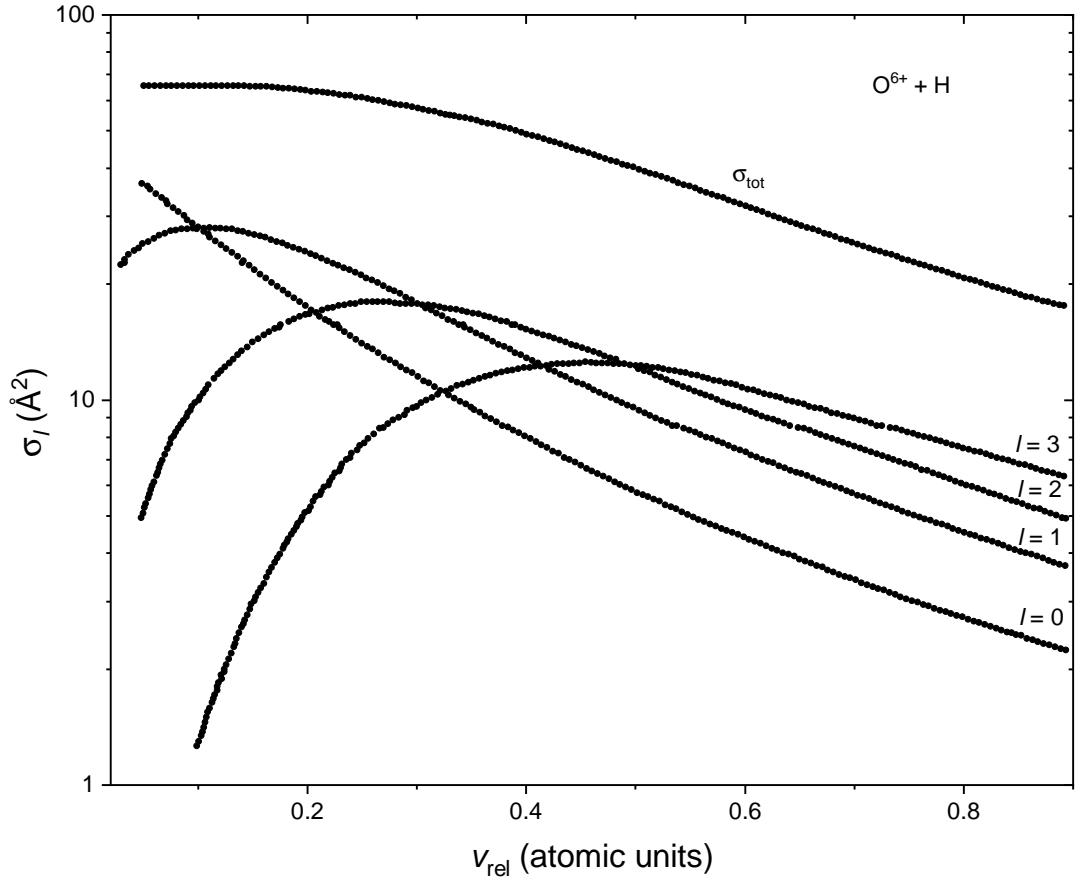
Figure 2.6: Calculated cross-section for collisions between O^{6+} and atomic hydrogen as a function of the relative collision velocity v_{rel} for different angular momentum states. The data is extracted from Ref. [43].

Higher angular momentum values appear at higher collision velocities.

Further extensions of the COB model like multiple electron capture and for partially charged ions, are given in Ref. [129] and will not be covered within the scope of this work.

2.3.4.2 The classical trajectory Monte Carlo method (CTMC)

A different, more sophisticated approach is given in Ref. [7] by utilizing a Monte Carlo method. The model is based on tracing a three-body system consisting of two protons and an electron by determination of the time-dependent phase space of each particle for a large number of particles from a microcanonical ensemble and employment of Kepler's equations and the Bohr-Sommerfield model for atomic hydrogen. An improved model for collisions between highly ionized atoms and atomic hydrogen is described in Ref. [132]. This method is applicable for high collision energies above $\sim 5\,\text{keV/u}$ and not in a good agreement for

relatively low collision energies as predominant in an EBIT plasma [55].

2.3.4.3 The multichannel Landau-Zener approximation (MCLZ)

An accurate model for low-energy collisions is given by the multichannel Landau-Zener approximation (MCLZ) [107, 179] by consideration of quasi-molecular energy configurations between an ion and a neutral for single-electron capture. It provides nlS-resolved cross sections for charge exchange processes [123]. The justification for the quasi-molecular state is the relative low collision velocity $v \ll v_0$ between projectile and target, where v_0 represents the speed of an electron on a classical orbit. The velocity of those electrons is high enough to adjust their motion steadily relative to the position of the two approaching nuclei. The adiabaticity of this collision process is affected by the electron transition time, which is determined by the relation of the time the electron is bound and being transferred between both nuclei [95]. For high collision velocities, the process can be considered as diabatic, for slow collision velocities it becomes adiabatic [113]. At larger internuclear distances R between the neutral target and the highly charged projectile, the interaction can be described by a diabatic potential curve [123] with

$$V_i = A \exp\left(-BR\right) - \frac{\alpha q^2}{2R^4}, \tag{2.47}$$

where A and B in the first term are coefficients estimated in Ref. [44] and the second term describes the polarization potential with the dipole polarizability α of the target and charge q of the projectile. During their approach, the target and the projectile move on an adiabatic potential curve represented as a dashed gray line in figure 2.7. Due to the non-crossing rule, according to Wigner and von Neumann [177], the potential curves of the adiabatic states will never cross. At a particular internuclear distance R_C, a transition from one curve to the other might occur with a specified transition probability which describes the process of a transfer of an electron from the target to the projectile. After transfer of the electron, both collision partners are positively charged, and the Coulomb repulsion dominates, leading to a movement of the system on the outgoing diabatic Coulomb potential curve described by

$$V_\mathrm{Coulomb} = \frac{(q-1)}{R} - \Delta V = V_f \tag{2.48}$$

with initial charge q of the projectile and the potential energy difference ΔV at the avoided curve crossing. $\Delta V = V_{if}$ is given by the Olson-Salop-Taulbjerg formula [133, 163]

$$\Delta V = V_{if} = \left(\frac{9.13 f_{nl}}{\sqrt{q}}\right) \exp\left(-\frac{1.324 R_\mathrm{C} a}{\sqrt{q}}\right) \tag{2.49}$$
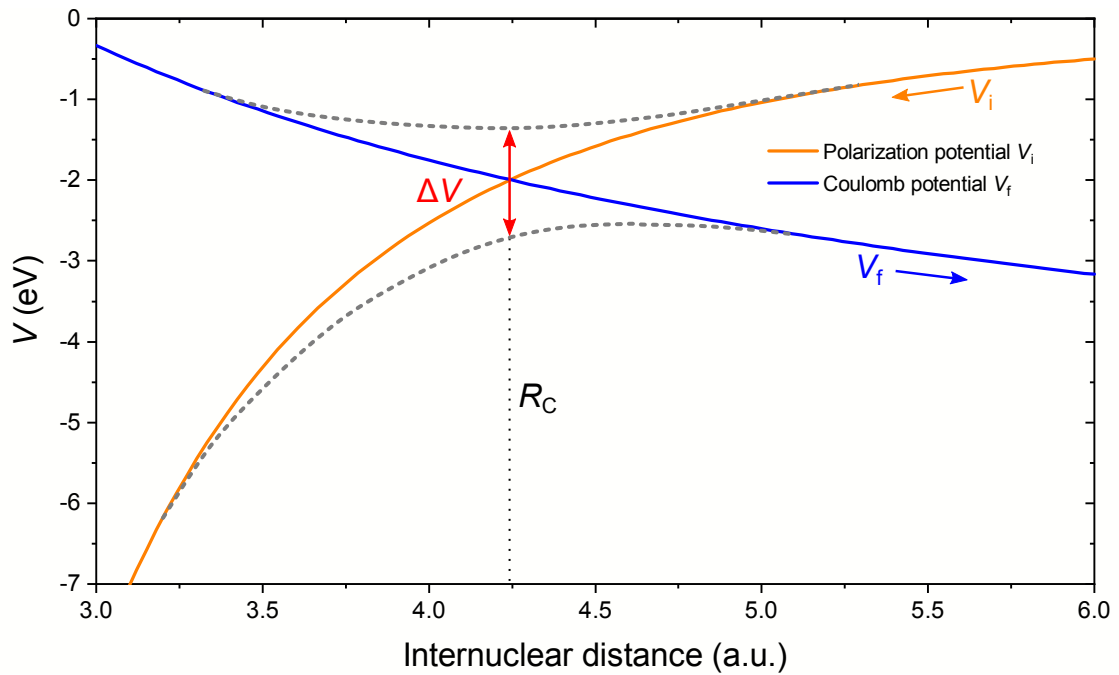
Figure 2.7: Illustration of the MCLZ approximation. At large internuclear distances, the system moves on an ingoing diabatic polarization potential curve represented in orange, and at small distances, the system moves on an adiabatic curve. At the avoided curve crossing distance R_C, a transition between both adiabatic curves can occur. Here the electron is transferred to the projectile. After the collision both, target and projectile are positively charged, and the system moves on a diabatic Coulomb potential curve represented in blue. Adapted from Ref. [53] and modified.

with a correction factor f_{nl} for electron capture in non-degenerate *l*-states given by

$$f_{nl} = (-1)^{n+l-1} \times \frac{\sqrt{2l+1}\,\Gamma(n)}{\sqrt{\Gamma(n+l+1)\Gamma(n-l)}} \qquad (2.50)$$

and a multiplicative factor $a = \sqrt{2I_{\mathrm{P}}}$ for a non-hydrogenic target with ionization potential I_{P}.

The total probability of a transition from the incoming potential curve to the outgoing curve is given by $2p(1-p)$ for one reaction channel, where p represents the probability of a single curve-crossing given by

$$p = \exp\left(\frac{-2\pi V_{if}^2}{\Delta F v_{\mathrm{rad}}}\right) \qquad (2.51)$$

with the difference in the slopes ΔF at $R = R_{\mathrm{C}}$ of the diabatic potential curves and the radial velocity v_{rad} which is a function of the impact parameter b. To generalize the approach for more than one final state, the total transition probability P_n [95] into the n-th final state for a system with N crossings can be expressed by

$$\begin{aligned}
P_n = p_1 p_2 \ldots p_n (1-p_n)[1 + (p_{n+1}p_{n+2}\ldots p_N)^2 + \\
(p_{n+1}p_{n+2}\ldots p_{N-1})^2(1-p_N)^2 + \\
(p_{n+1}p_{n+2}\ldots p_{N-2})^2(1-p_{N-1})^2 + \\
\ldots p_{n+1}^2(1-p_{n+2})^2 + (1-p_{n+1})^2].
\end{aligned} \qquad (2.52)$$

This process is illustrated in figure 2.8 where the incoming polarization potential is labeled as state 0, and the N final outgoing Coulomb potential states are labeled by state n, respectively, as a function of the internuclear distance R. The pseudo-crossings p_n which occur between the initial and the final state at $R = R_{\mathrm{C},n}$ are marked by red circles.

The total cross-section for a transition for more than two channels can be calculated by integration over all impact parameters b with

$$\sigma_{\mathrm{tot}} = \sum_{n=1}^{N} 2\pi \int_0^{R_{\mathrm{C}}} P_f(b) b \, \mathrm{d}b. \qquad (2.53)$$

For a bare ion collision, the critical internuclear distance R_{C} where the avoided curve crossing occurs [94] can be approximated by

$$R_{\mathrm{C}} \approx \frac{2n^2(Z-1)}{Z^2 - n^2}. \qquad (2.54)$$

With the MCLZ method, only n-resolved cross-sections can be calculated for bare ion
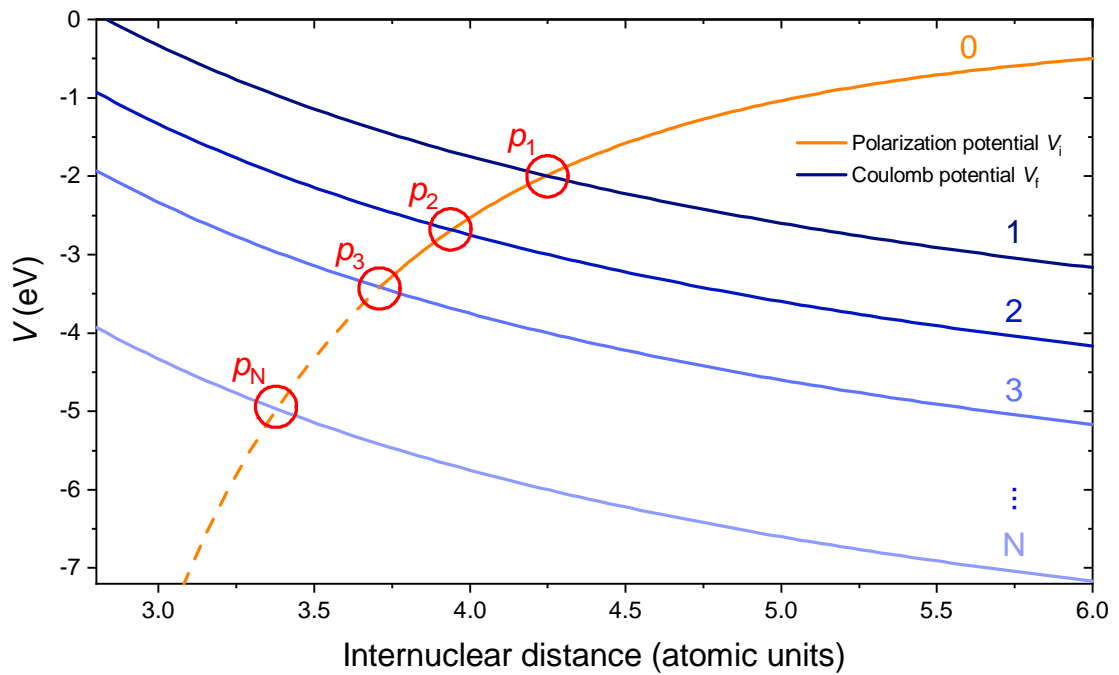
Figure 2.8: Illustration of the MCLZ approach by incoming and outgoing potential curves as a function of the internuclear distance R. The orange curve represents the incoming polarization potential curve labeled by state 0, and the blue-colored curves are N final Coulomb potential states labeled by n. The corresponding pseudo-crossings p_n between 0 and n are indicated by red circles. Adapted from Ref. [95] and modified.

collisions. To extract information about the population of the l-states the n-resolved cross-sections have to be multiplied by a distribution function W_{nl}. For high collision energies above $1\,\mathrm{keV/u}$, the angular momenta for each n-state are distributed statistically with

$$W_{nl}^{\mathrm{stat}} = \frac{2l+1}{n^2}. \tag{2.55}$$

For lower collision energies a low-energy weighting function is derived in Ref. [6, 95] with a distribution given by

$$W_{nl}^{\mathrm{lowe}} = (2l+1)\frac{[(n-1)!]^2}{(n+l)!(n-1-l)!}. \tag{2.56}$$

This distribution has a maximum at $l = 1, 2$ for $n \leq 8$. For higher values of the principal quantum number n the Stirling formula can be applied for the expressions of the factorials in equation 2.56 deducing the so-called separable distribution

$$W_{nl}^{\mathrm{sep}} = \frac{(2l+1)}{q}\exp\left(\frac{l(l+1)}{q}\right) \tag{2.57}$$

with a maximum of the distribution at $l \approx \sqrt{n}$. To notice is the explicit dependence on the charge q of the projectile. Another distribution that is applicable for very low collision energies [95] is the modified low energy weighting function (Eq. 2.56):

$$W_{nl}^{\mathrm{lowe,mod}} = l(l+1)(2l+1)\frac{(n-1)!(n-2)!}{(n+l)!(n-l-1)!}. \tag{2.58}$$

Here, preferably intermediate angular momentum states are populated, and the s-state ($l = 0$) provides a zero population.

2.3.4.4 Kronos model for charge exchange

In this work, the Kronos code [124] is utilized for the generation of synthetic charge exchange spectra. It was developed in 2016 by the Stancil research group and is a stand-alone charge-exchange cross-section database containing cross-sections for collisions of various projectiles with different charge states with some neutral targets for a broad range of collision energies. The calculations are mainly based on the multichannel Landau-Zener approach, and the energies of the levels are extracted from the NIST database. In the case of the absence of available data, in particular, for highly excited states, the energy levels are extrapolated by scaling relations. After calculating the nl-resolved cross-sections, a cascade model is applied to generate a theoretical CX spectrum. For this, the branching ratios for all possible transitions from $|n, l\rangle$ to the ground state $|1, 0\rangle$ are calculated, and the corresponding spectral lines are convoluted with a Gaussian with a width of the equivalent instrumental resolution. Examples of synthetic CX spectra obtained with the Kronos code

are shown in figure 2.9 for a collision of bare argon with atomic hydrogen at $25\,\mathrm{eV/u}$ for the distribution functions for the angular momenta presented in equations 2.55, 2.56, 2.57, and 2.58. Proper knowledge of the collision velocities and the principal quantum number n in which the electron is captured is required. Also, the capture of more than one electron is not considered in this model.

2.3.4.5 The Flexible Atomic Code radiative cascade model

Within the framework of this thesis, a cascade model based on calculations performed with the Flexible Atomic Code (FAC) [85] for the generation of theoretical CX spectra was developed together with S. Bernitt for the reconstruction of the angular momentum distribution for measured spectra. This model is based on the calculation of the branching ratio for all possible transition from an excited state $|n, l\rangle$ to the ground state $|1, 0\rangle$. By plotting the convolution of all possible spectral lines with their relative intensity with a Gaussian corresponding to the effective resolution of the utilized detector as a function of the transition energy, a synthetic spectrum can be generated. Every single initially excited state $|n, l\rangle$ will produce a characteristic spectrum that serves as a spectral basis vector. An example of the cascade spectra up to $l = 7$ for a population of $n = 9$ states of hydrogen-like argon is shown in figure 2.10. In general, the linear combination

$$S = \sum_{n=i}^{n=f} \sum_{l=0}^{n-1} a_{n,l} |n, l\rangle \tag{2.59}$$

of all basis vectors $|n, l\rangle$ with coefficients $a_{n,l}$ for all considered initially populated principal quantum numbers from n_i to n_f will produce a synthetic spectrum S. Here the spectra of the two possible spin states are averaged. By fitting the spectral basis vectors with the coefficients $a_{n,l}$ as free parameters to the experimentally obtained spectrum, the extraction of the angular momentum distribution becomes possible.

For verification of the predictive efficiency of this model, the four l-distribution models described by equation 2.55, 2.56, 2.57, and 2.58 are applied for the population of the $n = 9$ principal number state in hydrogen-like argon. The results are presented in figure 2.11.

The cascade model is in a good agreement with the MCLZ calculation, although exclusively capture in one single n-state is assumed by the cascade model. The slight difference for lower-energetic transitions into the M-shell and the L-shell could be explained by a non-zero fraction in adjacent principal quantum number states calculated by the MCLZ approach since the cross-section for capture into the single n-states of initially fully ionized systems is velocity-dependent. Thus, an assumption of capture into one unique principal quantum number state by the cascade model does not provide information about the relative collision velocity between projectile and target.
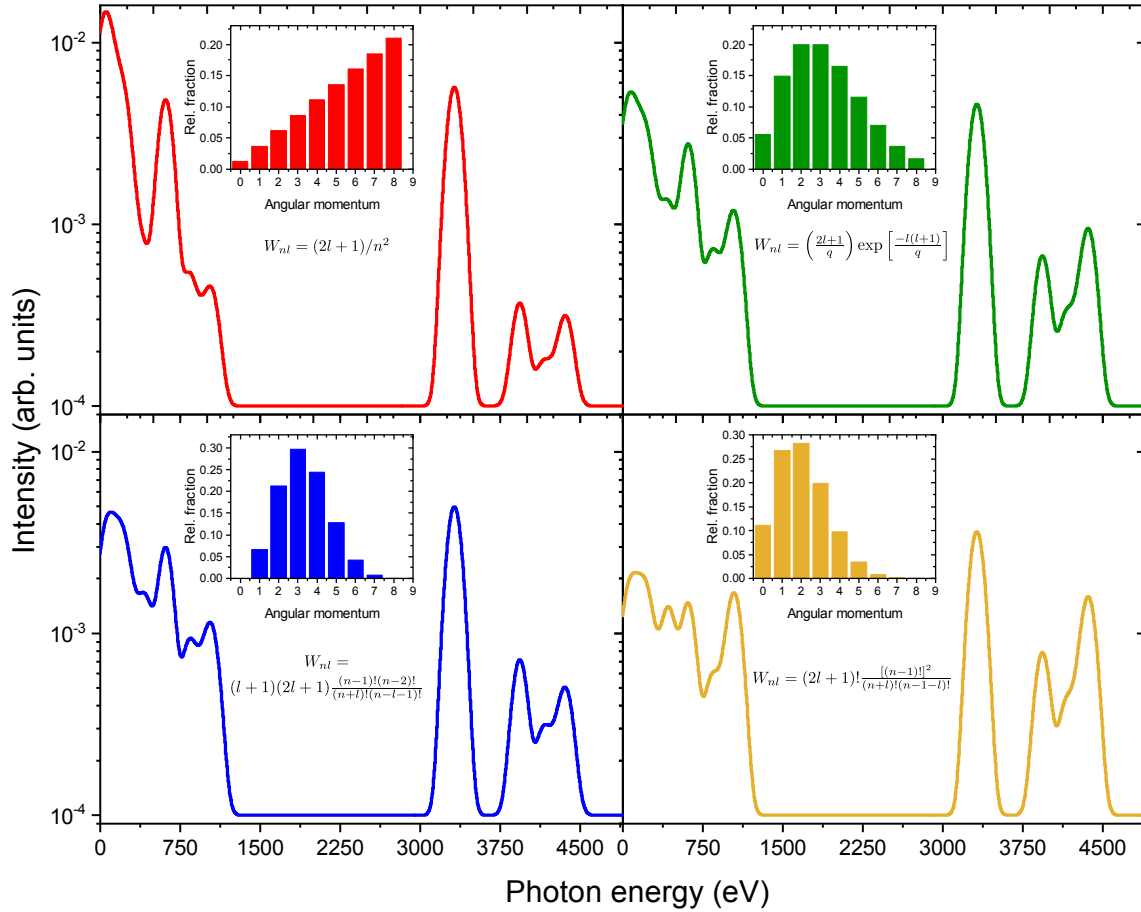
Figure 2.9: Synthetic CX spectra obtained by an MCLZ calculation performed with the Kronos code for a collision of Ar^{18+} with atomic hydrogen at a collision velocity of $25\,eV/u$ convoluted with an effective resolution of $FWHM = 153\,eV$. The relative intensity is plotted in logarithmic representation as a function of the photon energy. Different angular momenta distributions are multiplied for the n-resolved cross-sections. **Top left:** Statistical distribution for high collision velocities above $1\,keV/u$. **Top right:** Separable distribution for capture into high n-states. **Bottom right:** Low energy weighting function for low collision velocities below $1\,keV/u$. **Bottom left:** Modified low energy weighting function for the population of intermediate angular momenta. The insets in the four spectra represent the relative fraction of the angular momentum as a function of l.
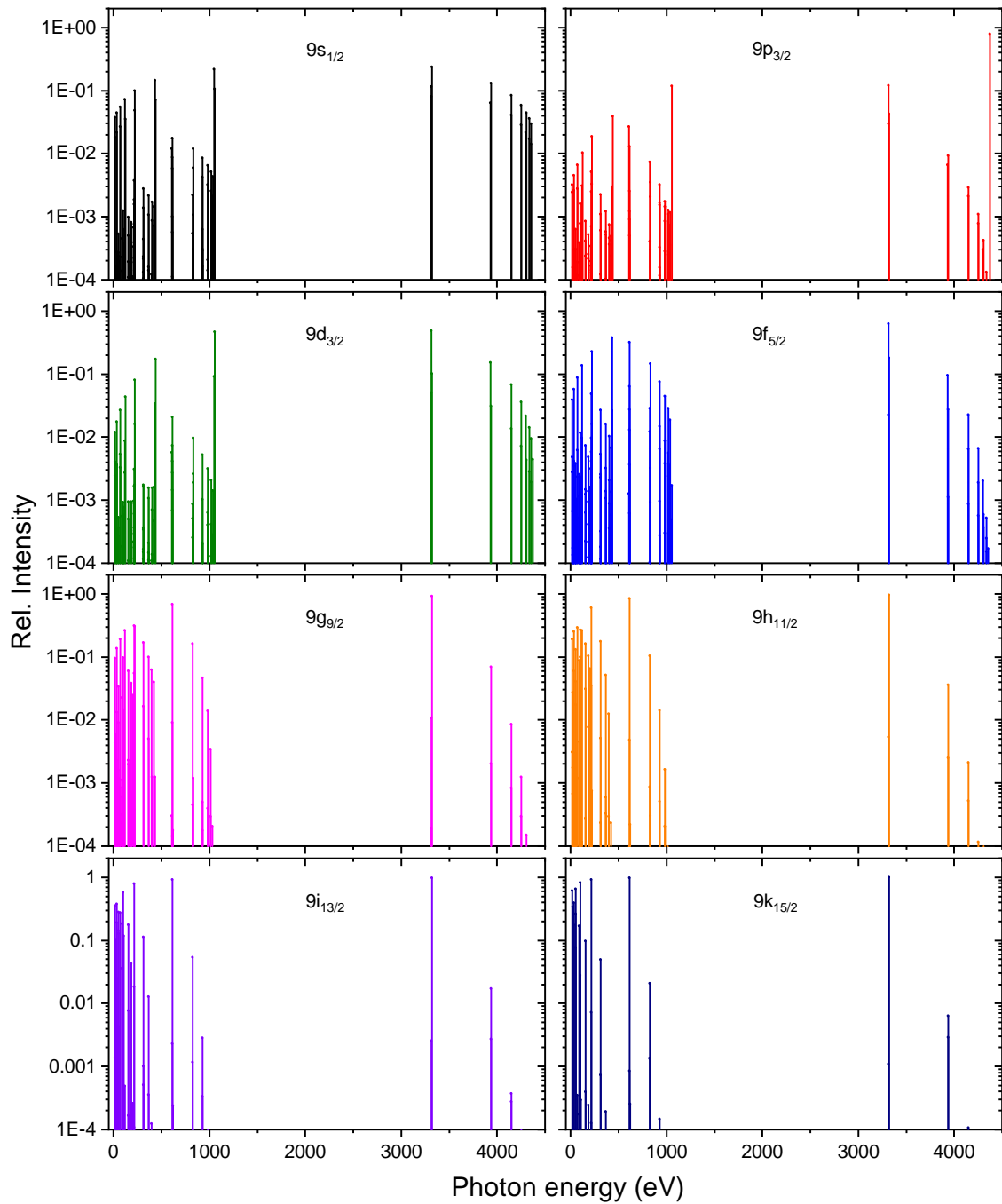
Figure 2.10: Calculated cascade spectra for a population of $|n = 9, l, J\rangle$ states for hydrogen-like argon up to $l = 7$ employing the flexible atomic code, where J represents the total angular momentum quantum number.
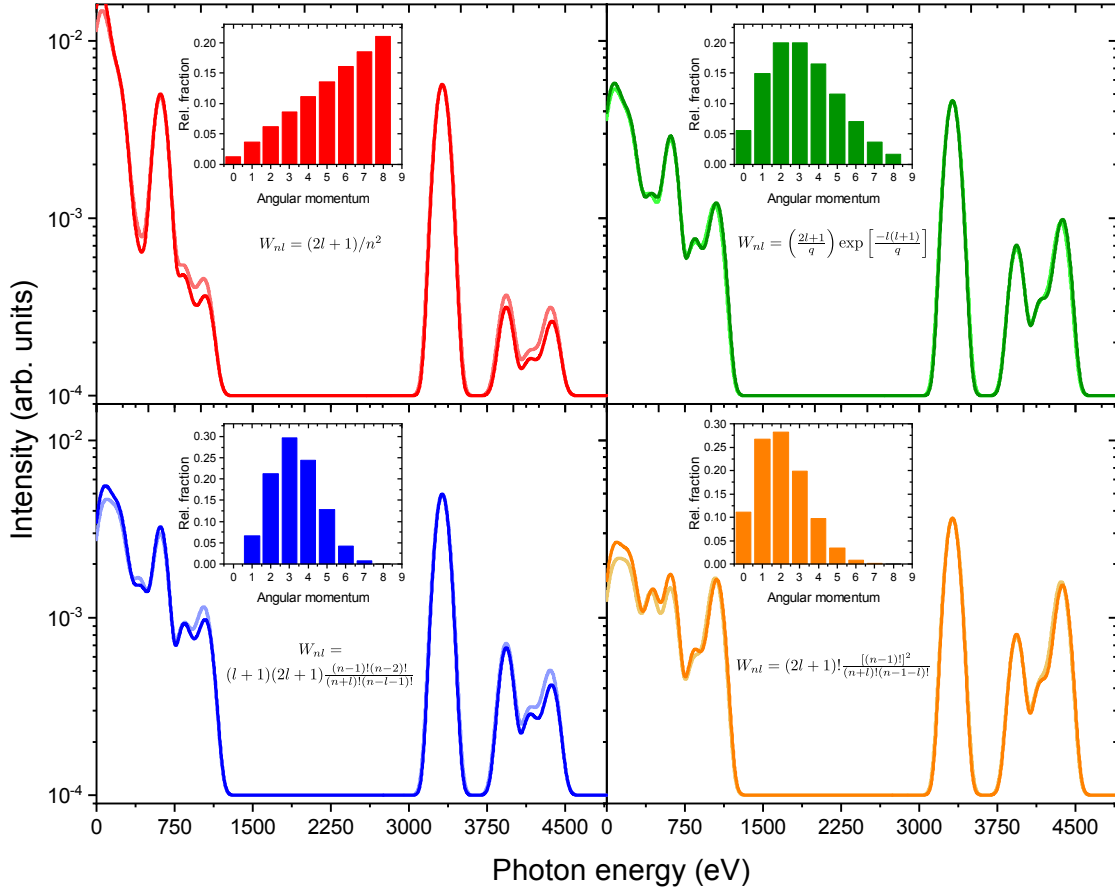
Figure 2.11: Calculated spectra with the FAC cascade model for *l*-distributions according to equations 2.55, 2.56, 2.57, and 2.58 for a population in $n = 9$ for hydrogen-like argon with the corresponding relative fractions of angular momenta shown in the insets. The overlayed shaded solid lines represent the Kronos calculation from figure 2.9, respectively.

For a second test of validity of the cascade model a CX spectrum is calculated with MCLZ for a collision of Ar^{18+} with atomic hydrogen at $100\,\mathrm{eV/u}$ collision energy and a separable l-distribution given in equation 2.57. A fit as described in equation 2.59 is performed by utilizing the least-square method to determine the coefficients of the spectral basis vectors given by the FAC cascade model for $n = 9$. The results are presented in figure 2.12.

The reconstruction result is overall in a good agreement to the distribution of angular momenta assumed by the MCLZ approach. Since the number of free parameters for the fit is 9 for $n = 9$ and the number of lines is in the same order, the fit results are reliable. Only a difference of the population of the s-state is observed which could originate from non-zero fractions of the population of adjacent n-states as discussed before since the population for one single principal quantum number is considered in the cascade model. This model calculates only the branching ratios for transitions of a given l-distribution of excited states into the ground state, not the charge exchange cross-sections. Within this work, this model is applied for hydrogen-like systems and helium-like systems after electron capture.

Furthermore, the charge exchange code which, was recently implemented in the flexible atomic code package is utilized for comparison with experimentally obtained charge exchange spectra, and with the Kronos code. The approach is also based on multichannel Landau-Zener method, but in contrast to Kronos, FAC performs ab-initio calculations for the charge exchange cross-sections, for the energy levels, and the corresponding transition rates.
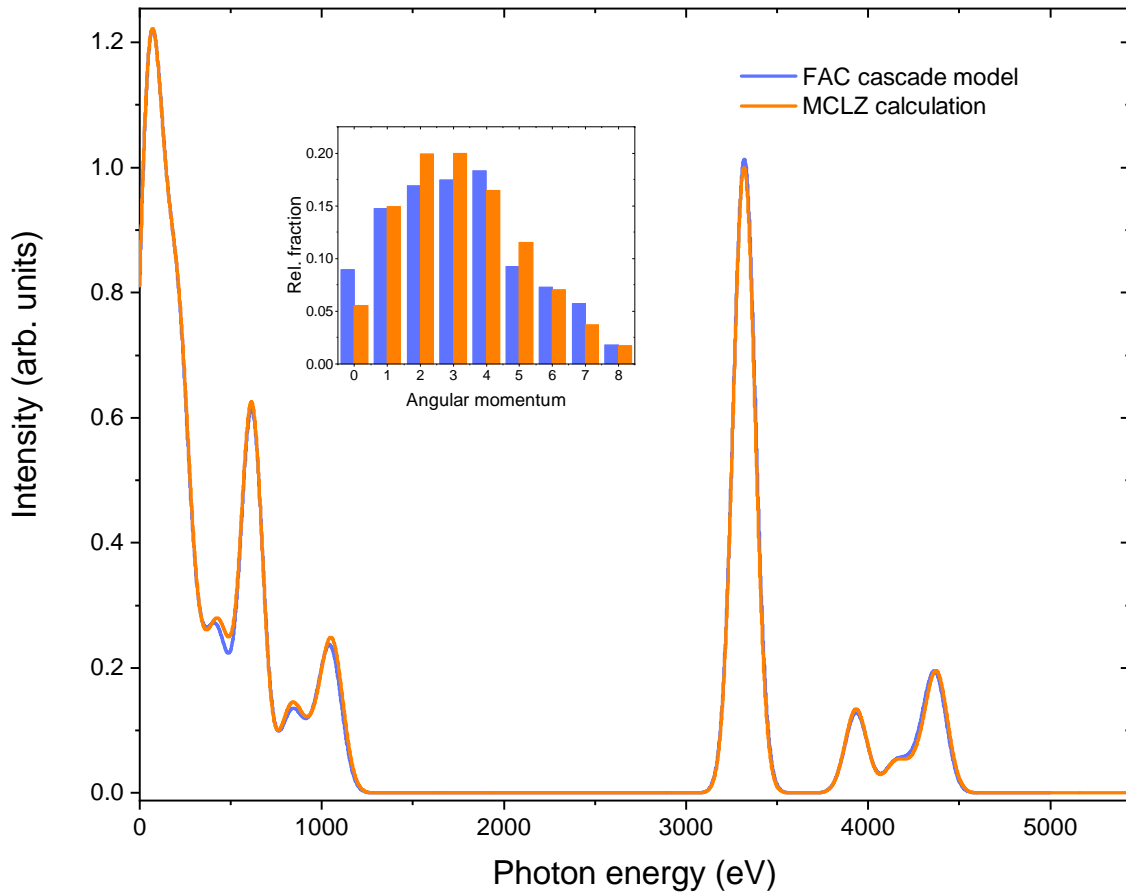
Figure 2.12: Validation of the FAC cascade model for the reconstruction of the angular momentum distribution. The orange curve represents an MCLZ calculation performed by the Kronos code for electron capture into Ar^{18+} with a collision energy of $25\,\mathrm{ev/u}$ and a low-energy l-state distribution. This spectrum serves as an input for the reconstruction for capture into $n = 9$ by determination of the spectral basis vector coefficients, depicted by a blue curve. The corresponding angular momentum distribution of the MCLZ calculation and the reconstruction is shown by orange and blue bars in the inset, respectively.

3 The electron beam ion trap

In the hot universe, most of the matter is present in a highly ionized form, where X-rays are produced mainly by the interaction of highly charged ions with free electrons. In order to interpret astrophysical X-ray spectra of these hot environments prevailing in active galactic nuclei, neutrons stars, supernova remnants, and many more, precise investigation of atomic processes in controlled laboratory plasmas are crucial. In the following, a brief description of devices for the production of highly charged ions, in particular, the electron beam ion traps, will be provided.

3.1 Production and trapping of highly charged ions

For the production of highly ionized plasmas, several experimental techniques are available whereby most of them are based on the interaction of high-energetic charged particles with matter. However, also production with intense laser radiation focussed onto a solid [122], droplets [165] or even with interaction synchrotron or free-electron-laser radiation with gas has been demonstrated [141, 153, 154, 52].

In both cases, the energy of the projectile has to be higher than the binding energy of the bound electron in the ion or atom. In a storage ring [72, 86, 5, 56, 158], a lowly charged ion is accelerated to relativistic kinetic energies and impinged onto a stripper foil or gas cell leading to ionization of the ion to higher charge states. Those ions are electro-statically confined in the storage ring. The advantage of this method is very high charge states and high ion currents, but this requires accelerator facilities and large-scale projects. Another device to produce HCIs is an electron-cyclotron-resonance ion source (ECRIS) which uses electrons kept on a cyclotron orbit by irradiation with microwaves in an inhomogeneous magnetic field to exceed the ionization potential of the bound electron. High ion currents can be reached with the disadvantage of a relatively broad distribution of the kinetic energy of the electrons which limits the maximum accessible charge state. To achieve a narrow range of the charge-state distribution and high ionization states with a high degree of control, an intense mono-energetic electron beam is crucial.

One of the first application of an electron beam to ionize neutrals and keep the ions radially confined by the negative space charge of the electron beam was described by L. M. Field et al. in 1947 [67]. Decades later the first electron beam ion source (EBIS) was successfully commissioned by E. D. Donets et al. in Dubna, U.S.S.R. [61] where the electron

beam is compressed to small diameters by utilization of a solenoid coil. In 1988 the concept of an electron beam ion trap (EBIT) was presented, which was a further development of the EBIS for production and trapping of highly charged ions [111, 119, 112]. Instead of a solenoid coil, a magnetic system in Helmholtz configuration is used which allows for spectroscopic access to the trap. In the following sections, the principle of operation of an EBIT is described.

3.2 Fundamentals of electron beam ion traps

3.2.1 Function principle

A schematic principle of operation is depicted in figure 3.1. The electrons are emitted from the cathode surface and accelerated by a potential difference between cathode and trap towards the trap center. By propagation along the magnetic field, the electron beam is being compressed due to the cyclotron motion of the electrons. In the central trap, the electron beam intersects a beam of neutrals gas atoms or molecules and ionizes them by electron impact ionization. The produced ions are trapped in the axial potential well of the trap electrodes and the radial potential of the electron beam. After passing the trap, the electron beam is dumped onto the surface of the collector. The semi-Helmholtz configuration of the coils of the superconducting magnet allows for direct observation of the ion cloud for spectroscopic investigations.

3.2.2 Electrostatic potential

The electrostatic potential in which the ions are located is defined by the voltages applied to the trap electrodes and by the superposition of the negative space charge generated by the electrons and the positive space charge generated by the ions, trapped in the radial negative space-charge potential. The contribution of the space charge Φ of the electron beam is given by the solution of the Poisson equation

$$\vec{\nabla}^2 \Phi = -\frac{\rho_e}{\epsilon_0} \tag{3.1}$$

with the local charge density ρ_e of the electrons and the permittivity of free space ϵ_0. The density ρ_e can be determined by consideration of an infinitely elongated cylindrical electron beam with radius r_H with

$$\rho_e = \frac{I_e}{\pi r_H^2 v}, \tag{3.2}$$

where I_e and v represents the electron-beam current and v the longitudinal velocity of the electrons, respectively. Due to the cylindrical symmetry of the concentrically located
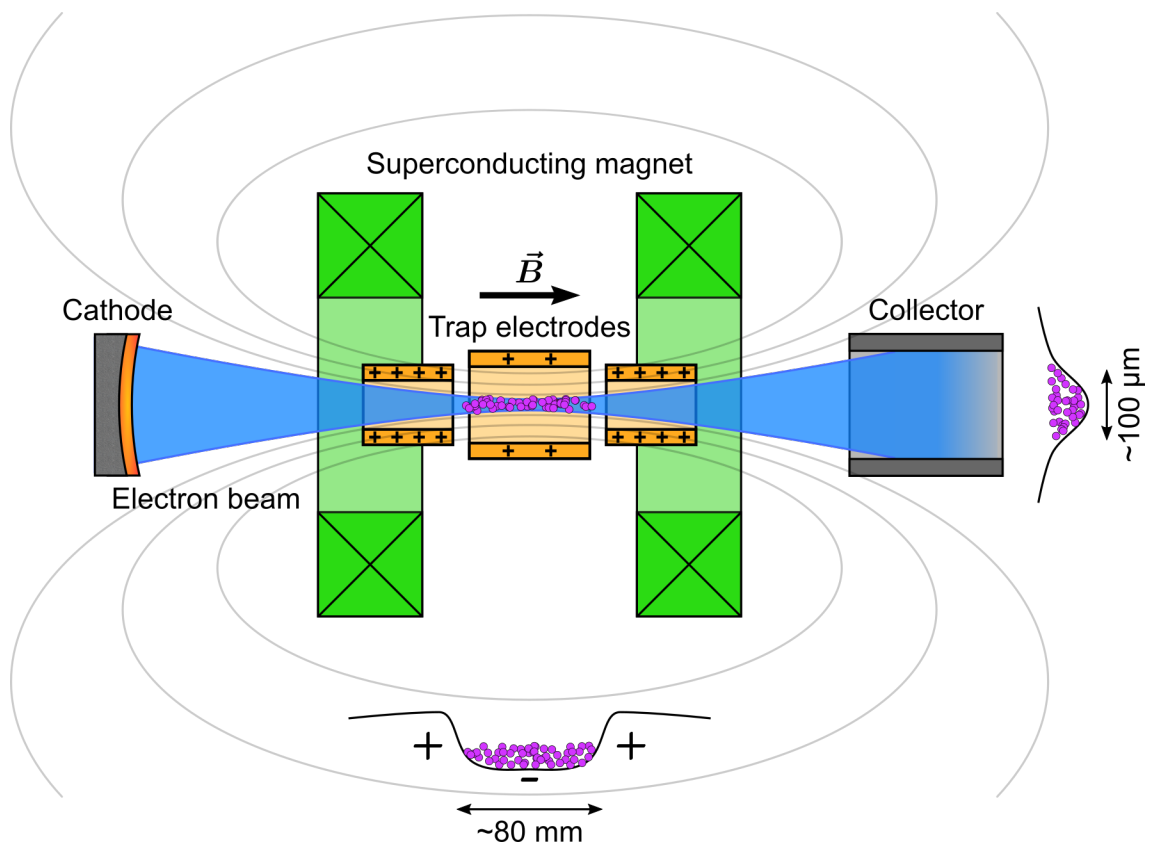
Figure 3.1: Scheme of the function principle of an electron beam ion trap. Adapted and modified from Ref. [60].

central trap electrode enclosing the electron beam, equation 3.1 reduces to

$$\frac{1}{r}\frac{\partial}{\partial r}\left(r\frac{\partial}{\partial r}\Phi\right) = -\frac{\rho_e}{\epsilon_0}. \tag{3.3}$$

The boundary condition of a well-defined potential Φ_D at the surface of the trap electrode with inner radius r_D leads to an analytical solution of the potential as a function of the radial distance r from the symmetry axis

$$\Phi(r) = \begin{cases} \Phi_D + \Phi_0\left[\left(\frac{r}{r_H}\right)^2 + 2\ln\left(\frac{r_H}{r_D}\right) - 1\right] & r \leq r_H \\ \Phi_D + \Phi_0 2\ln\left(\frac{r}{r_D}\right) & r > r_H \end{cases} \tag{3.4}$$

where the constant Φ_0 is defined as

$$\Phi_0 = \frac{I_e}{4\pi\epsilon_0 v}. \tag{3.5}$$

Hence, the total acceleration potential of an emitted electron from the surface of a cathode at a potential Φ_C in the center of the trap is defined by

$$U_{kin} = \Phi_D - \Phi_C + \Phi_0 2\ln\left(\frac{r_H}{r_D}\right) + \Phi_I + \Phi_A \tag{3.6}$$

along the symmetry axis for $r = 0$. Φ_I is the positive space-charge potential of the ions and Φ_A a potential which is a composition of material-dependent properties like the work function of the electrons from the surface of the cathode. Therefore, a higher space-charge potential generated by the electron beam reduces the total kinetic energy of the electrons.

3.2.3 Electron beam

The theory of a non-laminar long cylindrical electron beam, compressed by a homogeneous magnetic field is given in Ref. [89, 55]. The electron beam is considered as a perfect optical system with an initial thermal Maxwell distribution of the transverse electron velocities at a corresponding temperature T_C at the surface of a cathode. Also, the residual magnetic field B_C at the origin of the electrons is considered. The average over time of the electron-beam radius r_H is determined by

$$r_H = \sqrt{\frac{m_e I_e}{\pi\epsilon_0 evB^2} + \sqrt{\left(\frac{m_e I_e}{\pi\epsilon_0 evB^2}\right)^2 + \frac{8kT_C m_e}{e^2 B^2}r_C^2 + \frac{B_C^2}{B^2}r_C^4}} \tag{3.7}$$

at a location with a corresponding magnetic field B and the radius r_C of the cathode. The velocity v of the electron has to be described relativistically with

$$v = c\sqrt{1 - \left(\frac{m_e c^2}{m_e c^2 + eU}\right)},$$

(3.8)

where c represents the speed of light in vacuum and U the total acceleration potential presented in equation 3.6. A non-relativistic approach of the velocity would lead to an uncertainty of $\sim 1.2\%$ at a typical acceleration voltage of 8000 V.

3.3 Setup of CANREB-EBIS

In 2006 the FLASH-EBIT [64, 63], the first transportable cryogenic EBIT for experiments at ultra-brilliant light sources was built by S. W. Epp at the Max-Planck-Institut für Kernphysik. Four years later the HYPER-EBIT [20] was developed by T. M. Baumann for operation at higher electron-beam energies and currents.

The CANREB-EBIS (CANadian Rare isotope facility with Electron Beam ion source) [34] is based on a similar design as the FLASH-EBIT and the HYPER-EBIT, but in contrast to those, it is specialized for charge breeding of singly-charged rare, short-lived isotopes. A sectional view is presented in figure 3.2. An efficient and fast charge breeding requires high electron-beam currents. The CANREB-EBIS is designed for operation with an electron beam with energies up to 15 keV and currents up to 1000 mA. Bunches of singly charged ions with a longitudinal length of 1 µs and kinetic energy of 15 keV at a repetition rate of up to 100 Hz shall be accepted.

It consists basically of a high-current electron gun, a superconducting magnet in semi-Helmholtz configuration encasing the trap electrode assembly and an electron collector. The gun can be biased together with the collector to voltages from 0 kV up to 15 kV depending on the desired electron-beam energy. The common trap voltage will be set to 15 kV to match the energy of the incoming ion bunches.

Hereafter, the single components of the EBIS will be described. During the commissioning phase, the device acted mostly as a trap and not as a source, and therefore, it will be designated as CANREB-EBIT.

3.3.1 Vacuum system

The vacuum inside the EBIT is in the order of $10^{-9} - 10^{-10}$ mbar in the room-temperature environment. In the cryogenic region, it is estimated to be in the order of 10^{-13} mbar. An ultra-high vacuum (UHV) is crucial for the operation of the EBIT. Lower pressure means less residual gas atoms or molecules which would lead to an increased charge exchange rate
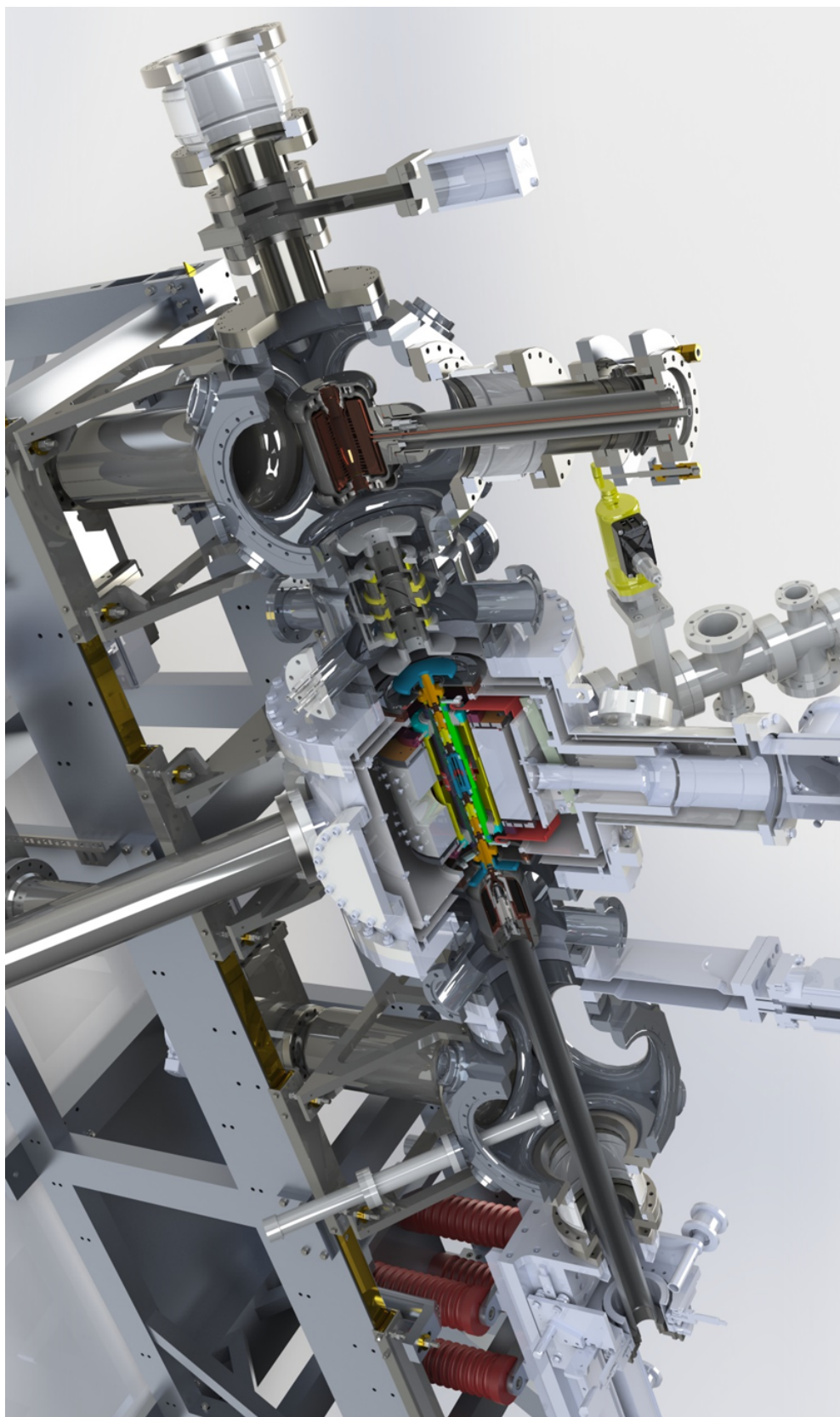
Figure 3.2: A sectional view of the CANREB-EBIS. On the right-hand side, the electron gun mounted on a supporting neck which is attached to an xyz-manipulator. In the center the magnet bore surrounding the trap electrodes, and the superconducting Helmholtz coils. On the left-hand side, ion-optics elements and the electron collector. Adapted from Ref. [34].
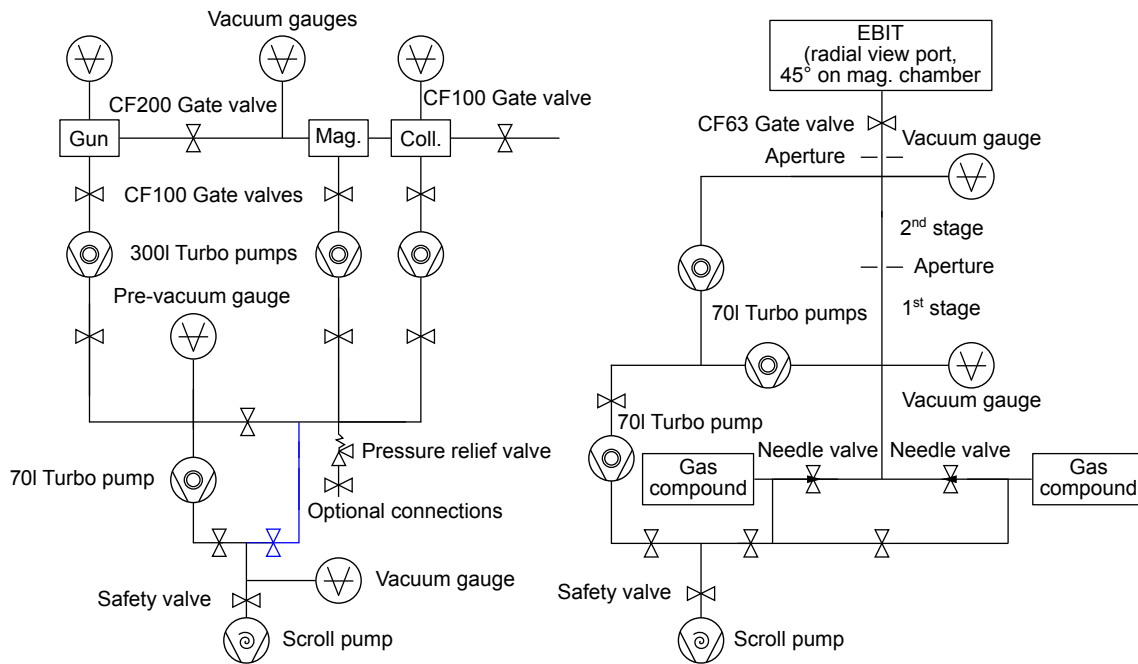
Figure 3.3: Schematic of the vacuum system of the EBIT. On the left-hand side, the main vacuum system and on the right-hand side, the injection vacuum system is depicted. The blue highlighted path is the bypass for pumping the magnet and collector independently of the gun in case of maintenance.

resulting in less production of ions in higher charges states. Additionally, the amount of contaminant ions in extraction is reduced.

The covering of the EBIT consists of three main chambers in total. Two cubic-shaped chambers with a side length of 325 mm enclosing the collector during operation and the gun during storage. Both chambers are connected to the cylindrical enclosure with a diameter of 470 mm of the superconducting magnet by two additional cylindrical chambers with 210 mm length. During the operation of the EBIT, the vacua of those chambers are connected. For maintenance of the magnet or collector, the gun can be retracted into the storage chamber and can be pumped independently by separating the gun vacuum from the main vacuum by a CF200 gate valve.

The schematic setup of the vacuum system of the EBIT is depicted in figure 3.3.

A 300 l turbomolecular pump (TMP) is attached to each chamber, respectively. The pre-vacuum of $\sim 10^{-6}$ mbar is provided by a 70 l TMP attached to the joined exhaust of the three TMPs leading to an increase of the compression rate for molecular hydrogen, which is the main contribution of the residual gas which remains at cryogenic temperatures. The pre-vacuum TMP is backed by a scroll pump.

To provide a target for ionization, a gas injection system was developed and attached to a 45 ° radial access port of the magnet chamber. The vacuum of this system can be separated
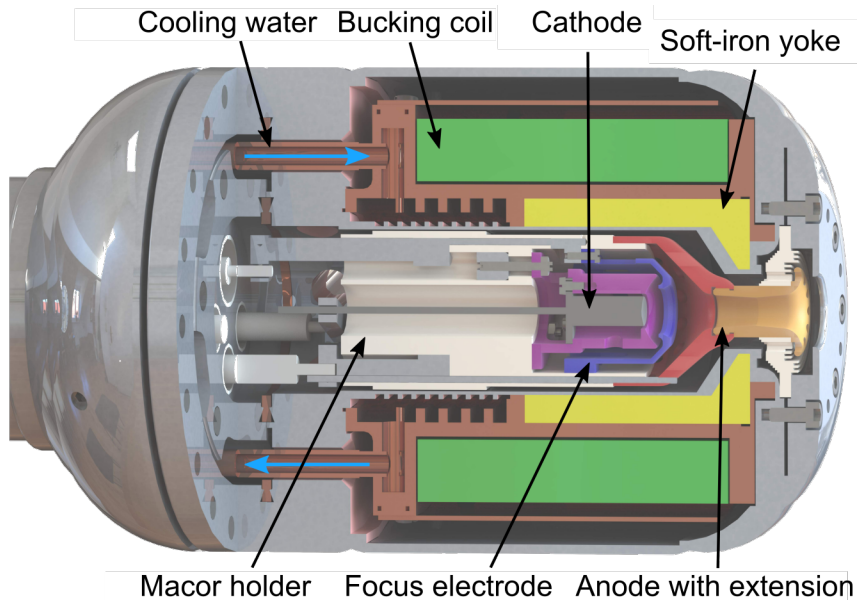
Cooling water Bucking coil Cathode Soft-iron yoke

Macor holder   Focus electrode   Anode with extension

Figure 3.4: Sectional view of the electron gun. Adapted and modified from Ref. [34].

with a CF63 gate valve from the main vacuum of the EBIT either for maintenance or to obstruct the path of the atomic gas beam to the interaction region with the electron beam in the trap center. A more detailed description of the injection system will be provided in section 3.3.7.

3.3.2 Electron gun

The electron beam is emitted from the electron gun, which is depicted in a sectional view in figure 3.4. The design is based on the gun of FLASH-EBIT and HYPER-EBIT with minor modifications. To reach higher electron-beam currents, a larger cathode with a diameter of 6.35 mm was installed which can emit up to $10\,\mathrm{A/cm^2}$ at a temperature around $1000\,°\mathrm{C}$.

The gun consists of electrostatic and magneto-static components arranged in a Pierce-type geometry [139]. In order to achieve high electron-beam currents, a thermionic barium dispenser cathode with type M-coating and a spherical radius of 10 mm is installed. The cathode material has a relatively low work function of $\sim 2\,\mathrm{eV}$ and emits at temperatures around $1000\,°\mathrm{C}$ providing better electron-beam compression according to Herrmann optical theory of electron beams [89]. The cathode is mounted concentrically to a holder (represented in purple in figure 3.4) with the same spherical radius as the cathode surface and is made out of molybdenum to withstand operation temperatures up to $1300\,°\mathrm{C}$ by indirect heating with currents up to $1.9\,\mathrm{A}$ at voltages of $\sim 6\,\mathrm{V}$. The holder including the cathode is encircled by the next element, the focus electrode, with 10 mm inner diameter. Due to the high sensitivity of the emission characteristics of the cathode surface to contaminations

with several elements, compounds and metals, and insensitive only to a limited number of materials, the focus electrode is made of molybdenum. By biasing this electrode, the emission current can be accurately controlled.

All electrodes are mounted on a holder made of an insulating machinable ceramic (Macor). Additionally, an OFHC anode is mounted at a distance of $\sim 5\,\mathrm{mm}$ to the focus electrode in order to reach higher electron-beam currents. It is attached to a Macor spacer which is connected indirectly to the water-cooled surface of the electromagnetic coil inside the gun head. The magnetic field produced by this coil can be adjusted by the application of a certain current to compensate for the residual magnetic field of the superconducting magnet at the surface of the cathode to facilitate the emission of electrons. Additionally, a soft-iron yoke is located between the cathode and the coil. The heat produced by impingement of the electrons on the collector surface, by the current flow through the coil inside the gun, and inside the collector is dissipated into a water-cooled circuit by means of a $2\,\mathrm{kW}$ water-to-air-chiller.

For precise adjustment of both, electron-beam energy and electron-beam current at maximum transmission and compression, the gun can be positioned precisely by an *xyz*-tilt-manipulator. Additionally, the $100\,\mathrm{cm}$ long neck is supported by two linear manipulators insulated with a $45\,\mathrm{mm}$ thick rod of ceramics.

During the commissioning of the EBIT, a maximum electron-beam current of $1000\,\mathrm{mA}$ at an electron-beam energy of $6\,\mathrm{keV}$ was achieved which was only limited by the $3\,\mathrm{kV}$ power supply of the cathode platform.

3.3.3 Superconducting magnet

For higher compression of the electron beam in the trap center, a custom-made superconducting magnet, manufactured by Cryogenic Ltd., is installed, reaching magnetic field strengths up to $6\,\mathrm{T}$. It consists of two superconducting NbTi coils with a critical temperature of $11\,\mathrm{K}$ in semi-Helmholtz configuration with a separation of $60\,\mathrm{mm}$. The separation is slightly larger than in real Helmholtz-configuration, leading to a minimum of the magnetic field in axial direction in the center of the trap and a maximum inside the two coils (compare figure 3.6), respectively. This allows for a more extended homogeneous region of the magnetic field along the axis of the central trap electrode. In the gap between the coils in total seven radial access bores are incorporated. Three of them with a diameter of $50\,\mathrm{mm}$ in a $90\,°$ arrangement and four of them with a diameter of $35\,\mathrm{mm}$ rotated in a $45\,°$ pattern with respect to the horizontal plane.

Concentrically aligned vacuum flanges and holes in the $40\,\mathrm{K}$ shield with respect to the bores allow for direct access to the ion cloud for spectroscopic investigations. The magnet is suspended with 12 tie rods attached to the inside of the vacuum chamber of the magnet,
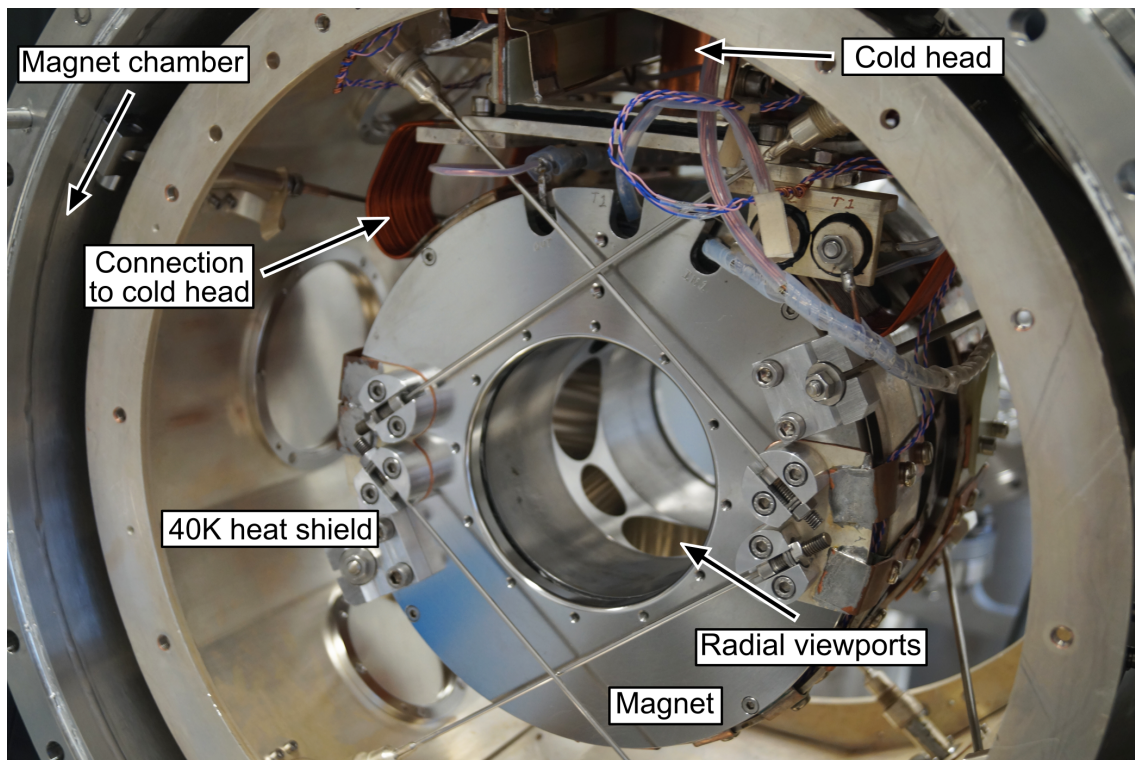
Figure 3.5: The superconducting magnet of the CANREB-EBIT. The front and the back covers of the 40 K heat shield are removed in this photograph.

8 in the radial direction and 4 in the axial direction. They are made of thermally low conducting stainless steel to reduce the heat load of the room temperature environment to the cold magnet.

The superconducting coils are cooled by a Sumitomo RDK-415D Gifford-McMahon type two-staged cold head with a cooling power of 35 W at 40 K and 1.5 W at 4 K, respectively. The silver-plated cylindrical heat shield is directly attached to the 40 K stage of the cold head and the magnet itself to the 4 K stage. Between the heat shield and the faces magnet chamber, respectively, an additional floating shield is attached to reduce the temperature gradient between room temperature and the 40 K stage. An additional thermal link via an OFHC sheet connects the drift tube assembly to the 4 K stage. The cold head is supplied by a Sumitomo F-50H helium compressor with a supply gas pressure of ~ 20 bar.

The superconducting magnet is charged by an external power supply by slowly increasing the current flow through the coils. A magnetic field of 6 T corresponds to a current of ~ 120 A. After charging the magnet, the system can be operated either in persistent mode by breaking the electrical contact to the power supply or under a constant current feed from the power supply.

3.3.4 Trap electrodes

A central component of an EBIT is the trap assembly (compare figure 3.7), denoted hereafter as drift tubes (DT) which is concentrically located on the symmetry axis between the both Helmholtz coils of the superconducting magnet. It consists of 11 cylindrical trap electrodes made of high-purity, oxygen-free copper (OFHC, oxygen-free high thermal conductivity) with a purity of 99, 996 % which are thermally connected via three high heat-conductive sapphire insulators to two half-shells, respectively (compare figure 3.8). This half-shells encase 9 of the 11 trap electrodes and ensure a good centering of the electrodes with respect to the symmetry axis and furthermore a parallel heat transport from the electrodes to the 4-K stage which results in a homogeneous cooling of the whole trap assembly. The half-shells are however connected via a sapphire insulator directly to the 4-K stage.

Four trap electrodes (C1 to C4) are located on the collector side of the central trap electrode (CDT) and four further electrodes on the gun side (G1 to G4). Two additional outermost electrodes, the so-called trumpets (TC and TG), are thermally connected to the 40-K stage of the magnet and mounted via three low heat-conducting polyether ether ketone (PEEK) insulators to the half-shells, respectively. The trumped-like, radially expanding shape of the electrodes additionally blocks direct irradiation of the trap region. These approaches lead to a reduction of thermal radiation to the 4-K region of the trap.

The half-shells are centered by two Macor insulators with respect to a high-voltage shield
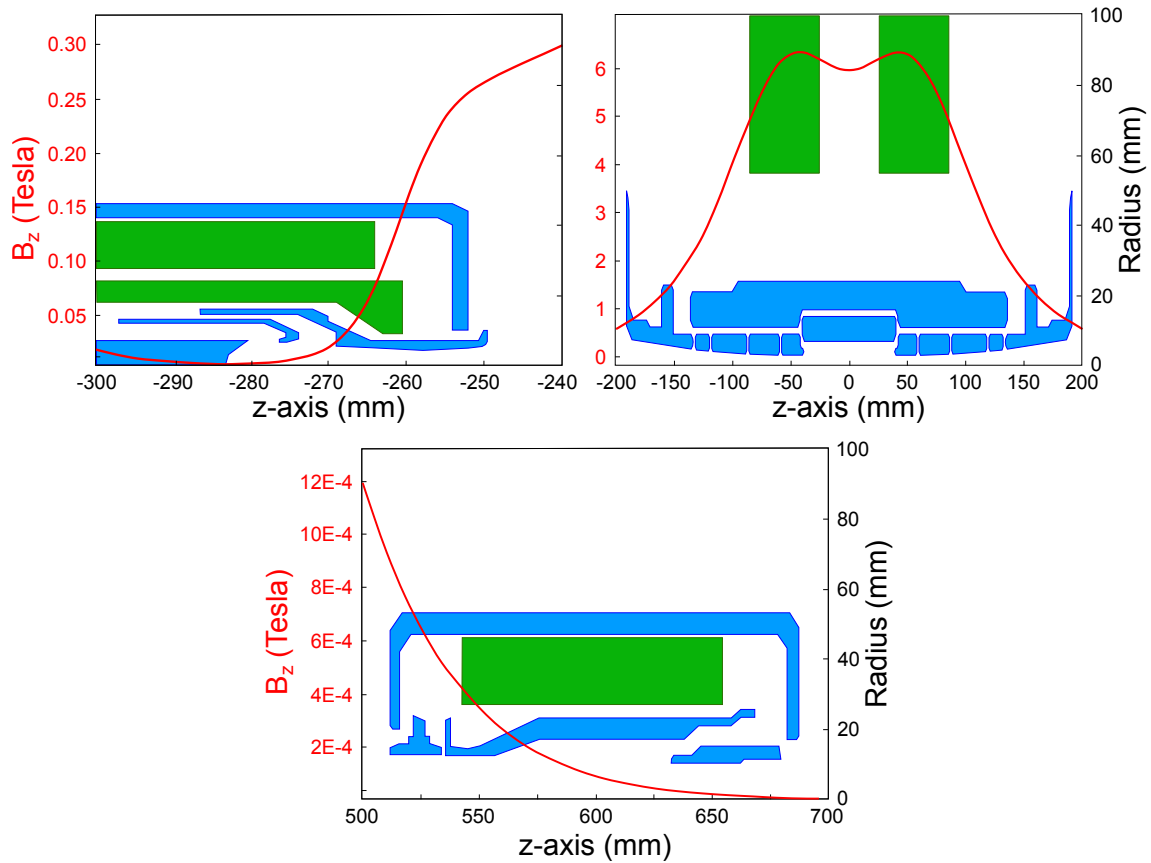
Figure 3.6: A sectional view of the upper half of the main components of the EBIT along the symmetry axis (z-axis). The setup is rotationally symmetric around the z-axis .The magnetic field of the superconducting magnet (red) is simulated with a finite-element method. Elements in green represent magneto-static components and in blue electrodes and enclosures. **Left:** residual magnetic field inside the electron gun. The field is reduced to zero at the cathode surface. **Right:** magnetic field of the semi-Helmholtz configuration with a minimum in the center and a maximum at the position of the coils, respectively. **Bottom:** residual magnetic field inside the collector.
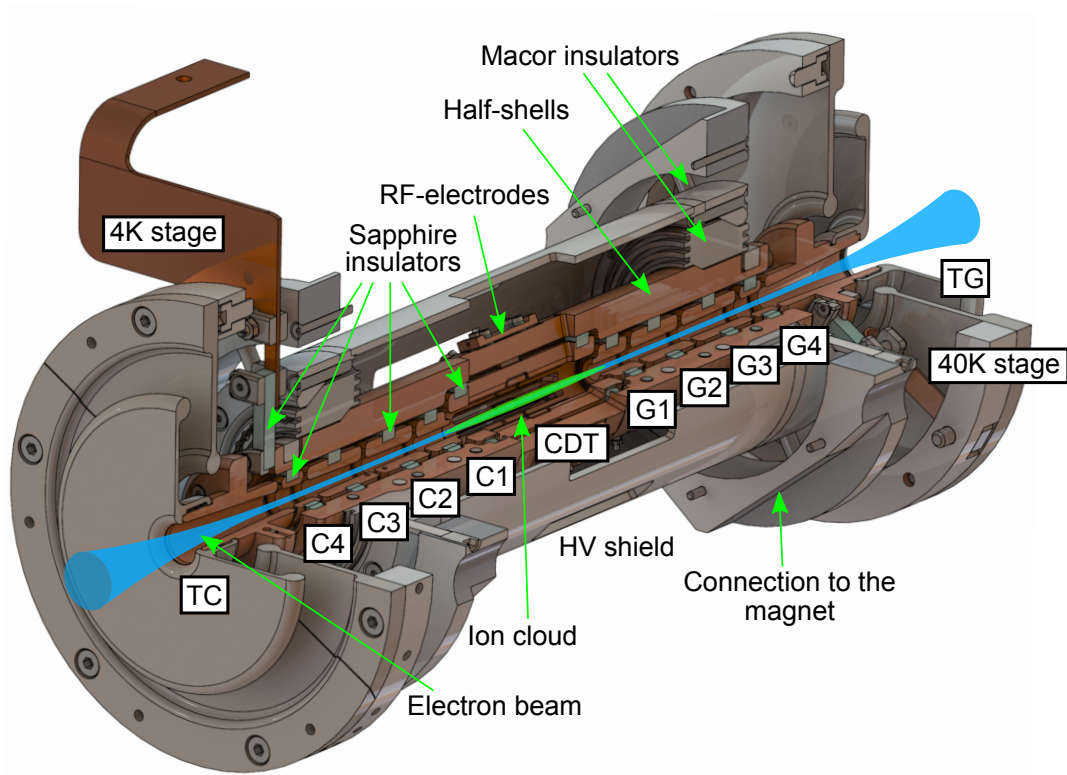
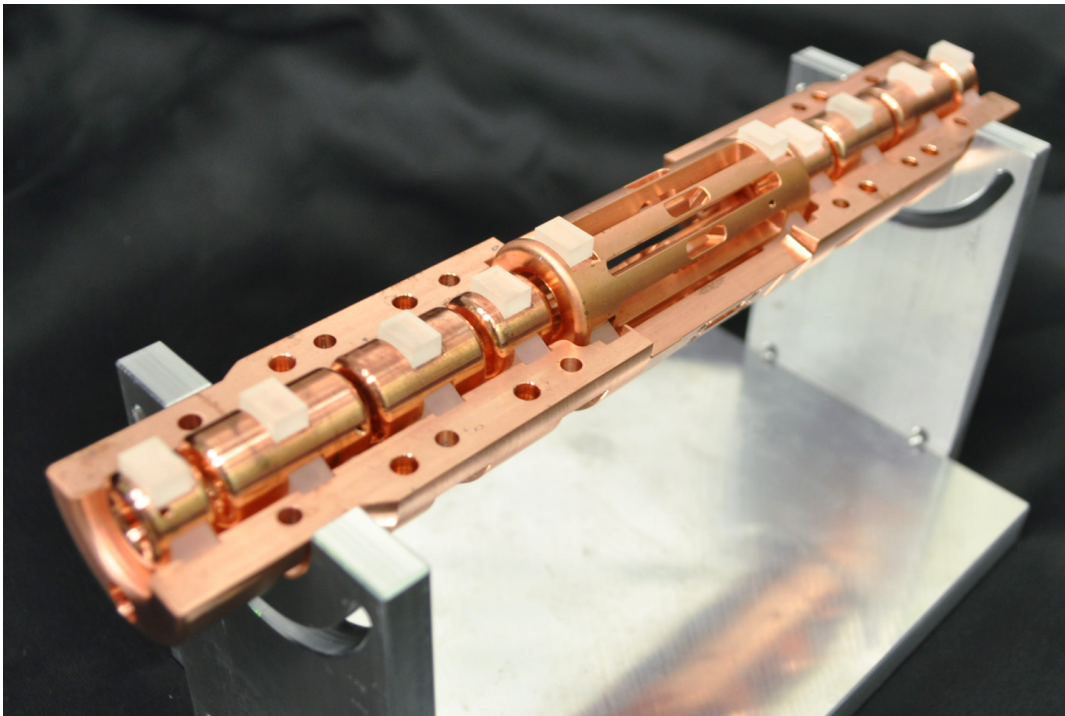**Figure 3.7:** Sectional view of the assembly of the trap electrodes.

Figure 3.8: Assemebly of the drift tube. Nine single electrodes are connected via three sapphire insulators, respectively, to two half-shells. The top one is removed for the photograph. The two outermost electrodes (TG and TC) are not mounted yet.

(HV-shield) which is connected to the common electrical ground of the vacuum chamber to protect the magnet from being damaged in case of a spark-over. This assembly is mounted and centered via six Macor insulators on each side to the magnet shaper.

The central trap electrode has a total length of 80.5 mm, an inner diameter of 14 mm and seven slits in the axial direction for radial view access to the trap center. The other electrodes have a length between 9 mm and 30 mm, where the inner diameter increases conically from 6 mm to 15 mm with increasing distance from the central drift tube. The total length of the drift tube assembly is 382 mm. To increase the electron-beam energy the whole drift tube assembly can be biased up to 15 kV with respect to the ground potential of the EBIT and an additional voltage up to 3 kV can be applied to the single trap electrodes. By application of different voltages to the individual trap electrodes, the potential landscape of the trap can be shaped arbitrarily, which allows for optimization of the trap settings for different experimental purposes. The convenience of having 11 trap electrodes implicates that the effective length of the trapping region can be extended up to 268 mm. For external injection of spatially long bunches of singly charged isotopes into the trap an extended trapping region is crucial to increase the efficiency of the charge breeding.

Additional connections on the half-shells allow for the installation of eight radio-frequency (RF) electrodes which can be extended into the central trap electrode. An application of an RF voltage to this octopole allows for removing ions with a certain charge-to-mass ratio, especially residual gas ions from the trap [108]. Within the scope of this work, these RF electrodes were not installed.

9 of the 11 electrodes are connected to a stainless-steel wire with a diameter of 0.6 mm. These wires are encased by a PTFE (polytetrafluoroethylene) sleeving with a wall thickness of 1 mm for electrical insulation. The two remaining electrodes (CDT and C1) are supposed to be switched in the order of microseconds between two high voltages for efficient trapping of externally injected ion beams or extraction of highly charged ions (compare figure 3.9). To avoid crosstalk to other electrodes and reduce its influence on the electrostatic potential of the trap, both are connected to a semi-rigid coaxial wire with a stainless-steel sheath and a beryllium-copper conductor. All wires are guided by drillings in a Macor-feedthrough ring. It keeps the cables in position and prevents spark-overs between wires and the common electrical ground. The grooves in the ring increase the path of undesirable creeping current.

To reduce the heat load on the trap caused by the thermal conductivity of the wires, those are thermally linked to the 40 K region. All wires are glued inside ceramic tubes with a thermally good conducting epoxy (Stycast 2850FT), suitable for ultra-high vacuum (compare figure 3.11) and for cryogenic operation. Those ceramics are radially glued to a feedthrough-ring made of aluminum which is directly connected to the front cover of the 40 K heat shield. The wires are guided by ducts made of PEEK to prevent an electrical contact to the shields. With this approach, the heat input into the trap is reduced from
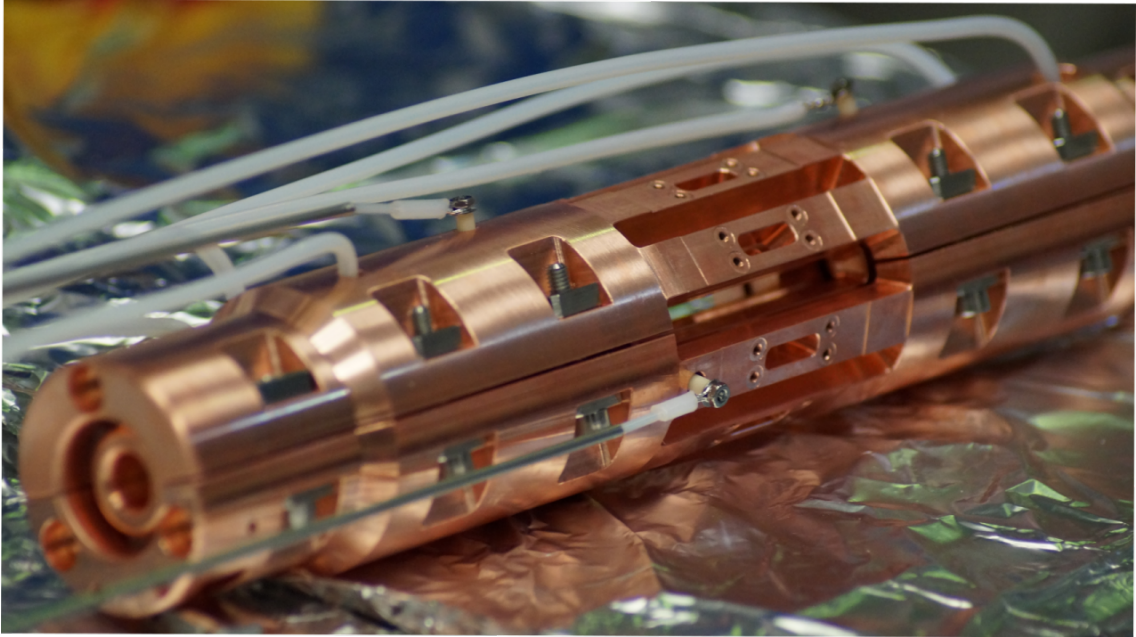
Figure 3.9: Electrical connections of the trap electrodes.
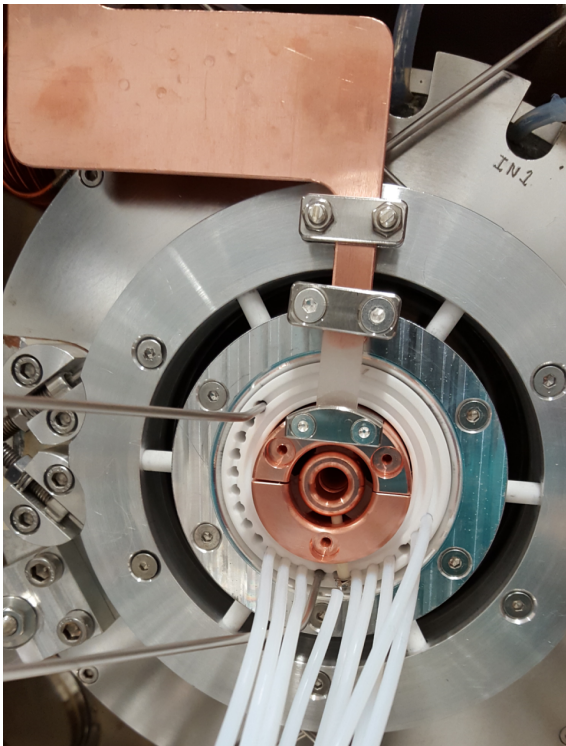
Figure 3.10: Electrical connections of the trap electrodes. 9 of the 11 electrodes are connected via stainless steel wires encased with PTFE hoses. The remaining two (CDT and C1) are supposed to be switched fast between two high voltages and therefore connected with semi-rigid coaxial cables to reduce the crosstalk. All cables are guided by drillings in the Macor-feedthrough and the insulator surrounding the drift-tube assembly.

Figure 3.11: Thermal connection of the wires of the trap electrodes to the 40 K stage and electrical insulation.

30 mW to 0.5 mW compared to a system without thermal anchoring to the 40 K stage.

3.3.5 Electrostatic lens

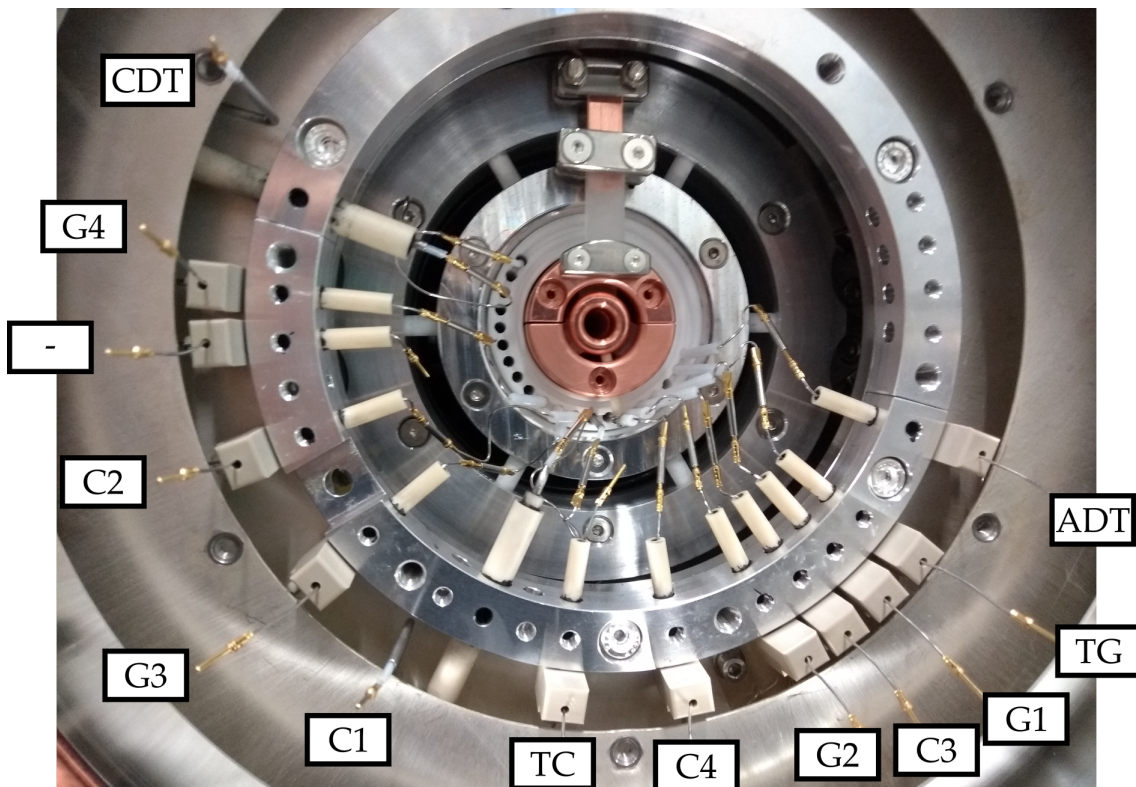Between the drift tube assembly and the collector, an ion-optical element is installed to optimize for the trajectories of the injected or extracted ions. The plainest method is an application of an Einzel lens. It consists of three hollow cylinders in series. The outermost is biased to a different potential than the one in the center, which allows for manipulation of the focusing properties. In this setup, a more advanced configuration has been chosen. The so-called Sikler lens [78, 152, 151] is based on the principle of an Einzel lens with the major difference that the central electrode is segmented into four parts. This allows for focusing as well as for steering of the charged particle beam in the horizontal and vertical direction. The advantage of the geometry of a segmented hollow cylinder compared to deflection plates is a significant reduction of aberrations.

The central cylinder is cut diagonally, rotated by 90° around the symmetry axis, and the cut is repeatedly performed, resulting in four individual segments (compare figure 3.12).
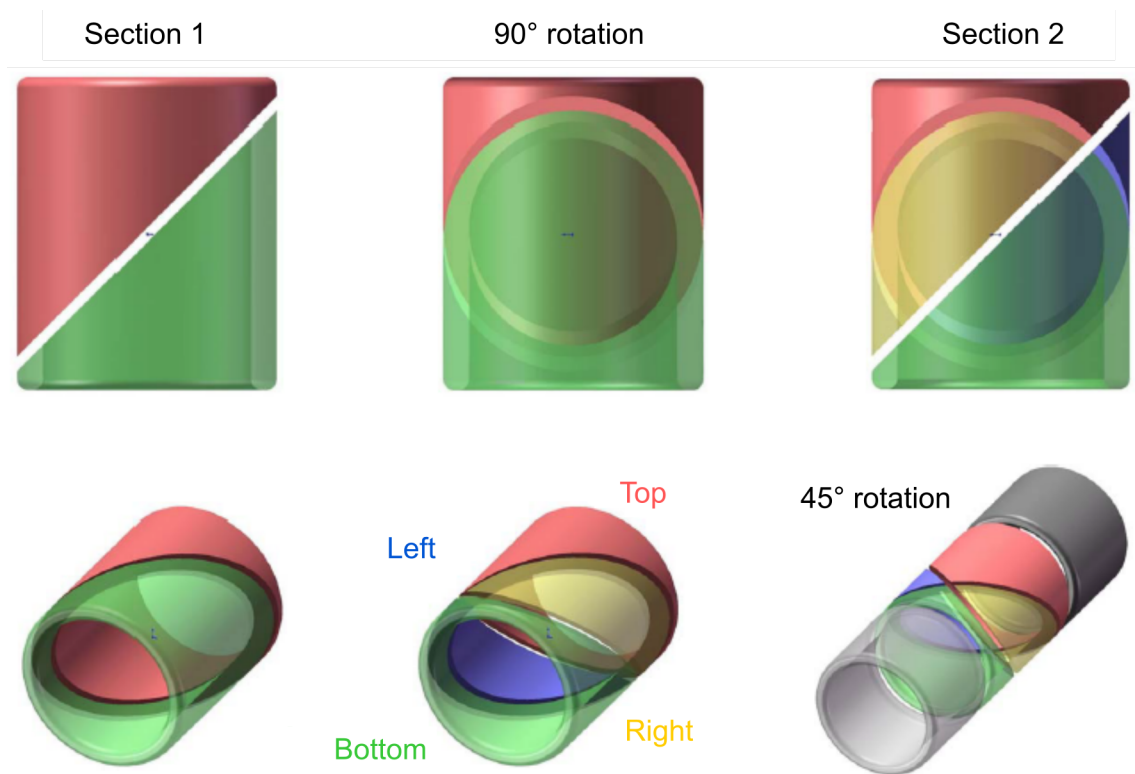
Figure 3.12: Schematic representation of the manufacturing of a four-fold segmented central electrode of a steerer lens (Sikler lens). Adapted from Ref. [152].
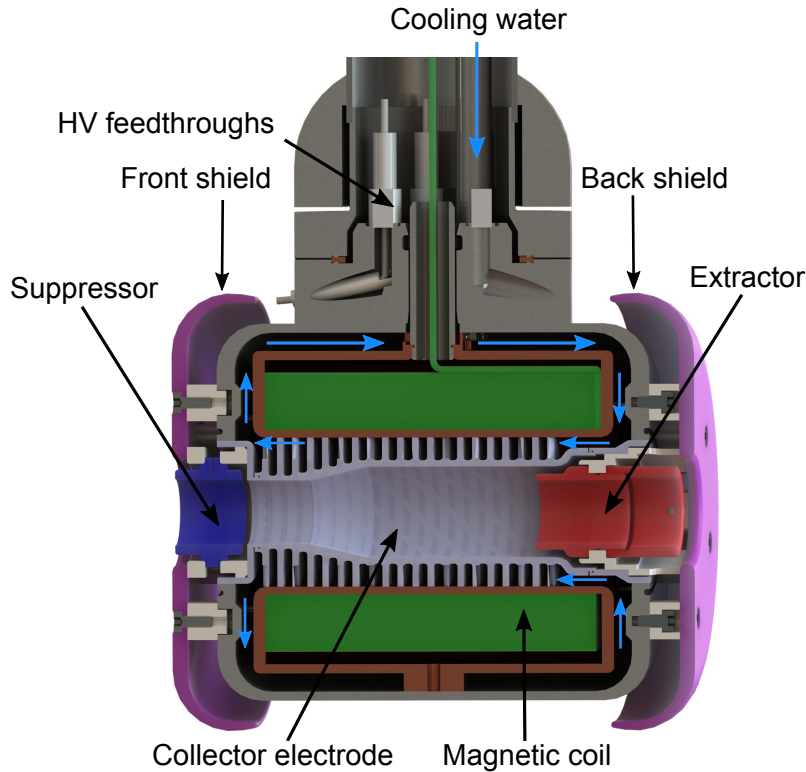
Figure 3.13: Sectional view of the model of the collector. Adapted and modified from Ref. [34].

3.3.6 Electron collector

The electrical circuit is closed by the impingement of the diverging electron beam on the surface of the hollow cylinder-shaped collector electrode. The remaining kinetic energy of the electrons is in the order of $E_{\text{kin}} = eU_{\text{cathode}} \approx 3\,\text{keV}$, which corresponds to a heat load of $\sim 3\,\text{kW}$ at an electron-beam current of $1\,\text{A}$ on the collector electrode. For an efficient dissipation of the heat, the collector electrode is equipped with cooling fins on the atmospheric pressure region of the collector to enhance the effective area of the surface. This surface is directly cooled by a constant flow of water by means of a water-to-air chiller. To increase the divergence of the electron beam to distribute the power dissipation on a larger surface a counteracting field to the residual field of the superconducting magnet can be generated by the application of current flow (typically $5\,\text{A}$ at a voltage of $0.5\,\text{V}$) through the collector coil.

At the front of the collector electrode a ring-shaped, slightly negative-biased suppressor electrode is attached in order to repel secondary electrons, emitted by impingement of the electron beam on the collector surface. On the rear side of the collector, an also second ring-shaped extractor electrode is mounted and biased to a more negative potential than
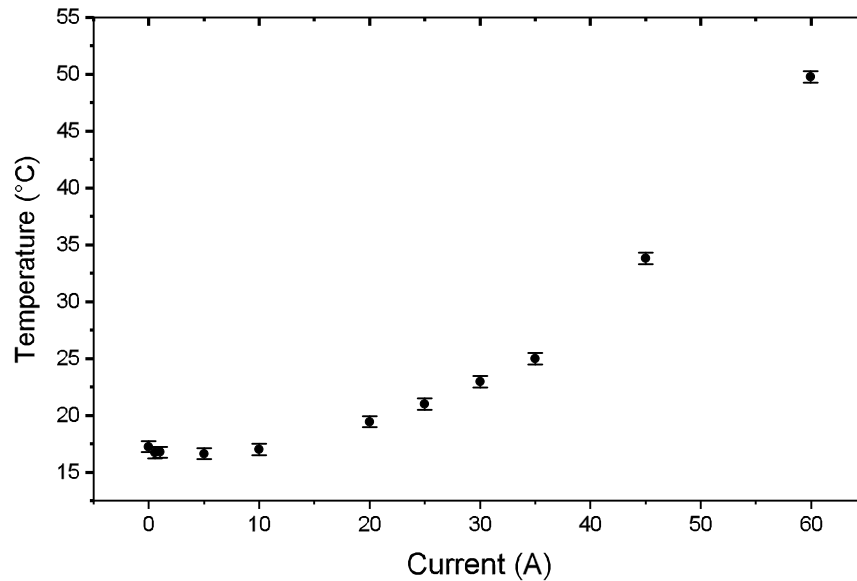
Figure 3.14: Measured temperature on the outermost surface of the collector coil with constant cooling-water flow as a function of the coil current.

the cathode (typically $-4\,\text{kV}$) to prevent electrons from escaping through the collector and eventually to damage downstream elements, e.g. glass windows. For a smoother transition of the electrostatic potential two polished shields of stainless steel terminate the entrance and exit of the collector assembly, so so-called front shield and back shield. Both can be biased to optimize for injection and extraction of ions or optimization of the electron beam trajectories.

The major change to the previous collector models is the use of a different epoxy with higher thermal conductivity (OMEGABOND 200) to adhere the coil windings to each other. The simulated heat dissipation is $51\,\text{W/layer}$ (6 layers in total with 24.5 windings per layer on average) leading to a temperature increase to $44\,°\text{C}$ on the outermost surface of the coil at a current of $50\,\text{A}$ which is in a good agreement with the measured value (compare figure 3.14). In this measurement, a temperature sensor is attached to the surface of the outermost layer of the collector coil, and the temperature is monitored as a function of the current flowing through the coil. The system is cooled by means of a water-to-air chiller.

3.3.7 Gas-injection system

For the provision of a target for ionization and spectroscopic investigation, a gas-injection system was developed. The design is based on the existing gas-injection system of the FLASH-EBIT [63] with some modifications. The sectional view is depicted in figure 3.15.
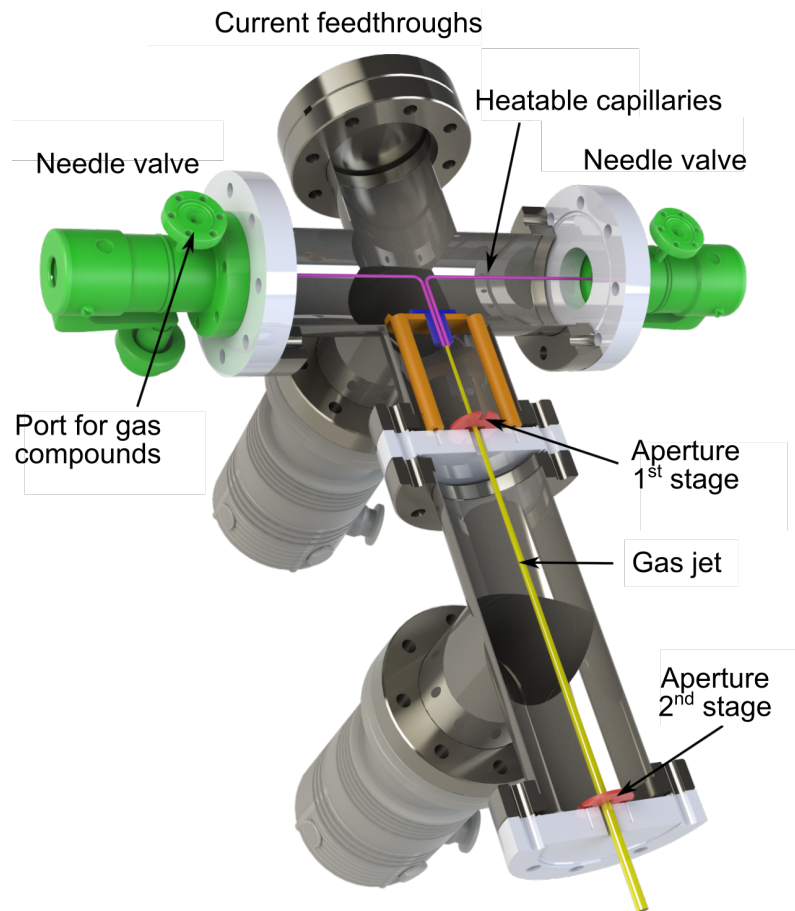
Figure 3.15: Sectional view of the model of the two-staged differentially pumped gas-injection system. Adapted and modified from Ref. [34].

(a) Support structure for the capillaries.   **(b)** Heatable capillaries for gas injection.

Figure 3.16: Internal parts of the first stage of the gas-injection system.

It is a two-staged differentially pumped system with the possibility of injecting two gas species into the trap. An aperture separates the first stage from the second stage, and the second stage from the EBIT, respectively. Each stage is pumped by a 70 l TMP whereby the exhausts are connected to a joint pre-vacuum system backed by a scroll pump.

Two needle-valves are attached to the 6-way cross of the first injection stage. A capillary in guided from the needle valve to a support structure mounted in front of an aperture in the first stage (compare figure 3.16a), respectively. Both capillaries are heatable (compare to figure 3.16b) to prevent condensation of injected e.g., organometallic compounds. At low pressures in the order of 10^{-6} mbar in the first stage, the mean free path of the molecules is large compared to the dimensions of the gas injection system. Thus the trajectories can be considered as ballistic, and the interaction between the molecules becomes negligible. Only a small fraction of the initial number of molecules enters the second stage as a collimated gas jet through an aperture with a size of $\sim 12 \times 4\,\text{mm}^2$. A second aperture between the second stage and the magnet chamber lets the gas jet enter into the radial bore of the magnet former after passing a third aperture attached to the 40 K heat shield and finally intersect the electron beam in the trap center where the molecules are dissociated by electron impact. By assuming an injection pressure in the second stage of $\sim 1 \times 10^{-9}$ mbar, and by geometrical considerations, a particle density of $\sim 300/\text{cm}^2$ can be estimated, which corresponds at cryogenic temperatures of 4 K to a gas pressure of $\sim 1 \times 10^{-13}$ mbar.

After crossing the electron beam, the gas jet exits the magnet on the opposite side of the injection system keeping the gas load inside the trap relatively low.

3.3.8 X-ray detector

The transition energies in highly charged ions are typically in the X-ray regime with photon energies in the *keV* range. Suitable systems for the detection of emitted X-ray photons are semiconductor detectors consisting of high purity germanium or silicon. These devices are expedient tools for the diagnostic of the trap content in an EBIT. The information about the investigated element, as well as the charge state, can be inferred from distinct spectral features. In this work, three different X-ray detectors were utilized, which will be briefly described in the following sections.

3.3.8.1 Silicon-drift detector

The charge exchange measurements were performed with the FLASH-EBIT, equipped with a silicon-drift detector. For the detection of K-shell photons whose energies are usually in the keV range, a silicon drift detector (SDD) is mounted to a 45 ° radial port of the FLASH-EBIT with the silicon wafer protruding into the 40 K stage and thus positioned in 141 mm distance from the trap center leading to an increase of the solid angle for higher detection efficiency. To be even capable of investigating L-shell transitions a windowless SDD model (KETEK VITUS SDD) with an active detection area of 80 mm^2 [80] has to be chosen allowing for the detection of photons in the range between 0.2 keV and 30 keV. The extension, where the crystal is positioned, is covered by a polished aluminum tube that is attached to the 40 K shield to reduce the thermal load from the SDD on the trap. The principle is based on the semiconductor diode consisting of a tetravalent IV main-group element like silicon in the utilized model. The setup of an SDD is depicted in figure 3.17. If the energy of an incoming photon is sufficient to overcome the band gap of the semiconductor material an electron can be raised from the valence band to an unoccupied energy level in the conduction band. This primary electron can cause a cascade effect by creating further electron-hole pairs. With this, the number of electron-hole pairs is proportional to the energy of the incoming photon. By the application of a high voltage, those pairs can be separated before they can recombine, and the electric current can be measured at the anode. Additionally, a drift field is applied parallel to the surface by biasing the outermost drift ring to a more negative potential U_{OR} than the innermost ring with U_{IR}. Due to this field gradient, the electrons are transported to the anode and the holes to the drift rings or the back electrode, respectively. The relatively small surface of the anode causes a reduction of the capacity and thus to a minimization of the electric noise [76].

To prevent optical light being detected, a carbon filter with a thickness of 900 nm was installed between trap and SDD. The detector-efficiency curve of the SDD with a beryllium window of 8 µm thickness provided by the manufacturer [80] is shown in figure 3.18. Since
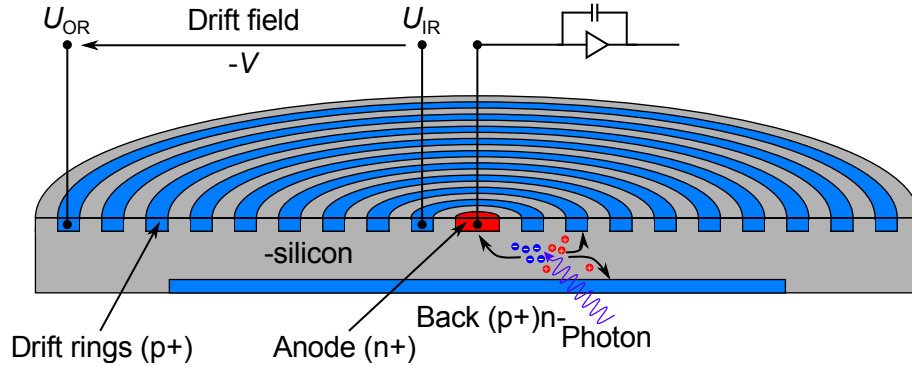
Figure 3.17: Schematic representation of the working principle of an SDD. Adapted and modified from Ref. [60].

the efficiency for a windowless model is not known, an estimation has been made based on calculations of the transmission through the carbon filter, a SiO_2 layer of 150 nm thickness and absorption in the 450 μm thick silicon waver. The single contributions are shown in figure 3.19. The total detector efficiency is the product of these contributions and is presented in figure 3.20. In the range between 2 keV and 10 keV where the measurements of this work are performed, the efficiency of the SDD is nearly constant.

3.3.8.2 Germanium detector

During the commissioning of the CANREB-EBIS, X-ray measurements have been carried out in order to characterize the setup. In the first observations, a high-purity germanium detector (model GL1010), manufactured by Canberra [117], was positioned externally in front of a beryllium window, mounted at a horizontal view port of the magnet chamber. Due to a relatively large effective thickness of the beryllium window on the EBIT and the window covering the detector and the air gap in between, the detector has a low-energy cut-off at ~ 2.5 keV. The photon-energy resolution is 300 eV at 5.9 keV. In the second campaign, a low-energy germanium IGLET detector, manufactured by ORTEC with higher energy resolution was connected directly to the EBIT vacuum to a horizontal viewport. The cut-off energy is lower than of the Canberra-type detector allowing for the detection of X-ray photons above ~ 1 keV energy. The detector crystal is mounted behind a 25 μm thick beryllium window on top of a retractable cold-finger. This allows for the positioning of the detector with an effective diameter of 11 mm close to the trap center, increasing the solid angle. The function principle of both detectors is illustrated in figure 3.21.

Two opposite surfaces of a high-purity germanium crystal are p- and n-doped, respectively. By the application of a positive voltage to the n-doped with respect to the p-doped layer, the setup is operated like a reverse-biased semiconductor diode. By absorption of a high-energetic photon in the highly depleted region of the crystal, an electron can be
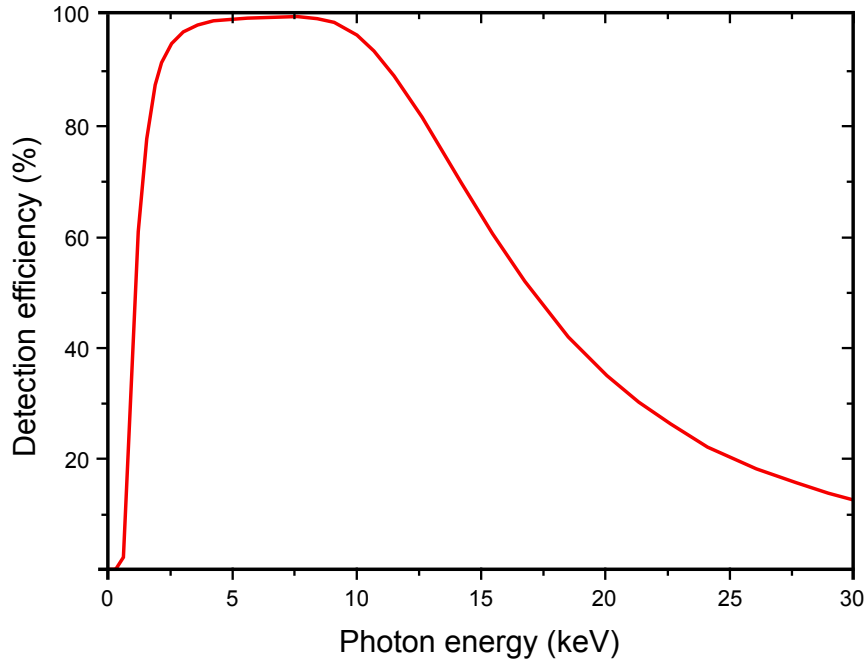
Figure 3.18: X-ray detection efficiency as a function of the photon energy with a Si wafer thickness of 450 µm and a 8 µm Be window. Adapted and modified from Ref. [80].

transferred from the valence band into the conduction band, leading to the production of electron-hole and a temporary electric flux. The amplitude of this pulse is directly proportional to the number of electron-hole pairs, and indirectly proportional to the photon energy. The resulting signal is amplified. Simultaneous detection of two independent photons within a pulse width can lead to assignment to one single event with the sum of the photon energies, which is denoted as a pile-up. In order to reduce the thermal noise and to increase the signal-to-noise ratio and the energy resolution, the crystal is liquid-nitrogen cooled.

3.3.9 EUV flat-field spectrometer

For the observation of charge-exchange-induced transitions not directly to the ground state, an extreme-ultraviolet (EUV) spectrometer, developed by T. M. Baumann within the scope of his diploma thesis in 2008 [19], was utilized by detection of EUV photons. The measurements were performed with the FLASH-EBIT, where the spectrometer was mounted to a radial port of the magnet. The setup is based on the concept of grazing incidence on the surface of a diffraction grating. Due to the strong absorption of EUV light by air, the imaging system is installed inside a UHV environment. The grating itself consists of a glass substrate with carved grooves under a blaze angle θ with variable line spacing along the length of the grating and is coated with a layer of gold to optimize for
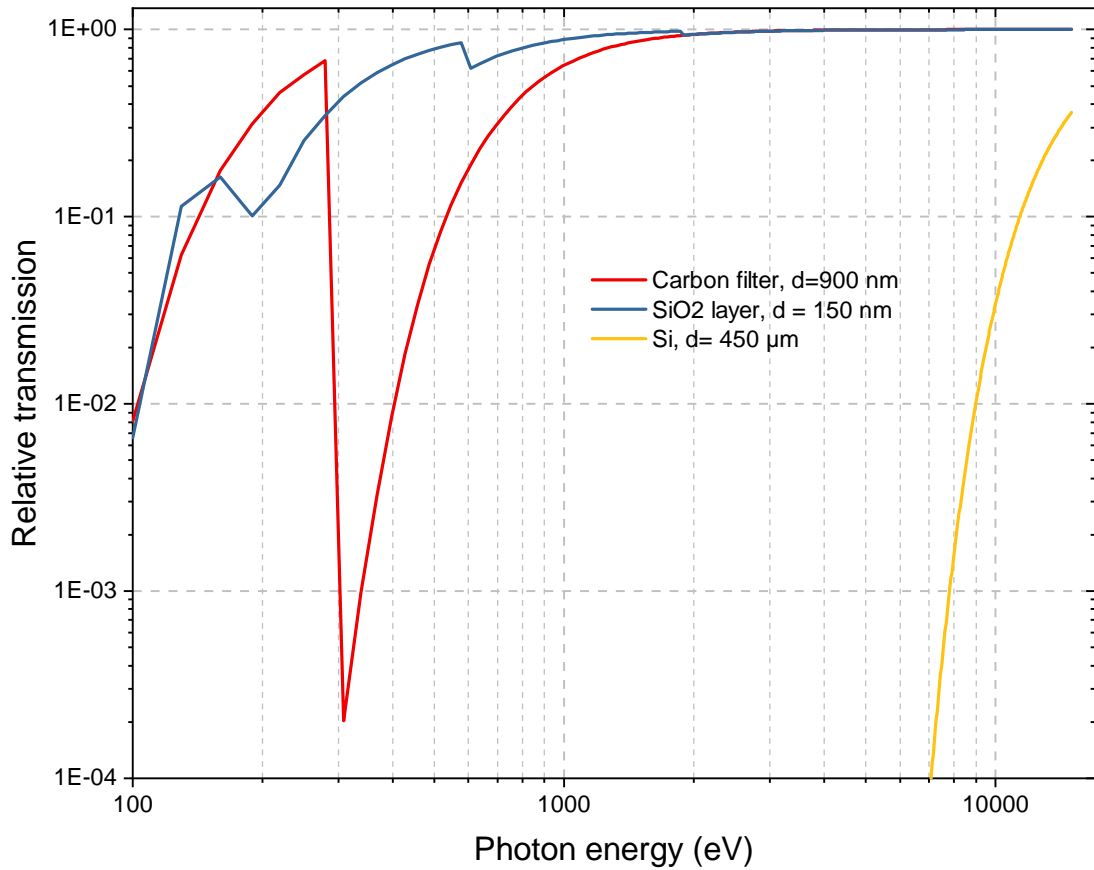
Figure 3.19: Estimation of the silicon drift detector efficiency with transmission through a 900 nm thick carbon foil, a 150 nm thick SiO_2 layer and absorption in the silicon wafer with a thickness of 450 μm as a function of the X-ray energy. The transmission curves are obtained from Ref. [2].
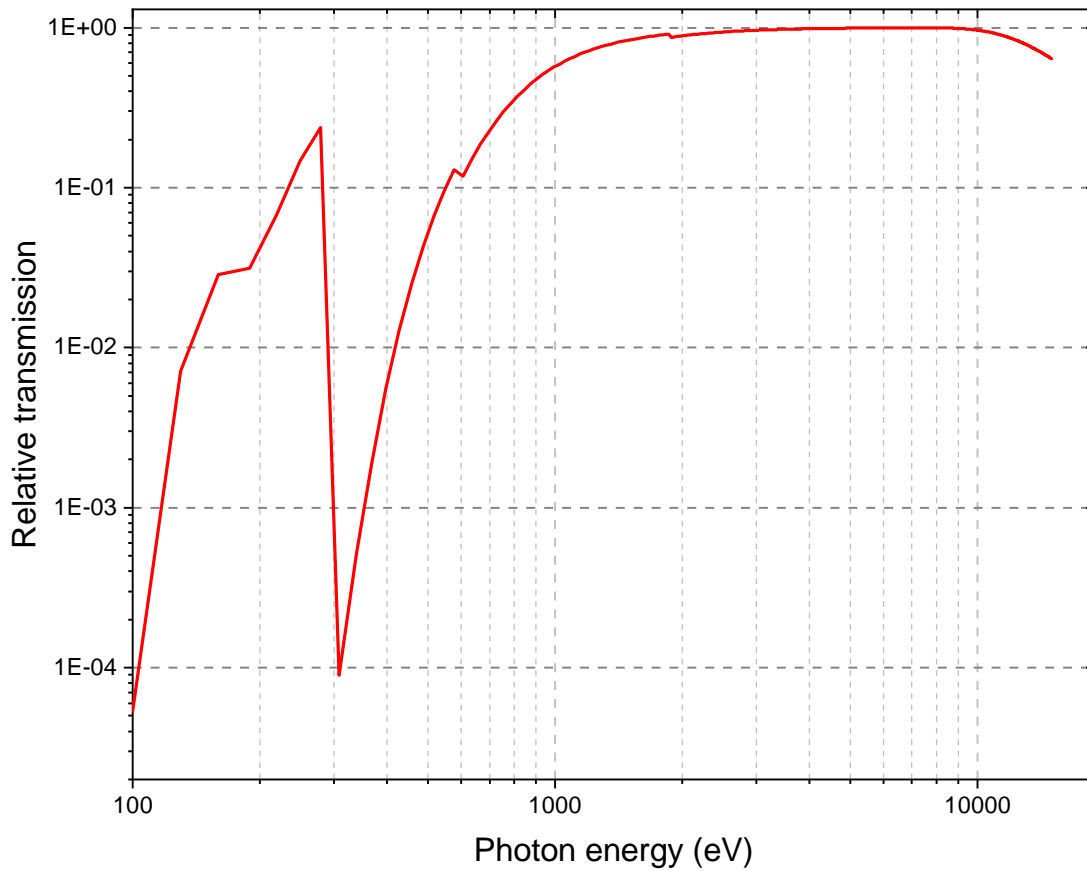
Figure 3.20: Estimation of the total SDD efficiency by the product of the single contributions of the transmission presented in figure 3.19.

Figure 3.21: Illustration of the operation principle of a germanium detector. A photon absorbed in the highly-depleted region generates electron-hole pairs. Application of high voltages to the p- and n-doped surfaces leads to a temporary electric flux, which amplitude is proportional to the photon energy. Adapted and modified from Ref. [31].
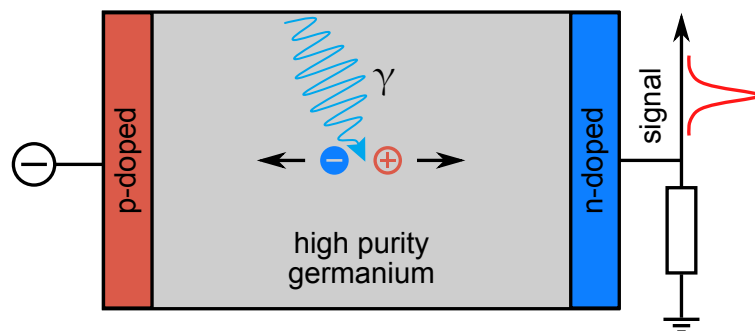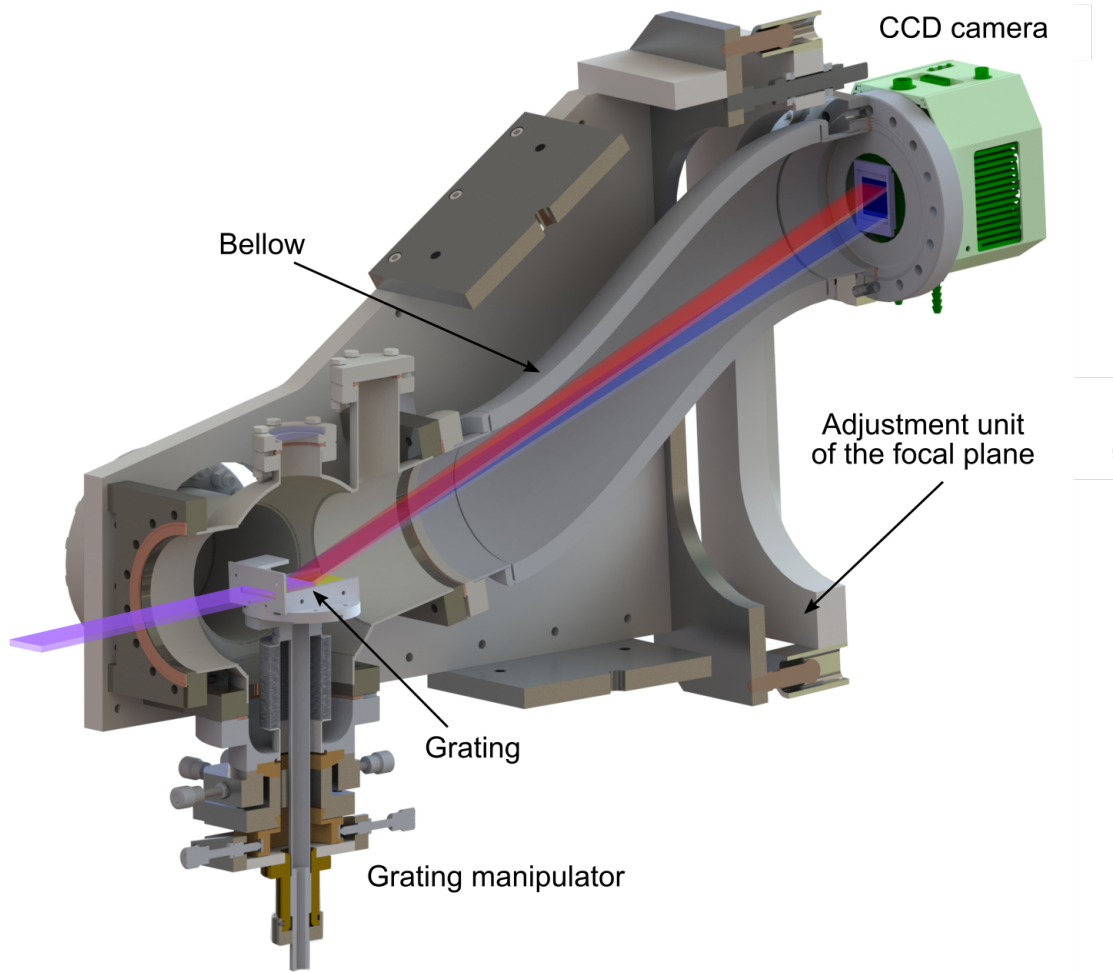
Figure 3.22: Sectional view of the EUV spectrometer equipped with a 1200 grooves/mm diffraction grating and a Peltier-cooled CCD camera.

the reflectivity for soft X-rays. On average the grating has 1200 grooves/mm. Additionally, a concave curvature with radius R is incorporated to the surface of the grating. This results in a focusing of the light on the surface of a plane, in contrast to a Rowland-circle configuration, where the light diffracted by a curved grating is focused on a circle [17]. By this approach, imaging errors like aberration and coma are reduced.

After diffraction, the EUV light is focused on the plane of a charge-coupled device (CCD) chip with 2048×2048 pixel on area of $27.6 \times 27.6 \, \text{mm}^2$. To ensure optimal focusing, the grating is manipulable in all three spatial dimensions as well as in azimuthal and elevation angle of the grating surface with respect to the radiation emitted by the ion cloud. The setup is a combination of an *xy*-stage and a goniometer. Additionally, the CCD camera which is mounted to a CF100 bellow, can be moved and tilted along the path of the
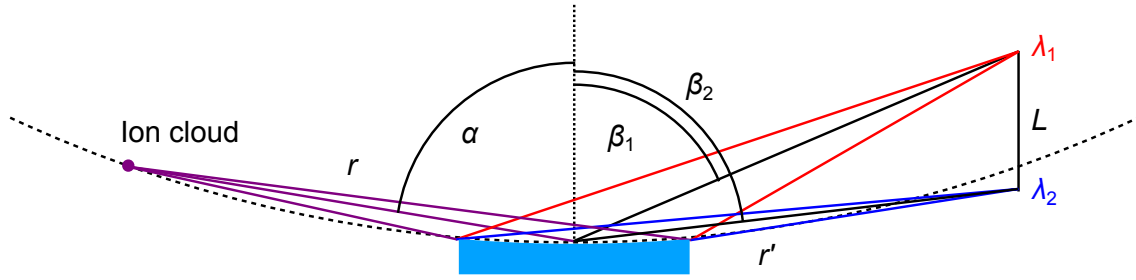
Figure 3.23: Schematic representation of the diffraction on a grating with the most important quantities. Adapted and modified from Ref. [19].

Table 3.1: Geometrical properties of the 1200 grooves/mm Hitachi-grating and the EUV spectrometer. Adapted from Ref. [20].

R (mm)	θ (°)	r (mm)	r' (mm)	α (°)	β_1 (°)	β_2 (°)	$\lambda_2 - \lambda_1$ (nm)	L (mm)
13450	1.9	564	563.2	87	75.61	83.04	$5 - 25$	75.73

diffracted light to match the focal plane.

Within one acquisition, a spectral range of 6 nm can be mapped onto the CCD sensor simultaneously. By the vertical movement of the camera, a wavelength range between 5 nm and 30 nm can be imaged.

A schematic representation of the diffraction on the grating is depicted in figure 3.23. An ion cloud with a diameter of $\sim 100\,\mu m$ acts as an elongated cylindrical light source in a distance of $r = 564\,mm$ from the grating. The angle of incidence α of the emitted light with respect to the normal of the surface of the grating is kept constant at $\alpha = 87°$. The light with a wavelength of λ_i is diffracted under an angle β_i with respect to the normal of the surface of the grating and focused on a plane in a distance of r'. Due to the geometry of the setup the grating equation

$$m\lambda = d_0(\sin \alpha - \sin \beta) \tag{3.9}$$

with diffraction order m and the distance between neighboring grooves d_0 can be revealed. This serves in first order as a geometrical calibration for the wavelength-dependent position of a spectral line on the CCD sensor by calculating the distance L between two wavelengths λ_1 and λ_2.

3.3.9.1 CCD camera

The spectral lines are imaged with a back-illuminated CCD camera manufactured by Andor. The vacuum-compatible chip is equipped with 2048×2048 pixel, each with a size of

$13.5\,\mu\text{m} \times 13.5\,\mu\text{m}$, on an area of $27.6 \times 27.6\,\text{mm}^2$. In front-illuminated models, the readout electrodes are mounted on top of the light-sensitive pixels which are directly attached to a silicon wafer with a thickness of $500\,\mu\text{m}$. This leads to absorption of EUV photons by the readout electrodes. In the back-illuminated version, the silicon wafer is thinned by removing material down to a thickness of $10\,\mu\text{m}$ and mounted in a way that the photons have first to pass the wafer before being detected inside the pixels.

Every single pixel can be considered as an individual semiconductor diode. An absorbed photon can excite an electronic transition from the valence band to the conduction band if the mean photon energy of $3.65\,\text{eV}$ is exceeded. The resulting signal is amplified and processed by an analog-to-digital converter (ADC). A digital event is registered with 0.7 electrons at a typical digitalization rate of $31\,\text{kHz}$, and thus, the number of digital events as a function of the photon energy is described by $N_{\text{A/D}} = E_\gamma / 0.7 \cdot 3.65\,\text{eV}$. The total efficiency depicted in figure 3.24, is defined as the ratio of the detected photon flux and the incoming photon flux impinging on the grating surface of a specific wavelength. It is the composition of the efficiency of the grating, which is strongly dependent on the spectral properties of the utilized materials (Si and Au) and the quantum efficiency of the CCD sensor. The total efficiency $N_{\text{A/D}}(E_\gamma)$ is composed of

$$N_{\text{A/D}} = D(E_\gamma) N_\gamma(E_\gamma) \frac{E_\gamma}{2.555\,\text{eV}}, \tag{3.10}$$

where $D(E_\gamma)$ represents the quantum efficiency of the CCD, and $N_\gamma(E_\gamma)$ the total number of impinged photons.

In order to detect weak spectral features, the signal-to-noise ratio has to be increased by reducing the noise. The electronic noise of a CCD is composed of the readout noise with typically two electrons per pixel at a digitalization rate of $31\,\text{khZ}$, the statistical noise and the dark current. The latter is produced by thermal excitation of electrons from the valence band to the conduction band. By cooling the CCD to $\sim -95\,°\text{C}$ with a Peltier element, the dark current is reduced to 8×10^{-5} electrons/pixel/s.

3.3.9.2 EUV shutter

Charge exchange (CX) becomes dominant in the magnetic trapping mode. To investigate CX in the EUV range with the CCD camera with a long exposure time one has to extract the photons emitted during the magnetic-trapping mode by suppressing the contribution of the photons when the electron beam is switched on. This is performed by means of a rotating shutter in front of the aperture of the grating mounted to a zero-length CF100 reducer with a $30\,\text{mm}$ bore in the center. The schematic setup is shown in figure 3.25.

The shutter installed in the horizontal plane consists basically of a disc with $27\,\text{mm}$ diameter with a rectangular hole of $19 \times 15\,\text{mm}^2$ mounted on a shaft actuated by a
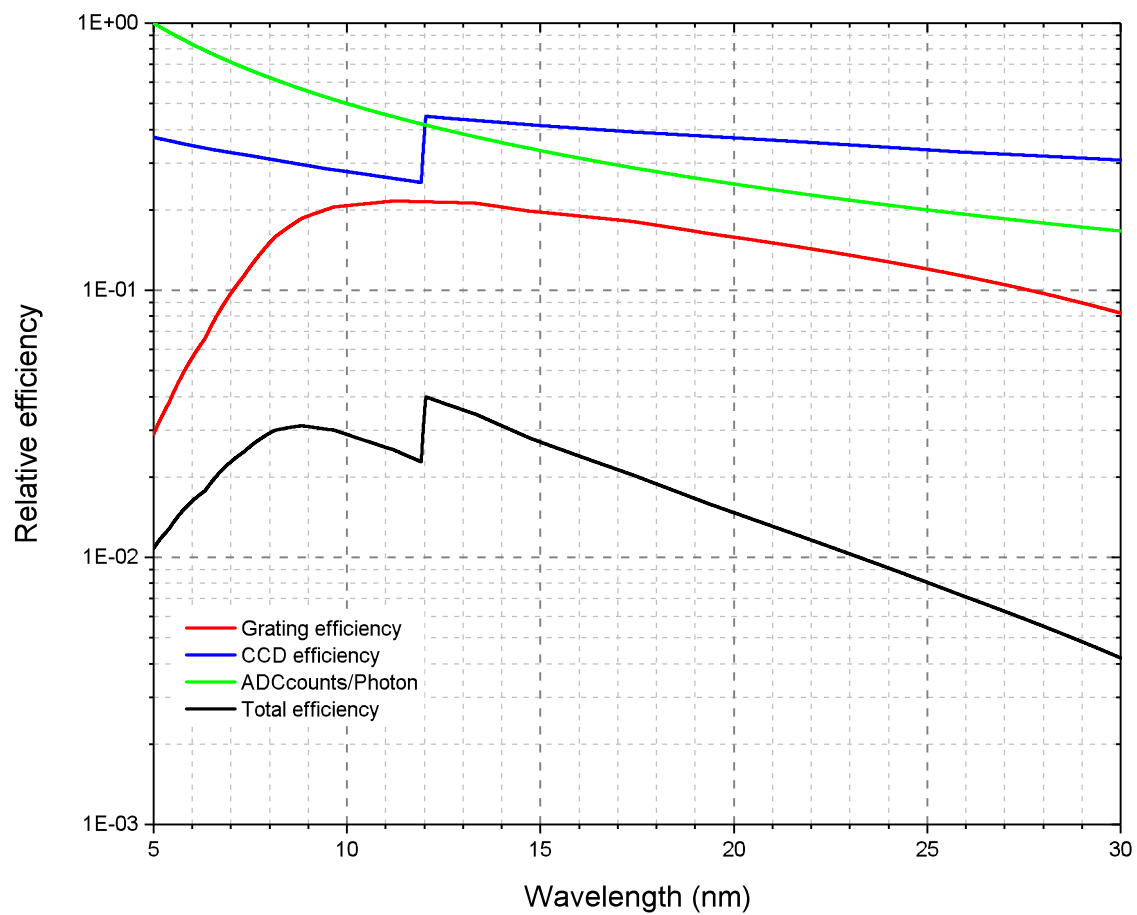
Figure 3.24: Efficiency of the grating, the CCD and the combination of both as a function of the wavelength. Adapted and modified from [20].
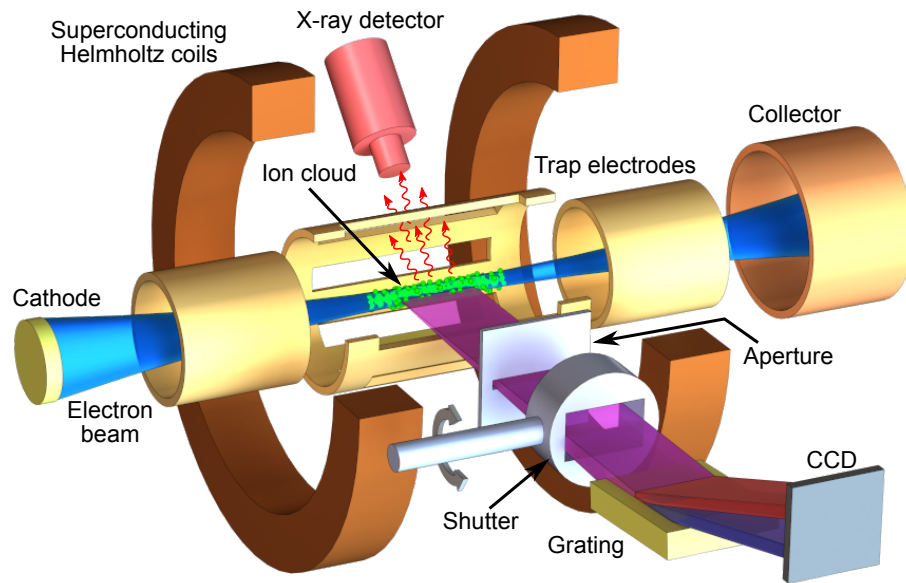
Figure 3.25: Schematical experimental setup. The EUV light emitted by the ion cloud in the central trap electrode, passes an aperture and is blocked by the mechanical shutter during the electron-beam on mode. In the magnetic-trapping mode, the shutter opens, and the diffraction grating is irradiated by the light. The interference pattern is acquired by the CCD camera.

rotary feedthrough. The feedthrough itself is driven by a stepper motor operated by a microcontroller (Arduino). When the electron beam is switched on, the shutter is in a closed position. Whenever the electron beam is switched off, a TTL pulse is transmitted to the Arduino, and the shutter opens within 55 ms, ensuring that no photons emitted during the electron-beam-on mode are detected. With these mechanisms, EUV photons emitted in the magnetic-trapping mode and electron-beam on mode are acquired separately by a CCD camera. Simultaneously, the X-rays emitted during the whole switching cycle are recorded by an SDD mounted to a 45 ° view port.

3.3.10 Laser ion source

For the characterization of ion injection properties and determination of suitable parameters for singly-charged ion injection at the designated end station at ARIEL of the EBIT, a laser ion source (LIS) [167, 176] has been attached directly to the CANREB-EBIT on the collector side at a distance of 1.4 m from the center of the trap.

The principle of operation is depicted in figure 3.26. An intense laser pulse in the order of $1 \times 10^{11}\,\mathrm{W/cm^2}$ with a duration of 7 ns, a wavelength of $\lambda = 532\,\mathrm{nm}$ and energy of 30 mJ is focused to $\sim 50\,\mathrm{\mu m}$ onto the surface of a target leading to the production of a hot dense plasma. After a specific time after the laser pulse, an HV pulse can be applied to the
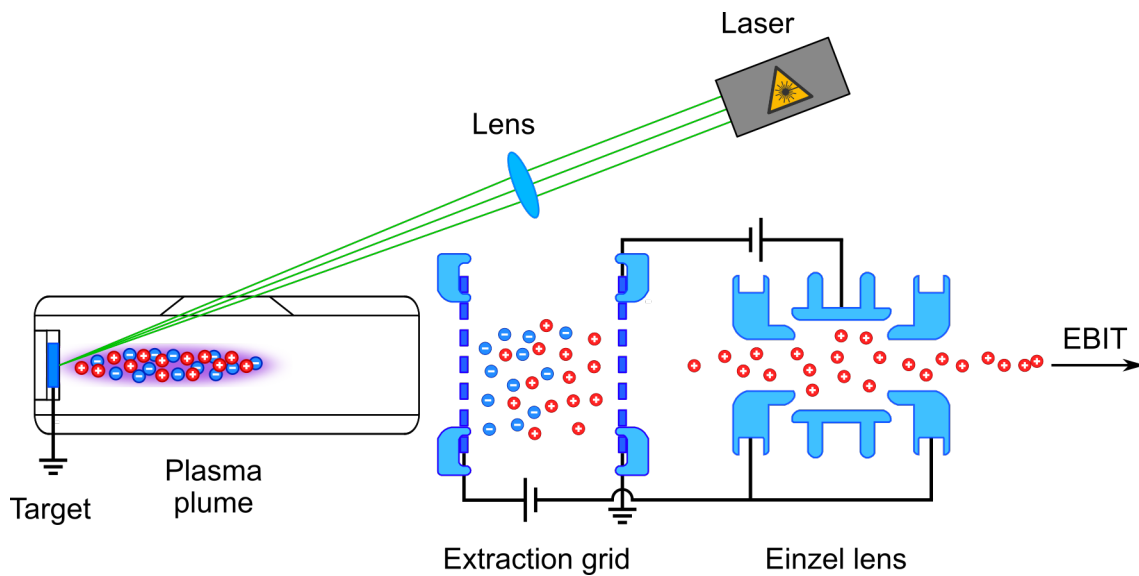
Figure 3.26: Illustration of the function principle of a laser ion source. The distances and lengths are not to scale. Adapted and modified from Ref. [176].

extraction grid, basically a set of two meshes with a separation of 3 mm, by utilization of a Behlke-type fast HV switch in order to separate the electrons from the ions and accelerate the latter towards the EBIT. An additional Einzel lens between EBIT and LIS can be utilized for focusing of the ion bunches into the trap center of the EBIT.

An additional feature is a rotatable revolver-shaped target holder for up to 5 targets which allows faster switching between different elements without breaking the vacuum.

3.3.10.1 Ion-detection unit

Between the laser ion source and the CANREB-EBIT, a detection chamber with a retractable Faraday cup and a pick-up ring was installed (compare figures 3.27b and 3.27a) in order to detect injected ions with the origin in the LIS or highly charged ions extracted from the EBIT.

After passing the Einzel lens of the LIS, the ion bunches enter the pick-up ring and induce image currents which can be detected. The pick-up ring is a cylindrical electrode with an inner diameter of 10 mm and is mounted inside a shielding which is connected to the electrical ground of the vacuum chamber to reduce electrical noise.

Behind the pick-up ring, a Faraday cup is mounted to a linear manipulator. It consists of an inner disc with a diameter of 5 mm and a concentrically aligned punched disk with an outer diameter of 20 mm, both separated and insulated by PEEK spacers. The geometry of the Faraday cup allows for bi-directional operation to detect either injected or extracted ions without rotating the cup and for a rough estimation of the transversal size of the ion
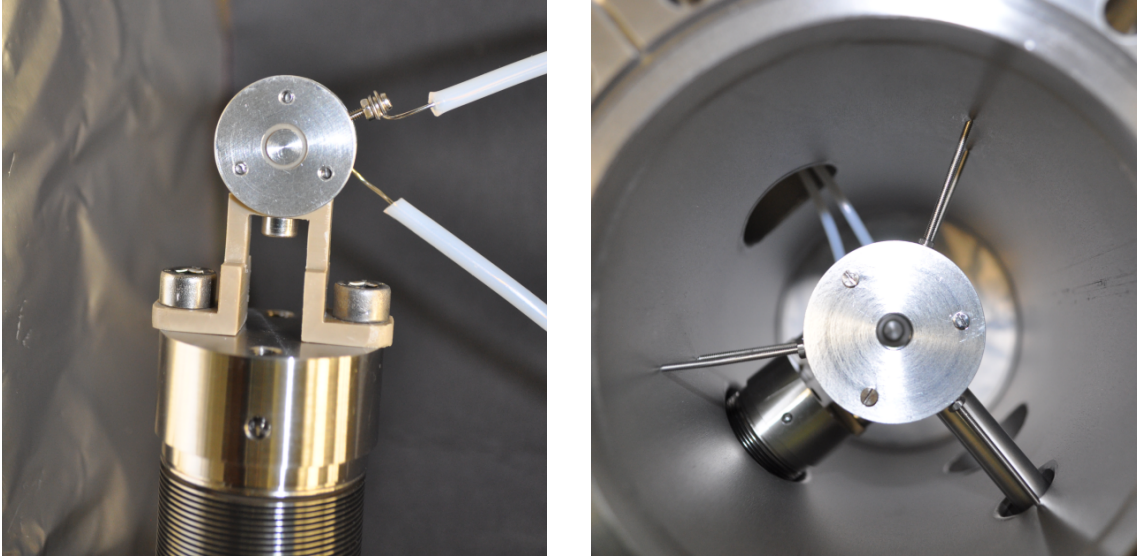
(a) Bi-directional, concentrical two-segmented Faraday cup for detection of injected ions or extracted ions.

(b) Ion-detection unit with the Faraday cup and a shielded pick-up ring in front of it. The Faraday cup is retractable.

Figure 3.27: Detection of injected or extracted ions.

bunches.

For an estimation of the transversal size of an injected ion bunch, the Faraday cup was inserted inside the beam, and the signal on the Faraday cup was measured with an oscilloscope by measuring the voltage as a function of the position of the cup. For each position, the signal was averaged over 100 shots. The results are shown in figure 3.28. The red curve represents the smoothed voltage measured on the inner ring and the blue curve for the outer ring.

The resulting signal S is a convolution of a rectangular-shaped signal $\mathrm{rect}(x)$ corresponding to the detector cross-section and a Gaussian $\mathrm{G}(x)$ corresponding to the transversal shape of the ion bunch.

$$S = \mathrm{rect}(x) * \mathrm{G}(x) \tag{3.11}$$

The distributional derivative of a convolution $\mathrm{D}(f * g)$ can be written as

$$\mathrm{D}(f * g) = (\mathrm{D}f) * g = f * \mathrm{D}g. \tag{3.12}$$

Therefore, the derivative of the signal measured on the cup is

$$\mathrm{D}S(x) = \mathrm{D}(\mathrm{rect}(x)) * \mathrm{G}(x) = (\mathrm{D}(\mathrm{rect}(x))) * \mathrm{G}(x). \tag{3.13}$$

The distributional derivative of a rectangular function can be represented as a Dirac delta
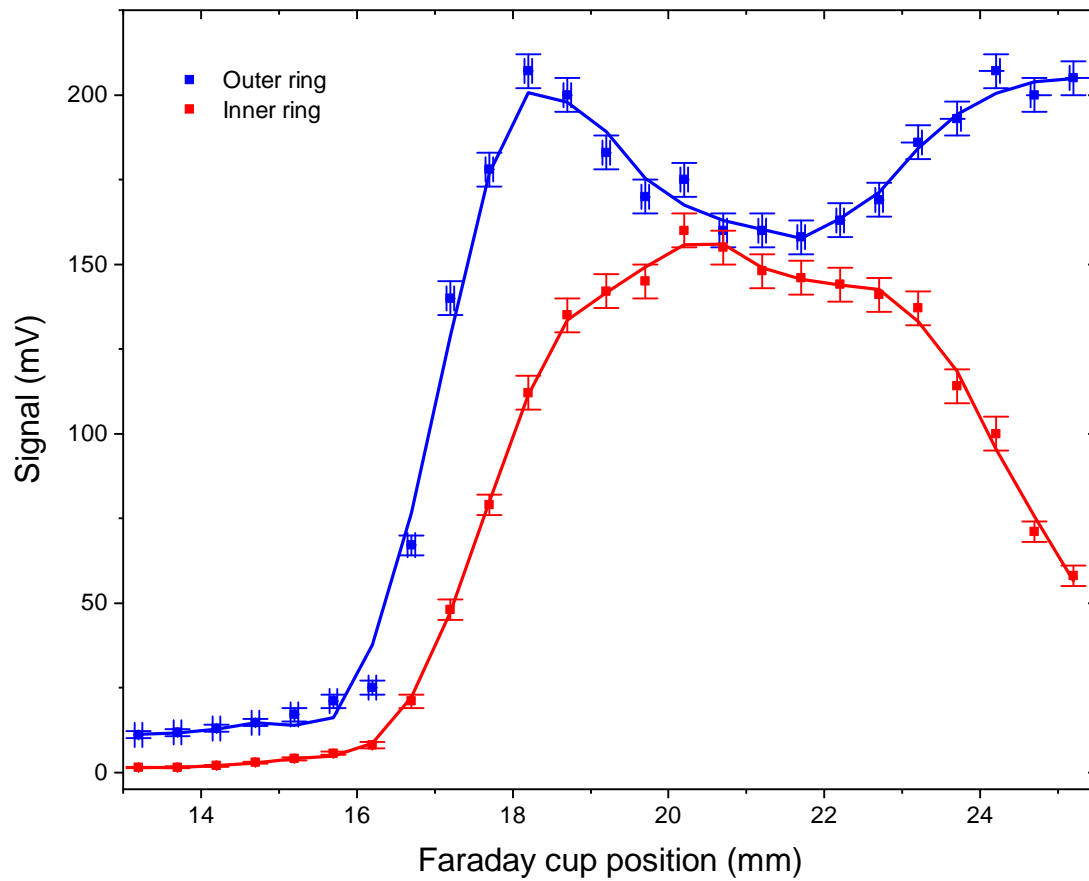
Figure 3.28: Estimation of the transversal size of an injected ion bunch. The Faraday cup was inserted stepwise inside the path of the ion bunches, and the voltage drop was measured as a function of the absolute position of the cup with an oscilloscope. Every data point was averaged over 100 shots of the LIS. The signal measured on the inner ring is represented in red and on the outer ring in blue.
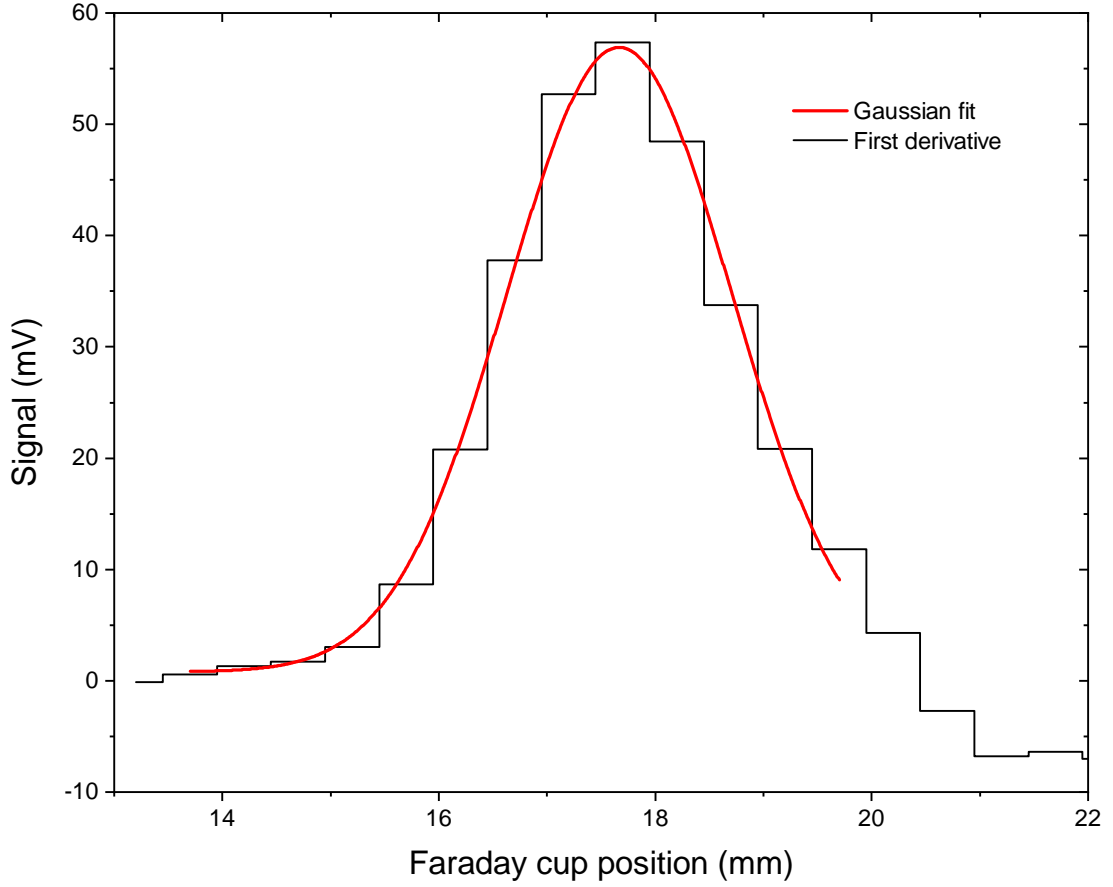
Figure 3.29: Estimation of the transversal ion bunch width by the first derivative of the signal measured on the inner ring (figure 3.28) of the ion detection system. The width is calculated to FWHM = 2.45(7) mm at a distance of ~ 0.4 m from the external ion source.

distribution. With this relations, the derivative of the signal S is a convolution of a Dirac delta distribution with a Gaussian which is again a Gaussian with the same properties. By application of the first derivative of the signal, the shape of the Gaussian-shaped ion bunch can be extracted directly. Figure 3.29 shows the derivative of the signal on the inner ring represented by the black curve and a Gaussian fit in red. The width of the ion bunch is estimated to FWHM = 2.45(7) mm at a distance of ~ 0.4 m from the surface of the target of the LIS. By assumption of an initial diameter of the bunch at the surface of the target of 0.2 mm which corresponds to the focal spot size of the laser beam, the transversal divergence of the beam can be estimated to $\sim 5.6 \times 10^{-2}$ mm/cm. Extrapolating the divergence leads to a transversal size of the ion bunch of ~ 8 mm in the center of the trap at a distance of 1.4 m from the surface of the target.
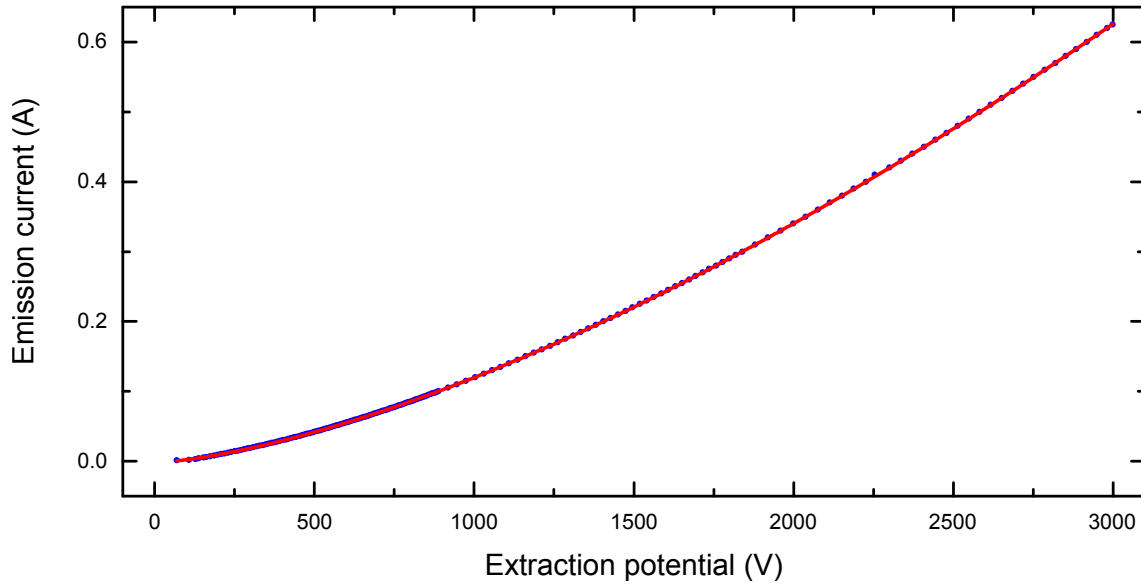
Figure 3.30: Emission current of the cathode plotted as a function of the bias of the cathode with focus electrode and anode at $0\,\mathrm{V}$. The red curve represents a fit according to the Child law. Adapted from Ref. [34].

3.4 Characterization of the CANREB-EBIS

In this chapter, the characterization of the CANREB-EBIS regarding the properties of the electron beam, charge breeding and ion injection, and extraction will be presented [34]. The charge-breeding studies, mainly based on the process of dielectronic recombination of highly ionized argon ions, were performed by the utilization of X-ray detectors. The extraction of ions detected with a Faraday cup and a time-of-flight method will be described qualitatively.

3.4.1 Electron-beam studies

An essential quantity for the characterization of an electron gun is the perveance, which is a measure of the emittance of the cathode. This parameter has been determined within the scope of the bachelor thesis of C. Warnecke [175] by setting the anode and the focus electrode to $0\,\mathrm{V}$, the central drift tube to $2800\,\mathrm{V}$ and varying the bias U_{cath} of the cathode stepwise. In figure 3.30, the emission current of the cathode is plotted as a function of the extraction potential.

The Child equation [47]

$$\bar{j} = \frac{I}{\pi r_{\mathrm{C}}^2} = \frac{4\epsilon_0}{9}\sqrt{\frac{2e}{m_e}}\frac{U^{3/2}}{d^2} \tag{3.14}$$

describes the mean current density $\bar{j}$ in the space-charge limit caused by the negative space

charge of the electron beam. The electrons are emitted from a cathode with radius r_C in an extraction potential U between cathode and anode with a spatial separation d. By fitting the reduced equation

$$I(U_\text{cath}) = A \cdot (U_\text{cath} - U_0)^p \qquad (3.15)$$

to the data, the perveance of $A = (4.11 \pm 0.04) \times 10^{-6}\,\text{A/V}^p$ or $4.11\,\mu\text{Perv}$ with $p = 1.491 \pm 0.001$ and $U_0 = 15(1)\,\text{V}$ can be extracted.

3.4.2 Charge-breeding studies

The first X-ray spectra were obtained in March 2017 by means of a liquid-nitrogen-cooled germanium detector manufactured by Canberra in order to determine the space charge generated by the electron beam.

In figure 3.31 the number of detected photons is plotted as a function of the X-ray photon energy with a fixed acceleration voltage of $5.8\,\text{kV}$, predefined by the potential difference between the cathode and the central trap electrode, and a trapping potential of $100\,\text{V}$ at different electron beam currents.

The unresolved structure below $5\,\text{keV}$ arises due to direct excitation and subsequent relaxation between electronic shells of trapped highly charged ions, mostly Ba and W. Photons with energies above $5.8\,\text{keV}$ can only be produced by recombination processes of ions with free electrons. This photon energy is given by the sum of the ionization potential of the ion and the kinetic energy of the recombining free electron.

Peaks due to radiative capture into open shells $n = 3, 4, 5, 6$ of highly stipped tungsten are indicated in the spectrum at $502\,\text{mA}$ by red, yellow, orange and green vertical lines, respectively. The recombination into the $n = 3$ shell releases a photon with the highest energy due to the higher binding energy of the ion. The charge states of the tungsten ions can be determined to a range of $46 \leq q \leq 52$. With higher electron-beam currents, the negative space charge increases and affects the kinetic energy of the free electrons. Therefore the released photons appear at lower energies. By plotting the peak positions as a function of the electron beam current the space charge ΔV_e can be extracted from the slope of the linear fit to

$$\Delta V_\text{e} = (-1.64 \pm 0.07)\,\text{eV/mA}. \qquad (3.16)$$

It should be remarked that ΔV_e is partially compensated by the positive space charge of the ion cloud.
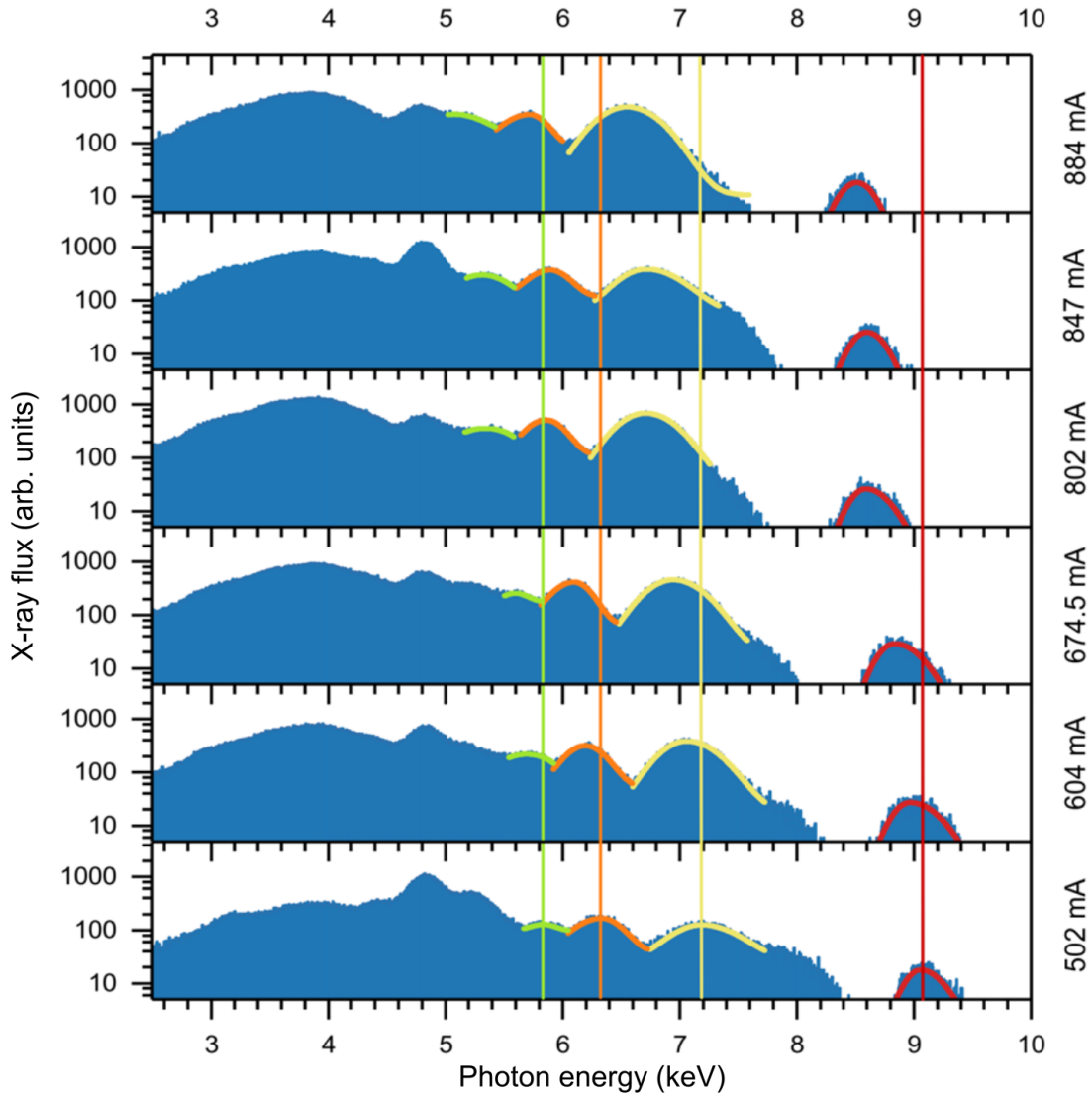
Figure 3.31: X-ray spectra of radiative recombination and direct excitation of highly charged tungsten ions for different electron-beam currents at $5.8\,\mathrm{keV}$ acceleration potential. The red, yellow, orange and green curves indicate recombination into the open $n = 3, 4, 5, 6$ shell of tungsten $46 \leq q \leq 52$, respectively. Adapted from Ref. [34, 175].
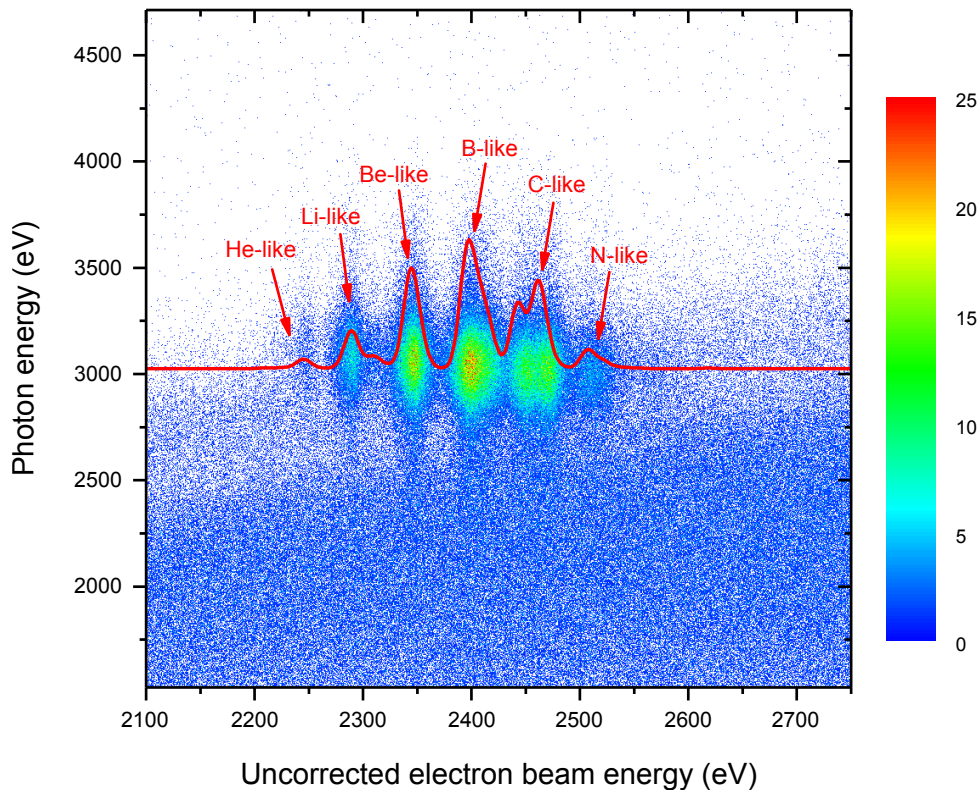
Figure 3.32: The spectrum of KLL dielectronic recombination of N-like up to He-like argon ions with 60 mA electron-beam current. The X-ray flux is displayed as a function of the electron-beam energy on the abscissa and the photon energy on the ordinate. The shift of the MCDF calculation (red curve) towards higher electron-beam energies indicate a combined space-charge potential of the electron beam and the ions of 47 eV. Adapted from Ref. [34].

3.4.2.1 Space-charge compensation

For the determination of the space-charge compensation of the HCIs, a technique based on the process of dielectronic recombination (DR) of highly stripped argon was chosen. Neutral argon was injected into the trap with an axial depth of 100 V and was ionized by the crossing electron beam with a current of 64 mA. The electron-beam energy was cyclically ramped between 2100 eV and 2750 eV, and the X-ray spectrum was simultaneously recorded. This results in a two-dimensional spectrum with the X-ray photon energy as a function of the electron-beam energy, as shown in figure 3.32.

Resonant recombination into N-like up to He-like argon can be observed. By comparison to the integrated K_α emission (solid red curve) obtained by a multi-configuration Dirac-Fock (MCDF) theory, a shift of 47 eV produced by the combined space charge of the electron beam and the HCIs can be determined.

This technique is the basis for investigation of the contribution of the space charge of the
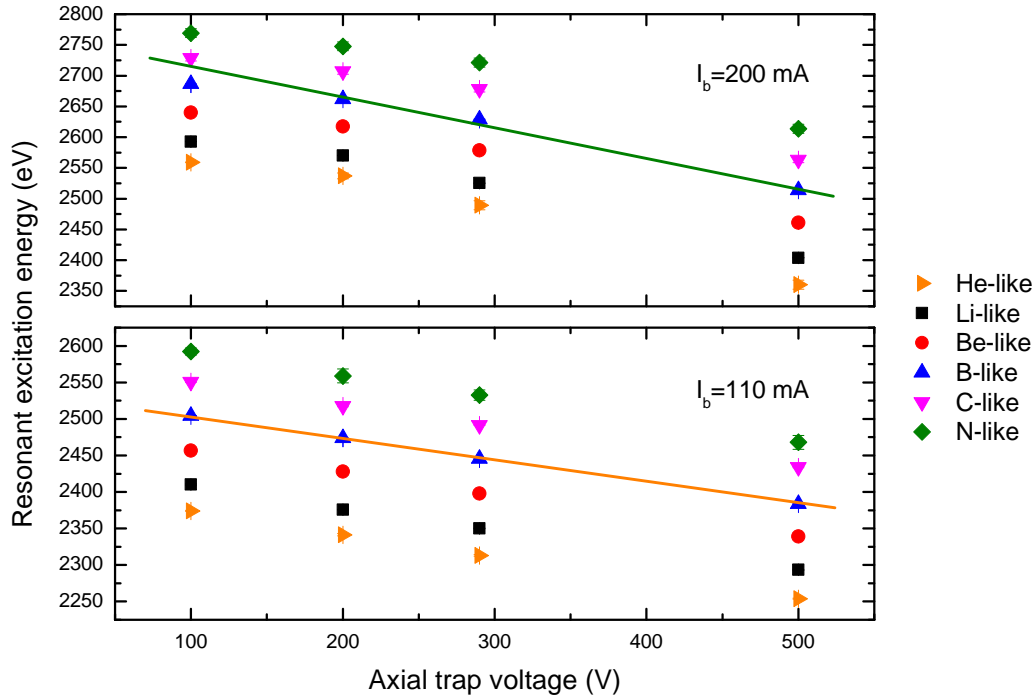
Figure 3.33: Resonance energy of KLL dielectronic recombination of highly charged argon (N-like to He-like) as a function of the axial trapping potential for an electron-beam current of 110 mA and 200 mA. With higher trap depth, higher space-charge compensation can be observed, which shifts the resonance energy to lower values. Adapted from Ref. [34].

HCIs. In figure 3.33, the position of different dielectronic resonances from N-like to He-like argon is recorded as a function of the trap depth at different electron-beam currents. In this measurement, the trap depth was increased by increasing the potential of the first electrodes surrounding the central drift tube.

With higher axial trapping potential, the resonance energies of the DR shift towards lower electron-beam energies. Due to the higher amount of ions in the trap, the negative space charge of the electron beam is highly compensated by the contribution of the positive space charge of the ions which increases the total kinetic energy of the free electrons. For an electron-beam current of 110 mA, the space charge compensation by the ions is $\Delta V_{ions} = -0.29 \pm 0.01\,\mathrm{eV/V}$.

3.4.2.2 Temporal evolution of charge states

In order to investigate the filling of the trap in more detail, the temporal evolution of the charge state distribution was observed by utilizing the technique of dielectronic recombination. A cyclic measurement with a period of one second of emptying the trap by

a short HV puls on the central trap electrode with a fast HV switch (Behlke GHTS-60) and observing the filling of the trap was performed while simultaneously ramping the electron beam energy from 2.1 keV to 2.75 keV over the DR resonances within 20 minutes.

By projecting the region of K_α emission in a photon energy range from 2750 eV to 3250 eV as in figure 3.32 onto the abscissa and plotting it as a function of the time after emptying the trap, a two-dimensional spectrum as in figure 3.34 can be obtained.

In this measurement, the electron-beam current was 64 mA. Directly after the dump, the resonances appear at higher electron beam energy due to the low amount of ions in the trap and thus almost no space-charge compensation. After a specific time, the trap is filled with more ions which compensate for the negative space charge of the electron beam. After ~ 400 ms a steady state is reached where the loss due to evaporation is in equilibrium with the saturation of the trap, a total shift of ~ -160 eV with respect to the uncompensated space charge of the electron beam can be observed.

From the information this plot provides, the electron beam radius can be estimated. Directly after emptying the trap and at the beginning of the charge breeding process, the strong Ar^{14+} DR resonance appears at ~ 2500 eV. According to the MCDF calculation, the resonance should appear at 2303 eV.

The electrostatic potential $\Phi(r)$ of an infinitely long electron beam is represented by equation 3.4 with

$$\Phi_0 = \frac{1}{4\pi\epsilon_0} \cdot \frac{I_b}{\dot{z}} \tag{3.17}$$

and the velocity of the electrons along the trap axis

$$\dot{z} = c_0 \sqrt{1 - \left(\frac{eU}{m_e c_0^2} + 1\right)^{-2}}, \tag{3.18}$$

where m_e represents the electron mass, e the electron charge and c_0 the speed of light in vacuum, Φ_0 can be calculated to $\Phi_0 = 20(1)$ V by assuming an electron velocity $\dot{z} = 2.84(2) \times 10^7$ m/s at an energy of 2303(20) eV where the resonance should appear. Φ_0 represents the potential difference between the center of the electron beam and its boundary. With an inner diameter $2r_D = 14$ mm of the central trap electrode, equation 3.4 can be solved for the electron beam radius and estimated to $r_e \approx 54(3)$ μm .

3.4.3 Ion production rate and trap filling

An essential characteristic of the trap is the filling rate, which is the amount of produced and trapped ions per time unit. Singly charged ions are captured efficiently due to the negative space charge of the electron beam, and thus, the trap is filled instantly. In contrast, the production and trapping of injected neutrals depend strongly on the electron-beam-current
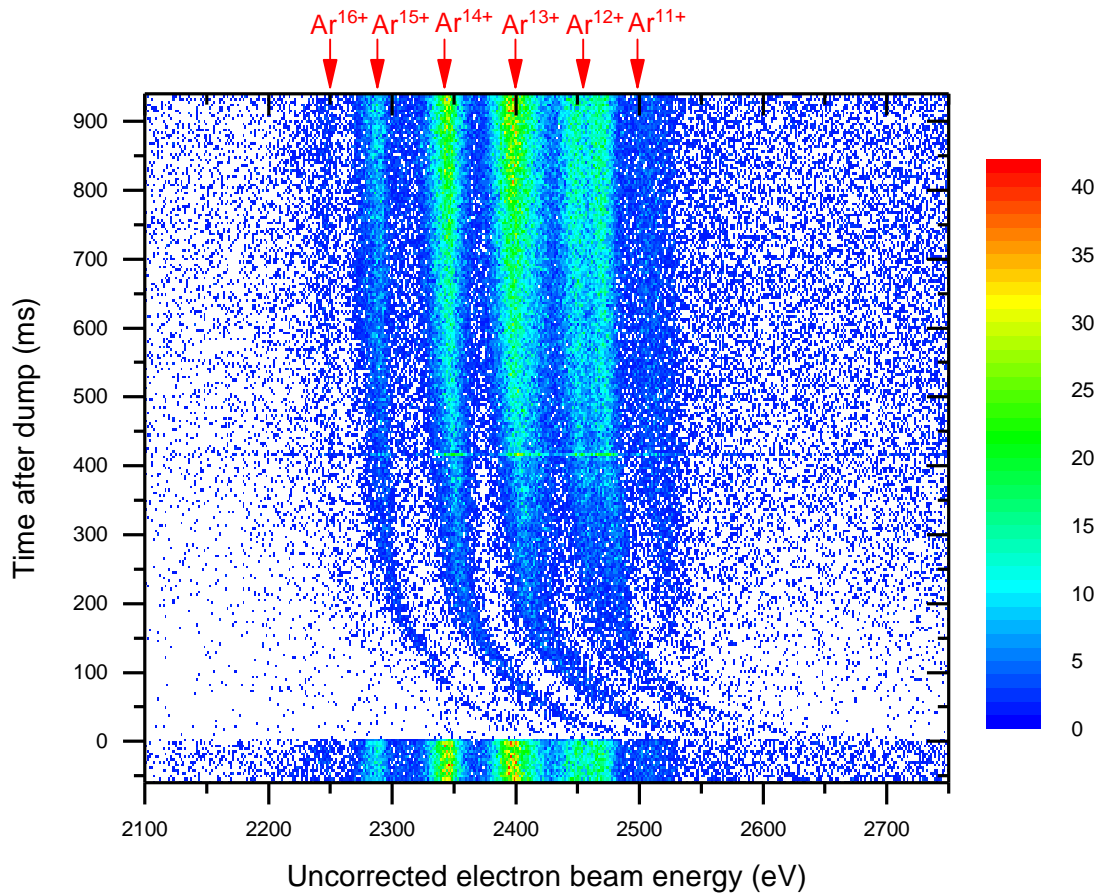
Figure 3.34: KLL-DR of highly charged argon as a function of the time after emptying the trap. At time $t = 0\,\text{s}$, the contribution of the space charge arises only from the electron beam with a beam current of $64\,\text{mA}$. With progressed time the trap starts filling with HCIs which compensate partially for the negative space charge of the electron beam, increasing their kinetic energy. Thus, the resonances appear at lower electron-beam energies with increasing time. Adapted from Ref. [34].
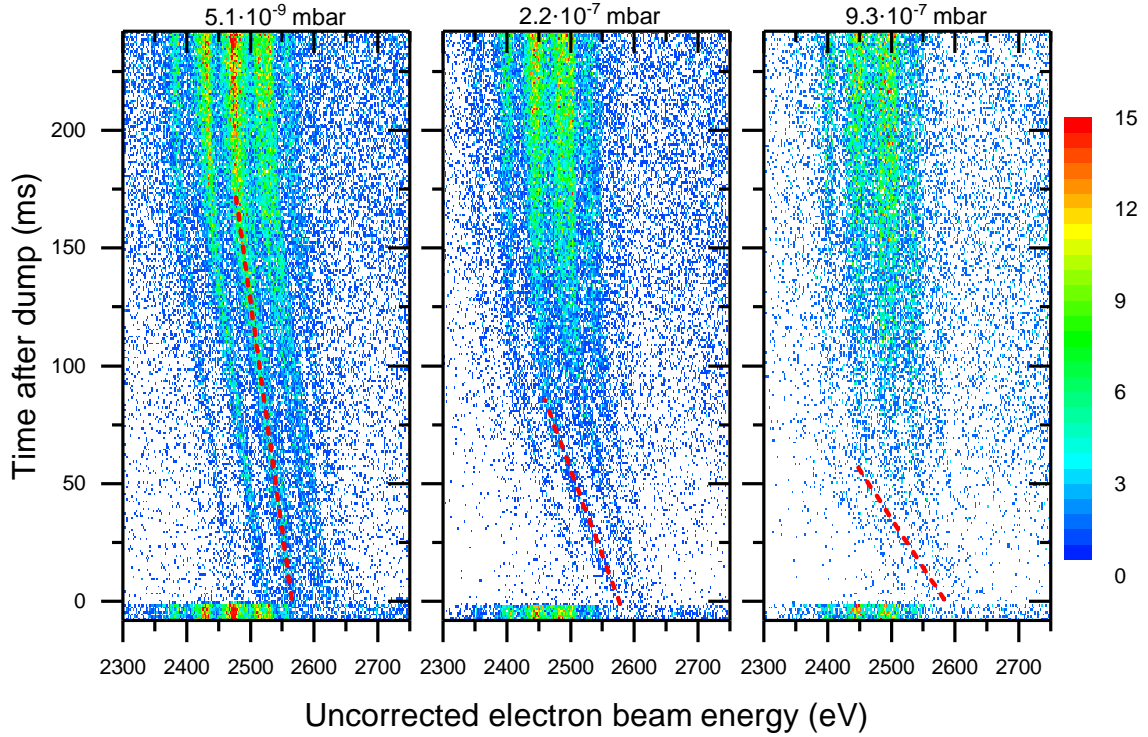
Figure 3.35: Trap filling with argon ions at different injection pressures of 5.1×10^{-9} mbar, 2.2×10^{-7} mbar, and 9.3×10^{-7} mbar, respectively. The measurement technique and data acquisition are the same as described in figure 3.34, but with an electron-beam current of 125 mA. Adapted from Ref. [34].

density and the density of the injected compound, and therefore, the filling rate is lower.

To investigate the filling rate of neutral argon, the measurement technique described in section 3.4.2.2 was utilized with an electron-beam current of 125 mA, an axial trap depth of 100 V and cycle duration of 300 ms for different injection pressures (compare figure 3.35). The scanning range of the electron-beam energy is reduced to 2300 eV to 2750 eV. The red dashed line indicates the slope of the filling of the trap for Ar^{13+} ions resulting from the beryllium-like dielectronic resonance. With higher injection pressures (measured at the second stage of the injection system), the ions are accumulating faster.

The space-charge shift is determined to 0.6 ± 0.02, 1.4 ± 0.1, and 2.6 ± 0.1 eV/ms for the injection pressures of 5.1×10^{-9}, 2.2×10^{-9}, and 9.3×10^{-7} mbar, respectively. These rates correspond to a filling of 4.3×10^5, 1.0×10^6 and 1.9×10^6 Ar^{13+} per millisecond, respectively. By integrating over the number of ions until the saturation of the trap is achieved, leads to a total trap capacity for these specific settings of $\sim 5.7 \times 10^9$ elementary charges. With higher electron-beam currents and a deeper axial trapping potential, this value can be exceeded by at least one order of magnitude.

3.4.4 Ion extraction measurements

For the characterization of extraction of HCIs from the EBIT, the voltage on the central trap electrode was switched between a value below and above the potential barrier of the downstream electrode by a Behlke GHTS-60 fast HV switch module. The charge-bred and extracted ions were detected on the Faraday cup in the ion-detection chamber between EBIT and LIS. The voltage drop over a $500\,\Omega$ resistor was measured as a function of the time after emptying the trap under various conditions with repetition rates of $1\,\mathrm{Hz}$ up to $100\,\mathrm{Hz}$. The signal was averaged over 30 single shots.

The electron-beam current was set to $200\,\mathrm{mA}$ at a beam energy of $\sim 4500\,\mathrm{eV}$ and an axial trapping potential of $100\,\mathrm{V}$ in these measurements. The base pressure with closed injection was $\sim 4 \times 10^{-9}\,\mathrm{mbar}$. In figure 3.36 the extraction signal is recorded for different injection pressures of $1.2 \times 10^{-6}\,\mathrm{mbar}$ (panel b)), $1.7 \times 10^{-7}\,\mathrm{mbar}$ (panel c)) and $7 \times 10^{-9}\,\mathrm{mbar}$ (panel d)), respectively of neutral argon (red curves) and closed injection (black curve) with a digital storage oscilloscope. The subfigures b), c) and d) represent the time-of-flight (TOF) spectrum for injection pressures of 1.2×10^{-6}, 1.7×10^{-7}, and $7.0 \times 10^{-9}\,\mathrm{mbar}$, respectively. In subfigure a) the total charge is integrated for six different injection pressures over a window of $4\,\mathrm{\mu s}$ including the highest peak of the TOF spectrum by the assumption of a charge-state distribution of Ar^{10+} up to Ar^{16+}. The black circles indicate a closed injection, the red circles injection of neutral argon with the corresponding injection pressure in the second stage. Those values for the integrated charge of the extracted ion bunch is the lowest limit due to a non-complete geometrical interception with the Faraday cup.

In figure 3.37, a similar measurement was performed by recording the Faraday-cup signal as a function of the axial trapping potential in the range between $-100\,\mathrm{V}$ above and $500\,\mathrm{V}$ below the potential barrier with a beam current of $200\,\mathrm{mA}$, beam energy of $\sim 4500\,\mathrm{eV}$, and an injection pressure of $\sim 5 \times 10^{-7}\,\mathrm{mbar}$ during open injection.

The subfigure a) is obtained by the same approach as in figure 3.36. Subfigures b), c) and d) represent the TOF spectrum of argon with an axial trap depth of $300\,\mathrm{V}$, $50\,\mathrm{V}$, and $-100\,\mathrm{V}$, respectively. The black curve represents the spectrum with a closed injection valve. A deeper axial trapping potential prevents ions from leaking out by evaporation effects, which leads to an increased yield of HCIs. Hereby the highest peak in the TOF spectrum shifts towards lower time-of-flight, which indicates higher charge states. Also, the TOF resolution for different charge states is reduced, which can be observed with an inverted trap in subfigure d).

However, in contrast to the fast pulsed extraction scheme producing short bunches of HCIs, the bunch length can be increased to seconds by slowly decreasing the axial potential barrier allowing a fraction of hottest ions to evaporate, as shown in Ref. [155, 154, 153].
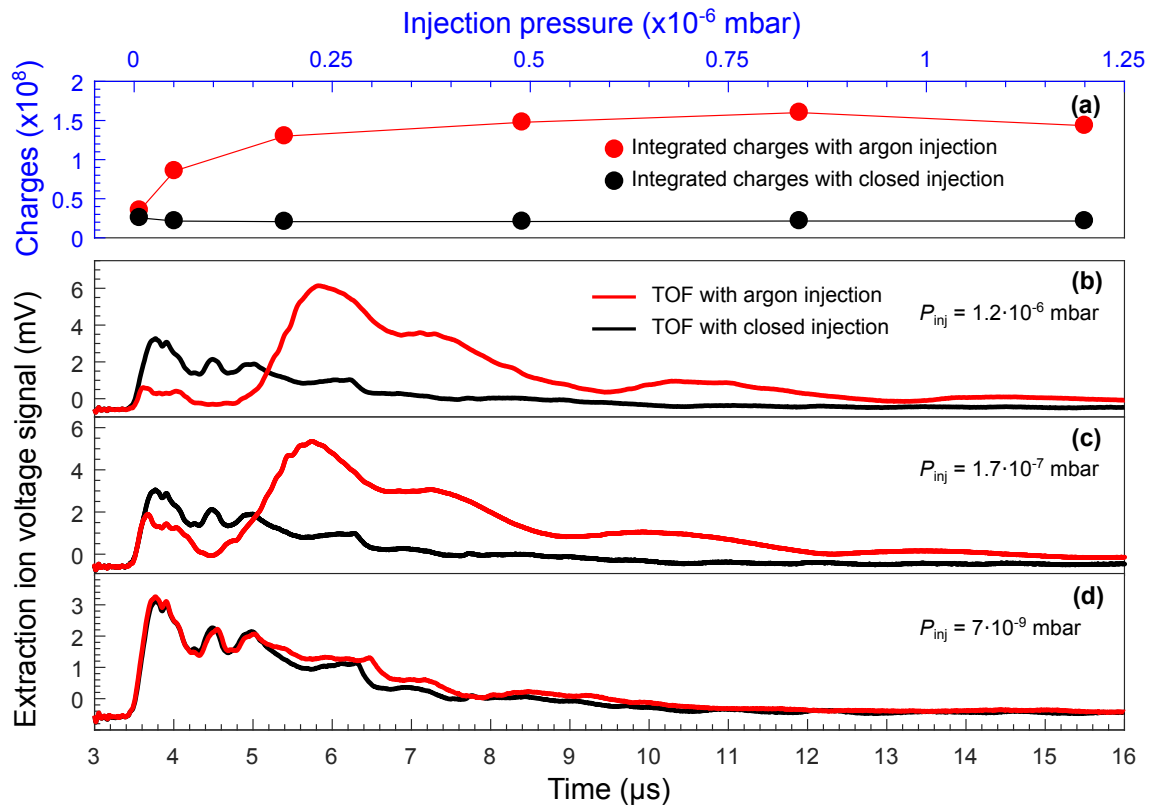
Figure 3.36: Measured signal of extracted argon ions on a faraday cup across a resistor of $500\,\Omega$ for different injection pressures of neutral argon into the EBIT with 1.2×10^{-6} mbar (b)), 1.7×10^{-7} mbar (c)) and 7×10^{-9} mbar (d)), respectively. Subfigure a) shows the integrated number of charges for six different injection pressures with closed injection (black circles) and neutral argon injection with the corresponding injection pressure (red circles). The electron-beam current was $200\,$mA. Adapted from Ref. [34].
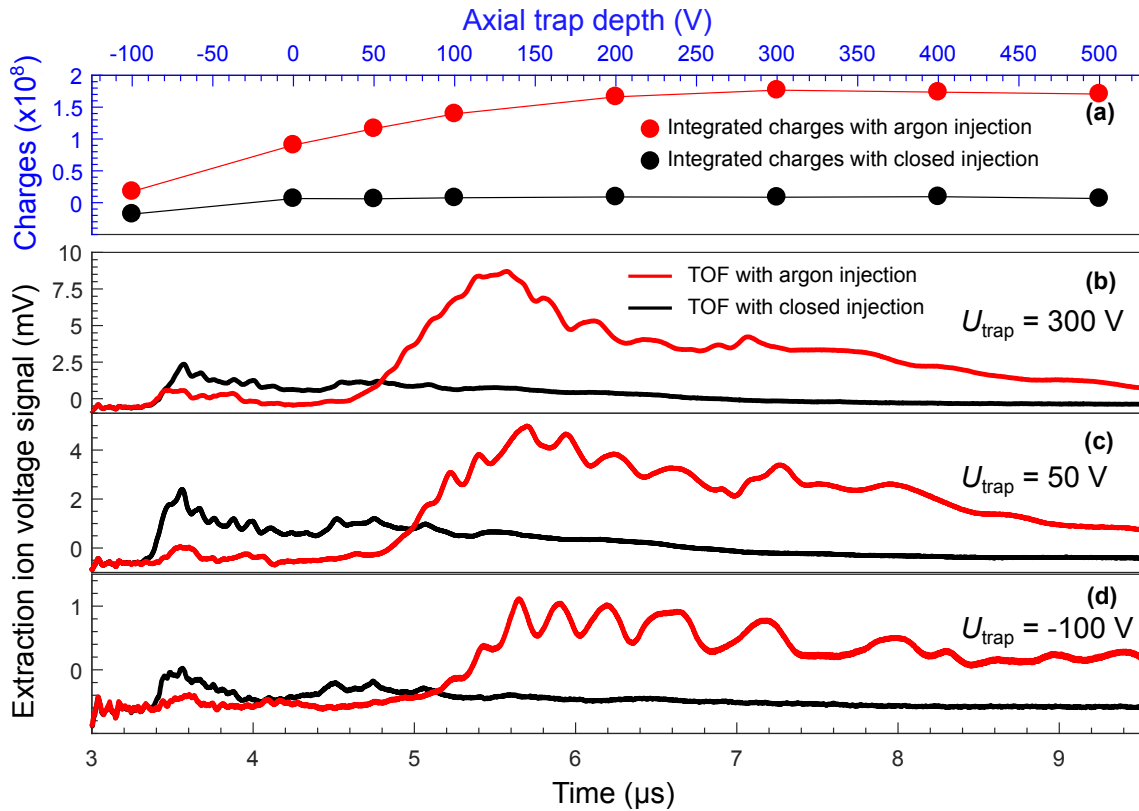
Figure 3.37: Ion yield of extracted argon ions measured on a Faraday cup for different axial trap depths. Negative values represent an inverted trap, where the central trap electrode is at a higher positive potential than the neighboring electrodes. Panels b) c) and d) show time-of-flight spectra obtained at trap depths of $300\,\text{V}$, $50\,\text{V}$, and $-100\,\text{V}$, respectively. Panel a) represents the integrated charges extracted from the EBIT as a function of the trapping potential. The beam current was set to $200\,\text{mA}$ at an energy of $\sim 4500\,\text{eV}$. The injection pressure during open injection was $\sim 5 \times 10^{-7}$ mbar. Adapted from Ref. [34].
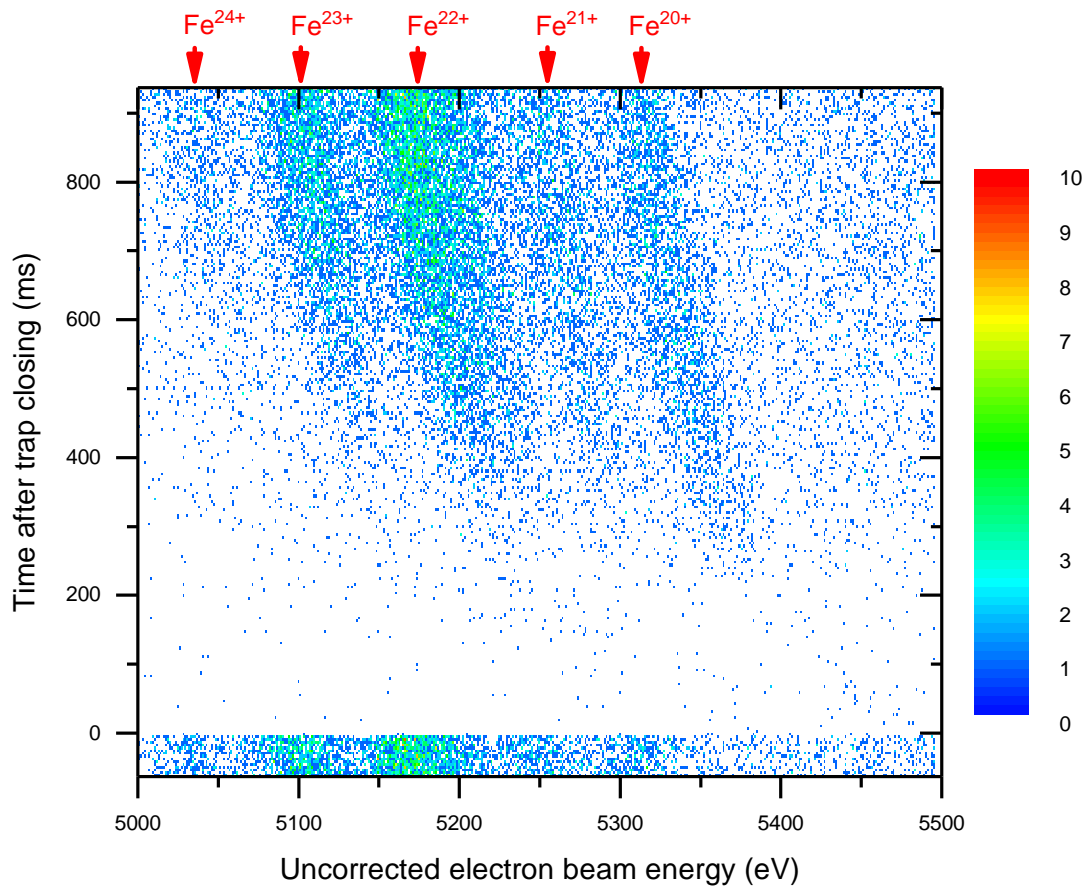
Figure 3.38: KLL-DR measurements of highly ionized iron. The measurement technique is the same as presented in figure 3.34. Lowly charged iron ions were provided by the laser-ion source, synchronized with the switching cycle of the voltage of the collector-sided, adjacent electrode of the central drift tube. The electron-beam current was 200 mA and the axial trapping potential 300 V. Adapted from Ref. [34].

3.4.5 Ion injection from the laser ion source

The CANREB-EBIS will be utilized as a charge breeder at the ARIEL facility at TRIUMF. Bunches of singly charged, rare isotopes will be injected into the EBIT in order to breed them to higher charge states. For a proof-of-principle test and determination of suitable parameters for ion injection, a laser ion source (see section 3.3.10) was utilized. The laser is focused to a diameter of ~ 0.2 mm onto an iron target.

In figure 3.38 a similar measurement technique as in 3.4.2.2 was used with an electron-beam current of 200 mA, an axial trapping potential of 300 V, and a scanning range of the electron-beam energy from 5000 eV to 5500 eV where the KLL-DR of highly charged iron including space-charge effects is expected and a cycle period of 1000 ms.

By the application of a 3 kV pulse to the acceleration grid with a delay of 3.75 µs with

respect to the laser pulse, the produced iron ions were guided into the trap with an open potential-barrier on the collector side electrodes. 18 μs after the trigger of the laser pulse the potential on the next downstream electrode of the central trap electrode was switched to a higher value employing a fast HV switch (Behlke GHTS-60) in order to raise the potential barrier while the ion bunch is inside the trap to prevent those ions from escaping. This is denoted as the beginning of the cycle at $t = 0$ s. The trapped ions were ionized to higher charge states of Fe^{24+} up to Fe^{20+} undergoing resonant dielectronic recombination with free electrons. A similar behavior of the compensation of the negative space charge of the electron beam by positively charged HCIs, as shown in figure 3.34, was observed. The breeding times are considerably high, and the statistics are relatively low. This can be referred to the fact of a faulty electrical connection of the Sikler lens (chapter 3.3.5) which therefore could not be used for focussing or steering, leading to a bad intersection of the ion trajectories with the electron beam and a decreased charge breeding efficiency.

3.4.6 Integration of the EBIS into the CANREB facility

In January 2018 the EBIS has been shipped and installed at the designated end station in the ARIEL experimental hall at TRIUMF. After three days of pumping, a pressure in the higher 1×10^{-7} mbar range in the magnet chamber, and 6.5×10^{-9} mbar in the gun chamber has been achieved. The manufacturing and installation for the high voltage cages and ducts surrounding the electron gun and the collector and the common electrical platform for the trap assembly have been performed by scientists and technicians at TRIUMF. In July 2019 the integration of the CANREB-EBIS as a charge breeder at the CANREB facility has been initialized. In figure 3.39 an overview of the project is illustrated. The singly-charged rare isotopes provided by ISAC or ARIEL are bunched and pre-cooled by a radio-frequency cooler/buncher and transported to the EBIS where the charge breeding to a specific charge state occurs. Subsequently, the highly charged ions are extracted and transported to a NIER spectrometer where the composition and charge states of a bunch are analyzed. In this photograph, the EBIS and the beamline have been separated due to maintenance.
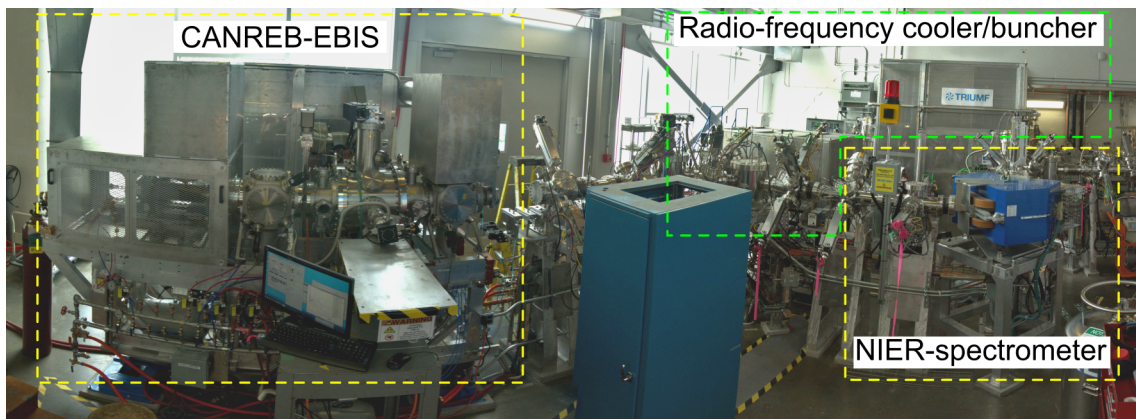
Figure 3.39: The integration of the CANREB-EBIS into the CANREB project of the ARIEL facility at TRIUMF. The main components are highlighted: the radio-frequency cooler/buncher, the EBIS and the NIER-spectrometer. The photograph was acquired in July 2019.

4 Experiments on charge exchange

4.1 Experimental setup

The charge-exchange measurements are performed at the FLASH-EBIT equipped with a grazing incidence EUV-spectrometer described in chapter 3.3.9 for a wavelength range of $5\,\mathrm{nm}$ and $35\,\mathrm{nm}$, a 3-meter normal incidence VUV-spectrometer for $\sim 40\,\mathrm{nm}$ to $250\,\mathrm{nm}$ in Rowland configuration and a silicon drift detector for the X-ray range as shown in figure 4.1. The technical details on the VUV spectrometers will not be given within the scope of this work. Further information can be found in [33].

4.1.1 Data acquisition system

For data acquisition and signal processing the commercial MPA3-system (multi-parameter data acquisition system) from FAST ComTec [79] was used. The system provides up to 16 ADCs (analog-to-digital converter) with a digital resolution of 13 Bit each converting an analog signal to a digital signal and allocate it to an integer value between 0 and 8191. Each ADC can be operated in three different modes.

The SVA (sampling voltage analyzer) mode digitizes an input voltage between zero and ten volts. In this mode usually, signals are processed which can be represented by a continuous voltage characteristic like the electron beam energy for measurements of dielectronic recombination, or time for cyclically repeated measurement schemes. For the allocation of a voltage to a specific channel, the SVA has to be triggered externally.

In the PHA (pulse height analyzer) mode, the height of a signal pulse is digitized and assigned to the corresponding channel. In this mode, usually, the energy of a detected photon is mapped where the height of a pulse is proportional to the energy of the photon.

The TDC (time-to-digital converter) allocates a time difference between a start pulse and a stop pulse between $50\,\mathrm{ns}$ and $20\,\mathrm{\mu s}$ with a resolution of $0.025\,\mathrm{ns}$. This mode is often utilized for determination of the spatial information of an event on a position-sensitive photon detector like a microchannel plate with a delay-line anode. Here the time difference between a start and a stop pulse in the two delay lines, respectively, can be converted into a position on the detector where the photon was impinged on.

The acquired data can be processed in real-time with the program MPANT where conditions for coincidences can be defined to create one- or two-dimensional spectra.
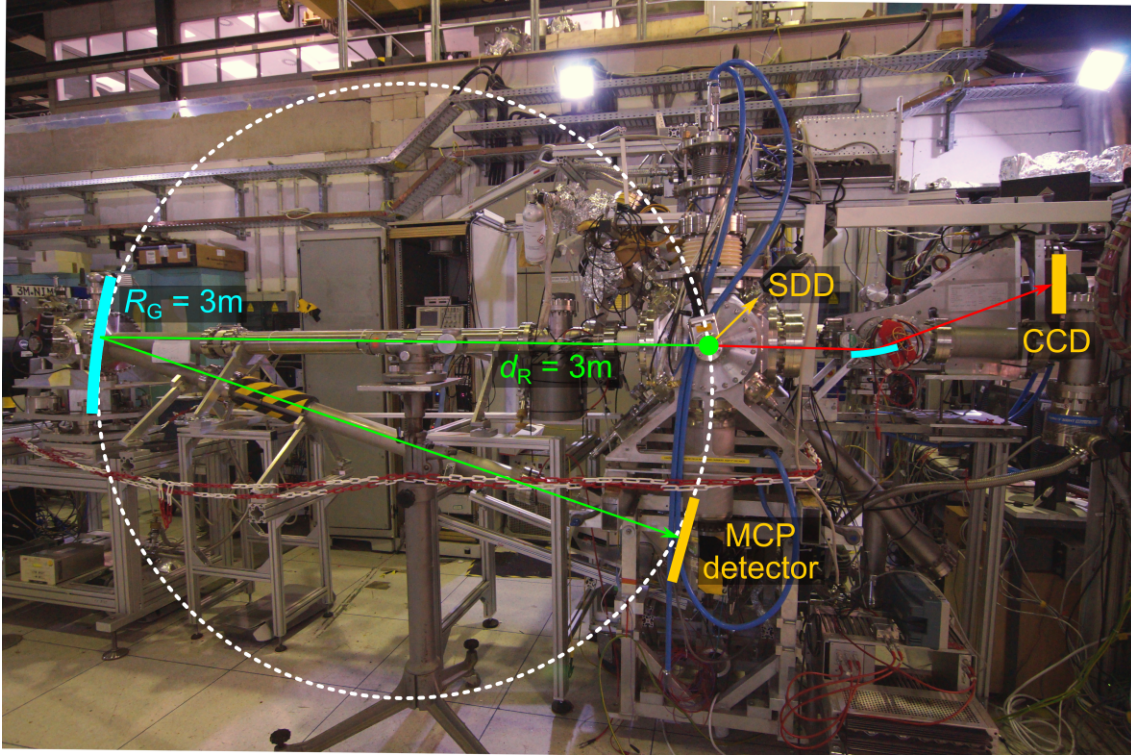
Figure 4.1: Photograph of the experimental setup. The image was acquired along the electron-beam axis from the collector side. On the left-hand side, the 3-meter normal-incidence VUV spectrometer [33] is attached to a radial viewport of the EBIT, equipped with a spherical grating at three meters distance from the trap center and an MCP detector at a distance of three meters from the surface of the grating in order to detect VUV photons. On the right-hand side, the extreme-ultraviolet grazing-incidence spectrometer is installed. On the 45° port with respect to the horizontal plane, an X-ray detector is mounted.

Additionally, a file with all relevant information about every single registered event is written in a file in a binary format.

4.1.2 Measurement scheme

The experimental setup is illustrated in figure 4.2 schematically. For the charge exchange measurements, it is necessary to separate the detected photons emitted during interaction with free electrons and interaction with neutral gas. Extraction of the contribution of the latter is only possible by producing the HCIs of interest by electron-impact ionization, subsequent switching off the electron beam and keeping those ions magnetically confined inside the trap. The only process in the so-called magnetic trapping mode (MTM) which can lead to emission of photons on a longer timescale is charge exchange. Here it is crucial
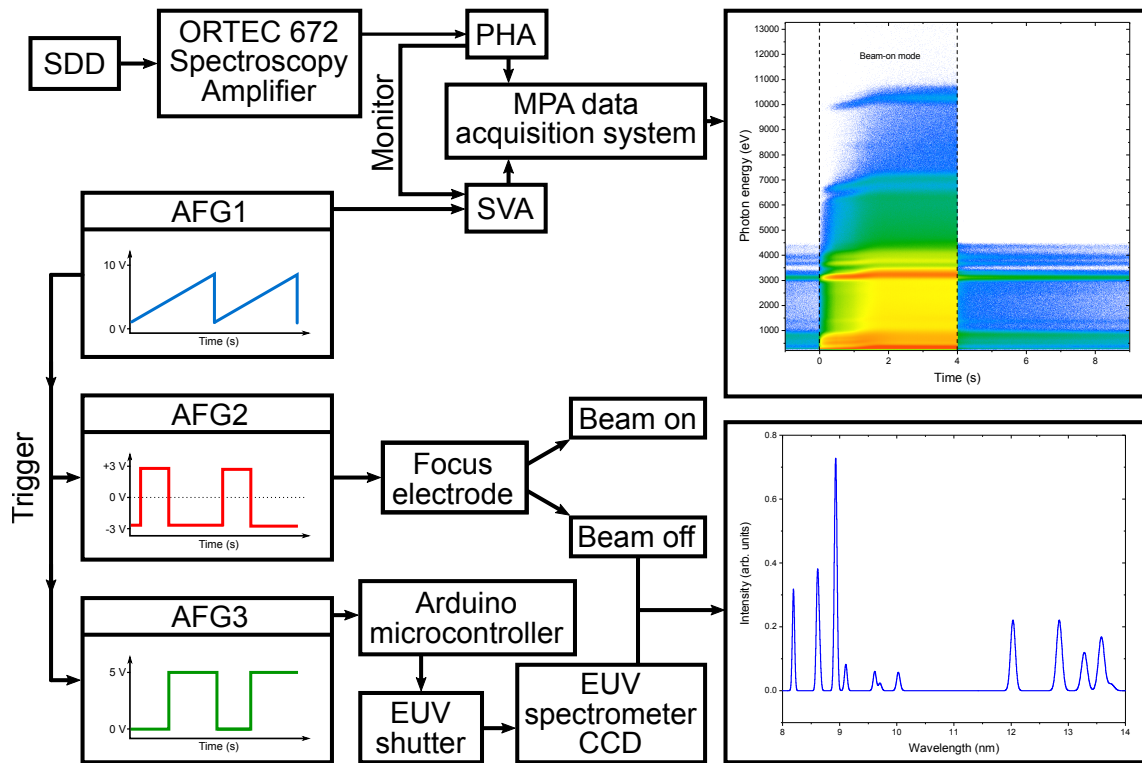
Figure 4.2: Schematical illustration of the experimental setup and the data acquisition system. Three channels of arbitrary function generators were utilized to provide information of the time within the switching cycle of the electron beam, the signal for switching on and off the beam, and for the rotation of the mechanical shutter attached in front of the EUV grating. Further details are described in the text.

to have a precise knowledge if a photon was detected during the beam-on or the magnetic trapping mode. For this purpose, the electron beam was switched off cyclically, and the X-ray photon energy was recorded as a function of the time within the period P. To provide this time information, an arbitrary function generator (AFG1) served as an output for a linear ramp signal between $0\,\mathrm{V}$ and $10\,\mathrm{V}$ with period P, where a specific voltage corresponds to a particular time within the period. This parameter was fed into the SVA. A second function generator (AFG2) controlled the electron-beam current. A rectangular-shaped signal was amplified by a factor of 1000 by a high voltage amplifier manufactured by TREK (model 623B) where the output was connected to the focus electrode. Applying a highly positive voltage leads to emission of an electron beam, and a highly negative value switched it off. This function generator was triggered by the trigger output of AFG1 to ensure a constant phase between both signals. The photons detected by a silicon-drift detector (SDD) (compare section 3.3.8.1) were processed by an Ortec 672 spectroscopy amplifier which served as an amplifier and a constant fraction discriminator to provide a

rigorous timestamp independent of the height for every single pulse. Every single event was analyzed subsequently by the PHA. Simultaneously a monitor output signal from the PHA was fed into the SVA as a trigger to assign a detected event to a time within the cycle. The outputs of the PHA and the SVA were connected to the MPA module. By setting certain conditions of coincidences, a two-dimensional spectrum with the X-ray energy on the abscissa and the time within the cycle on the ordinate can be extracted.

In addition, a third function generator (AFG3) controlled the shutter between the EBIT and the grating of the EUV-spectrometer (compare section 3.3.9). It was triggered by AFG1 and provided a rectangular-shaped signal which was delayed with respect to the signal of AFG2. To ensure that the CCD is only exposed during the electron-beam-off mode a 5 V signal was transmitted on the falling edge of the signal of AFG2 to an Arduino microcontroller that controlled a stepper motor outside the vacuum which rotated the shutter. After 50 ms, the shutter was completely open. At the end of the cycle, the shutter was closed 0.5 s before the electron beam was switched on again.

The events detected by the MCP of the VUV-spectrometer were fed simultaneously into the MPA data acquisition system and therefore it can also be assigned to a corresponding time within the cycle.

An example of all three AFG signals is presented in figure 4.3. The green signal is the linear ramp signal of AFG1 to provide time information within the switching cycle, the blue curve is the rectangular signal of AFG2 for switching of the electron beam, and the orange curve shows the 5 V pulse of AFG3 to rotate the shutter.

4.1.3 Switching the electron beam

During the electron-beam on mode, the X-ray spectrum is dominated by the interaction of ions with free electrons. In the magnetic trapping mode, where no free electrons are present, charge exchange is the dominant process. In order to separate those processes and to eliminate the contribution of the interaction with free electrons, the electron beam has to be switched off rapidly. For the fast switching of the electron beam, a pure rectangular signal in the range of -3 V and 3 V was fed into the input of the power supply of the focus electrode and amplified by a factor of 1000.

The time required for the switching can be estimated by measuring the collector current directly as a function of time. The result for switching on and off the electron beam is shown in figure 4.4. The time t_{On} required to switch on the electron beam from 0 mA to 167 mA is $t_{\mathrm{On}} = 305 \, \mu$s and the time t_{Off} to switch off the beam $t_{\mathrm{Off}} = 230 \, \mu$s. This is an upper limit because the measured signal was not corrected for the capacitance of the collector as well as the capacitance of the coaxial leads, which results in apparently higher switching times.
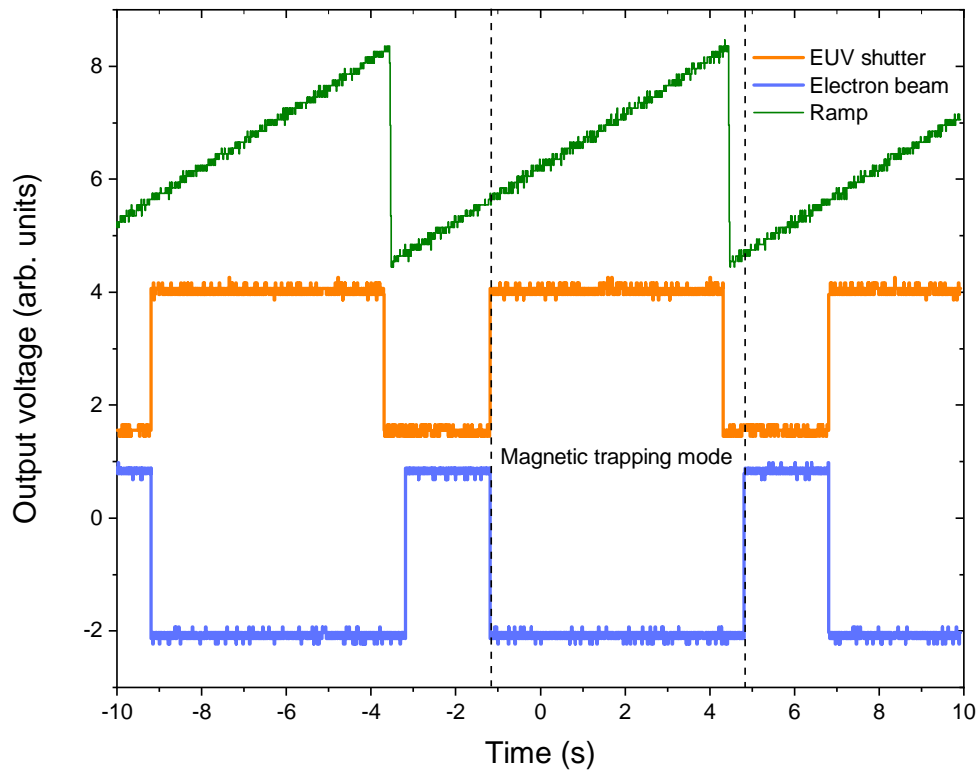
Figure 4.3: Periodic signal of the synchronized channels of the experimental charge exchange setup as a function of time. The green curve encodes the time within the switching cycle, the orange one controls the mechanical shutter of the EUV spectrometer, and the blue one switches the electron-beam current. In the magnetic-trapping mode, the electron beam is switched off, and the mechanical shutter opens.
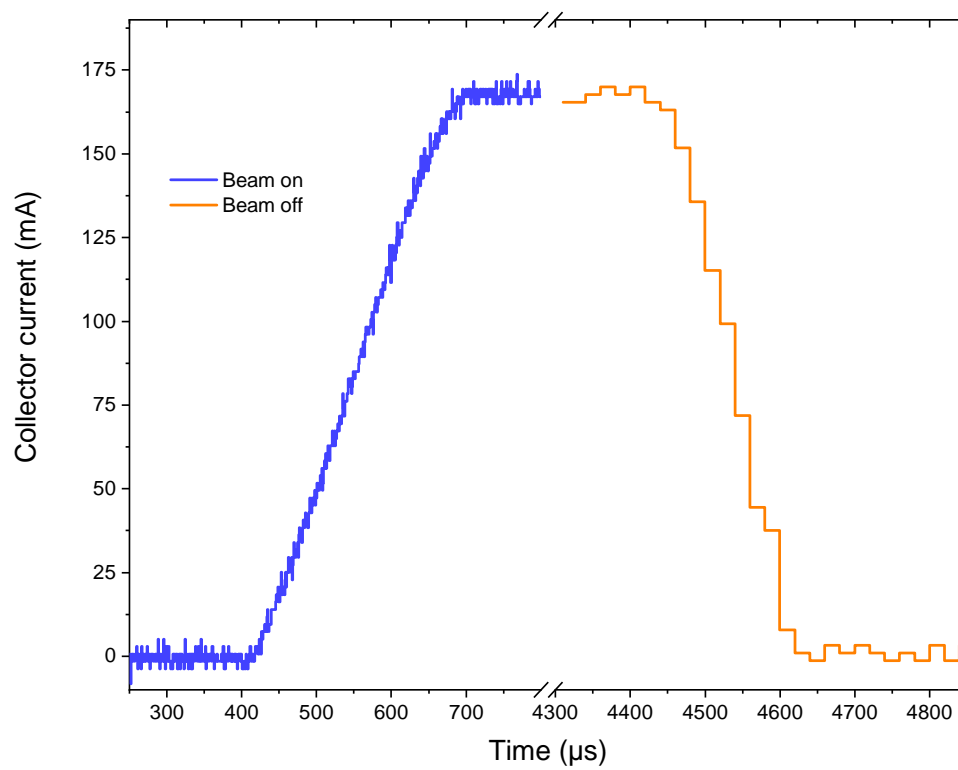
Figure 4.4: Collector current as a function of time measured during the switching cycle of the electron beam with an oscilloscope. The blue curve illustrates switching on the beam and the orange curve switching off, respectively. The different binning is due to the utilization of different sampling rates.
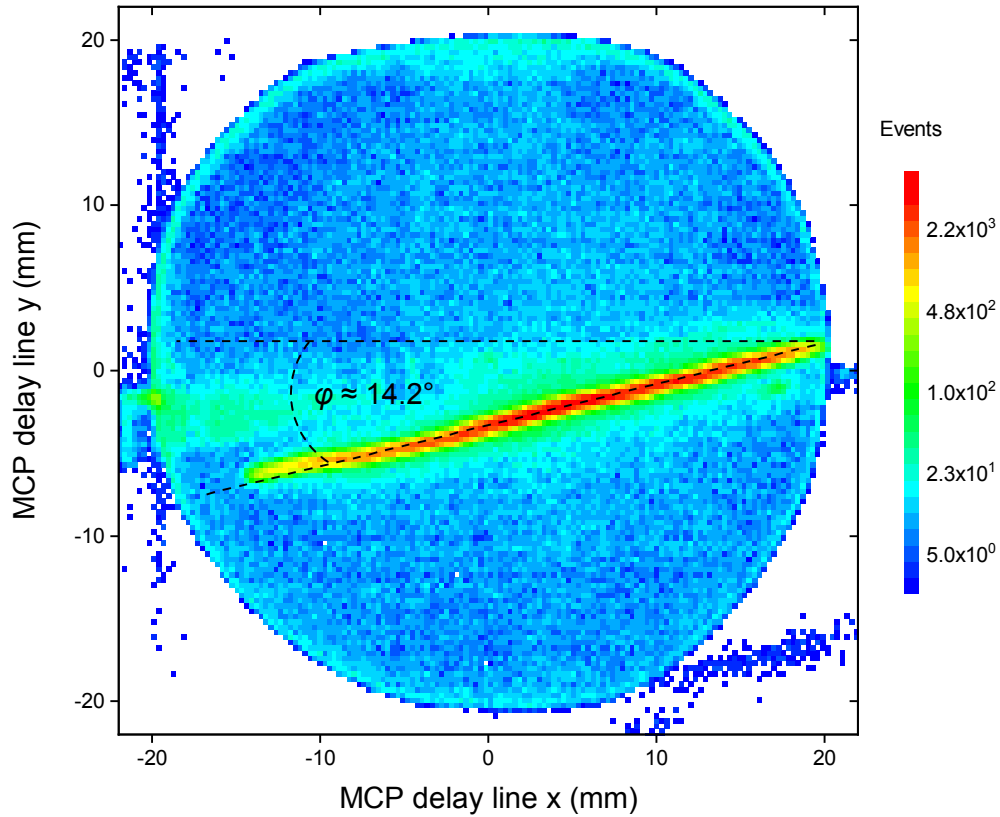
Figure 4.5: Image of the zeroth diffraction order of the ion cloud acquired with the position-sensitive MCP detector of the VUV spectrometer. The detector is inclined by 14.2° with respect to the dispersive axis of the setup.

Additionally, the dynamics of the ion cloud has been investigated by observation of the zeroth-order diffraction with the VUV spectrometer as a function of the time within the switching cycle. In this charge exchange measurement neutral argon was injected into the trap and ionized by an electron beam with a nominal beam energy of 4520 eV and a beam current of 200 mA with an axial trapping potential of 500 V. In figure 4.6 the temporal evolution of the ion cloud is presented as a function of time within the cycle.

Here, the spectra were acquired with a microchannel-plate (MCP) detector equipped with a delay-line anode which provided temporal and spatial information about the impinging photons. Since the orientation of the delay line was not perfectly aligned with respect to the dispersive axis of the diffraction grating, the resulting image of the cloud is intrinsically inclined, as illustrated in figure 4.5. The inclination angle is determined to $\phi \approx 14.2°$. After correction for the inclination, the image is collapsed onto the dispersive axis. By plotting the resulting one-dimensional histogram as a function of the time within the
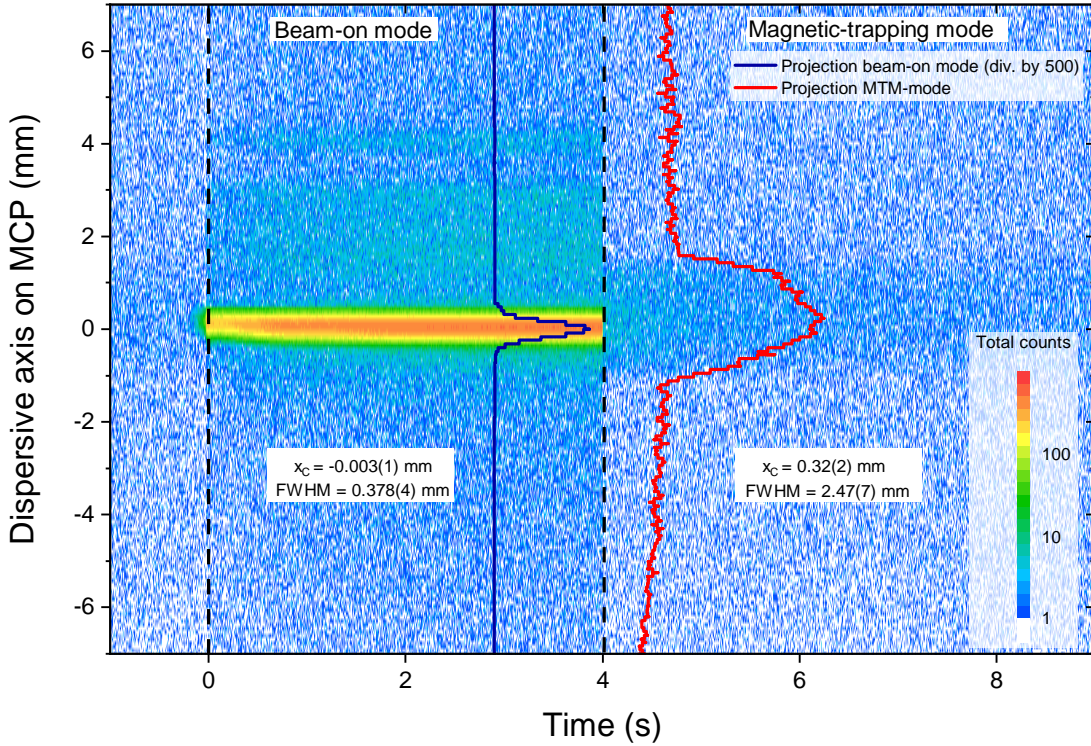
Figure 4.6: Projection of the zeroth-order onto the dispersive axis as a function of the time within the CX cycle acquired with the VUV spectrometer. After switching off the electron beam at 4 s an expansion, as well as displacement by one half-width of the initially compressed ion cloud, can be observed.

switching cycle of the electron beam, the dynamics of the ion cloud can be extracted, as shown in figure 4.6. Since the diameter of the active area of 40 mm is known, and the VUV spectrometer setup provides a 1 : 1 magnification of the object size, the diameter and the centroid position of the ion cloud can be extracted directly from a Gaussian fit. The initial size of the ion cloud is determined to FWHM $= 378(3)\,\mu$m. After switching off the electron beam at $t = 4$ s, the cloud expanded to $1680(12)\,\mu$m and moved by $305(40)\,\mu$m. This shift could be caused by a non-perfect alignment of the propagation axis of the electron beam with respect to the central axis of the magnetic field. A similar result was observed with different electron-beam energies. The increase of the width can be explained by diffusion processes in the magnetic field. In the case of non-interacting particles, the transversal motion of the ions with respect to the magnetic field does not change. The diameter of the cloud is characterized by the cyclotron radius. For collisions between like particles, the center-of-mass remains stationary, which does not affect the overall transversal trajectories [46]. Collisions between charged particles and neutrals cause a diffusion of the ions across the magnetic field. After each collision, the guiding center shifts randomly in the order of

a cyclotron radius of the corresponding ion. Collisions between unlike particles also shift the center-of-mass towards lower ion density. These effects lead to slow expansion of the ion cloud as a function of time. The behavior of the ion density can be described by a model based on the simplified Vlasov equations with the absence of an electron beam [54]. The density ρ as a function of time t and position r is then given by

$$\frac{\partial \rho(r,t)}{\partial t} = -K \frac{\partial \rho(r,t)}{\partial r} \frac{\partial}{\partial r} \left(\frac{1}{\rho(r,t)} \frac{\partial^2 \rho(r,t)}{\partial r^2} \right), \tag{4.1}$$

where K represents the diffusion constant

$$K \approx \frac{8\sqrt{kT}m^{3/2}}{387\pi\sqrt{\pi}B^4\epsilon_0^2} \ln \Lambda \tag{4.2}$$

with the Coulomb logarithm Λ, ion mass m and ion temperature T. In this experiment the temperature is given by $T \approx 0.2qV_0 = 1700\,\text{eV}$, where V_0 represents the axial trapping potential and q the charge of the ion. To remark is a scaling of the diffusion time with the fourth power of the magnetic field in the denominator. Thus, the diffusion in a magnetic field of 6 T is effectively reduced by a factor of 16 compared to a magnetic field of 3 T.

A careful investigation of the ion-cloud dynamics is presented in figure 4.7. Here, the plot from figure 4.6 is segmented into several temporal slices with a width of 0.1 s directly before and 0.1 s after switching off the electron beam and 0.5 s for the other consecutive slices. Within each slice, all detected events are projected onto the dispersive axis, and a Gaussian fit is performed in order to determine the width and the position of the ion cloud. The values extracted for the position and the width of the ion cloud for each slice are presented in figure 4.8 as a function of the time within the switching cycle in the bottom panel and the top panel, respectively. Also, the values during the electron-beam on mode are displayed, where $t = -4\,\text{s}$ is the time where the beam was switched on. Directly after switching on the electron beam, the ion cloud moved steadily by 0.1 mm before it shifted abruptly due to the absence of the electron beam after switching off the beam. The width increased correspondingly before the expansion of the ion cloud at $t = 0\,\text{s}$. This measurement indicates a slight misalignment of the electron gun with respect to the magnetic field axis.

An estimation of the kinetic energy can be performed by the utilization of the cyclotron motion with a radial velocity of

$$v_\text{c} = \frac{q}{m} rB, \tag{4.3}$$

where r is the cyclotron radius, B the magnetic field, and q and m the charge and the mass of the ion, respectively. The diameter of the ion cloud in the steady-state after the expansion is FWHM $= 1.8(1)\,\text{mm}$. By the assumption of hydrogen-like argon as ionic
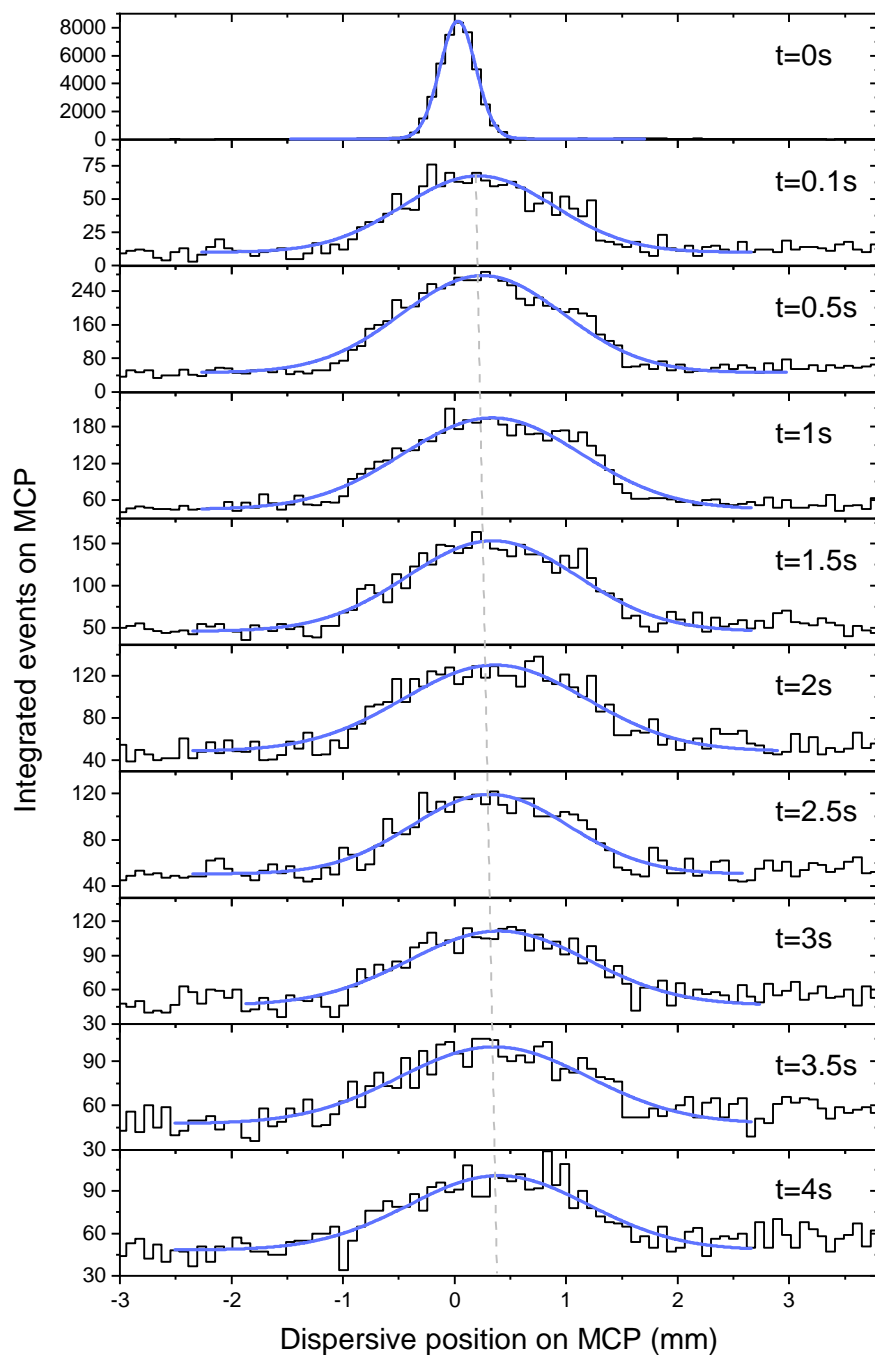
Figure 4.7: Temporal evolution of the ion cloud with regards to the position and the width after switching off the electron beam at $t = 0\,\mathrm{s}$. The single frames are projections of consecutive temporal slices from figure 4.6 onto the dispersive axis of the VUV spectrometer setup.
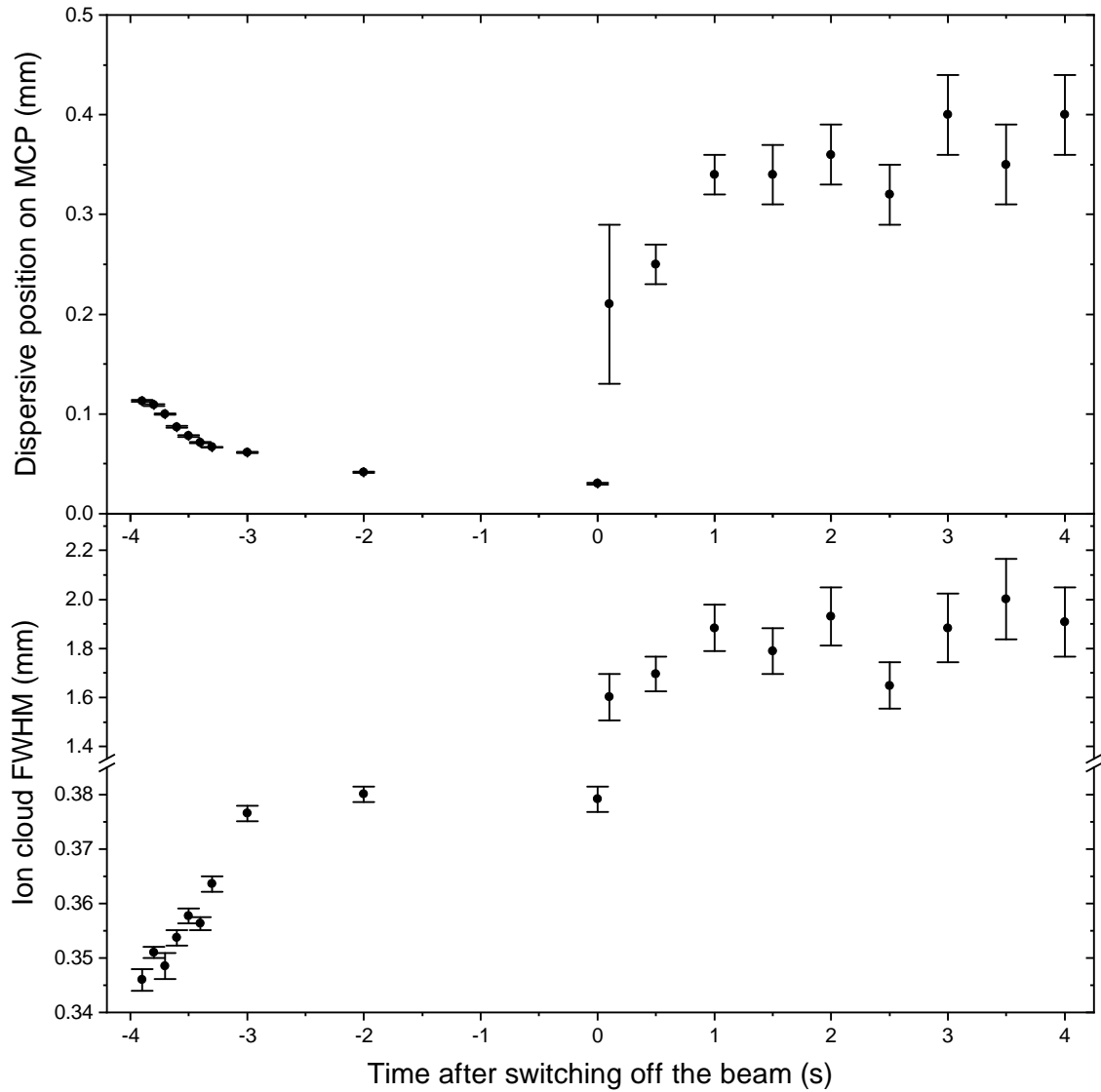
Figure 4.8: Dynamics of the ion cloud extracted from figure 4.7. In the top panel, the position of the ion cloud on the MCP detector and in the bottom channel the corresponding width is plotted as a function of the time within the switching cycle of the electron beam. At $t = -4\,$s the electron beam was switched on and at $t = 0\,$s switched off again.

species, the kinetic energy can be estimated to $E = 1/2mv_c^2 \approx 254(14)\,\text{eV/u}$. To remark is, that this value represents the upper limit since the ion cloud was observed in the zeroth diffraction order. Thus, hydrogen-like argon does not exclusively contribute to the observed radiation. Since oxygen is a highly-abundant contaminant, for instance, from previous measurements, an intense transition of beryllium-like oxygen at 62.6 nm could constitute a significant fraction of observed photons.

4.2 Charge exchange in highly charged sulfur

4.2.1 An unidentified X-ray emission line-like feature at 3.5 keV

In 2014 independent observations of an X-ray emission-like line feature at a photon energy of 3.5 keV in several spectra of galaxy clusters have attracted particular attention in the astrophysical community. The first detection of this line is reported in [39] where the feature was observed in the Perseus galaxy cluster and the galaxy M31 (Andromeda Galaxy) with X-ray instruments of the XMM-Newton space telescope. An independent analysis of 73 stacked X-ray spectra of galaxy clusters obtained by XMM-Newton given in [42] confirmed the existence of the unidentified line feature (ULF). The reason for the excitement was a lack of a direct assignment to a known atomic transition in standard wavelength databases which gave rise to a tide of speculations and publications about the origin of this line, particularly about a possible dark matter origin. Among those, the hypothesis of a decaying dark matter particle candidate - the sterile neutrino, has been emphasized. The argumentation for this supposition is based on a non-availability of an atomic transition in this wavelength region in standard databases for thermal plasmas [42, 70].

Further investigations have been carried out by observations of the Perseus cluster core [170] employing the Suzaku X-ray space telescope [120] and the Galactic center [38]. In these publications, an upper limit for the flux of the ULF has been estimated, but due to model and statistical uncertainties, no coherent evidence for the existence of the line could be provided.

While other alternative models propose decay of dark matter into other exotic candidates like the axion-like particle which is converted to a photon inside the magnetic field of galaxies and clusters [48], other groups report a non-detection of the ULF [8, 16, 92, 118, 77, 161]. Another publication even rules out the origin of the ULF in the decay of dark matter due to the incompatibility of the observed spheroidal dwarf galaxies Draco with the expected distribution of dark matter within this system [96]. A recent study from the $\sim 30\,\text{Ms}$ observation of the ambient halo of the Milky Way utilizing the XMM-Newton telescope strongly disfavors the decay of sterile neutrino by setting a firm limit on the

lifetime of dark matter in the expected mass range between 6.7 keV and 7.4 keV [58]. To investigate the issue cautiously, all possible sources leading to X-ray emission in this spectral range have to be excluded. The models utilized for the description of thermal plasmas rely on standard spectral databases, and atomic structure calculations since the catalog of laboratory spectra is far away from completeness [26].

One possible explanation of the ULF with an origin in an atomic process which is strongly supported in this thesis is given in [83]. The cautious explanation is based on the process of charge exchange, where an entirely-stripped sulfur ion captures an electron from neutral atomic hydrogen, leading to the population of a high principal quantum number state of $n = 9$ leading to emission of 3.5 keV photon from a subsequent Rydberg-transition into the ground state. Since the hot plasma present in galaxy clusters contains significant amounts of hydrogen-like and fully-stripped sulfur ions [126] interacting with clouds of hydrogen, the process has to be investigated and furthermore considered in astrophysical modeling. Other publications suggest $1s^2 2l - 1s2l3l'$ transitions at 3.62 keV of lithium-like argon induced by dielectronic recombination [75], which is a resonant electron capture process where a free electron recombines into a bound state by excitation of a core electron. However, the issue of the origin of this emission line is not fully resolved hitherto, and further theoretical and experimental investigations are required.

In this work the scenario of electron-capture by fully-ionized sulfur ions with subsequent K-shell emission is investigated.

4.2.2 X-ray measurements

The measurements were carried out in January 2016 [149] with FLASH-EBIT [63], utilizing the same technique as described in section 4.1. CS_2 gas was injected into the EBIT acting as well as a source of the highly charged projectiles S^{15+} and S^{16+} and as a target of neutral gas. The ions produced by electron-impact ionization were kept magnetically confined after switching off the electron beam and interacted with the constant inflow of the neutral target CS_2 inside the trap region.

A comparably deep axial trapping voltage of $U_{\text{trap}} = 1100$ V was chosen, corresponding to an ion temperature of $\sim 0.2qU_{\text{trap}} = 110$ eV/u, where q is the charge of the ion. The electron beam current was 150 mA at an electron beam energy of $E_e \sim 4.6$ keV, above the ionization threshold for the production of bare sulfur and $E_e \sim 3.6$ keV, below the threshold, respectively. The total cycle time of switching the electron beam was 16 s with 6.6 s in the magnetic trapping mode subcycle, corresponding to a duty cycle of 40 %. The photons emitted during the beam-on mode and the MTM were detected by an SDD with a resolution of FWHM ~ 150 eV, close to the detector resolution of the XMM-Newton

X-ray space telescope, equipped with a MOS (metal oxide semiconductor) CCD-array behind the X-ray telescope with a grating spectrometer [169, 178] and a pn CCD-camera [160]. A high-resolution measurement of the transitions could be achieved employing a microcalorimeter as presented in CX measurements at the Lawrence Livermore National Laboratory (LLNL) [22, 109] with a disadvantage of a comparably small solid angle compared to an SDD and significantly longer acquisition time.

The energy calibration of the SDD was performed using a set of measurements of dielectronic recombination of highly charged sulfur, argon and barium ions. Dominant resonant K-shell X-ray transition energies of helium-like argon and sulfur, and direct excitation of L-shell transitions ($n = 3 \rightarrow n = 2$) of Ba^{46+} were studied and assigned to calculated transitions obtained by the flexible atomic code (FAC) [85]. A good agreement of those calculations with previous experimental results of dielectronic recombination [148, 150] makes the calculated transition energies sufficiently confidable for the present calibration of this experiment.

The theoretical uncertainty for the transition energies was chosen conservatively to 10 eV due to a not precisely known distribution of charge states of the trapped ions. The raw spectra are one-dimensional histograms, where the number of detected events are represented as a function of the corresponding channel of the ADC, which is proportional to the energy of the photons detected. The number of ADC channels was binned by a factor of 8, resulting in 1024 channels in this experiment. Gaussian distributions were fitted to each known transition to determine the centroid position in terms of ADC channels precisely. The result is shown in figure 4.9, where the calculated transition on the ordinate is assigned to an ADC channel on the abscissa with the corresponding residuals of the linear fit. A reduced χ^2 of 1.33 indicates slightly underestimated uncertainties. The linear scaling factor of 9.34 eV/ADCchannel and an offset of 102.7 eV is determined.

A two-dimensional spectrum, as in section 4.1, with an electron-beam energy of $E_e = 4.6$ keV, above the ionization threshold for fully ionized sulfur with $I_p = 3494.2$ eV, is shown in figure 4.10.

During the beam-on mode at an electron beam energy of 4.6 keV, various principal quantum number states of hydrogen-like sulfur, helium-like sulfur, and lower charge states are populated by electron-impact excitation. By subsequent decay into the ground state, K-shell photons are emitted with energies between 2 keV and 3.5 keV where the latter represents the series limit or the binding energy of a K-shell electron. These transitions are indicated by labels a) to e) in the figure. Photons at higher energies than the electron-beam energy are produced by recombination processes with mono-energetic free electrons. Radiative recombination into the $n = 2$ state of S^{15+} and S^{16+}, labeled with f) leads to emission of a photon with an energy of ~ 5 keV consisting of the sum of the binding energy of an L-shell electron after recombination and the kinetic energy of the free
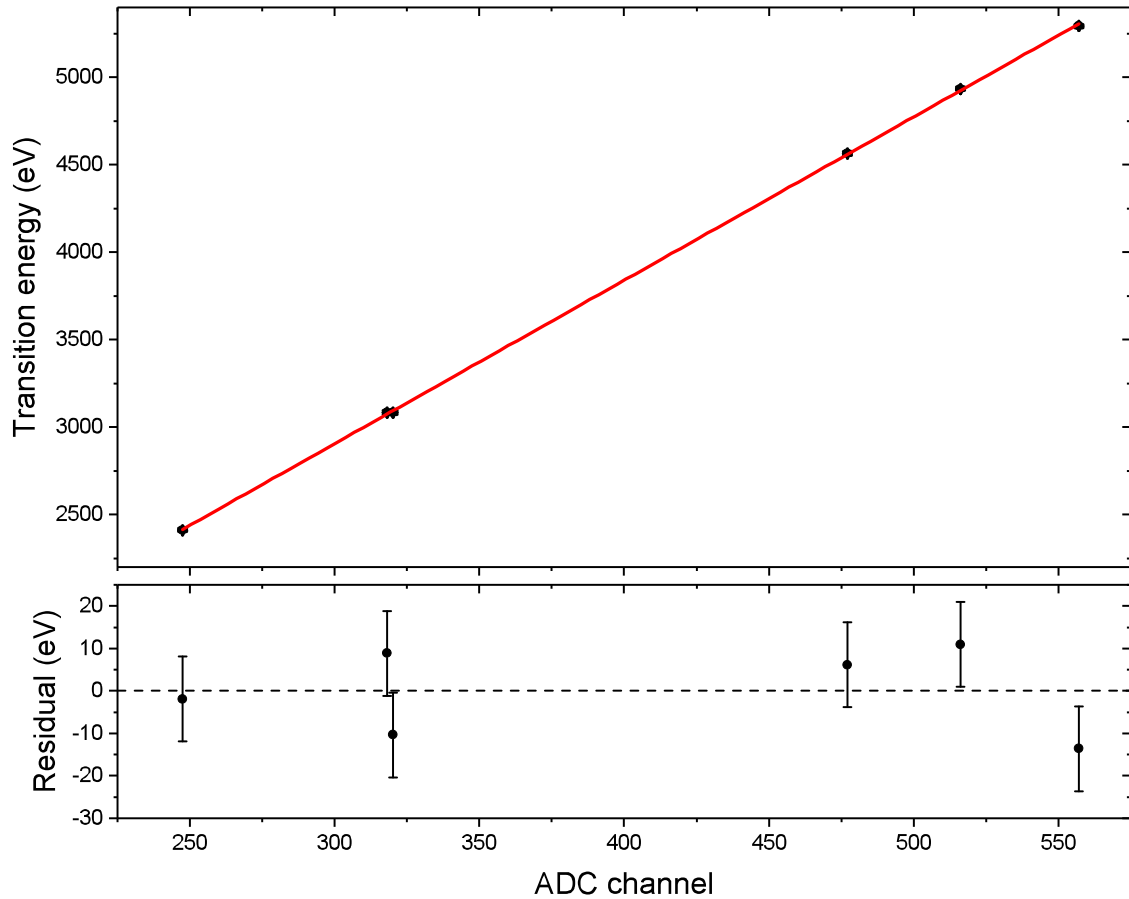
Figure 4.9: Energy calibration of the X-ray detector. **Top:** calculated resonant K-shell transitions of helium-like argon and sulfur ions and direct excitation of transitions $n = 2 \rightarrow n = 3$ of Ba^{46+} are represented as a function of the ADC channel of the data acquisition system. **Bottom:** corresponding residuals of the linear fit.
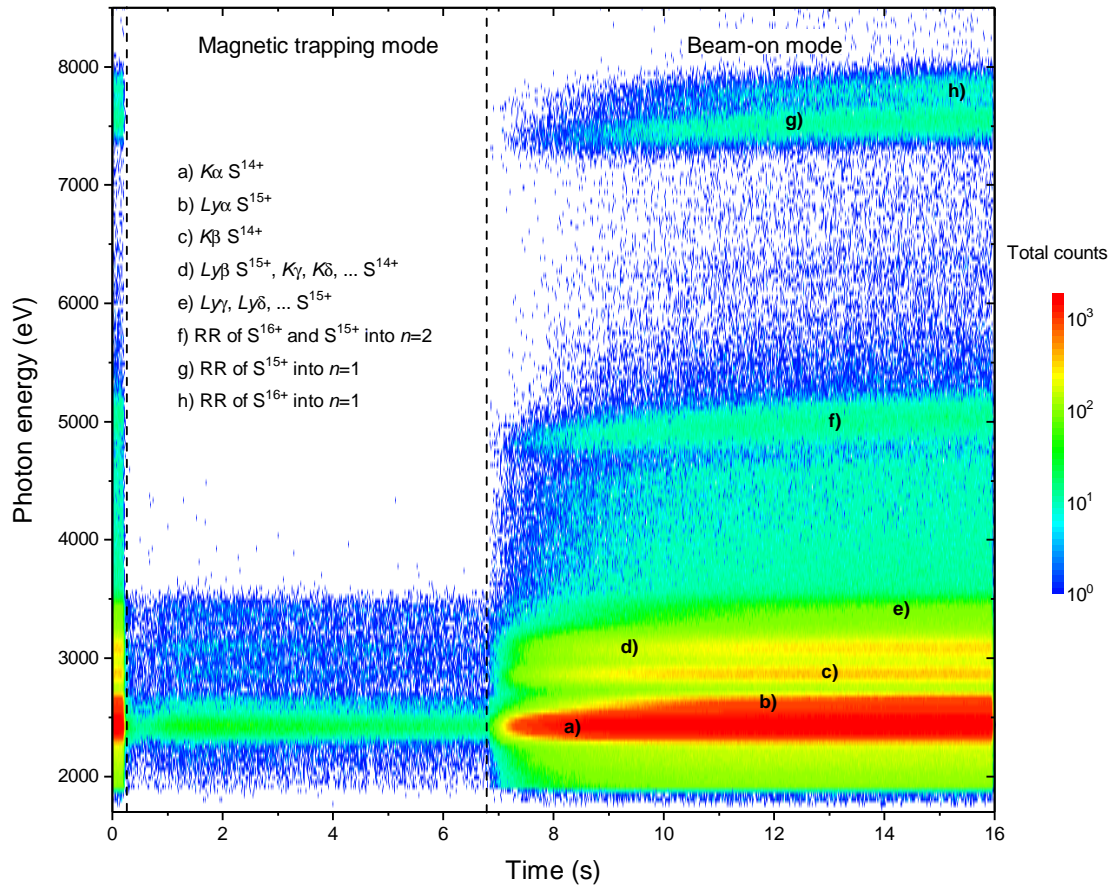
Figure 4.10: Two-dimensional charge exchange spectrum of highly charged sulfur with an electron-beam energy above the ionization threshold for the production of bare sulfur. The photon energy detected with an SDD is plotted as a function of the time within the switching cycle of the electron beam. The experimental technique was performed analogously to the results shown in figure 4.21. The magnetic-trapping subcycle is plotted from 0.2 s to 6.8 s of a total cycle time of 16 s.

electron. Radiative recombination into the ground state of S^{15+} and S^{16+} is indicated by label g) and f), respectively providing X-rays with energies up to 8 keV.

From the radiative recombination of S^{16+} with a free electron of the nominal kinetic energy of 4.6 keV, the contribution of the negative space charge induced by the electrons can be estimated. The binding energy of an electron in the ground state of S^{15+} is 3494.2 eV. The photon energy released during this process at the beginning of the breeding cycle at $t \approx 6.8$ s is approximately 7.65 keV. At this time the number of ions produced which partially compensate for the negative space charge of the electron beam is comparably low. Consequently, the measured photon energy of h) is the sum of the nominal kinetic energy E_e of the electron, the binding energy I_p of the captured electron into the ground state and the space charge E_{SC} with a negative sign

$$7650 \, \text{eV} = E_e + I_p - E_{SC} \tag{4.4}$$

Therefore the negative space charge can be estimated to $E_{SC} = 444 \, \text{eV}$.

At the end of the breeding subcycle, the photon energy appears at slightly higher energies of ~ 7.8 keV. As mentioned before, the ions produced over the time compensate partially for the negative space charge of the electron beam. From the difference of the photon energy at the beginning and the end of the subcycle, this contribution of the positive space charge $E_{SC,Ion}$ of the ions is determined to 150 eV, which corresponds to a compensation of $\sim 34 \%$.

During the magnetic-trapping mode, the contribution of excitation processes and recombination processes of free electrons vanishes and the only process leading to the emission of X-rays is charge exchange of S^{15+} and S^{16+} with CS_2. The metastable states populated by electron-impact excitation, decay comparably fast into the ground state, for He-like sulfur less than one micro second [51] which is much smaller than the resolution of the TDC of ~ 8 ms with the settings used in this experiment. Long-termed emission of K-shell photons in the MTM requires a vacancy in the K-shell that only fully-stripped sulfur and hydrogen-like sulfur can fulfill. Highly excited principal quantum numbers $n_{CX} = 15 \dots n_{CX} = 3$ are populated by the capture of a weekly bound electron of the CS_2 molecule in the MTM resulting in subsequent X-ray transitions from $n_{CX} \to n = 1$ in a range from ~ 2.75 keV to ~ 3.5 keV. Other transitions where the electron can not decay directly into the ground state due to selection rules feed the $n = 2$ state resulting in a Ly_α transition at ~ 2.6 keV and an intense K_α line at ~ 2.4 keV for capture into fully ionized sulfur and hydrogen-like sulfur, respectively.

A set of measurements, as shown in figure 4.10, was performed for different electron-beam energies between 3.4 keV up to 7 keV at a constant injection pressure of CS_2 in the second stage of $\sim 1 \times 10^{-8}$ mbar. Collapsing all the events detected by the SDD in the MTM onto
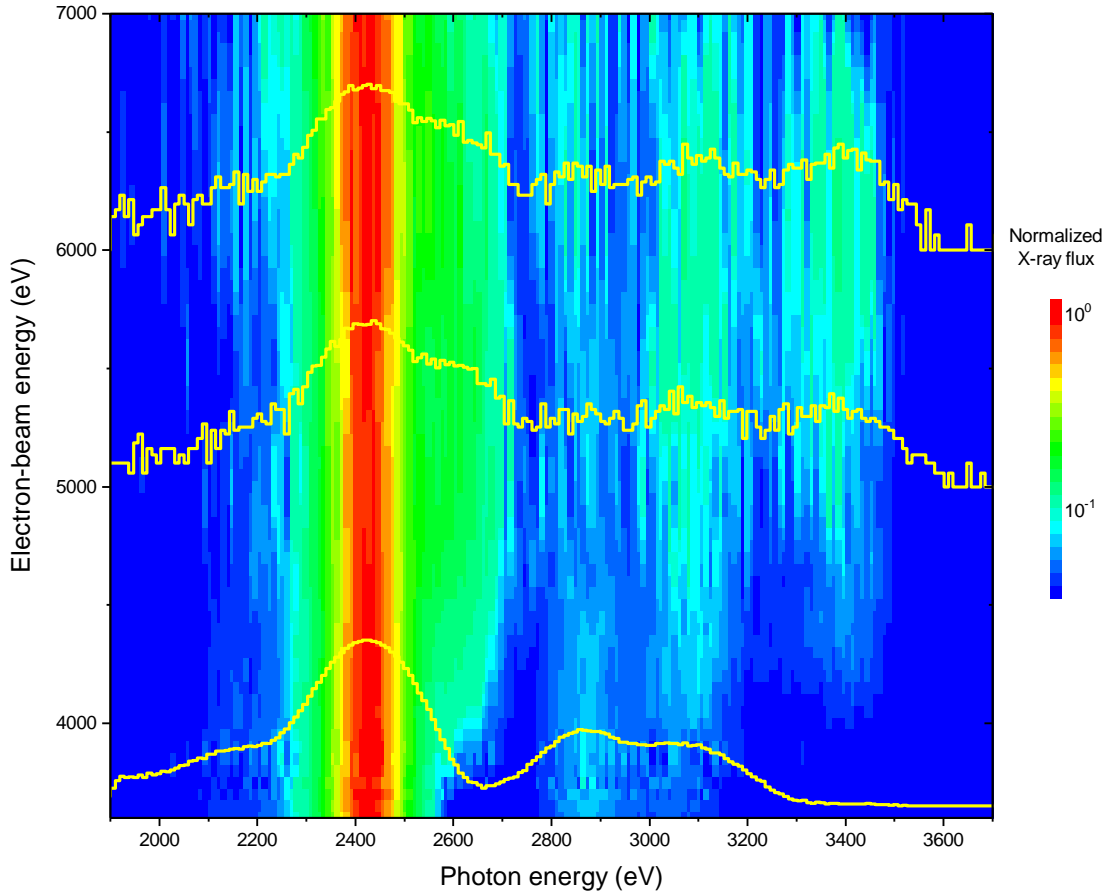
Figure 4.11: X-ray emission induced by charge exchange of highly charged sulfur in the magnetic trapping mode as a function of the electron-beam energy in the breeding subcycle. The normalized X-ray flux is represented by a logarithmic color scale.

the axis of the photon energy yields one-dimensional histograms with the X-ray energy on the abscissa. Representing the spectra as a function of the electron beam energy on the ordinate provides a two-dimensional spectrum, as shown in figure 4.11, where the normalized intensity to K_α is represented by a logarithmic color scale. The yellow insets depict the generic one-dimensional spectra at electron-beam energies of 3.6 keV, 5 keV, and 6 keV, respectively.

The minimum real electron-beam energy required to produce fully-stripped sulfur is 3494.2 eV. By the addition of the combined space charge potential $U_{\mathrm{SC;comb.}}$ composed of the negative contribution of the electron beam with 444 eV and the positive contribution of the ions with 150 eV yielding $U_{\mathrm{SC,comb.}} \approx 294$ eV, leads to an uncorrected electron-beam energy of ~ 3.79 keV. A distinct appearance of Rydberg transitions $n_{\mathrm{CX}} \approx 15 \ldots n = 4 \to n = 1$ in the range between 3.3 keV to 3.5 keV can be seen at uncorrected electron-beam energies above 3.8 keV, indicating the presence of S^{16+}.
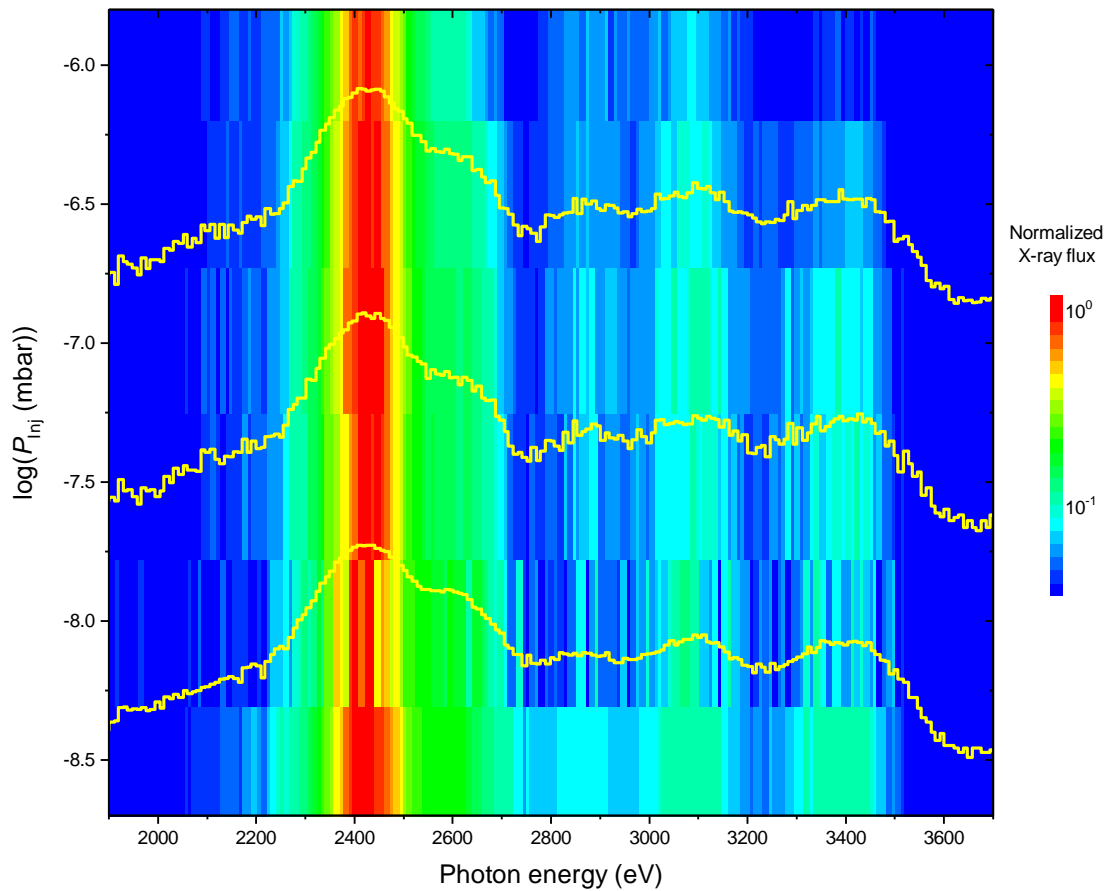
Figure 4.12: X-ray emission induced by charge exchange of highly charged sulfur in the magnetic trapping mode as a function of the injection pressure of CS_2 gas in the second stage of the differentially pumped injection system. The normalized X-ray flux is represented by a logarithmic color scale.

Additionally, a similar measurement as presented in figure 4.11 was performed by variation of the injection pressure in the second stage of the differentially pumped injection system at a fixed electron beam energy of $5\,\text{keV}$. Spectra in the magnetic trapping mode of six different pressures between $1.15 \times 10^{-6}\,\text{mbar}$ and $2.7 \times 10^{-9}\,\text{mbar}$ were recorded. In figure 4.12, the logarithm of the injection pressure on the ordinate is plotted as a function of the photon energy on the abscissa, detected by the SDD. The normalized intensity to K_α is represented by a color scale.

The injection pressure affects the recombination rate of S^{16+} and the number of ions produced. The higher the injection pressure, the higher the recombination rate with neutral gas resulting in a reduced production of fully-stripped sulfur. Apart from that, the total number of ions produced is increased. A balance between a relatively high fraction of S^{16+} and a comparably high count rate was found at injection pressures in the order of
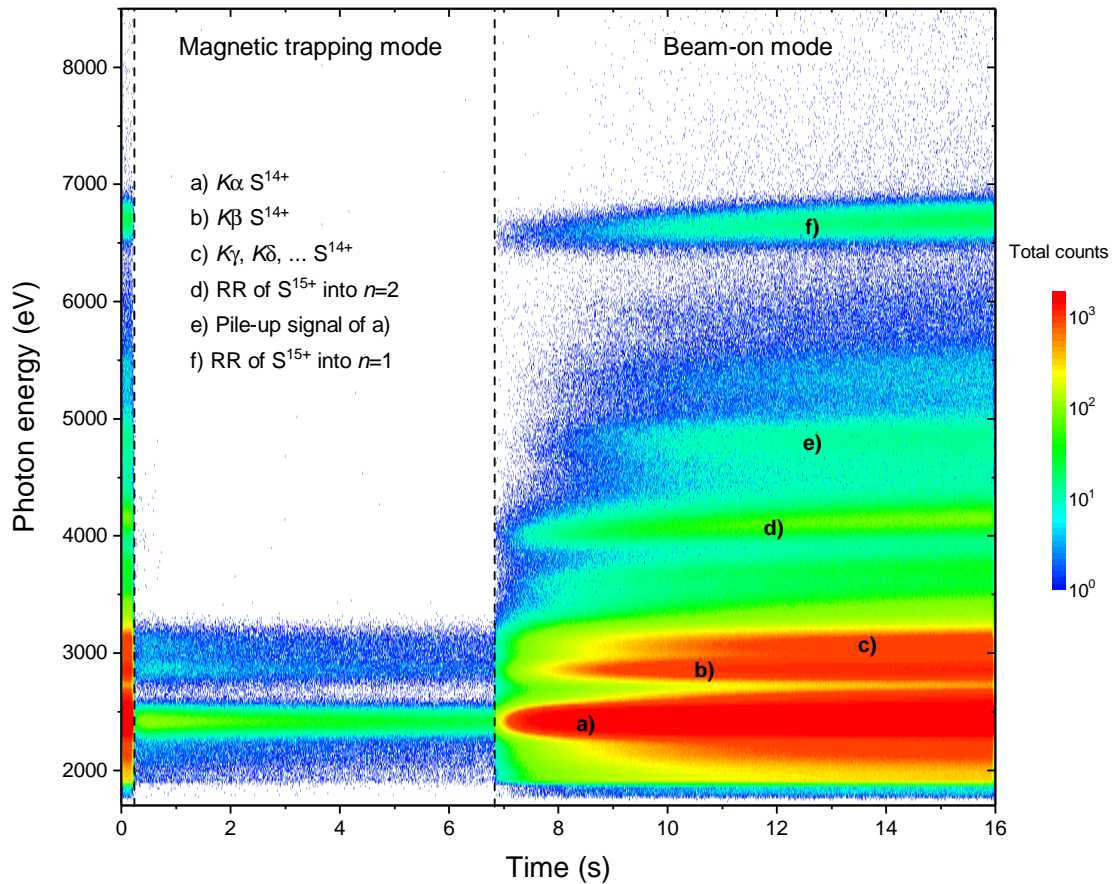
Figure 4.13: Two-dimensional charge exchange spectrum of highly charged sulfur with an electron-beam energy below the ionization threshold for the production of fully-ionized sulfur. The measurement was performed analogously to the results shown in figure 4.10.

$\sim 1 \times 10^{-8}$ mbar.

By choice of an electron-beam energy below the threshold for ionization of fully ionized sulfur, a CX spectrum of pure S^{15+} can be obtained. The two-dimensional spectrum shown in figure 4.13 was acquired with the same conditions as in figure 4.10 with an injection pressure of $\sim 1 \times 10^{-8}$ mbar and an electron-beam current of 150 mA.

The contribution of the Rydberg transitions above 3.2 keV as in figure 4.11 of hydrogen-like sulfur vanishes and the spectrum of charge exchange of pure hydrogen-like sulfur with CS_2 remains.

By collapsing all events acquired during the MTM in the spectrum with an electron-beam energy of 4.6 keV, which is above the ionization threshold for production of fully-ionized sulfur, yields a one-dimensional histogram in figure 4.14 a). The choice of an electron-beam energy below this threshold provided a CX spectrum of pure hydrogen-like sulfur with CS_2 in figure 4.14 b). For the extraction of a CX spectrum of pure S^{16+}, the respective

Table 4.1: Extracted transition energies of S^{15+} after the capture of an electron from the centroid positions obtained by fitting Gaussian distributions to the experimental spectrum in figure 4.14 c). The theoretical transition energies are calculated by FAC.

	Transition	Transition energy (eV)	Theory (eV)
Ly_α	$n = 2 \rightarrow n = 1$	2610 ± 1	2619.832
Ly_β	$n = 3 \rightarrow n = 1$	3110 ± 5	3105.922
Ly_γ	$n = 4 \rightarrow n = 1$	3280 ± 20	3275.938
$Ly_{\delta,\epsilon}$	$n = 5, 6 \rightarrow n = 1$	3400 ± 44	3370.459
$Ly_{\zeta,\eta,...}$	$n \geq 7 \rightarrow n = 1$	3470 ± 60	≥ 3423.013

contribution of S^{15+} has to be eliminated from figure 4.14 a). The K_β transition of S^{15+} at $\sim 2.87\,keV$ is present in both spectra and is well-separated from other transitions which establish it to a well-chosen candidate for normalization. After subtraction of both spectra, the contribution of CX of fully ionized sulfur is obtained in figure 4.14 c).

The blue vertical lines represent the calculated transition energies with the corresponding oscillator strengths of radiative cascades obtained by FAC for energy levels up to $n = 15$ for both, S^{15+} and S^{14+} after recombination. For experimental determination of the transition energies of the cascades, a fit of five Gaussian distributions to the experimental data is performed by fixing the shared width to the corresponding instrumental resolution of FWHM $= 150\,eV$, and treating the centroid positions and the amplitudes as free fit parameters. The reduced χ^2 value of the fit is 1.06 indicating a good agreement with the data. The result is summarized in table 4.1. The obtained transition energies for the various Lyman transitions are in a good agreement with the values predicted by theory.

The results are also compatible with the high-resolution CX measurements performed with a microcalorimeter at the LLNL-EBIT [32] where He and SF_6 served as targets for collisions with S^{16+}.

The hardness ratio $\mathcal{H}$ as defined in equation 4.7 in section 4.3.2 is determined in the present measurements to $\mathcal{H}_{CS_2} = 0.72 \pm 0.02$ which is in a good agreement with the result of $\mathcal{H}_{SF_6} = 0.714 \pm 0.116$ given in [32] for collisions of S^{16+} with SF_6.

4.2.3 Comparison with charge-exchange models

4.2.3.1 Comparison with the SPEX package

The experimentally obtained spectrum for capture by bare sulfur is compared in figure 4.15 to calculations described in [83] as implemented as an independent model in the SPEX package [98], which provides velocity-dependent cross sections for charge exchange with n, l- and S-resolved final states. The calculation is based on an MCLZ method
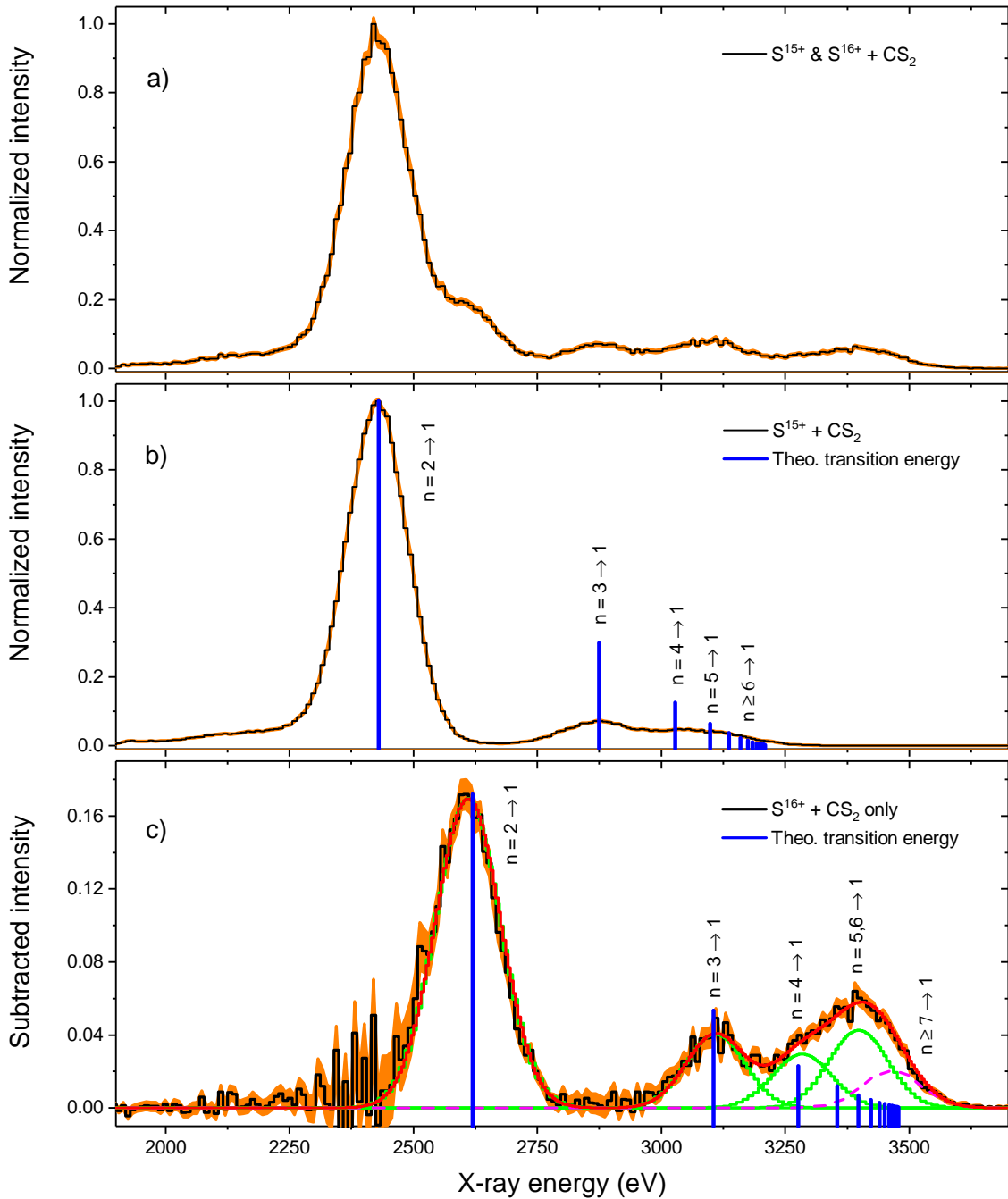
Figure 4.14: The procedure of extraction of the contribution arising from CX of fully-stripped sulfur with CS_2. **a)** Spectrum in the MTM above the ionization threshold for S^{16+} shows a mixture of capture into S^{16+} and S^{15+}. **b)** CX spectrum below the ionization threshold for S^{16+} yields a pure CX spectrum of S^{15+}. **c)** Normalizing the spectra from a) and b) to the K_β transition of S^{15+} and subtraction provides an extracted CX spectrum of pure S^{16+}. The blue vertical lines indicate theoretical transition energies obtained by FAC.
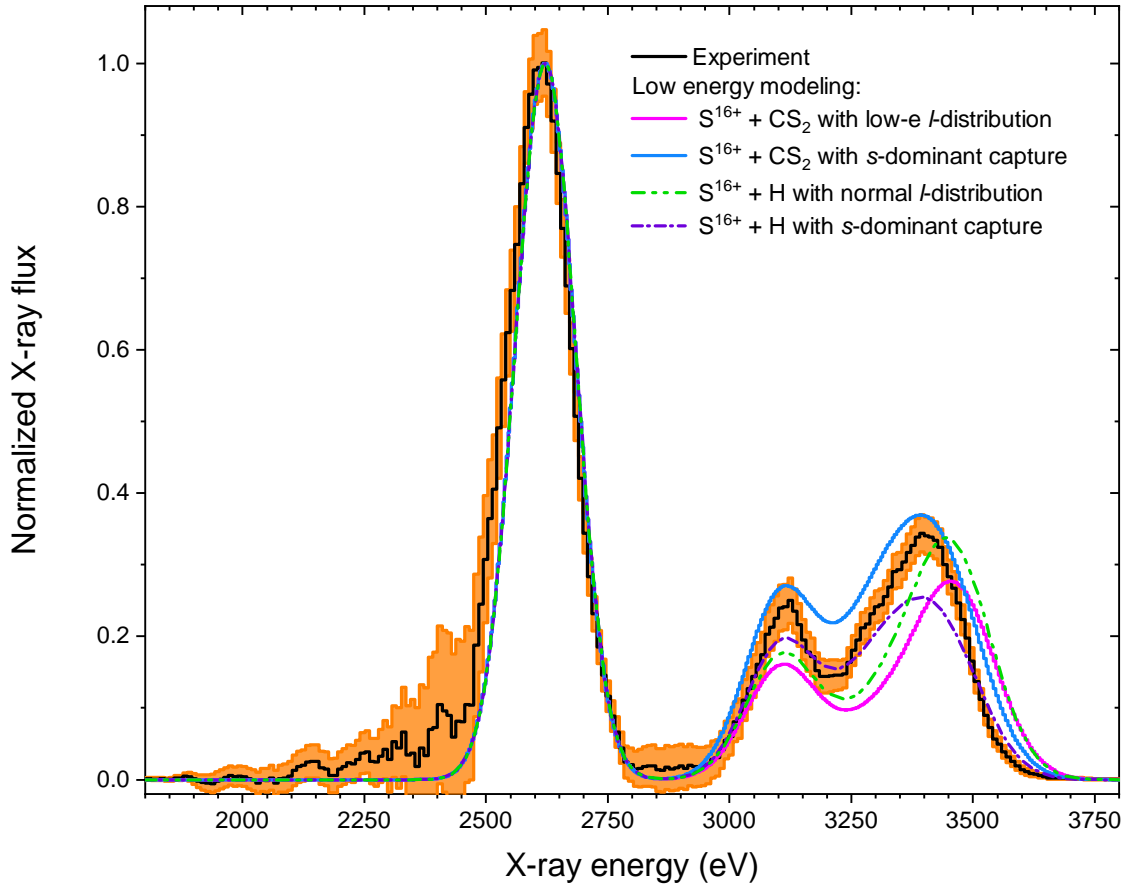
Figure 4.15: Charge exchange spectrum of fully ionized sulfur as a projectile and CS_2 as a target. The black curve is the data from figure 4.14 c) with the corresponding statistical uncertainties plotted in orange. Modeling with the SPEX package provides synthetic CX spectra of S^{16+} with H for a low-energy weighting l-distribution presented in equation 2.56 (green dashed line), scaled for a CS_2 target (magenta solid line), S^{16+} with H with an s-dominant l-distribution (violet dashed line), and scaled for a CS_2 target (blue solid line).

with the assumption of single-electron capture and an atomic hydrogen target. Since the most abundant element in the universe is atomic hydrogen, the assumption is reasonably representative for astrophysical modeling. After determination of the n- and l-resolved capture cross-section based on atomic data, radiative relaxation channels to the ground state are calculated. Since the catalog of n- and l-resolved cross-sections is incomplete, intrinsic scaling relations allow for interpolation for missing data.

For the modeling of the distribution of angular momenta l, the low-energy weighting function described in equation 2.56 was utilized with a high population of $l = 1, 2$. This distribution is valid for low collision energies between 10–100 eV/u [95, 6, 102]

as prevailed in an EBIT environment. The green-colored dashed line in figure 4.15 represents the calculation for collisions of fully-stripped sulfur with atomic hydrogen based on the low-energy weighting distribution of angular momentum states as described above, convolved with a Gaussian distribution with a width corresponding to the instrumental resolution of FWHM = 150 eV. The prediction of this model is a pile-up of higher Rydberg transitions at ~ 3450 eV, which is slightly shifted to higher energies compared to the experimental data shown as a black line with the corresponding uncertainty band in orange. To achieve a better agreement with the measurement speculations of an enhanced population of the s-states have to be anticipated. Since the relaxation to the ground state of an initial s-population of n has to bypass via transitions to p-states of adjacent lower principal quantum states $n-1$ in the electric dipole approximation, the peak should appear at slightly lower X-ray energies. The approach is to introduce an s-dominant distribution by modifying the low-energy weighting function to $W_{nl'}^{\text{lowe}'}$ with $l' = l - 1$, as reported in [123, 130]. The result of this distribution is depicted as a violet-colored dashed line.

Since the target was not atomic hydrogen, but CS_2 the most populated n has to be scaled according to equation 2.38 leading to an estimation of $n = 12$ with an ionization potential of CS_2 with $I_p = 10.1$ eV [68].

The predictions of the scaled model are depicted in figure 4.15 as a magenta-colored solid line for the low-energy weighting function and as a blue-colored solid line for the s-dominant distribution of angular momenta. The latter provides a better agreement to the measured spectrum in terms of centroid positions and intensity ratios.

4.2.3.2 Comparison with the FAC cascade model

For comparison, the radiative cascade model presented in section 2.3.4.5 is applied to the experimentally obtained spectrum for the collision between S^{16+} and CS_2. As described above, the most populated principal quantum number state of $n = 12$ according to equation 2.38 is assumed. The result of the fitting algorithm for all possible angular momentum states is shown in figure 4.16.

The fit is represented by a solid magenta-colored line, the inset in the figure shows the relative fraction of the population of angular momentum states determined by the coefficients of the spectral basis vectors obtained by the fit. As predicted by the SPEX model with an assumed s-dominant l-distribution the capture of the electron occurs predominantly into the $|n = 12, l = 0\rangle$ state shifting the peak as expected to slightly lower photon energies compared to the synthetic spectrum obtained with a low-energy distribution of angular momenta. However, in contrast to the l-distribution of the s-dominant capture model, the population of adjacent angular momentum states is highly suppressed. Furthermore, a small fraction of the population of higher angular momenta contradicts the decrease of the
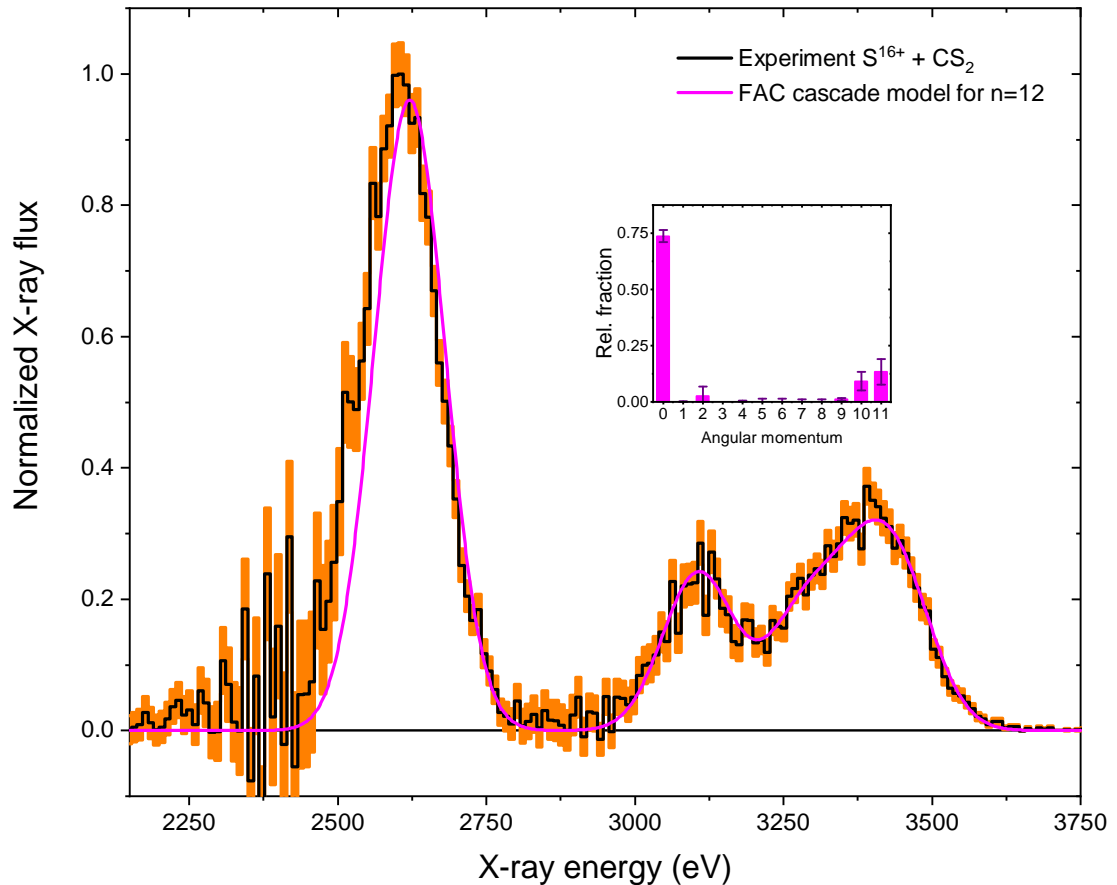
Figure 4.16: Comparison of the measured spectrum with the radiative cascade model calculated by means of FAC, as described in section 2.3.4.5. The magenta-colored solid line represents the least-squares fit, and the inset shows the relative fraction of the population of angular momentum determined by the fitting coefficients.
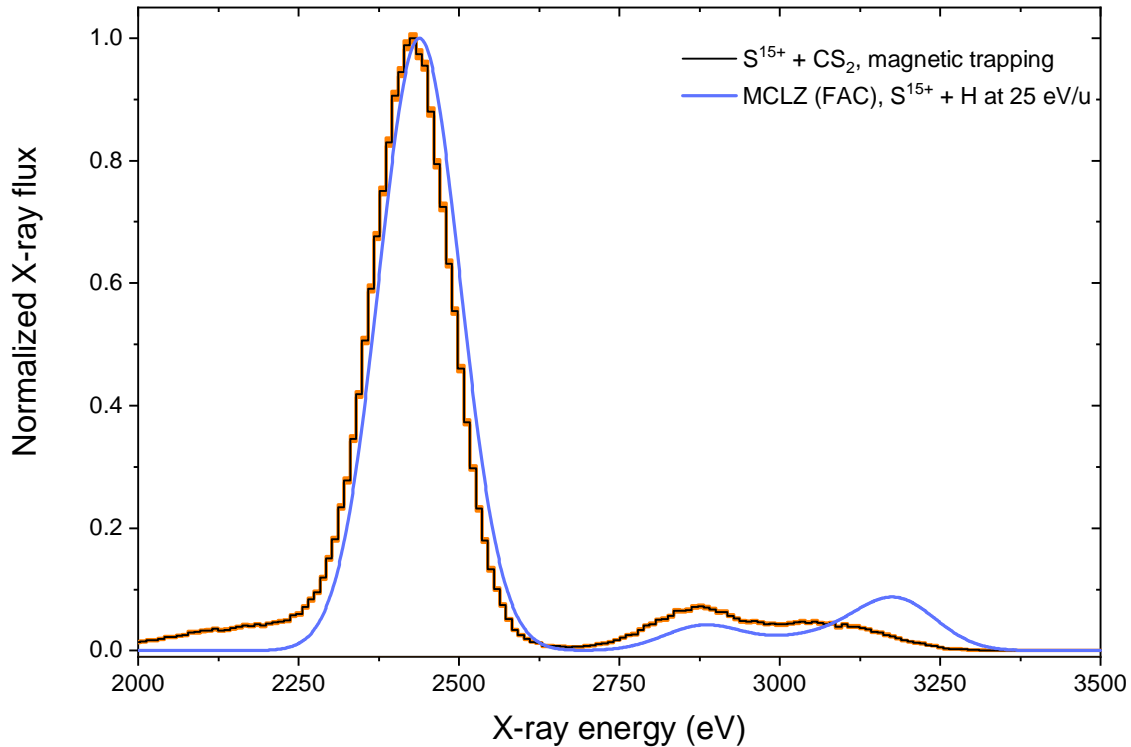
Figure 4.17: Charge-exchange spectrum of S^{15+} with CS_2 in magnetic-trapping mode is illustrated in black with the corresponding uncertainties in orange. The synthetic CX spectrum calculated by the MCLZ approach of FAC with atomic hydrogen as a target is shown in blue.

population to higher angular momenta resulting from equation 2.56 with $l' = l - 1$. However, those populations are not significantly different from zero within the 3σ uncertainty.

Additionally, the charge exchange spectrum of $S^{15+} + CS_2$ is compared in figure 4.17 to the MCLZ calculation provided by FAC for collisions of hydrogen-like sulfur with atomic hydrogen, since CS_2 is not available as a target.

The FAC model for collisions of hydrogenic systems with neutral gas overestimates the relative intensity of the higher Rydberg transitions and underestimates the K_β transition. Although an ab-initio calculation for the l-distribution is performed, instead of a multiplication of established distribution functions to the total n-resolved cross-section as for initially bare systems, the agreement with the experiment is deficient.

4.2.3.3 Comparison with the KRONOS code

The experimentally obtained spectrum for CX of fully ionized sulfur is compared to the MCLZ calculation performed by the Kronos code. The synthetic spectra for different distributions of angular momenta at low collision energies of 25 eV/u are overlayed with the
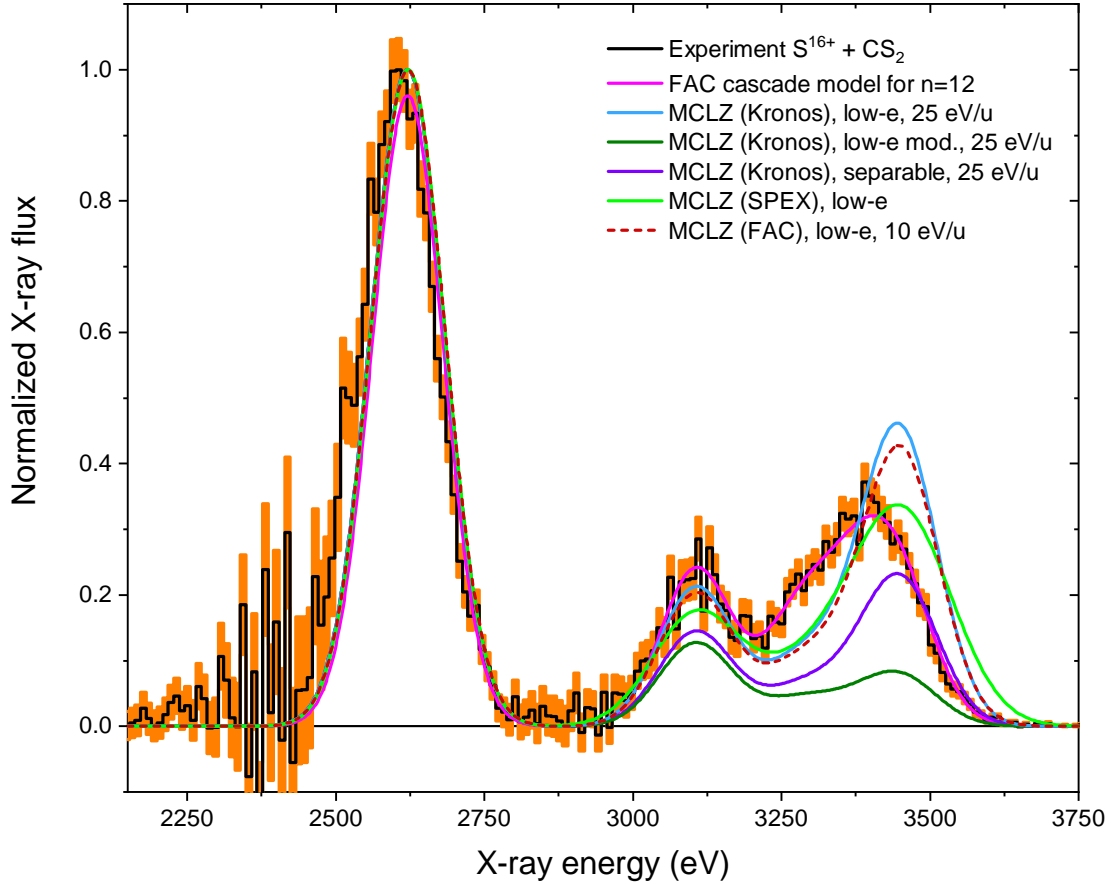
Figure 4.18: Comparison between the experimental CX spectrum of S^{16+} with CS_2 and different MCLZ approaches with different angular momentum distributions for collision with atomic hydrogen.

data in figure 4.18. As a target species, atomic hydrogen is assumed. The corresponding angular momentum distributions were described in chapter 2.3.4.3. Furthermore, a synthetic CX spectrum provided by the MCLZ approach of FAC for S^{16+} + H at a collision energy of 10 eV/u with a low-energy l-distribution is shown as a dashed curve.

To note is a discrepancy between the MCLZ approach performed by the Kronos code and the MCLZ method of the SPEX package for the same assumption of a low-energy distribution of the l-states, illustrated by a light blue and a light green curve, respectively. Also, a slight discrepancy between both approaches and the FAC MCLZ calculation is observed. In particular, the relative intensities of transitions from $n \geq 3$ to the ground state with respect to the Lyman-α transition is predicted significantly higher by Kronos than by the calculation of SPEX and FAC. The discrepancy can not be explained by different transition rates utilized by Kronos, SPEX, and FAC since hydrogenic systems can be calculated accurately. Different collision velocities do not change the overall shape of

the spectrum significantly. The only explanation remaining, is a possible difference in the numerical calculation of the multichannel transition probabilities of both approaches.

Furthermore, the peak at higher Rydberg transitions at $\sim 3460\,$eV is shifted by one principal quantum number towards higher energies with respect to the experiment. As already pointed out in subsection 4.2.3.1, the agreement between model and experiment improves by the inclusion of an *s*-dominant capture leading to a shift of the peak to lower Rydberg transitions. Since the *nl*-states are degenerate for hydrogen-like systems after capture, the cross-sections for capture into specific angular momenta can not be calculated ab-initio by the MCLZ approach, as already discussed in chapter 2.3.4.3. Nevertheless, to extract information about the *l*-state resolved cross-sections, ordinarily the total CX cross-section is multiplied with certain distribution functions. Such unique *s*-dominant distributions are not included in most charge exchange codes.

4.2.4 Comparison with astrophysical observations

In this measurement, the higher Rydberg transitions $n \geq 7 \rightarrow 1$ were determined to $3.47(6)\,$keV. Since the experimental investigations are consistent with theoretical predictions, models and other publications [32] for transition energies of the high Rydberg transitions, the model presented in section 4.2.3 and the corresponding data is compared to recent astrophysical observations. As described in the introduction, an unidentified line feature (ULF) at a photon energy of $E_\gamma = 3.5\,$keV has been reported in [42, 39, 38, 170] with a proposed origin in the decay of sterile neutrinos with a mass of $m_S = 2E_\gamma = 7.1\,$keV. In [42] spectra of 73 different galaxy clusters including Perseus, Centaurus, Ophiuchus and others obtained by the MOS [169] and PN [160] instruments of the XMM-Newton X-ray space telescope [178] were stacked and a centroid position of the ULF was determined to 3.51–$3.57\,$keV with a statistical significance greater than 3σ. In the spectrum of the Perseus galaxy cluster [170], the centroid position of the ULF was determined to 3.51–$3.59\,$keV, in the Andromeda nebula and the Perseus cluster to 3.46–$3.53\,$keV [39] and in the Galactic center to $3.54\,$keV [38].

The residuals presented in figure 4.19 are constructed by subtraction of a model from the data and normalized by the model. The model itself is based on a thermal plasma approach [42] with a multi-temperature collisional equilibrium plasma [156] and atomic transition energies extracted from the AtomDB database [70].

For comparison, the CX model shown in figure 4.2.3 is plotted in each residual spectrum as a light blue dotted line for the *s*-dominant angular momentum distribution and as a magenta-colored dashed line for the low-energy weighting function. To note is, that the K_β transition of hydrogen-like sulfur at $3.12\,$keV predicted by the charge exchange models is not present in the residuals of the models of [42, 170, 39]. This is due to the fact that
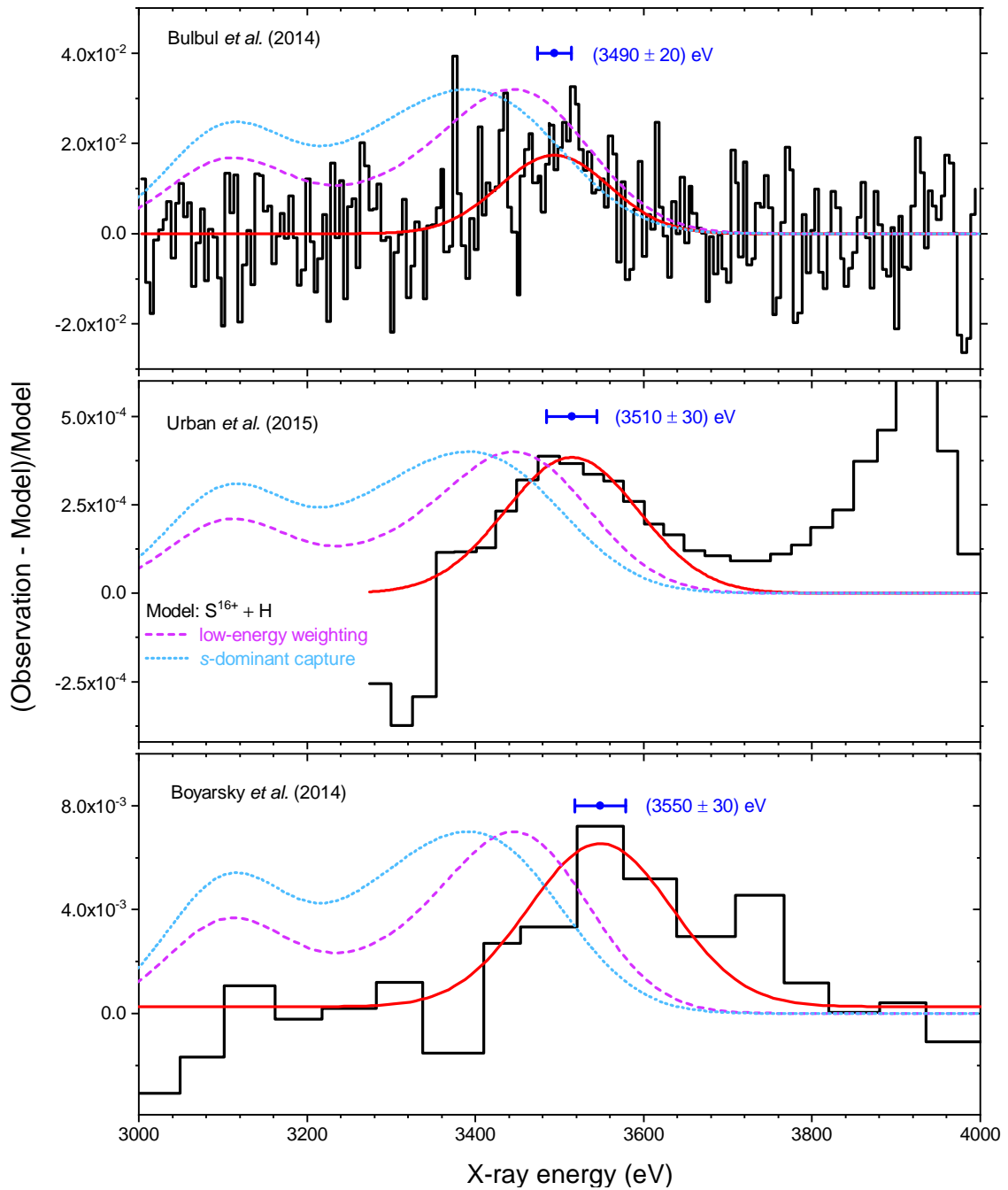
Figure 4.19: Residuals of thermal plasma modeling of astrophysical observations reported in [42, 170, 39] with excess at 3.5 keV. The centroid of this unidentified line is indicated by a blue circle with the corresponding uncertainty. Overlayed in each image are the synthetic CX-induced spectra of $S^{16+} + H$, presented in figure 4.15 for a low-energy distribution of angular momenta, depicted in magenta and for the *s*-dominant capture in light-blue.

a strong transition of helium-like argon was included in the thermal plasma models at the position where the K_β transition of S^{15+} was expected. Since the thermal plasma models were optimized for zero excess of the residuals, comparably weak charge-exchange induced transitions coinciding with the energies of strong collisional-induced transitions were suppressed. Moreover, the contribution of the transition at $3.31\,keV$ of hydrogen-like argon can be overestimated by the model due to a coincidence with the transition energy of charge exchange induced transitions from $n = 4, 5 \rightarrow n = 1$ of S^{15+}. This overestimation leads to an apparent shift of the centroid of the $3.5\,keV$ line to slightly higher photon energies with respect to the actual value. This displacement can be roughly estimated by considering a Gaussian with a centroid at an energy of the S^{15+} transition at $3.47\,keV$, which was observed in the CX experiment, and a blend of an Ar^{16+} transition and CX-induced S^{15+} transitions at $\sim 3.31\,keV$ with corresponding X-ray fluxes in the order of 5×10^{-3}–$1.5 \times 10^{-2}\,photons\,cm^{-2}\,s^{-1}\,keV^{-1}$ presented in [42]. An overestimation of the argon transition by $20\,\%$ leads to an apparent shift of the peak after subtraction by $\sim 10\,eV$ to higher energies. A slight uncertainty of the astrophysical observation in this order could explain the discrepancy between the $3.5\,keV$ line and the proposed CX-induced S^{15+} Rydberg transitions.

In February 2016, the high-resolution X-ray satellite Hitomi was launched, equipped with a soft X-ray spectrometer (SXS) consisting of a microcalorimeter array with 35 pixels and a spectral resolution of FWHM $= 4.9\,eV$. One of the few accomplished missions of Hitomi, before it broke down in March 2016, was the observation of the Perseus galaxy cluster in order to investigate the origin of the $3.5\,keV$ line. The acquired X-ray spectrum is shown in figure 4.20. In the top panel, the X-ray flux is plotted as a function of the photon energy in the observer frame [8].

The red curve represents the best-fit model assuming a plasma temperature of $kT = 3.5\,keV$, a velocity dispersion of $180\,km/s$ and a solar abundance of the elements of 0.54. Strong X-ray transitions of highly charged chlorine, sulfur, argon potassium, and calcium ions are indicated by labels at the corresponding transition energies on the top. The red and the blue bracket indicates the position and uncertainty band of the observed line feature at $3.5\,keV$ by the XMM-Newton MOS instrument [169] in the 74 stacked spectra of galaxy clusters and the Perseus galaxy cluster presented in [42]. In the bottom panel, the residuals of the fit, which are the ratios of the data and the model, are presented.

The line feature at $3.5\,keV$ detected in previous observations of XMM-Newton is not present in this spectrum. Furthermore, the reported flux for the line at a relatively high level is not visible in the present spectrum. Proposed X-ray fluxes of an adjacent K_α transition of K^{17+} and K_β satellite lines of Ar^{16+} at an exceptional level [42] were also not observed. Weak spectral features with a significance of 1.5σ at $3.4\,keV$ indicate high-n transitions to the ground state of S^{15+} supporting the explanation of the charge exchange
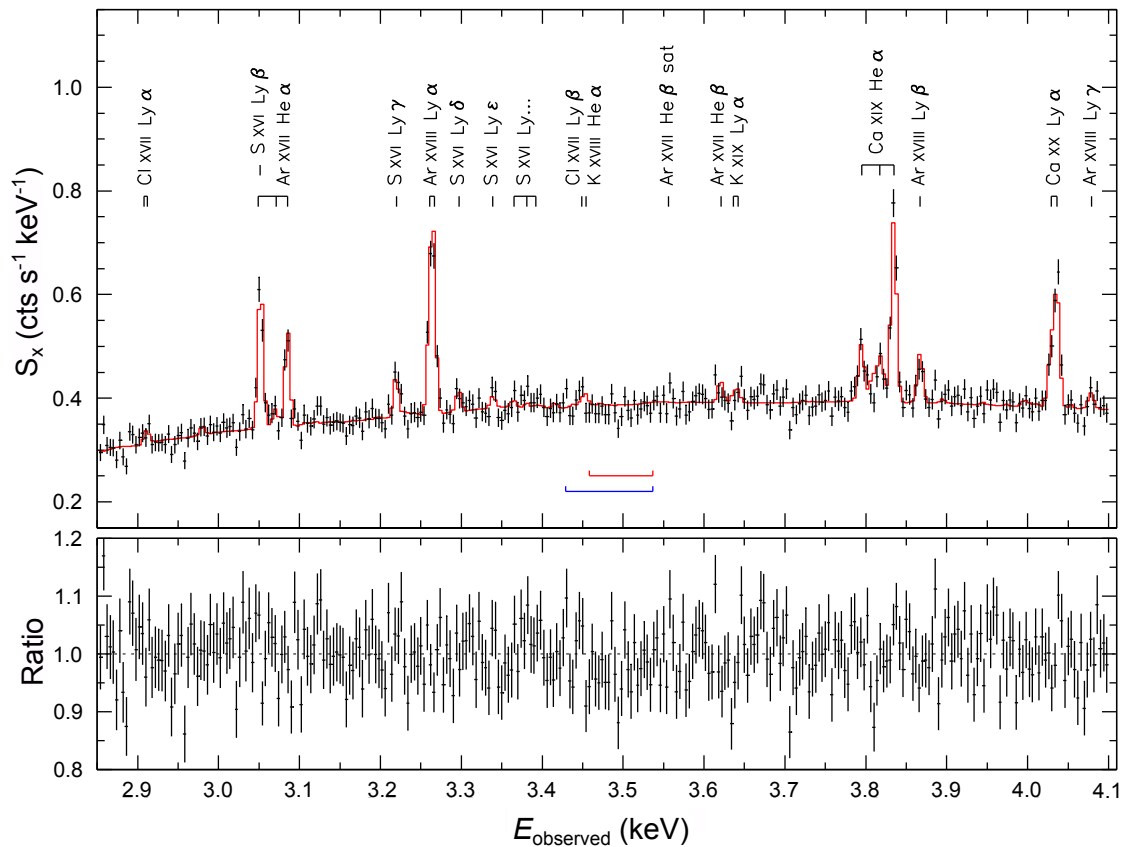
Figure 4.20: High-resolution X-ray observation of the Perseus galaxy cluster obtained by the Hitomi X-ray satellite. In the top panel, the observed X-ray spectrum with the photon energy in the observer frame is illustrated. The overlayed red curve represents the best-fit of the model. The bottom panel shows the residuals of the fit. The red and the blue brackets indicate the uncertainty bands of the observed 3.5 keV line reported in [42] by means of the XMM-Newton MOS instrument in the stacked-cluster spectrum and the Perseus cluster, respectively. Adapted from [8].

mechanism proposed by [83]. However, the signal is comparably weak and requires longer exposure times to approve or discount the charge exchange scenario. This process was not observed so far in the intracluster medium, and a conclusive detection of this process would be of particular importance for the astrophysical community. The launch of the X-Ray Imaging and Spectroscopy Mission (XRISM) [3] is planned for 2021 as a successor X-ray satellite of Hitomi. In the long term an independent mission of the European space agency (ESA) is planned for 2031 where the Advanced Telescope for High ENergy Astrophysics (ATHENA) X-ray satellite [18], equipped with a microcalorimeter with a spectral resolution of FWHM = 2.5 eV [135] should be launched in order to investigate hot gas structures and to search for supermassive black holes.

4.3 Charge exchange in highly charged argon

In this work, extensive charge-exchange measurements on highly ionized argon were carried out in addition to the sulfur CX measurements in order to understand the population of the angular-momentum states after electron capture. Argon is a noble gas, which enables a straightforward injection into the trap, serving as a target and a projectile, likewise. For a better understanding of the CX process, it is a suitable candidate, since a large variaty of comparative measurements were already performed [78, 24, 11, 91, 32, 109] in an EBIT and in extraction measurements, where the argon ions interacted with neutral targets in a gas cell. Argon is a well-studied element, where the transition energies are documented in standard databases, which simplifies the identification of spectral lines. Furthermore, the chare-exchange recombination spectroscopy with highly charged argon is a well-established technique for plasma diagnostics in magnetically-confined fusion plasmas [143, 104, 21].

4.3.1 X-ray measurements

Within the frame of this work charge exchange measurements of highly stripped argon were performed in the X-ray range according to a measurement scheme described in section 4.1.2. Here the time of a switching cycle of the electron beam was 10 seconds in total with a breeding time of 4 seconds and a measurement time of 6 seconds in the magnetic trapping mode. The electron-beam current was switched between $0\,\mathrm{mA}$ and $220\,\mathrm{mA}$. The axial trap depth was set to $500\,\mathrm{V}$ by application of a positive voltage to the neighboring electrodes of the central drift tube. Neutral argon was injected into the trap with an injection pressure of $\sim 2 \times 10^{-7}\,\mathrm{mbar}$ in the second injection stage corresponding to $4 \times 10^7\,\mathrm{atoms/cm^3}$ in the center of the trap, serving as a source for the production of highly charged argon and as a constant supply of neutral gas which interacts in the magnetic trapping mode with the HCIs. A two-dimensional spectrum with a nominal electron-beam energy of $6.02\,\mathrm{keV}$ which suffices to produce bare argon ions with the production-threshold energy of $4.42\,\mathrm{keV}$

is shown in figure 4.21, where the X-ray photon energy acquired with an SDD is plotted as a function of the time within the switching cycle. The photon energy was calibrated with Ly_α and Ly_β transitions calculated with FAC and the energy of the silicon escape peak at the low-energetic part of the spectrum, using a linear fit.

At time $t = 0\,\text{s}$ the electron beam was switched on. Ions were produced, and the trap started to fill with ions. From the radiative recombination of hydrogen-like argon and bare argon into with a free electron into $n = 1$ labeled with i) and j), respectively, the time where the trap is in equilibrium between production of ions and loss of ions was approximately 2.5 s. The photon energy is the sum of the binding energy of the corresponding shell in which the electron is captured and the kinetic energy of the free electron. With progressing time the trap was filled with more positively charged ions which increased the kinetic energy of the free electrons due to higher compensation of the negative space charge of the electron beam (which has a maximum at $t = 0$) resulting in higher photon energy for the radiative recombination process.

At time $t = 0$ no ions were trapped, and thus the only space-charge contribution arised from the electron beam. The RR of H-like argon appears in the spectrum at $E_{\text{RR,H}-\text{like}} = 9825(25)\,\text{eV}$ which is the sum of the binding energy of the He-like argon of $E_{\text{B,He-like}} = 4121\,\text{eV}$ after the capture of the free electron and the real kinetic energy of its, which can be calculated to $E_{\text{RR, H-like}} - E_{\text{He-like}} = 5704(25)\,\text{eV}$. The nominal kinetic energy of 6020 eV was reduced by the contribution of the negative space charge of the electron beam, which can be estimated to $316(25)\,\text{eV}$. With a relativistic consideration of the velocity of the free electrons

$$v = c_0\sqrt{1 - \left(\frac{eU_e}{m_e c_0^2} + 1\right)^{-2}}, \tag{4.5}$$

where c_0 represents the speed of light in vacuum, U_e the real kinetic energy of the free electrons and m_e the mass of the electron, the velocity can be calculated to $4.4 \times 10^7\,\text{m/s}$. Inside the central trap electrode with a length of $\sim 8\,\text{cm}$, a free electron requires 1.8 ns to traverse it. With the time of flight and a total beam current of 220 mA, the total number of electrons inside the trap can be estimated to $N_e = 2.5 \times 10^9$. The negative space charge of $316(25)\,\text{eV}$ caused by N_e electrons corresponds in first-order approximation to a space charge of $\rho_e = 1.3(1) \times 10^{-7}\,\text{eV}$ induced by one electron.

From the slope of 258 eV/s of the increasing photon energy due to the compensation of the negative space charge by the increasing number of positively charged ions inside the trap, the filling rate can be estimated to $(258\,\text{eV/s})/\rho_e = 2.0(2) \times 10^9$ charges/s corresponding to $1.3(1) \times 10^8\,\text{Ar}^{16+}/\text{s}$ after recombination. The equilibrium of the ion production rate and
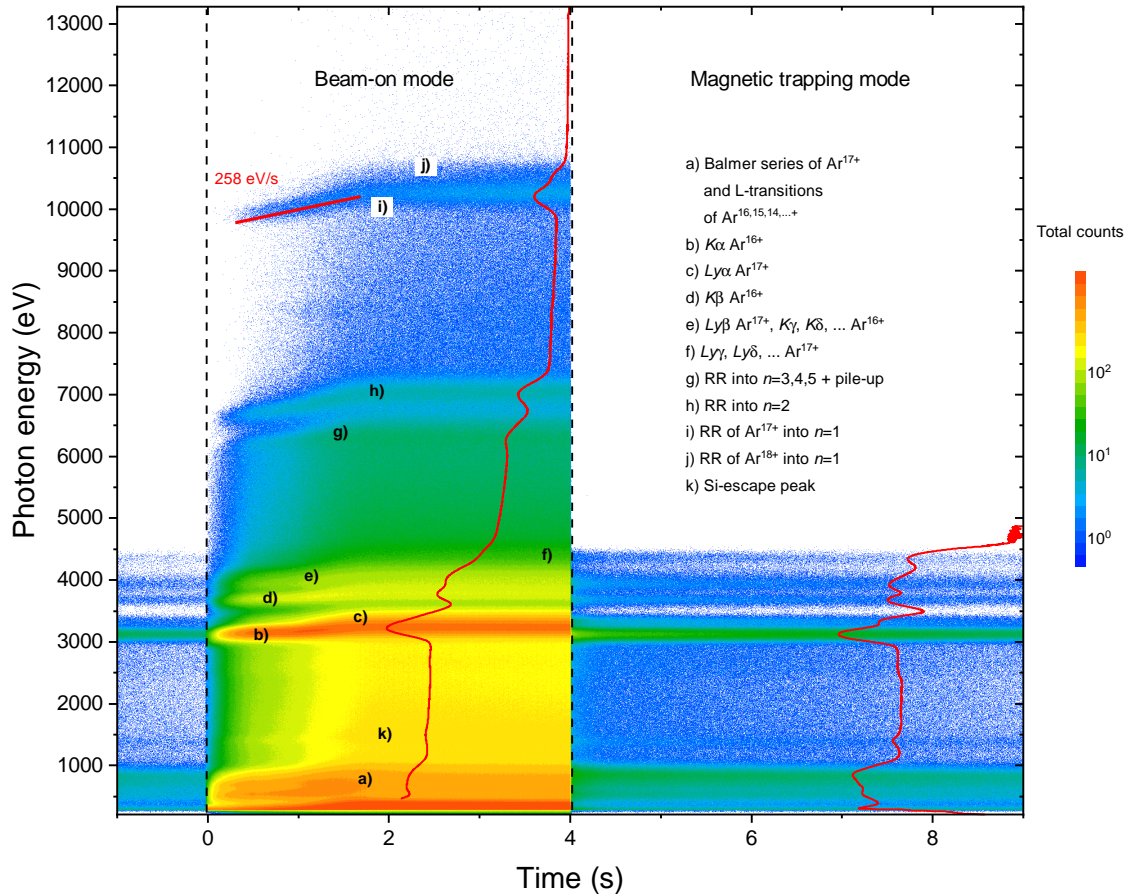
Figure 4.21: Two-dimensional charge exchange spectrum of highly charged argon with an electron-beam energy above the ionization threshold for bare argon. The photon energy detected with an SDD is plotted as a function of the time within the switching cycle of the electron beam. From zero to four seconds, the electron beam was switched on leading to the emission of photons due to different processes of recombination and direct excitation. After switching off the beam at four seconds, the only contribution which can lead to emission of photons is charge exchange. The red curves overlayed are the projection of the beam-on mode and the magnetic trapping mode, respectively to the axis of the photon energy in logarithmic representation.

the ion-loss rate was reached after 1.5 seconds, where the photon energy of i) did not change anymore. Thus the total trap capacity can be estimated approximately to $2.0(2) \times 10^8$ ions with a trap depth of $500\,\mathrm{V}$ used in this measurement. In this equilibrium, the photon energy during the RR process was $10\,250\,\mathrm{eV}$, which is $425\,\mathrm{eV}$ higher than directly after switching on the electron beam. Also, radiative recombination into $n = 2$, labeled with h) and into $n = 3, 4, 5, ...$, labeled with g) can be seen. Due to an instrumental resolution of the silicon-drift detector of FWHM $= 153\,\mathrm{eV}$, the recombination into those shells is not charge-state resolved anymore.

During the beam-on mode, also direct excitation of several transitions can be seen. At the beginning of the cycle, mainly Li-like and He-like argon ions were produced and K-shell transitions like K_α ($n = 2 \to n = 1$), K_β ($n = 3 \to n = 1$), and K_γ ($n = 4 \to n = 1$), denoted by b), d) and e), respectively can be observed. After two seconds a signature c) of the Ly_α transition ($n = 2 \to n = 1$) of hydrogen-like argon becomes visible. In the low-energetic region a), mainly transitions into the L-shell and transitions between high Rydberg states are present. The horizontal line k) is the so-called silicon escape peak which is an instrumental artifact caused by recombination of an electron into the K-shell of silicon leading to the emission of a photon with an energy, reduced by the K_α transition of silicon of $1.74\,\mathrm{keV}$ [4].

After four seconds the electron beam was switched off, and all contributions of interactions between free electrons with ions vanished. The only processes which can lead to emission of photons are metastable states and charge exchange of the ions with neutrals. In this energy range, the metastable states have a comparably short lifetime in the order of several $\sim \mathrm{\mu s}$ [50, 166]. The process which is responsible for the long term emission of photons is, therefore, charge exchange. Here, an electron from initially neutral argon is captured into a Rydberg state of the highly charged projectile. In the magnetic trapping mode line b) is the result of the last step of a cascade from $n = 2 \to n = 1$ of initially hydrogen-like argon and helium-like after capture into a high n-state. Line c) results from the $n = 2 \to n = 1$ transition of an initially bare argon ion and hydrogen-like after the capture at the end of the cascade. Transitions from higher principal quantum number states can be seen in the MTM in d) and e). The line labeled with f) represents the transitions near to the series limit of $4.42\,\mathrm{keV}$ of hydrogen-like argon. Transitions above this photon energy are not possible in the MTM.

Transitions from Rydberg states into the L-shell, M-shell, and transitions between those can be observed in a). The red curve represents the projection of the corresponding mode of the switching cycle onto the axis of the photon energy in the logarithmic scale.

Collapsing all events detected within the region of the $\mathrm{K}_\alpha, \mathrm{Ly}_\alpha, \mathrm{K}_\beta, \mathrm{Ly}_\beta$, and $\mathrm{Ly}_{\gamma, \delta, ...}$ onto the time axis, respectively, yields figure 4.22. After switching off the electron beam at $4\,\mathrm{s}$, the number of photons decreased by two orders of magnitude. One contribution to the

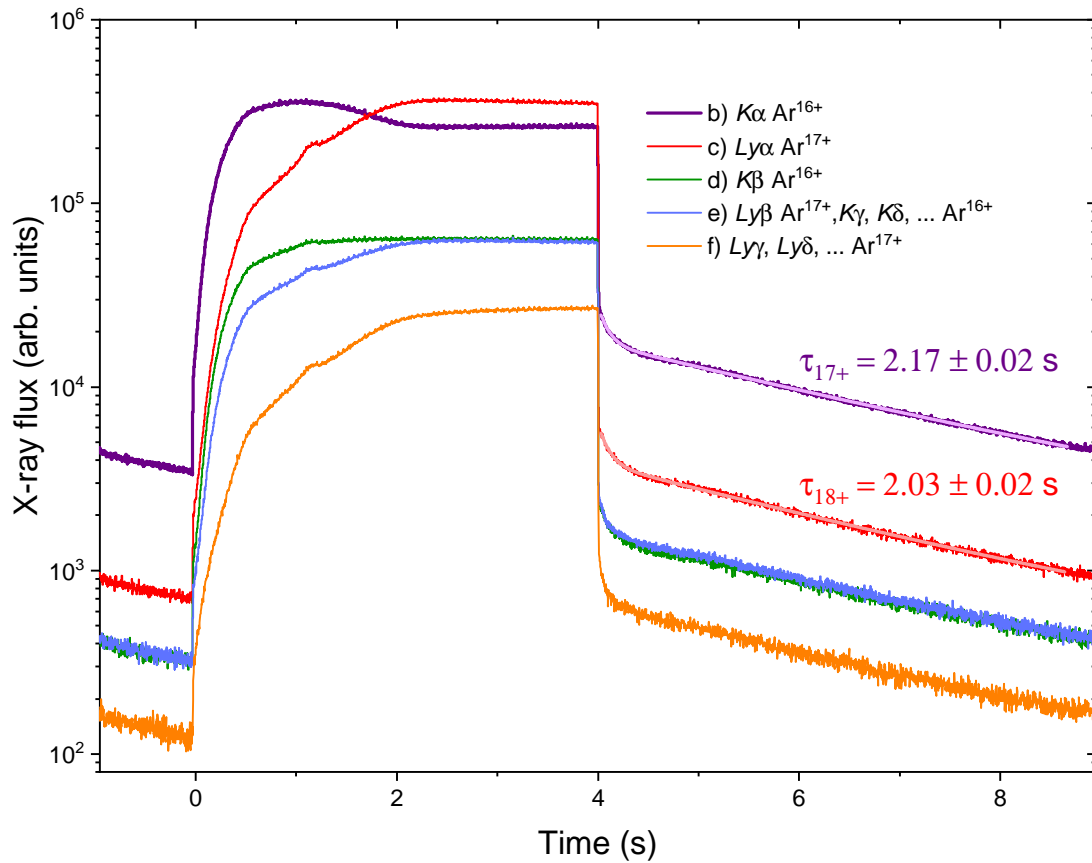**Figure 4.22:** Projection of the regions of $K_\alpha, Ly_\alpha, K_\beta, Ly_\beta,$ and $Ly_{\gamma,\delta,\dots}$ from figure 4.21 onto the time axis. The longer time constant of the K_α transition results from feeding of the helium-like charge state by subsequent capture of two electrons into initially fully ionized argon.

decay of the count rate is the absence of the electrons which excite the K-shell transitions. A second effect is the loss of high energetic ions from the trap. On a longer timescale, the decay is dominated by charge exchange. By fitting a double exponential decay to the data provides the timescale of the loss of the ions of ~ 100 ms. The second exponential decay yields the timescale of the loss of ions due to charge exchange. For the Ly_α transition, the time constant is determined to $\tau = 2.17(2)$ s and for the K_α transition $\tau = 2.03(2)$ s. The longer decay time of the helium-like transitions can be explained by recombination of initially fully ionized argon decaying to the ground state by emission of Ly_α radiation and subsequent capture of a second electron feeding the helium-like charge state.

A similar measurement, as presented in figure 4.21, was performed with an electron-beam energy below the ionization threshold for bare argon at $E_e = 4.4$ keV at an electron-beam current of 200 mA. The highest charge state possible is, therefore, hydrogen-like. The spectrum is shown in figure 4.23.

The radiative recombination appears at lower photon energies due to the lower electron beam energy. The spectral feature of RR into $n = 1$ of bare argon shown in figure 4.21 as j) vanished and only the contribution of RR into $n = 1$ of hydrogen-like argon can be seen now in j). The intensity of the direct excitation of the Ly_α transition at 3320 eV is comparably low because less hydrogen-like ions were produced at 4.4 keV electron-beam energy than at 6 keV. In the MTM this line vanishes because in this mode it can only be produced by capture of an electron into a bare agon which was not produced with the nominal electron-beam energy 4.4 keV in this measurement. An additional spectral feature at ~ 11.5 keV in the beam-on mode which was not visible in figure 4.21, because it was outside of the range of the ADC, is a pileup signal of the K_α line at ~ 3.1 keV and the RR line j) at ~ 8.4 keV.

By projecting all events within the magnetic trapping mode onto the axis of the photon energy, a one-dimensional histogram with the photon energy on the abscissa can be obtained as presented in figure 4.24.

All transitions presented here can only be induced if a vacancy in the K-shell is available. Since all metastable states are already decayed on this time scales, all lines have their origin in the bare and the hydrogenic charge state. The blue curve is extracted from the two-dimensional spectrum below the ionization threshold for bare argon, the orange curve above the threshold. The blue spectrum is scaled by a factor of 4.8 to normalize it to the K_β line of He-like argon at 3.68 keV which is present in both spectra. A subtraction of the spectra leads to the extraction of the pure contribution of charge exchange of bare argon, which is presented in figure 4.25.

The black curve represents the data of CX of the pure bare argon, the orange lines are the statistical uncertainties, and the vertical dashed lines are calculations of the
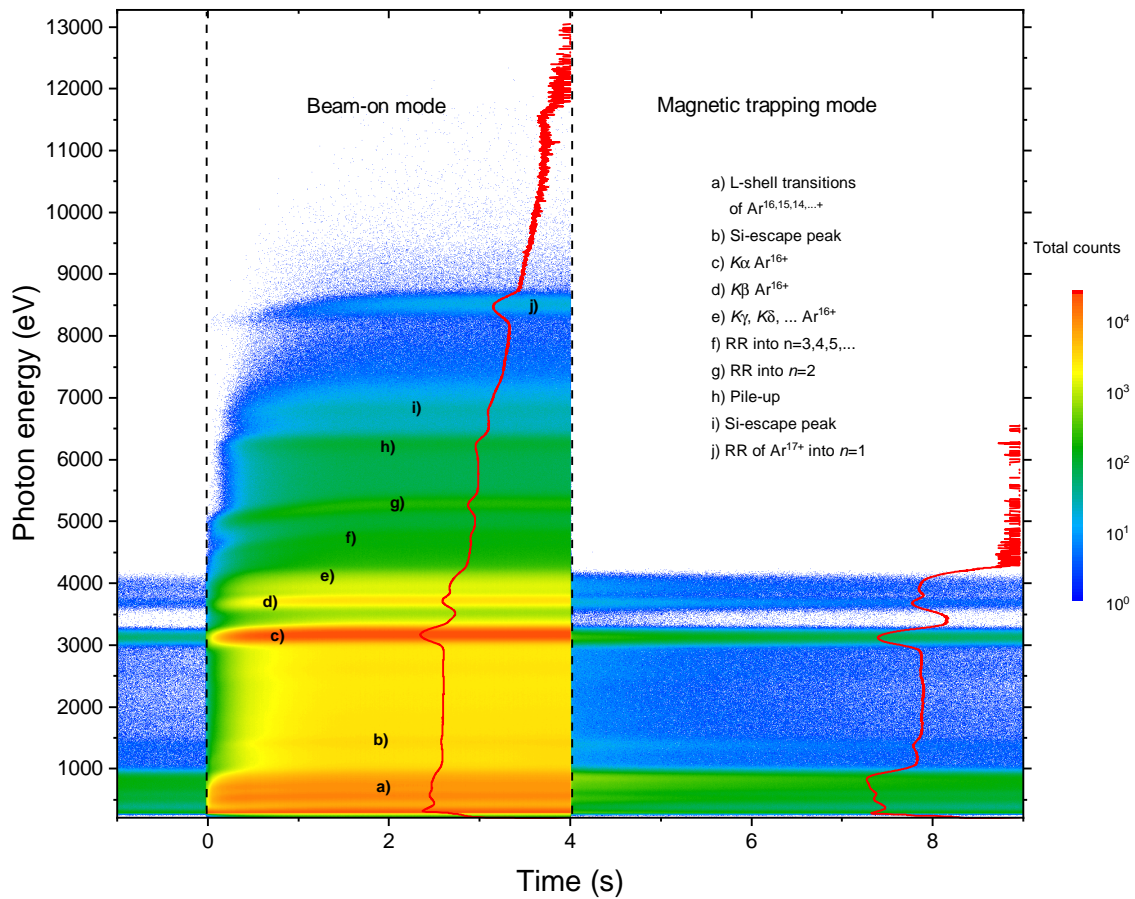
Figure 4.23: Two-dimensional charge exchange spectrum of highly charged argon with an electron-beam energy below the ionization threshold for bare argon. The photon energy detected with an SDD is plotted as a function of the time within the switching cycle of the electron beam. The spectral features are described in figure 4.21. The maximal reachable charge state is hydrogen-like. Therefore the RR or CX into bare argon is not present in this spectrum.
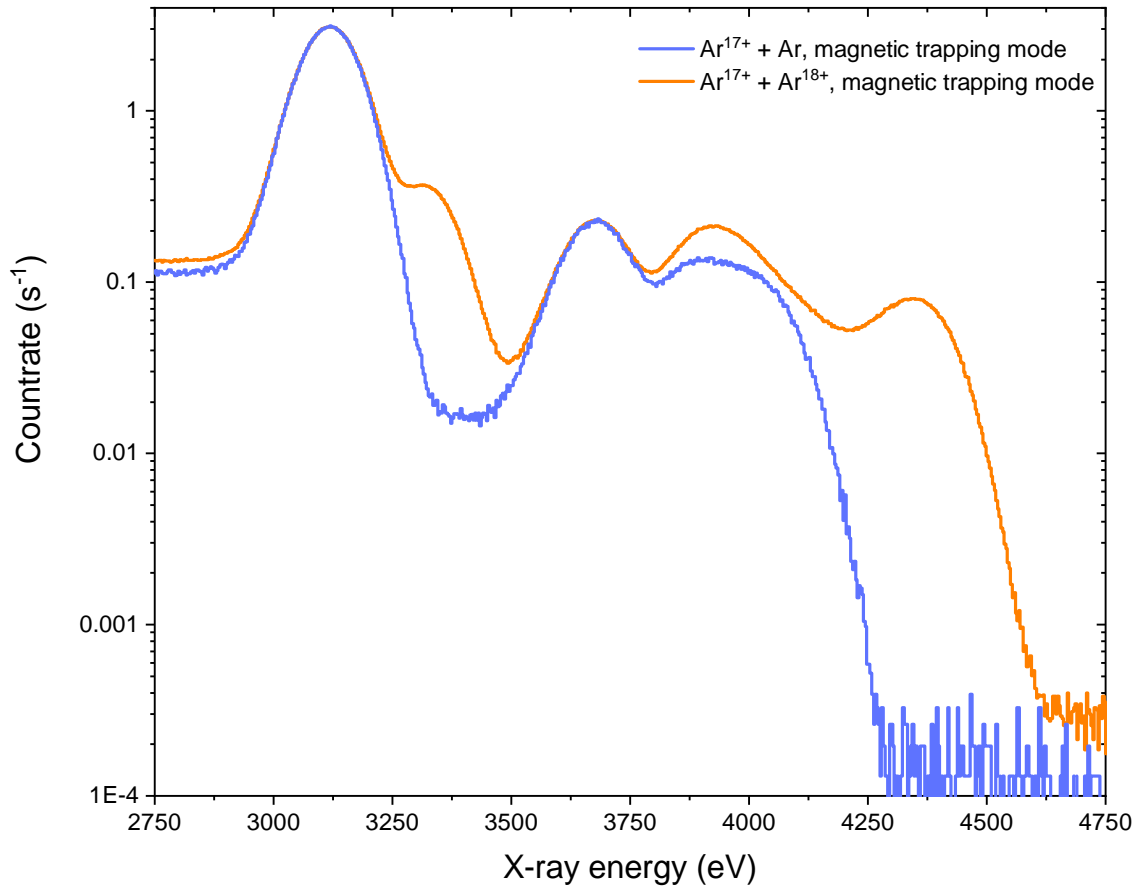
Figure 4.24: Projected CX spectra of Ar^{18+} and Ar^{17+}, normalized to the K_β transition of Ar^{16+} at 3680 eV, which is present in both spectra in order to extract the pure contribution of capture into the fully ionized system.
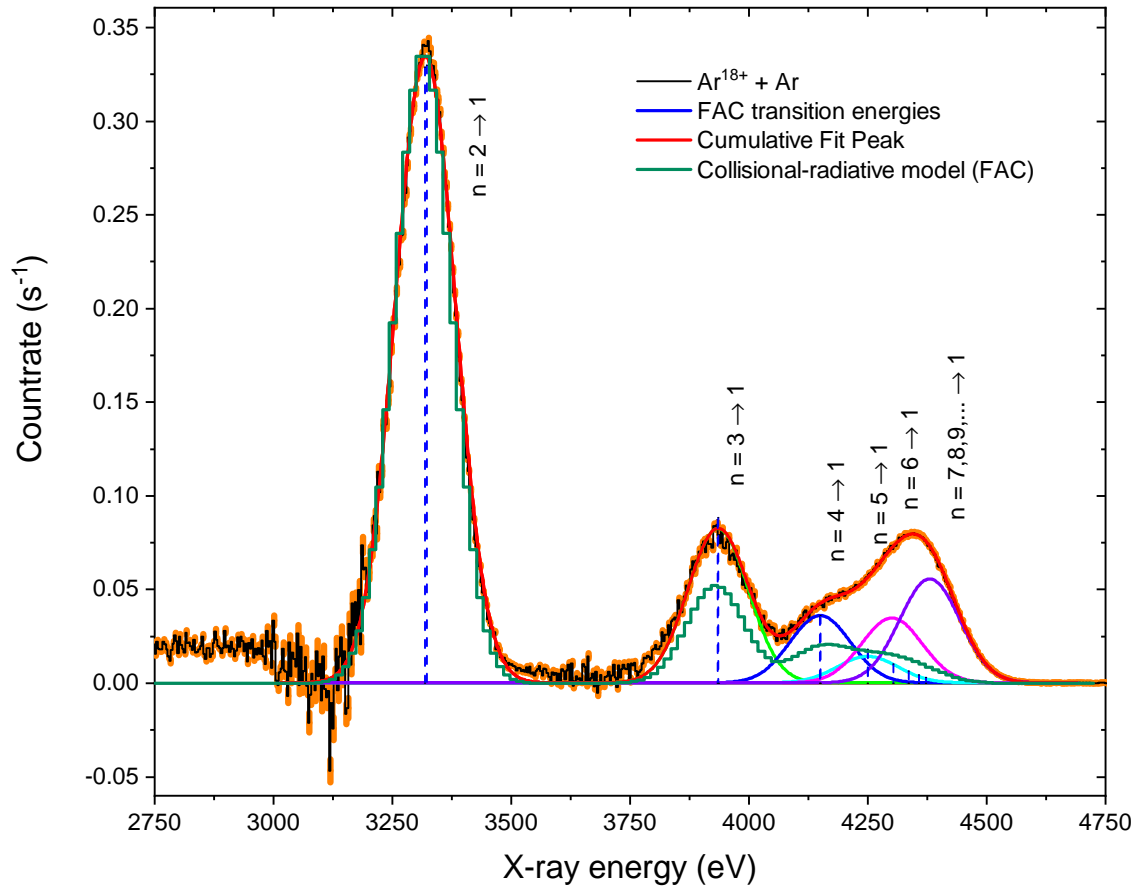
Figure 4.25: Charge exchange spectrum of pure Ar^{18+} with neutral argon by subtracting the spectra in the magnetic trapping mode above and below the ionization threshold for the production of bare argon as presented in figure 4.24. The data is shown in black with the corresponding error bars in orange, a collisional-radiative model in green and a fit of 6 Gaussian distributions with fixed centroids and the amplitude as a free parameter.

theoretical line position performed with FAC. The Gaussian distributions of the transitions $n = 2 \to 1, n = 3 \to 1, ..., n = 7, 8, 9, ... \to 1$ are fitted with fixed centroids according to the FAC calculation with the amplitude as a free fit-parameter. The width of all Gaussians, except for $n = 7, 8, 9, ... \to 1$, is shared. The green curve is a synthetic collisional-radiative (CR) spectrum calculated with FAC which would be expected for a thermal plasma with a mono-energetic electron beam of 6 keV kinetic energy. Compared to the CRM, the intensity of the transitions from higher Rydberg states $n = 7, 8, 9, ...$ to the ground state in the CX spectrum is higher by a factor of ~ 7. Thus, charge exchange is an efficient mechanism for the population of higher energetic states.

A cautious inspection of the temporal, spectral evolution in the magnetic trapping mode by projecting sequential slices with a width of 148 ms from 74 ms to 1850 ms in the two-dimensional spectrum 4.21 after switching off the electron beam onto the axis of the photon energy provides a cumulatively stacked spectrum, as illustrated in figure 4.26. It shows the mixed spectrum of $Ar^{18+} + Ar$ and $Ar^{17+} + Ar$ above the ionization threshold for fully-stripped argon. The spectra at times beyond 1850 ms are not evaluated due to a lack of statistics because at these times, most of the ions were lost or recombined to lower charge states.

The same procedure was performed for the spectrum below the ionization threshold for bare argon with the same width of the temporal slices, as shown in figure 4.27.

Normalization to K_β, as presented in figure 4.24 for each slice above and below threshold and subtraction of both spectra provides the temporal evolution of the pure contribution of fully-stripped argon, which is shown in figure 4.28.

The dashed light gray line indicates a total shift of the peak at higher photon energies of 28 eV within 1776 ms to lower energies. As described in chapter 2.3.4, capture into low angular momentum states in a specific principal quantum number state would cause an increase of the photon flux at higher energies because the electron can decay directly from a $|n, l = 1\rangle$ state to the ground state $|1, l = 0\rangle$. If the electron is captured into higher angular momentum states, it has to decay via several cascades to the ground state leading preferably to the emission of several lower energetic photons. Therefore, the shift of the peak in this spectrum to lower energies indicates capture into higher angular momentum states or decrease of the principal quantum number state with increasing time. The shift of 28 eV corresponds at these energies to a shift of the principal quantum number by $\Delta n = -2$ which can be achieved by the population of angular momentum states with an increase of $\Delta l = +2$ with respect to the initial l at $t = 0$.
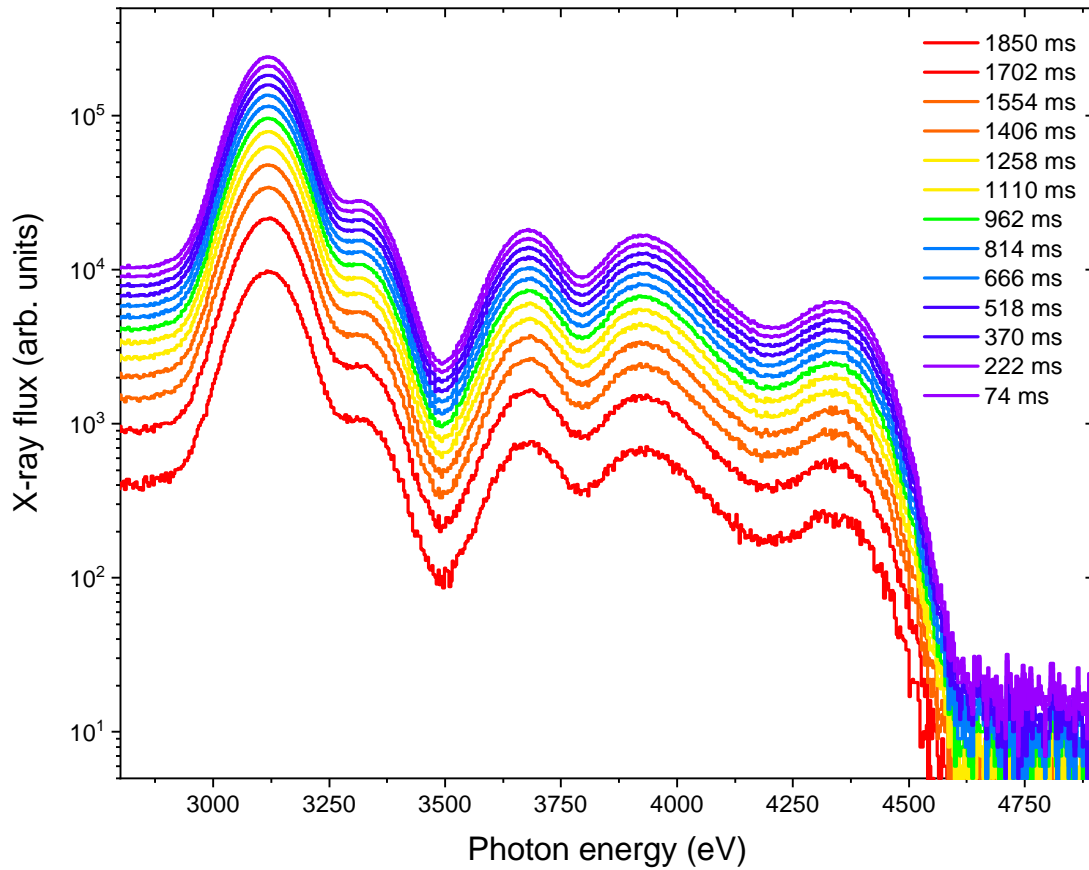
Figure 4.26: Temporal evolution of the CX spectrum of Ar^{17+} and Ar^{18+} with neutral argon and residual gas in MTM from figure 4.21 obtained by projection of consecutive slices with a width of 148 ms onto the X-ray energy axis. The X-ray flux is plotted as a function of the X-ray energy for each slice for starting from 74 ms up to 1850 ms after switching off the electron beam.
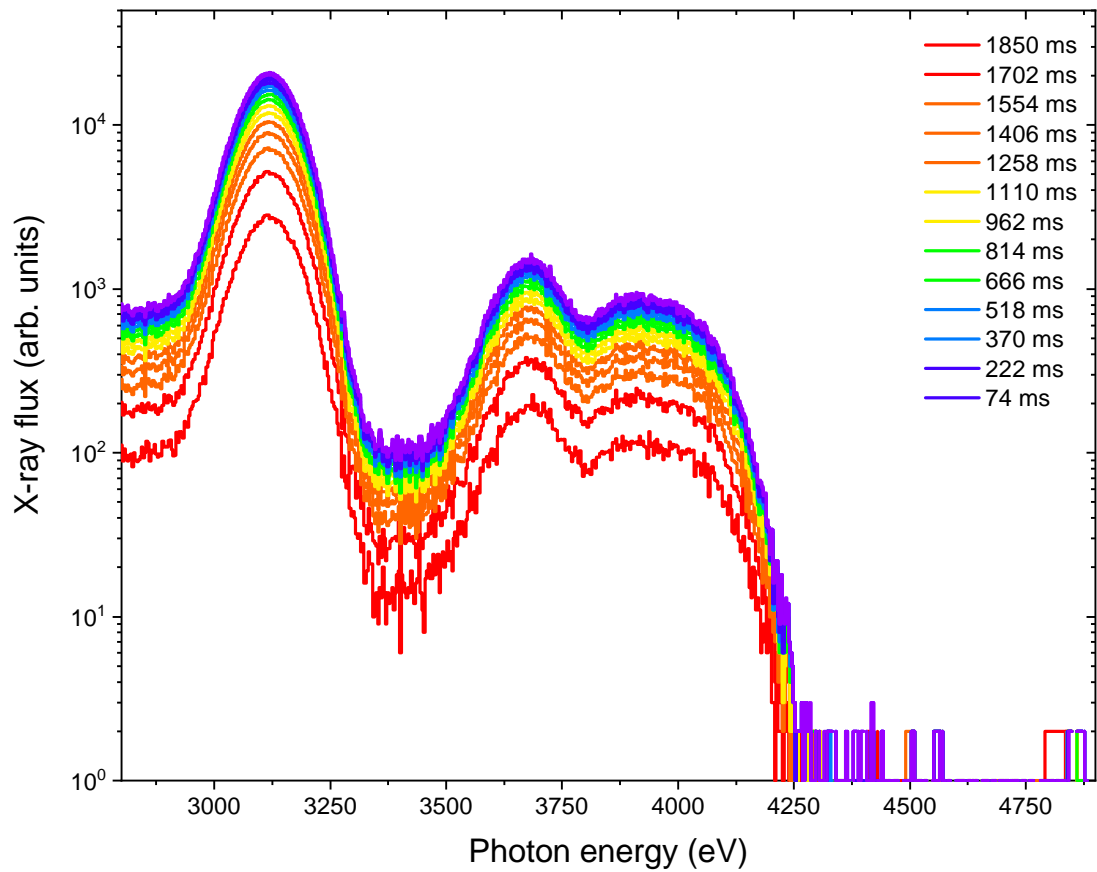
Figure 4.27: Temporal evolution of the CX spectrum from figure 4.23 for CX of Ar^{17+} with neutral argon and residual gas. The plotting is performed analogously to figure 4.26.
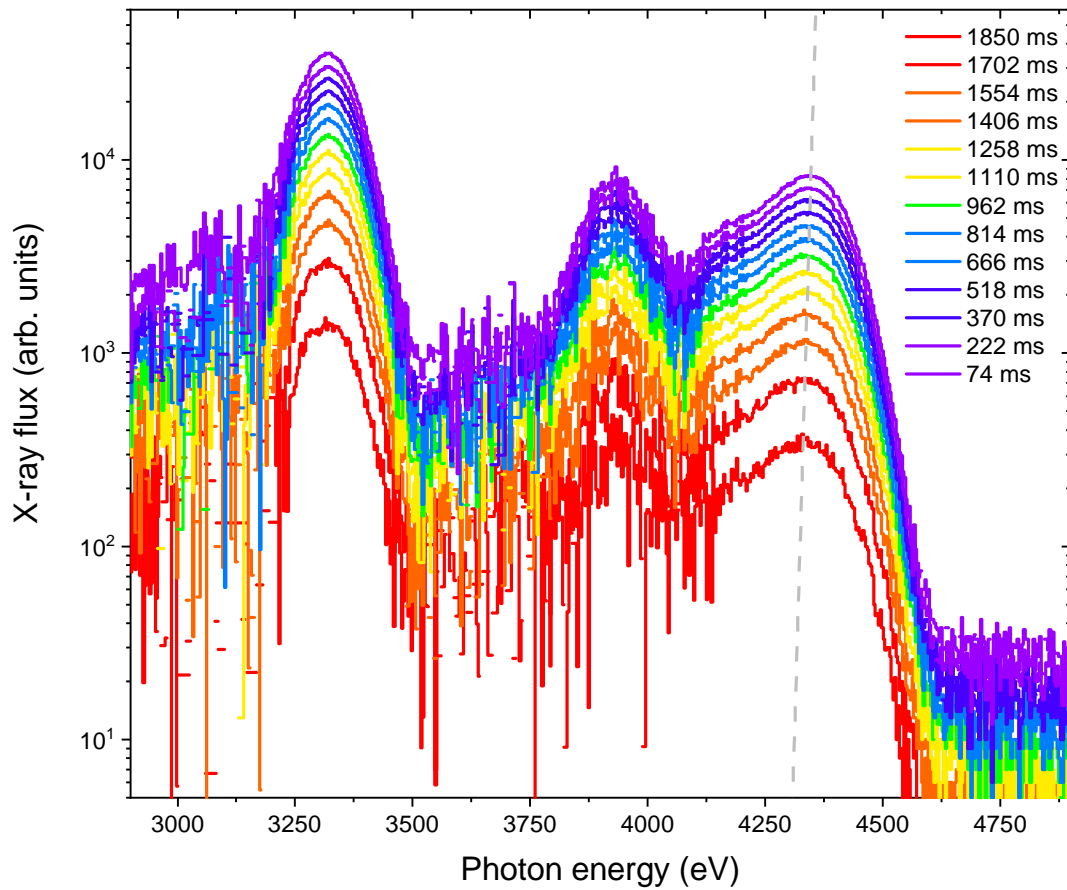
Figure 4.28: Temporal evolution of the CX spectrum of the pure contribution of Ar^{18+} with neutral argon and residual gas. For each temporal slice above and below the ionization threshold of Ar^{18+} from figures 4.26 and 4.27, respectively, the corresponding spectrum is normalized to the Ar^{16+} K_β transition with subsequent subtraction of both spectra. The dashed gray line indicates a shift of the higher energetic X-ray peak to lower energies with increasing time after switching off the electron beam.

4.3.2 Argon charge exchange at different axial trapping potentials

A systematic investigation of charge exchange of Ar^{18+} at different axial trapping potentials has been performed. The times of the electron-beam on mode and magnetic-trapping mode within the measurement cycle were modified with respect to the cycle described in section 4.3.1. Here the breeding time was extended to 6 s to get a higher yield of fully ionized argon ions. The magnetic-trapping cycle was decreased to 4 s since the exponential decay time is in the order of 0.4 s. The constant injection pressure of neutral argon in the second injection stage was between 1×10^{-7} mbar and 4×10^{-7} mbar and the electron-beam current 200 mA.

The charge exchange spectrum of $Ar^{18+} + Ar$ is presented as a function of the axial trapping potential V_0 above the ionization threshold for the production of fully-stripped argon in figure 4.29 for $V_0 = 3, 45, 100$ V and 500 V, and below threshold in figure 4.30 for $V_0 = 45, 100$ and 500 V, respectively. Trapping of ions below the ionization threshold with an electron-beam energy of 4.4 keV and a trap depth of 3 V was not possible.

For the K-shell transition in figure 4.30, no significant difference of the line intensities as a function of the axial trap depth can be observed. Only a slight increase of line intensities at ~ 800–1000 eV with shallower trapping potentials is noticeable. Since several of hundreds argon L-shell transitions for different charge states and K-shell transitions of other elements, i.g. oxygen, are present in this energy range, it was not possible to resolve them with the utilized X-ray detector. Although the investigation of L-shell transitions would be fruitful for the understanding of the radiative cascades from high Rydberg states, this subject will not be evaluated quantitatively within the frame of this work due to a lack of spectral resolution. Furthermore, the detector efficiency was roughly estimated by energy-dependent absorption properties of materials with not well-known thicknesses and varies strongly by orders of magnitudes in this energy range (compare to figure 3.20) which challenges an expressive analysis of the data. To remark is, that the spectrum was not corrected for the detector efficiency. For the K-shell transitions, a correction is not relevant because the efficiency is almost one in this energy range. However, other groups report signatures of iron L-shell CX of oxygen-like up to helium-like iron ions [25], high-resolution L-shell CX measurements of helium-like sulfur [71] and neon-like nickel [32].

In both spectra, the photons detected in the range between 1200 eV and 2900 eV have most-likely an origin in various M-shell transitions of lower charge states of residual barium and tungsten ions emitted from the cathode co-trapped with argon. Since the transitions are energetically close to each other and can not be resolved by the SDD, it results in a quasi-continuous band with enhanced count rate in this energy range.
In contrast to the measurement below the ionization threshold, an increase of hydrogen-like
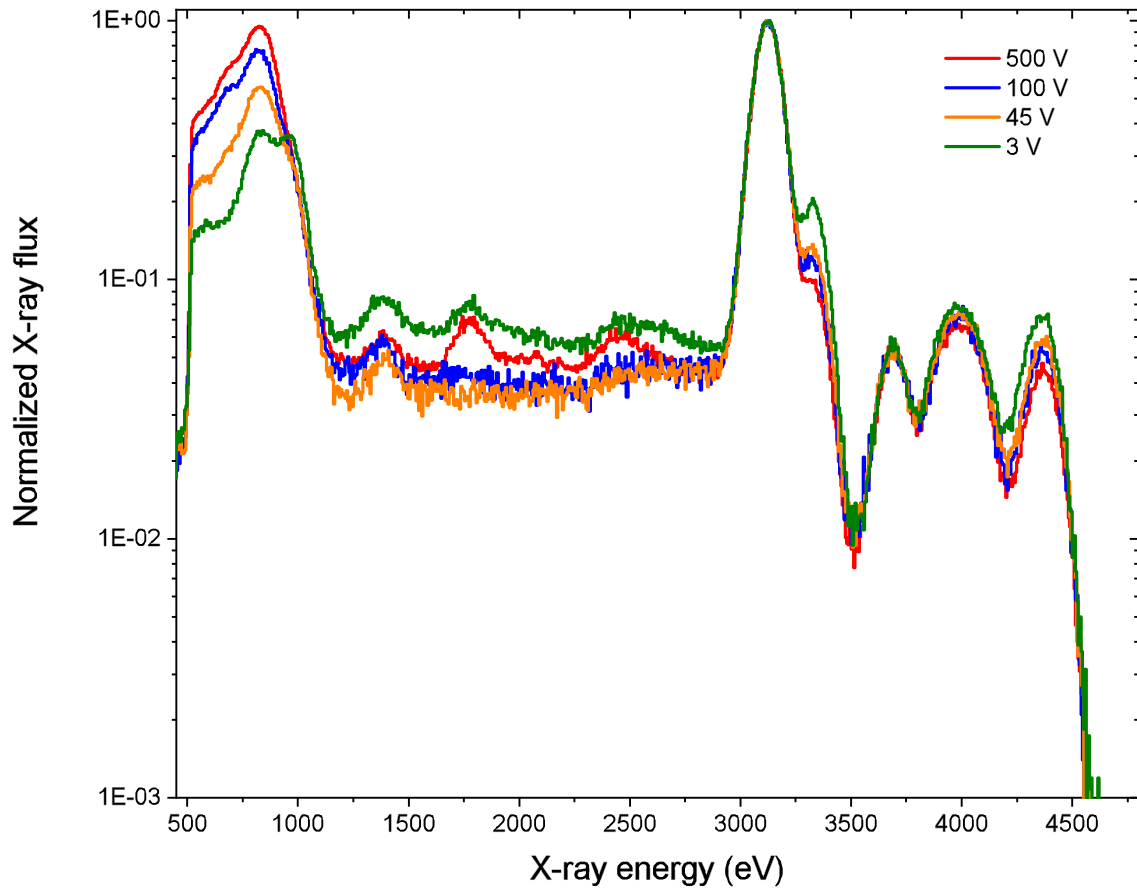
Figure 4.29: CX spectra of Ar^{18+} and Ar^{17+} with neutral argon at different axial trapping potentials between 3 V and 500 V in the full photon energy range covered by the X-ray detector and normalized to the Ly_α transition of Ar^{17+}. The structure at an X-ray energy of $\sim 900\,eV$ are $n_{CX} \to n = 2$ transitions of argon with a blend of emission lines from residual oxygen.
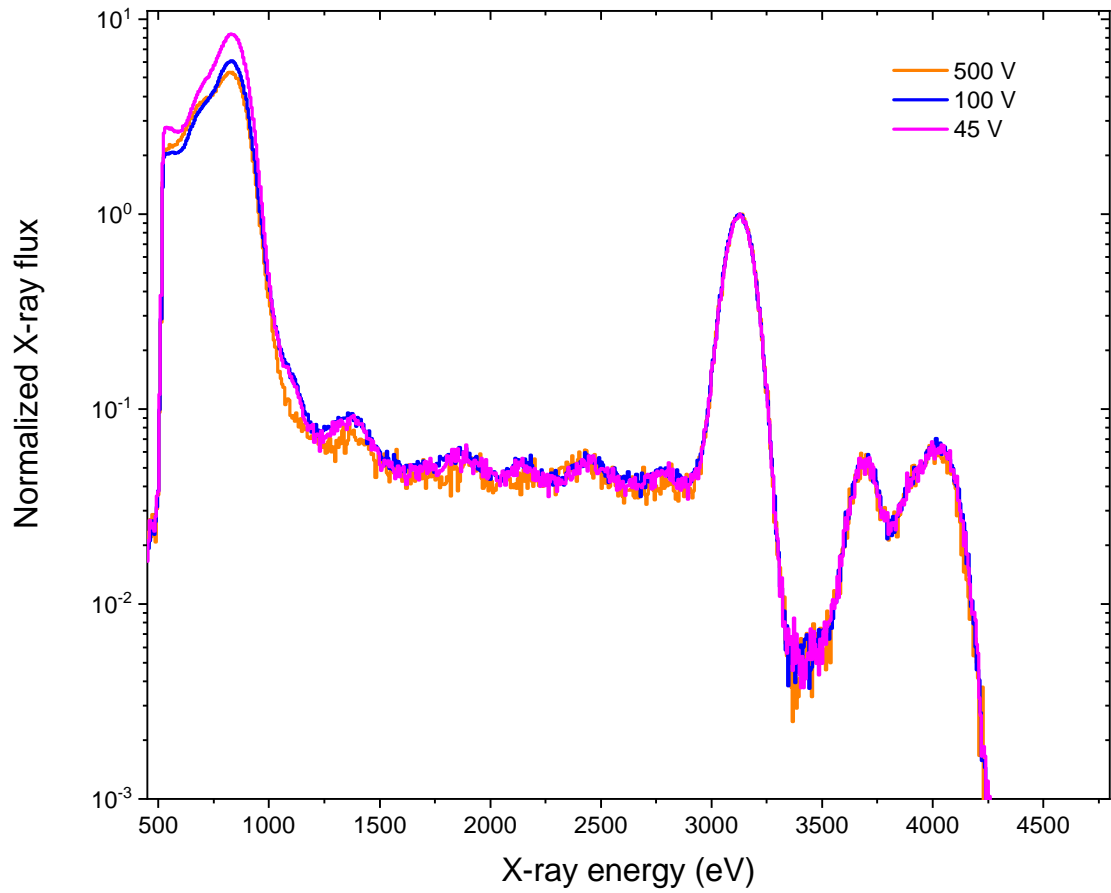
Figure 4.30: CX spectrum of Ar^{17+} and neutral argon below the ionization threshold for fully ionized argon at different axial trapping potential. The measurement scheme is performed analogously, as presented in figure 4.29.

line intensities after capture and an overall decrease of the line intensities at ~ 800–$1000\,\mathrm{eV}$ with shallower axial trap depths was observed above the ionization threshold in figure 4.29. Lower charged ions rather escape from shallow traps than higher charged ions, which could explain the decrease of intensity. The peak at $\sim 600\,\mathrm{eV}$ decreased with lower trap depths and an appearance of a peak at $\sim 940\,\mathrm{eV}$ was observed, which could be possibly assigned to transitions of hydrogen-like argon ions from $n \geq 5 \to n = 2$. For quantitative analysis, more systematic measurements and an X-ray detector with a higher spectral resolution like a microcalorimeter are required.

4.3.3 Comparison with charge-exchange models

First and foremost, the X-ray spectrum obtained for collisions of Ar^{17+} with a mixture of neutral argon and residual gas from figure 4.24 and the CX spectrum of $\mathrm{Ar}^{17+} + \mathrm{H}_2$ is compared to the multichannel Landau-Zener approach of FAC in figure 4.31.

The model assumes collisions with molecular hydrogen with an ionization potential of $15.42\,\mathrm{eV}$ at a collision energy of $40\,\mathrm{eV/u}$. The axial trap depth in the present measurements was $V_0 = 500\,\mathrm{V}$, corresponding to a collision energy of $E_{\mathrm{coll}} \approx 42\,\mathrm{eV/u}$ according to $E_{\mathrm{coll}} = 0.2qV_0$ [55]. The data can not be represented by the calculation. As already demonstrated in section 4.2.3, the FAC model for collisions of hydrogenic systems with neutral gas overestimates the relative intensity of the higher Rydberg transitions from $1sn$ with $n \geq 5$ to $1s^2$, and underestimates the K_β transition. The spectrum of $\mathrm{Ar}^{17+} + \mathrm{H}_2$ is in a better agreement with the MCLZ calculation, but the intensities of higher Rydberg transitions are overestimated by the model.

The helium-like hardness ratio $\mathcal{H}_{\mathrm{He}}$ is defined as the ratio of all transitions from $1sn$ with $n \geq 3$ to $1s^2$ and the K_α transition with $1s2l$ to $1s^2$. In this experiment, it was determined to $\mathcal{H}_{\mathrm{He}} = 0.137 \pm 0.001$ for $\mathrm{Ar}^{17+} + \mathrm{Ar}$ and res. gas and $\mathcal{H}'_{\mathrm{He}} = 0.140 \pm 0.004$ for $\mathrm{Ar}^{17+} + \mathrm{H}_2$ by fitting four Gaussians in total to the experimental spectrum and calculating the ratio of the areas of the peaks. The total error was calculated with an error propagation of the uncertainties of the corresponding single areas. According to the MCLZ calculation, the hardness ratio is $\mathcal{H}_{\mathrm{He}} = 0.171$, which is significantly higher than the experimental value. One influence could be the fact that only single-electron capture is considered by theory. A double capture with subsequent autoionization would decrease the most probable quantum number n in which the second electron is finally captured, leading to a decrease of the hardness ratio. However, it is doubtful if this effect can solely cause a discrepancy of $\sim 25\,\%$.

The charge exchange spectrum from figure 4.25 of the pure contribution of Ar^{18+} with neutral argon and residual gas and the comparison to the MCLZ approach of the Kronos code with atomic hydrogen as a target is shown in figure 4.32 for different distributions
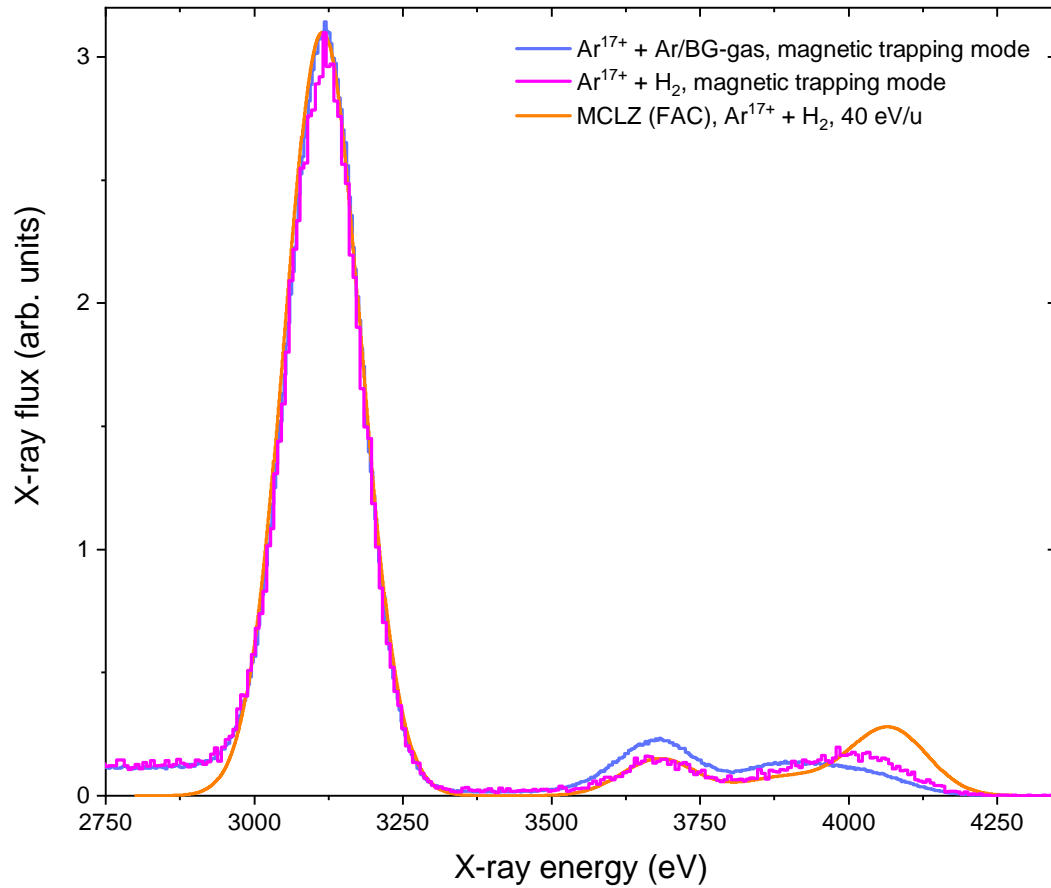
Figure 4.31: Charge exchange spectrum of Ar^{17+} with neutral argon and residual gas in magnetic-trapping mode is illustrated in blue. The magenta-colored curve represents the CX measurement of Ar^{17+} with a gas pulse of molecular H_2. The synthetic CX spectrum calculated by the MCLZ approach of FAC with molecular hydrogen as a target is shown in orange.

of angular momenta at a collision energy of 25 eV/u. The synthetic spectra assuming a low-energy, separable, and modified low-energy l-distribution are illustrated by solid green, blue, and yellow lines normalized to the Ly_α transition, respectively. The ab-initio calculation performed with FAC for a low-energy l-distribution is shown as a dashed curve. The synthetic spectra generated with Kronos and FAC are in good agreement with each other. Only a slight difference in the intensity of the transition at ~ 4380 eV can be observed, which could be explained by slightly different theoretical transition rates. To note is, that none of the assumed l-distributions of the MCLZ calculations can describe the experimental results satisfactorily. The model assuming a low-energy distribution of angular momenta overestimates the intensity of the higher Rydberg transitions to the ground state. The separable distribution, by contrast, underestimates the relative intensity Ly_β transition. The modified low-energy distribution calculates, in general, a comparably low contribution of transitions from $n \geq 2 \rightarrow n = 1$. Furthermore, the peaks at higher X-ray energies are slightly shifted by ~ 30 eV towards higher energies with respect to the experiment, indicating an overestimation of the maximum quantum number n in which the electron is captured. The experiment indicates a peaking around ~ 4346 eV corresponding to a $n = 7, 8 \rightarrow n = 1$ transition, whereas the maximum of the peak of the calculation is around ~ 4375 eV corresponding to $n = 10 \rightarrow n = 1$.

The inset on the right-hand side of the figure illustrates the reconstruction results of the l-distribution for a given principal quantum number $n = 9$ by the FAC cascade model. The blue-colored bars represent the reconstruction without any restrictions to the fitting parameters, particularly all angular momenta $l = 0, \ldots 8$ for $n = 9$ are included. Since the energy resolution of the SDD detector did not suffice to resolve at least nine lines, the fit is overdetermined with nine free parameters. By restricting the number of allowed angular momenta up to $l = 5$, a more reliable reconstruction can be performed. The exclusion of higher angular momenta is legit since the relative fraction decreases with higher l.

Furthermore, a higher population of higher angular momentum states is expected for comparably high collision energies, which is not given in an EBIT. However, the reconstruction results for $l = 0 \ldots \ldots 5$ are plotted as magenta-colored bars in the inset with the corresponding fit, shown as a solid, magenta-colored curve overlayed with the data. The results of both reconstruction approaches do not differ within the error bars, which are estimated by a Monte-Carlo approach. Here the standard deviation of reconstruction results for 20 spectra with a slight randomly distributed variation in the X-ray flux is considered as the uncertainty. To notice is a weak agreement with the separable angular momentum distribution assumed by the MCLZ model. The population of the $l = 0$ and $l = 2$ state is underestimated by the MCLZ model in comparison to the FAC reconstruction, whereas the relative fraction of the $l = 1$ and $l = 4$ state is slightly higher. Since the separable l-state distribution depends explicitly on the charge and not the principal quantum number n,
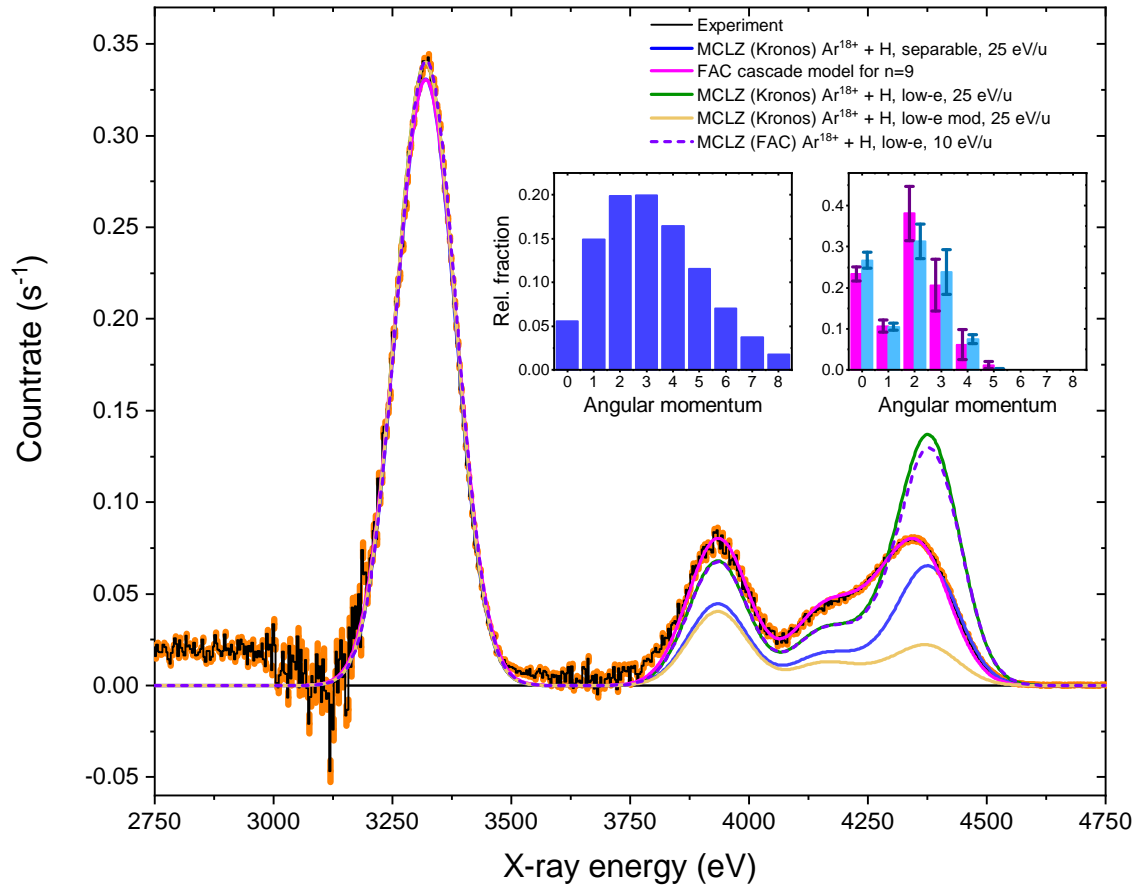
Figure 4.32: Comparison between the experimentally obtained CX spectrum of Ar^{18+} interacting with neutral argon and residual gas. The MCLZ calculations performed by Kronos for collisions of Ar^{18+} with atomic hydrogen assuming three different l-distributions are shown as solid green, blue, and yellow curves, respectively. The MCLZ spectrum generated with FAC is shown as a dashed curve. The inset on the left-hand side illustrates the relative fraction of angular momenta for the separable l-distribution. The inset on the right-hand side represents the reconstruction results of the FAC cascade model for inclusion of all possible angular momenta as blue and a restriction up to $l = 5$ as magenta-colored bars.
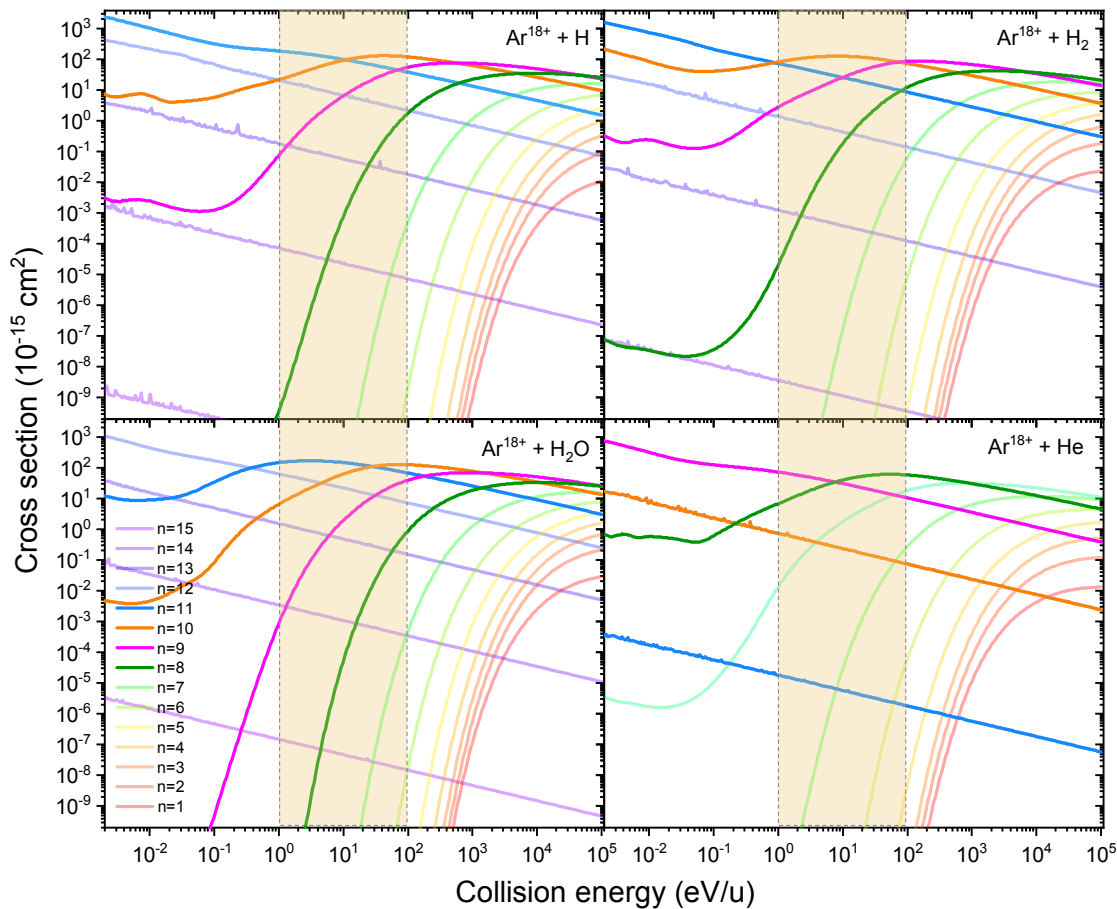
Figure 4.33: Charge exchange cross-section for collisions of Ar^{18+} with different neutral targets and capture into different principal quantum number states n as a function of the collision energy between projectile and target. The yellow rectangle illustrates the region of typical collision energies in an EBIT. The calculations are performed with the Kronos code [124].

the relative fractions are not affected by electron capture into several principal quantum number states. However, about the physical interpretation of the discontinuity of the distribution, it can be only speculated and will not be discussed further.

In figure 4.33, the absolute CX cross-sections obtained by MCLZ calculations of Kronos for electron capture from different targets into different n-states are plotted as a function of the collision energy between the fully ionized Ar^{18+} and the neutral target. The yellow-colored rectangle indicates the region of collision energies typically predominant in an electron beam ion trap. For neutrals with low ionization energy, the electron capture occurs mostly into the $n = 10$ and $n = 11$ state. For higher ionization potentials, the electron is captured into lower principal quantum number states of $n = 8$ and $n = 9$.

In figure 4.34 the synthetic MCLZ CX spectra utilizing the corresponding n-resolved

cross-section from figure 4.33 with the assumption of a separable distribution of angular momenta is shown for atomic hydrogen, molecular hydrogen, water molecule, and helium as a neutral target for different collision energies in a range between $2.5 \, \mathrm{eV/u}$ and $2500 \, \mathrm{eV/u}$. Since MCLZ provides only n-resolved cross sections for CX of fully ionized projectiles, the l-distribution has to be multiplied to the CX cross-section. The choice of this distribution does not affect the overall intensity ratios of the $n_{\mathrm{CX}} \to n = 1$ transitions. Different neutral targets result only in a slight change of the most probable principal quantum number n, in which the electron is captured, which affects the centroid position of the peak at higher X-ray energies. This is due to different polarizabilities of the neutral species since an incoming polarization potential is assumed by the MCLZ approach, as described by equation 2.47. With increasing collision energy, the peak of the distribution of the most probable state n shifts to lower values. Since the typical range of collision energies in an EBIT is in the order $\sim 1 \, \mathrm{eV/u}$ to $\sim 100 \, \mathrm{eV/u}$, the expected shift can not be observed within the resolution of the X-ray detector.

However, the main composition of the neutral target gas was represented by argon atoms in this experiment, but it is not provided as a donor species in the database of the MCLZ calculation. Since the ionization energy for neutral argon is $15.76 \, \mathrm{eV}$, molecular hydrogen with an ionization potential of $15.42 \, \mathrm{eV}$ can be instead utilized as a collision partner in the MCLZ calculation. However, the most probable principal quantum number in which the electron is captured after interaction with molecular hydrogen is $n = 10$ in the typical collision energy range in an EBIT, which was not observed in the experiment. One possible explanation could be a significant amount of residual gas atoms with comparably high ionization energy, like helium, which would lead to a population of lower principal quantum number states.

4.3.4 Argon charge exchange with different targets

In figure 4.35, the charge exchange spectra of fully ionized argon with different neutral targets are compared. The interaction with a mixture of residual gas in the magnet with a pressure of $3 \times 10^{-9} \, \mathrm{mbar}$ and neutral argon with an axial trapping potential of $500 \, \mathrm{V}$ as shown in figure 4.32 is displayed in a) and the interaction with a pulse of H_2 with an axial trap depth of $1000 \, \mathrm{V}$ in b). Technical details on the pulsed injection system can be extracted from the bachelor thesis [13], which has been supervised within the scope of this work. CX between Ar^{18+} and neutral argon in represented in d) with a residual magnet pressure below a measurable range of $< 5 \times 10^{-10} \, \mathrm{mbar}$ at an axial trap depth of $500 \, \mathrm{V}$. For the measurement of fully-stripped argon with neutral neon, the argon gas bottle was removed and replaced by a bottle of neon. The argon in the injection system and the magnet chamber remained for a certain amount of time allowing for the production of
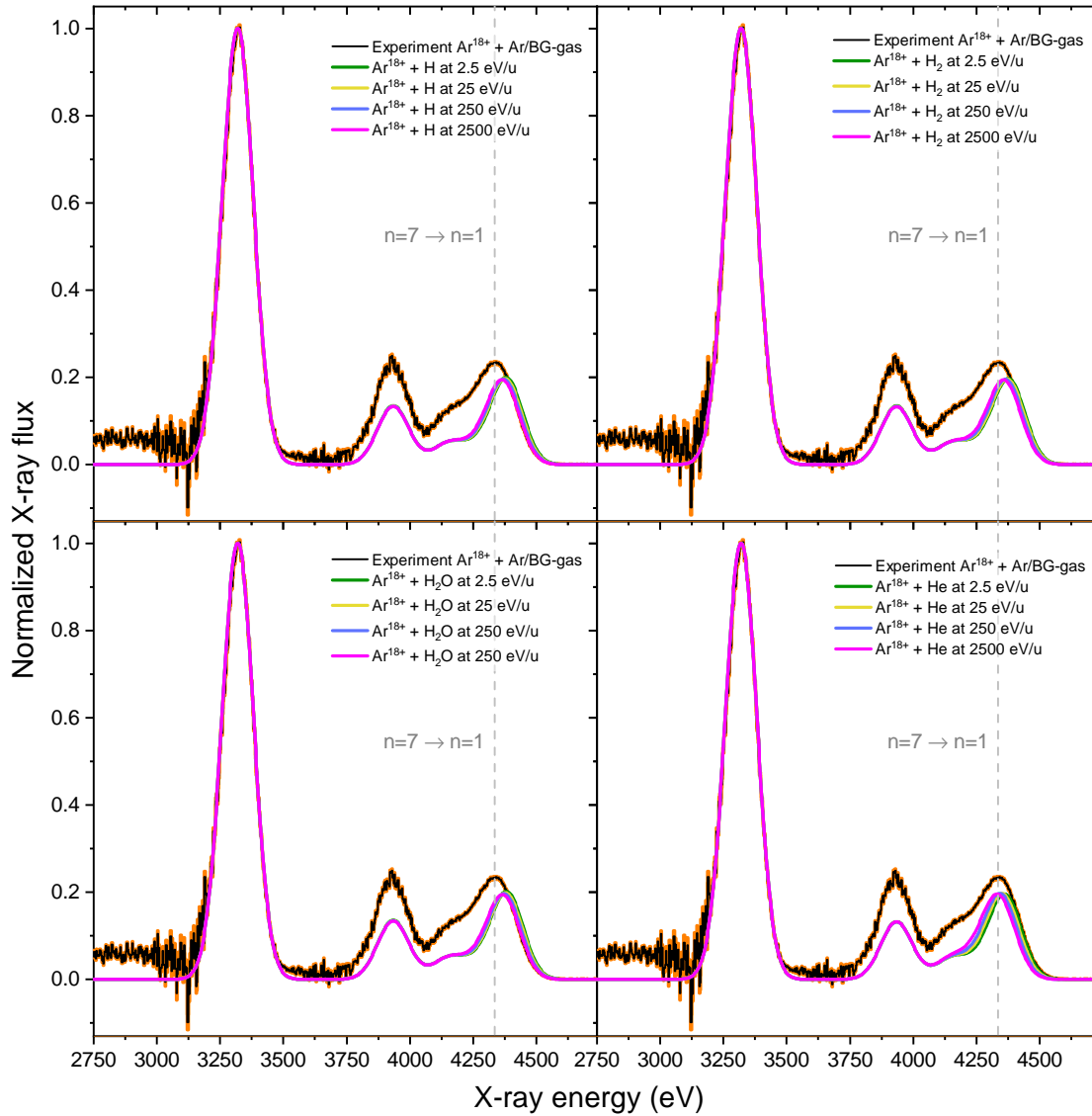
Figure 4.34: Synthetic CX spectra for collisions of Ar^{18+} with different neutral targets and a separable l-distribution based on MCLZ calculation performed by Kronos. The intensities are normalized to the Ly_α transition of hydrogen-like argon. In each panel, the dependence of the resulting CX spectrum for each target is illustrated for different collision energies between $2.5\,eV/u$ and $2500\,eV/u$. For comparison, the experimental result is shown in each panel. The vertical grey dashed line represents the transition energy from $n = 7$ to $n = 1$ of $4336.1\,eV$ calculated with FAC as a reference.

Ar^{18+} projectiles which interacted with a constant inflow of neutral neon. The trap content was therefore a mixture of neon and argon. This measurement was performed with the same settings as in the measurement of a). For determination of the ratio of the number density of neon ions and argon ions, the intensity of the radiative recombination lines during the electron-beam on mode into the $n = 1$ level of fully ionized argon and neon ions, respectively, was compared to radiative recombination cross-sections calculated by means of the flexible atomic code for an electron-beam energy of 6000 eV. The intensity $I_{RR}^i \propto n_i \sigma_{RR}$ is proportional to the product of the number density n_i and the RR cross-section of the corresponding species i. The relative fraction of the number density of neon and argon ions is therefore

$$\frac{n_{Ne}}{n_{Ar}} = \frac{I_{RR}^{Ne} \sigma_{RR}^{Ar}}{I_{RR}^{Ar} \sigma_{RR}^{Ne}} = \frac{I_{RR}^{Ne}}{I_{RR}^{Ar}} \frac{3.7 \times 10^{-24}\,\text{cm}^2}{5.1 \times 10^{-25}\,\text{cm}^2} \approx 6.5. \tag{4.6}$$

The relative fraction of argon ions in the gas mixture is determined to 14 %. By subtraction of the corresponding fraction of spectrum d) for collisions of Ar^{18+} with neutral argon from the mixed spectrum, the pure contribution of the interaction between Ar^{18+} and neon can be extracted. The result is shown in c).

The electron-beam energy for the production of fully ionized argon was 6015 eV for the measurement of spectra a), c) and d) and 8010 eV for spectrum b). The beam energy below this ionization threshold for the production of a maximum achievable hydrogenic charge state was 4420 eV for normalization and subtraction of this contribution to extract the pure spectrum of CX of fully-stripped argon as described in section 4.3.1. The higher electron-beam energy does not change the overall shape of the CX spectrum. The reason for this choice was a higher yield of Ar^{18+} ions in the second measurement campaign where spectrum b) was acquired with a pulsed gas jet during MTM of molecular hydrogen.

Since no significant dependence of the trap depth on the ratio of Lyman-α and higher Rydberg transitions was observed, it is legit to compare the charge exchange spectrum a) to b), c) and d).

For each spectrum, the cascade model described in section 2.3.4.5 with a population of the most probable principal quantum number state $n = 9$ is fitted to the data and represented as a solid magenta-colored line. The corresponding relative fractions of the l-state population determined by the coefficients of the spectral basis vectors are represented as a magenta-colored bar chart. For comparison, the synthetic spectrum calculated by an MCLZ method implemented in the Kronos code [124] with a collision energy of 25 eV/u and with a separable distribution (compare equation 2.57) for spectrum a) and b) and with a low-energy distribution (equation 2.56) for spectrum c) and d) is plotted in light blue. The corresponding relative fractions of the angular momenta are illustrated as bar charts with the respective color code. To remark is, that the number of free fitting parameters of the FAC cascade model exceeds the number of resolved spectral lines. Thus,
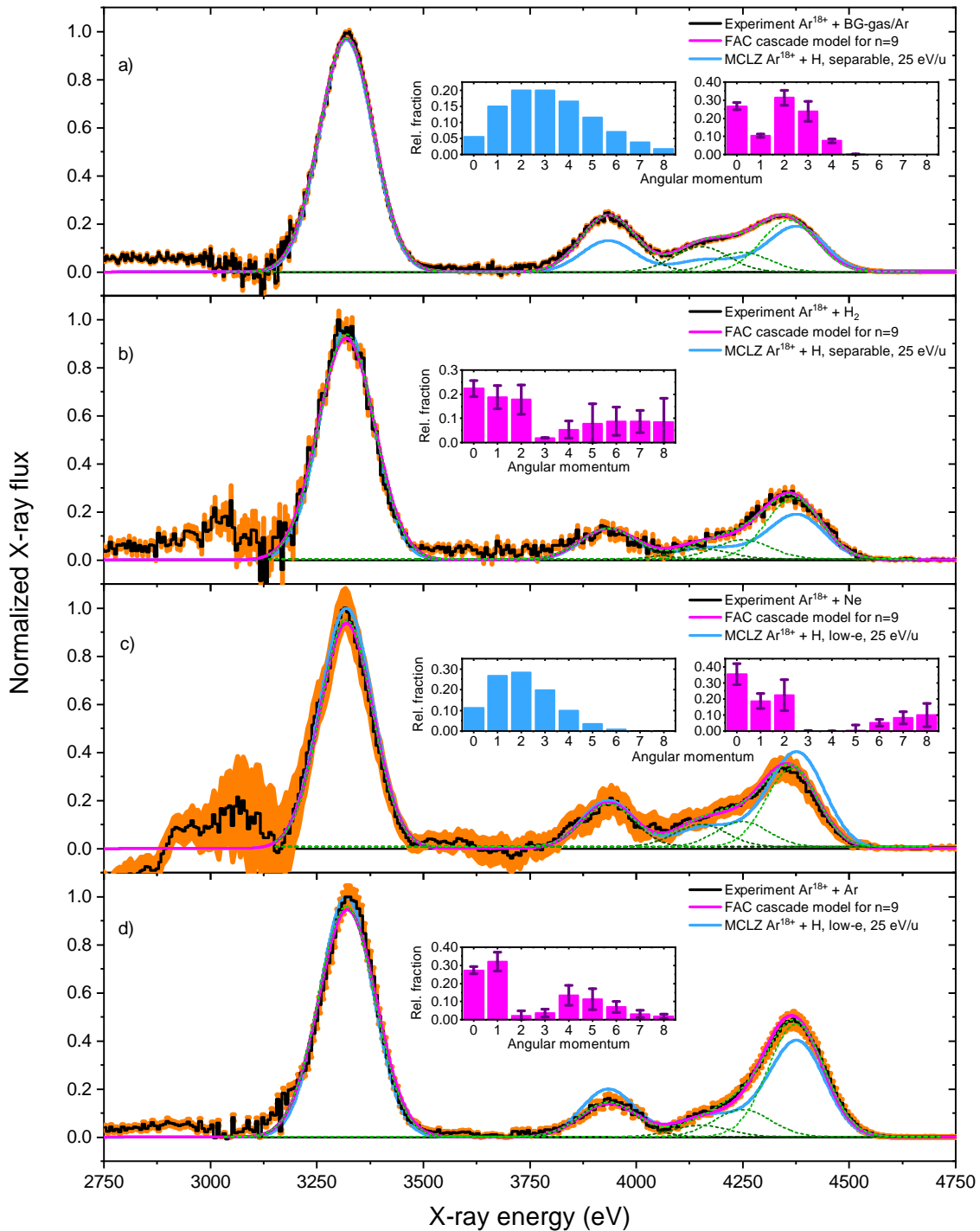
Figure 4.35: Charge exchange spectra of collisions of Ar^{18+} with a mixture of argon and residual gas (a)), with molecular hydrogen (b)), with neon (c)) and with neutral argon (d)). The magenta-colored solid line represents the fit according to the radiative cascade model described in section 2.3.4.5 with the corresponding relative fraction of the population of angular momenta shown as a magenta-colored bar chart. The light-blue curve is a model calculated by an MCLZ approach with Kronos for different l-distributions.

Table 4.2: Extracted hardness ratios and Lyman-α to Lyman-η ratios from figure 4.35 for CX between Ar^{18+} and different neutral targets.

	res. gas&Ar	H$_2$	Ne	Ar
$\mathcal{H}$	0.656 ± 0.001	0.54 ± 0.02	0.75 ± 0.08	0.804 ± 0.030
Ly$_\alpha$/Ly$_\eta$	4.515 ± 0.006	3.70 ± 0.13	3.0 ± 0.3	2.05 ± 0.08

the fit is overdetermined, and the discontinuities in the extracted relative fractions of angular momenta will not be discussed further. Only a qualitative tendency of the relative population can be examined. For each spectrum five Gaussians, plotted as green-colored dashed lines are fitted to the data for determination of the hardness ratio $\mathcal{H}$ which is defined as the ratio of the flux F of highly excited transitions with $n \geq 3 \rightarrow n = 1$ to the flux of Lyman-α with $n = 2 \rightarrow n = 1$:

$$\mathcal{H} = \frac{\sum_{i=3}^{\infty} F_{n \rightarrow 1}}{F_{n=2 \rightarrow n=1}}, \tag{4.7}$$

where F represents the flux of the corresponding transition. The corresponding error bars are determined by the uncertainty of the areas of the Gaussians. The hardness ratio is a non-monotonic function of collision energy with either a maximum or a minimum at a specific energy, dependent on the projectile species [53]. This energy dependence could be utilized as a diagnostic tool for ion velocities in astrophysical environments like solar flares [23].

The determined hardness ratios are listed in table 4.2. Additionally, the ratio of Lyman-α and Lyman-η is shown since the hardness ratio solely does not represent the shape of the spectrum, especially the qualitative l-distribution. A lower Ly$_\alpha$/Ly$_\eta$ indicates a capture predominantly into lower angular momentum states.

In figure 4.36, the hardness ratios from table 4.2 are plotted as a function of the ionization potential of the corresponding target. The values calculated by an MCLZ approach utilizing the Kronos code are presented in light blue for all available neutral targets for a collision energy of 45 eV/u and with a low-energy distribution of angular momenta according to equation 2.56. Additionally, all known measurements of CX in an EBIT of Ar^{18+} with A, where A is the target, are depicted. The green triangle represents the CX measurement of Ar^{18+} and neutral argon [12], the dark cyan colored star the measurement of Ar^{18+} and molecular hydrogen [109] and the orange triangle [24], as well as the magenta-colored lozenge [32] Ar^{18+} and neutral argon. The latter two measurements were performed at the LLNL-EBIT [26] equipped with a microcalorimeter for high-resolution detection of X-rays [110]. The hardness ratios from collisions of Ar^{18+} and molecular hydrogen, neutral argon and neutral neon determined in this work are shown as black circles. From this plot, no
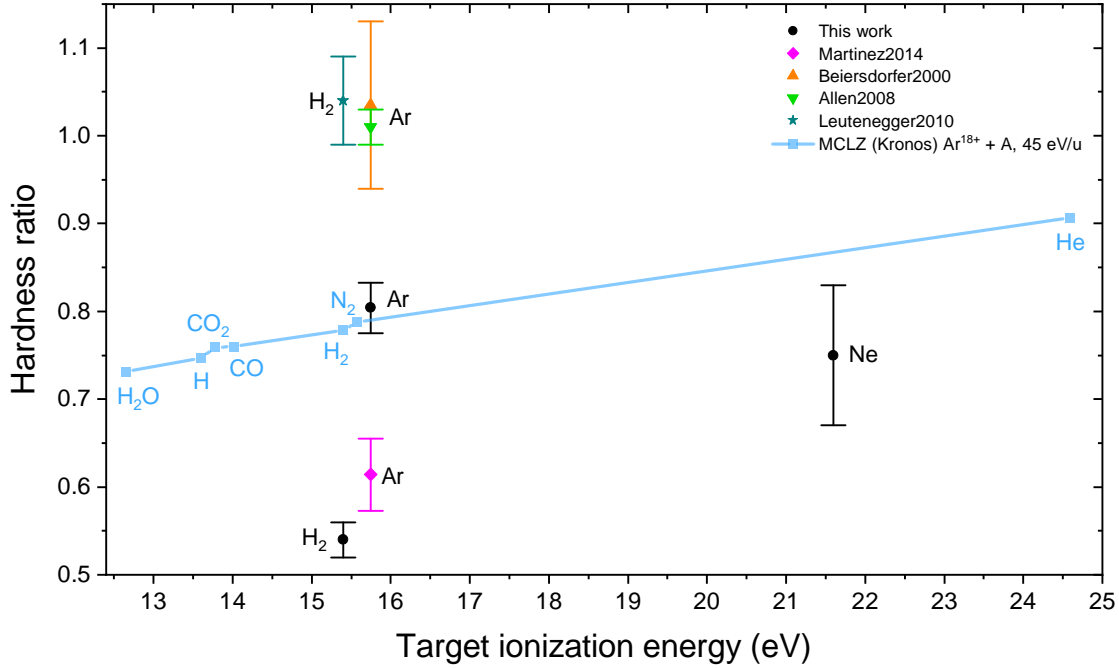
Figure 4.36: Hardness ratios for collisions between Ar^{18+} and different targets as a function of the ionization potential of the corresponding target. All measurements were obtained in the magnetic-trapping mode in an EBIT. The calculation was performed with an MCLZ approach utilizing the Kronos code for a collision energy of $45\,\mathrm{eV/u}$ with a low-energy l-distribution.

obvious scaling of the hardness ratio with the ionization potential of the target can be extracted.

Furthermore, the four CX measurements of Ar^{18+} with Ar, although performed at similar collision energies between $10\,\mathrm{eV/u}$ and $45\,\mathrm{eV/u}$, the values for $\mathcal{H}$ determined in this work and [32] differ significantly from [24, 12]. This discrepancy already indicates unknown systematic effects in these measurements. The axial trap depths used in this experiments are in the order of $45\,\mathrm{V}$ up to $1000\,\mathrm{V}$, which determines the collision energies. On the other hand, the axial trap depth had a small effect on the change of the hardness ratio in this experiment. A similar observation is reported in [12].

Additionally, the hardness ratios obtained by different Ar^{18+} + Ar CX measurements in magnetic trapping mode inside an EBIT as well as in extraction mode are presented as a function of the collision energy between projectile and target in figure 4.37. For the measurements performed within the frame of this work, the collision energy E_{coll} is estimated by the semi-empirical formula

$$E_{\mathrm{coll}} = 0.2qV_0 \tag{4.8}$$
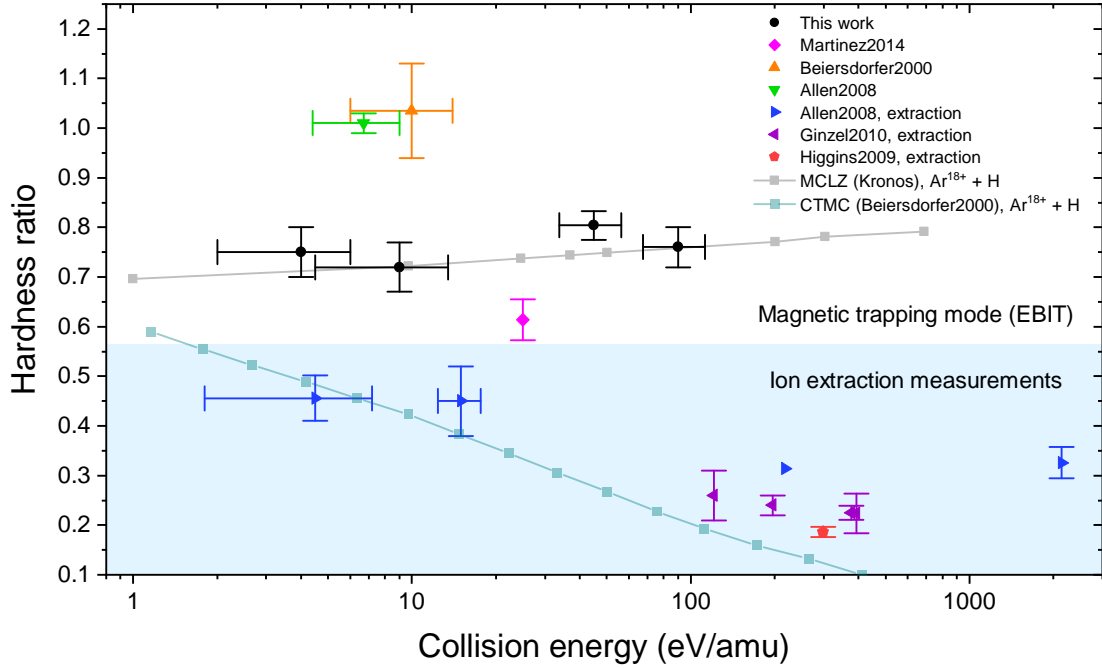
Figure 4.37: Hardness ratio as a function of collision energy between projectile and target obtained from $Ar^{18+} + Ar$ CX measurements in magnetic-trapping mode and extraction mode (light-blue box). An MCLZ calculation for $Ar^{18+} + H$ with a low-energy l-distribution is represented in gray and a CTMC calculation [24] in cyan.

given in [55], where q represents the charge of the ion species and V_0 the axial trapping potential. The corresponding error bars are estimated conservatively to 25 % for higher axial trapping potentials and to 50 % for lower voltages due to uncertainties in the power supply voltages and electric field penetrations.

All extraction measurements are highlighted inside the light-blue box. The theoretical hardness ratio shown in grey is calculated by an MCLZ method utilizing the Kronos code for collisions of fully ionized argon and atomic hydrogen with a low-energy distribution of angular momenta. First of all, a significant deviation between the measurements inside an EBIT and between extracted ions is conspicuous. Furthermore, the hardness ratios in magnetic-trapping mode do not show a systematic dependence on the collision energy. Second, the theory predicts an increase of $\mathcal{H}$ with increasing collision energy, which contradicts the observations of a decreasing hardness ratio. Another model based on classical-trajectory Monto-Carlo calculations [24], plotted as a dark cyan line, predicts a decrease of the hardness ratio with increasing collision energy.

Besides the discrepancy of similar EBIT experiments among each other, a significant difference between EBIT and extraction measurements, a non-trivial scaling with the ionization potential of the target and the neglection of multi-electron capture another

issue is reported in [109]. A simultaneous charge exchange measurement with co-trapped fully ionized argon and phosphorous ions with molecular hydrogen was performed. The hardness ratio of the phosphorous Lyman-series was higher by a factor of two compared to the argon Lyman-series.

In conclusion, further systematic experimental and detailed quantum-mechanical investigations of target and projectile are crucial in order to understand the nature of the charge exchange process.

4.3.5 Discussion of possible error sources

4.3.5.1 Magnetic field

A technical difference between this experiment and the measurements presented in [12, 24, 32] is the magnetic field of the EBIT in the trap center. The EBIT used in [12, 24, 32] has a magnetic field of $3\,\mathrm{T}$, and the EBIT utilized in this work a field of $6\,\mathrm{T}$. The estimation of the upper-velocity limit of the cyclotron motion in the magnetic field of argon ions with charge $q = 18$ and atomic mass $m = 40$ by consideration of a lower limit of the cyclotron radius of $r = 50\,\mathrm{\mu m}$ yields an orbital velocity

$$v = \frac{q}{m}rB \tag{4.9}$$

in the order of $10\,\mathrm{km/s}$ for the $B = 6\,\mathrm{T}$ magnetic field. The typical axial velocity due to the axial trapping potential well is in the order of $100\,\mathrm{km/s}$. Since no strong dependence of the overall shape of the X-ray spectrum on the collision velocity in this energy range is expected, the contribution of the velocity due to the motion in a magnetic field is negligible. A decrease of the magnetic field by a factor of two had no significant effect on the overall shape of the CX spectra.

4.3.5.2 Switching off the electron beam

After switching off the electron beam, the initially compressed ion cloud expands abruptly due to Coulomb repulsion of the positive charges, since the radial potential of the negative space charge of the electron beam vanishes. This Coulomb explosion could result in an increase in the kinetic energy of the ions. The energy-release can be estimated by the negative space charge of the electron beam, which was typically in the order of $\sim 300\,\mathrm{eV}$. The conversion of this potential energy to the kinetic energy of the ions leads to an increase of the kinetic energy of $\sim 25\,\mathrm{eV/u}$, which is not sufficient to explain the significant discrepancies. On the other hand, it has been experimentally shown, that switching off the electron beam requires $\sim 300\,\mathrm{\mu s}$, which is comparably long with respect to the orbital period of the cyclotron motion in the order of $t = 1/f_{\mathrm{C}} \approx 1/40\,\mathrm{MHz} = 25\,\mathrm{ns}$ with the

cyclotron frequency f_C. Thus, this process can be considered as adiabatic and no heating should occur. Additionally, the ion cloud is evaporatively cooled by escaping hot ions from the trap. However, neither the heating nor the cooling of the confined plasma can cause the required difference in the collision velocity in order to explain the discrepancies.

4.3.5.3 Collision energy

According to the MCLZ calculation, a difference of several orders of magnitudes in the collision energy is necessary in order to explain the discrepancies in the hardness ratios. Since the maximum applicable axial trapping potential is $3000\,\text{V}$ in this setup, the maximum difference in the collision energy would be in the order of $\sim 300\,\text{eV/u}$.

4.3.5.4 Charge exchange with singly-charged ions

Another possible effect could be the charge exchange between singly charged ions and highly charged ions resulting from the primary CX of highly charged ions and neutrals. To estimate the thermal energy required to overcome the Coulomb barrier, the moment of the electron transfer is considered. Directly after this transfer, an Ar^{16+} and an Ar^{2+}, separated by ~ 8 atomic units, remain. The Coulomb potential between both ions is in the order of $V_{\text{Coulomb}} \approx 70\,\text{eV}$. The typical thermal energy of the ions in magnetic-trapping mode is sufficient to overcome this barrier. This could result in the population of different n-states and l-states than for electron capture of neutrals. However, the maximum number of singly charged ions is equal to the number of highly charged ions after the primary CX. Thus, the number density of singly charged targets is negligible compared to the neutral-gas density in the interaction region. Therefore, this effect can be considered as negligible.

4.3.5.5 Residual gas

The pressure in the magnet chamber was in the extreme case in the order of $3 \times 10^{-9}\,\text{mbar}$, measured with an ionization gauge located at room temperature, corresponding to a particle density of $\sim 1 \times 10^6\,/\text{cm}^3$ in the cryogenic region. The target gas pressure in the second gas injection stage is typically in the order of $\sim 3 \times 10^{-7}\,\text{mbar}$. From geometrical considerations, the particle density of the target gas in the interaction region of the trap is $\sim 6 \times 10^7\,/\text{cm}^3$, which is 1.5 orders of magnitude higher than the residual gas density. The difference of the hardness ratios in the two CX measurements with neutral argon as target gas and with a mixture of argon and residual gas, respectively, is $19\,\%$, which could be conceivably explained by the amount of the contamination. Since in subsequent measurements the residual gas pressure improved to less than $5 \times 10^{-10}\,\text{mbar}$ in the magnet chamber, the contribution of possible contaminations is even smaller by

one order of magnitude. Thus, this effect can be considered as negligible for relatively low residual gas pressures in the EBIT.

4.3.5.6 Ionization potential

A trivial scaling of the hardness ratio with the ionization potential was not found, although the MCLZ theory predicts a steady increase with higher ionization energies for single-electron capture. Furthermore, other publications report CX of Mg^{12+} with different neutral targets [110], measured with a microcalorimeter. The hardness ratio extracted from the CX spectrum of Mg^{12+} + He was higher by a factor of two compared to collisions with H2, CO_2, and Ne. A significant difference in the hardness ratio is also observed with two different bare projectiles and neutral helium [109]. This anomaly is still not fully understood, and further sophisticated charge exchange models are required in order to investigate this collision process.

4.4 Charge exchange in highly charged oxygen

4.4.1 X-ray measurements

Since oxygen ions are highly abundant in solar flares, interacting with neutral matter, the spectroscopic investigation of the charge exchange process for this ion species is of great interest to the astrophysical community. A similar measurement procedure, as presented in section 4.1.2, was performed for charge exchange measurements in the X-ray regime for highly charged oxygen with neutral O_2. The total switching cycle of the electron beam was $10\,\mathrm{s}$ with $8\,\mathrm{s}$ in beam-on mode and $2\,\mathrm{s}$ in magnetic-trapping mode. The electron-beam current was $200\,\mathrm{mA}$ at a nominal beam energy of $1.72\,\mathrm{keV}$, above, and $1.02\,\mathrm{keV}$, below the ionization threshold for the production of fully ionized oxygen in this measurement. The real electron-beam energy was reduced by the negative space charge of the electron beam below $871.3\,\mathrm{eV}$, which is required for the production of O^{8+}. An axial trapping potential of $550\,\mathrm{V}$ and an injection pressure of $2 \times 10^{-7}\,\mathrm{mbar}$ in the second injection stage was utilized. A projection onto the photon energy axis of the spectrum in the MTM above the ionization threshold is illustrated in light blue in the top panel of figure 4.38 and red below the threshold. The energy-dependent intensity was corrected for the estimated detector efficiency described in chapter 3.3.8.1.

After normalization to the helium-like K_α transition, which is present in both spectra, the pure hydrogen-like contribution can be extracted after subtraction. The acquisition time and the count rate in the measurement below the ionization threshold were much lower; thus, the number of detected events had to be multiplied by a factor of 1760. The statistical uncertainties are represented in shaded colors. The resulting spectrum is shown

in the bottom panel of figure 4.38. The $\text{Ly}_\alpha, \text{Ly}_\beta$, and $\text{Ly}_{\gamma,\delta,\dots}$ transitions are represented by Gaussian fits in blue, orange, and green, respectively.

Since the roughly estimated detector efficiency described in chapter 3.3.8.1 could deviate significantly from the actual efficiency in the investigated energy regime, no quantitative analysis concerning intensity ratios will be performed.

If the electron-beam energy is reduced to a value below the ionization threshold for the production of hydrogen-like oxygen, still helium-like X-ray transitions are observed in MTM, although a minimum charge state of hydrogen-like is required to provide a vacancy in the K-shell for recombination in $n = 1$. During the electron-beam on mode, the metastable $1s2s\,^3S_1$ level of helium-like oxygen is populated with a lifetime of 956 µs [50]. The excited electron can be ionized by a free electron of the electron beam, if the interaction occurs within the lifetime, although the kinetic energy of a single electron does not suffice for ionization. By reducing the electron-beam energy below the excitation threshold for this level with an energy of 560.984 eV [62], the M1 transition $1s2s\,^3S_1 - 1s^2\,^1S$ vanishes in the MTM.

Due to a relatively long lifetime of this metastable state, the decay can be measured with the utilized data-acquisition system. To gain higher statistics, the duty cycle of the switching of the electron beam was increased to 50 % with a repetition rate of 10 Hz and a beam current of 200 mA at 1.72 keV nominal electron-beam energy. The axial trapping potential was the same as in the CX measurement described before. The number of events detected within the region of interest, including this transition is plotted as a function of the time within the switching cycle in figure 4.39. As already described in chapter 4.1.3, the upper limit of the time required to switch off the electron beam was in the order of 300 µs. At 56 ms the beam can be considered as switched off. Afterward, the decay in intensity was caused by transitions of metastable states. On much longer time scales in the order of seconds, the decay is dominated by charge exchange. This contribution can be considered as constant for the narrow time window in MTM in this measurement.

A fit of a single exponential decay function yields a lifetime of 1027(71) µs which is in a good agreement with the experimental result presented in [50] and with theoretical predictions [62, 97] within the statistical 1σ-uncertainty.

However, for expressive analysis of charge exchange of highly charged oxygen, followed by K-shell emission, a detector with a higher energy resolution is required. Such measurements utilizing a microcalorimeter with a resolution < 10 eV are presented in Ref. [22] simulating X-ray emission from comets in an EBIT.
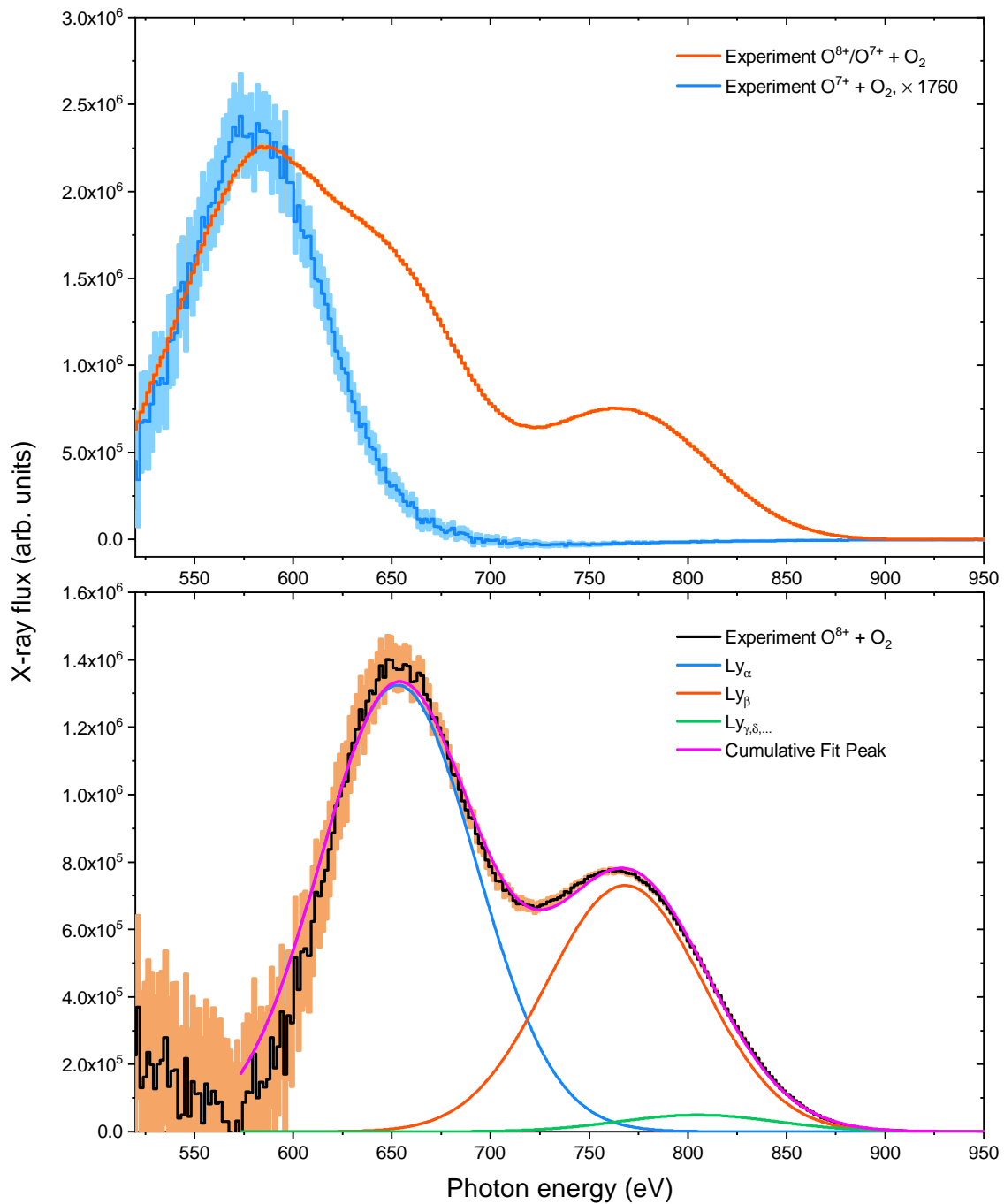
Figure 4.38: Top: X-ray emission from O^{6+} (blue curve) and O^{7+} (red curve) after CX of O^{7+} and O^{8+} with molecular oxygen, respectively. **Bottom:** Pure hydrogen-like CX emission spectrum after CX of O^{8+} with O_2 after subtraction of both spectra, normalized to the K_α transition in the top panel.
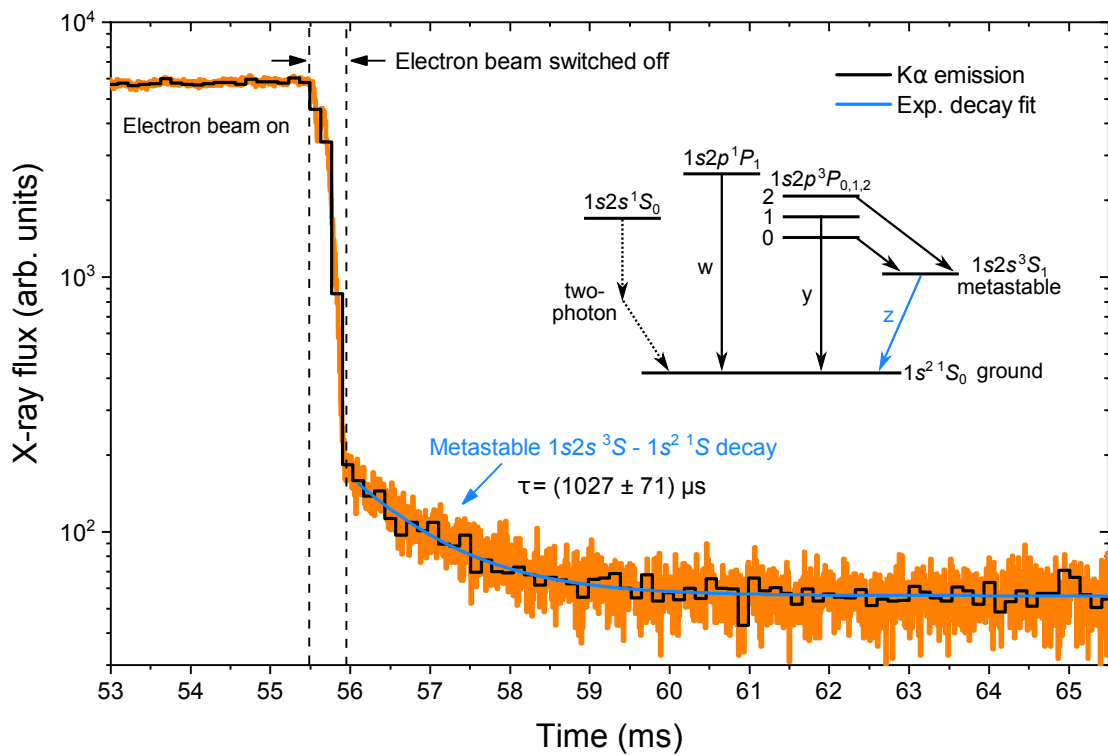
Figure 4.39: K_α emission from the metastable $1s2s\,^3S_1 - 1s^2\,1S_0$ transition of O^{6+} as a function of the time within the switching cycle of the electron beam. The level scheme of helium-like oxygen in the inset is adapted from [50].

4.4.2 Extreme ultraviolet measurements

Since the measurements in the X-ray regime suffer from a poor spectral resolution, only a limited number of spectral lines can be resolved. Thus, the application of the FAC cascade model for extraction of the l-state distribution can not be performed reliably, since the number of free fitting parameters exceeds the number of resolved transitions. A sophisticated solution is the investigation of the extreme-ultraviolet regime, where more spectral lines can be resolved. The transitions are mostly from higher energetic states to the L-shell or M-shell, dependent on the ionic species, and not directly to the ground state.

In addition to the X-ray measurements, the first simultaneous in-situ CX measurement in the EUV range in an EBIT was performed utilizing the setup described in section 3.3.9. The mechanical shutter was triggered by the falling slope of the rectangular signal controlling the emission current. Immediately after switching off the electron beam, the shutter opened entirely within $\sim 70\,\mathrm{ms}$ exposing the CCD only in the magnetic trapping mode. The total time of the switching cycle was $8\,\mathrm{s}$ with two seconds of breeding time and $6\,\mathrm{s}$ in the MTM. The shutter was closed before switching on the beam, ensuring that no photons emitted during interaction with the electron beam are detected. The corresponding duty cycle of the EUV setup in the MTM was, therefore, $68.8\,\%$.

The CCD camera utilized for all EUV measurements was slightly inclined with respect to the plane of the grating resulting in a tilt of the spectral lines. For each measurement with a typical duration of $1800\,\mathrm{s}$, the two-dimensional image was corrected for the tilt and the slight bend of the spectral lines. Additionally localized, intense events caused by cosmics, were removed, and a projection of the spectrum onto the dispersive axis was performed yielding one-dimensional histograms with the CCD pixel number on the abscissa and the arithmetic average of the events per pixel per time unit. The acquisition of the background was performed by closing the valve to the gas injection system in CX mode leading to a substantial reduction of projectile ions and neutral targets. Closing the shutter to the EUV spectrometer would obstruct stray light from the trap resulting in a distortion of the real background conditions. The same background was also used for the measurements during the beam-on mode. In this case, closing the valve to the injection system would affect the trap content and increase the number of fluorescent residual gas ions. The resulting one-dimensional histograms are corrected for the wavelength-dependent spectrometer efficiency presented in section 3.3.9.

For the acquisition of spectra during the beam-on mode serving as a calibration for the spectrometer, only the cycle of the shutter was inverted to expose the CCD only during the beam-on mode and retain otherwise the experimental conditions. The nominal electron-beam energy is $1350\,\mathrm{eV}$ at a beam current of $170\,\mathrm{mA}$. As a calibration species, highly charged oxygen from beryllium-like to helium-like charge states was deployed. In
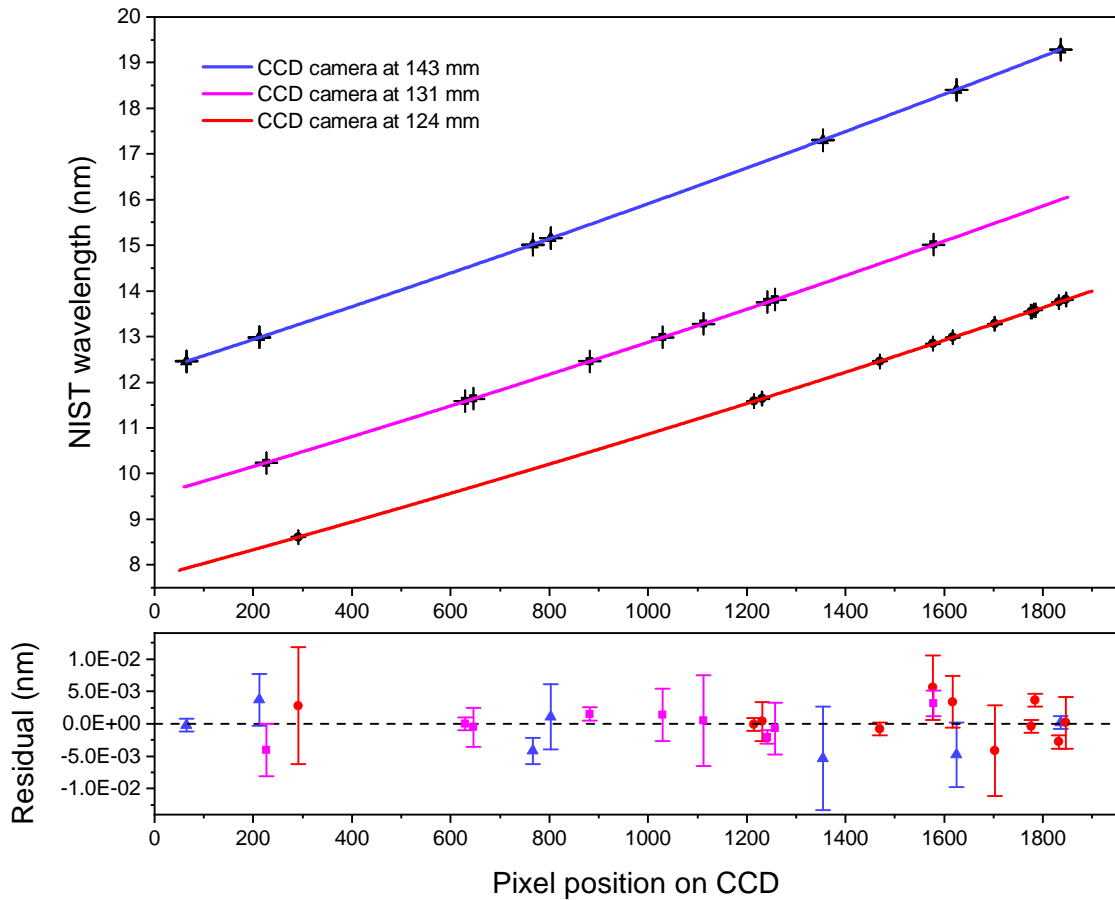
Figure 4.40: Top: Calibration of the EUV spectrometer. Transition wavelengths of highly charged oxygen are plotted as a function of the dispersive position on the CCD for three different positions of the CCD camera with overlapping regions. **Bottom:** Corresponding residuals of the second-order polynomial fits. Blue triangles, magenta squares, and red circles represent the residuals of the calibration fits at camera positions of 143 mm, 131 mm, and 124 mm, respectively.

figure 4.40 the wavelength extracted from the NIST database [45, 137, 168, 35, 90] is plotted as a function of the position of the corresponding spectral line on the dispersive axis of the CCD for three different positions of the CCD camera to cover a broader wavelength range. The calibration at a camera position of 131 mm is utilized for the argon charge exchange measurements in EUV portrayed in chapter 4.4.3.

The calibration lines are summarized in table 4.3. The error of the pixel position results from the fitting error of the centroid of the Gaussian. In the presence of a blend of several lines, the weighted average of the transition wavelength incorporating the resonance strength of the transitions is considered. The calibration polynomials of second order are

determined to

$$\lambda_{143\,\text{mm}} = 1.995(21) \times 10^{-7}x^2 + 3.4772(43) \times 10^{-3}x + 12.2339(16) \tag{4.10}$$

$$\lambda_{131\,\text{mm}} = 2.049(64) \times 10^{-7}x^2 + 3.157(13) \times 10^{-3}x + 9.5148(61) \tag{4.11}$$

$$\lambda_{124\,\text{mm}} = 1.90(10) \times 10^{-7}x^2 + 2.94(3) \times 10^{-3}x + 7.737(22) \tag{4.12}$$

for CCD camera positions of $143\,\text{mm}$, $131\,\text{mm}$ and $124\,\text{mm}$, respectively, where x represents the pixel number on the CCD.

4.4.2.1 Charge exchange of highly ionized oxygen in the EUV range

In figure 4.41 the comparison of the EUV spectrum of highly charged oxygen in the beam-on mode (top panel), the corresponding CX measurement in the magnetic-trapping mode (center panel) and the CX mode below ionization threshold for production of hydrogen-like oxygen are illustrated. The composed spectrum consists of spectra acquired at two different CCD camera positions of $124\,\text{mm}$ and $143\,\text{mm}$ covering a spectral range of $\sim 7.5\,\text{nm}$ to $\sim 20\,\text{nm}$ with an overlapping region between $12\,\text{nm}$ and $14\,\text{nm}$. The electron-beam energy in this measurement of $1350\,\text{eV}$ at a beam current of $170\,\text{mA}$ was sufficient to produce fully ionized oxygen. The neutral target for charge exchange was provided by the constant inflow of molecular oxygen from the gas-injection system with a pressure of $\sim 4 \times 10^{-7}\,\text{mbar}$ in the second injection stage. The measurements below the ionization threshold were performed with a nominal electron-beam energy of $730\,\text{eV}$ and a beam current of $75\,\text{mA}$. The axial trapping potential was $500\,\text{V}$ in all measurements.

To note is the broadening of the spectral lines in CX mode due to an expansion of the ion cloud by a factor of ~ 4.4 resulting from the absence of the negative line-charge of the electron beam which has the highest contribution to the radial confinement of the ions in the beam-on mode. Furthermore, a shift of the ion cloud has been observed in the MTM mode with respect to the beam-on mode as shown in figure 4.6 which results in a spectral shift in the EUV range of $\sim 0.02\,\text{nm}$ according to the geometrical calibration [19] derived from the grating equation.

Transitions of the hydrogen-like, helium-like, lithium-like and beryllium-like charge states are labeled by red, orange, violet, and blue numbers, respectively. Lines 8) and 10) could not be assigned to highly charged oxygen and result probably from residual gas ions. The other identified lines are presented in table 4.4 with the corresponding wavelength extracted from the NIST database. The line centroids and uncertainties of blends of several lines are calculated by a weighted average with the corresponding Einstein coefficients. Transitions marked with an asterisk are not listed as transitions in the database. These wavelengths are calculated from the energetic difference of the corresponding states. All

Table 4.3: Calibration of the EUV spectrometer with highly charged O^{6+} to O^{4+} for three different positions of the CCD camera to cover a broader wavelength range. The transition wavelengths are extracted from Ref. [45, 137, 168, 35, 90] with a minimum uncertainty of 1×10^{-4} nm. Larger errors originate from a weighted averaged transition wavelength for a blend of several transitions.

| Transition	NIST wavelength (nm)	Pixel position	Charge state
CCD camera at 124 mm:			
$1s5d-1s2p$	8.6113 ± 0.009	291.2 ± 0.1	He-like blend
$1s^24p-1s^22s$	11.5826 ± 0.001	1214.3 ± 0.1	Li-like blend
$1s^25d-1s^22p$	11.6391 ± 0.003	1230.8 ± 0.5	Li-like blend
$1s^22s5p\,(J=1)-1s^22s^2\,(J=0)$	12.4616 ± 0.001	1469.64 ± 0.12	Be-like
$1s3d-1s2p$	12.8449 ± 0.005	1576.9 ± 0.1	He-like blend
$1s^24d-1s^22p$	12.9837 ± 0.004	1616.7 ± 0.1	Li-like blend
$1s3s-1s2p$	13.2805 ± 0.007	1702.06 ± 0.12	He-like blend
$1s^22s4p\,(J=1)-1s^22s^2\,(J=0)$	13.5523 ± 0.001	1776.6 ± 0.9	Be-like
$1s3d\,(J=2)-1s2p\,(J=1)$	13.5820 ± 0.001	1783.7 ± 1.8	He-like
$1s3s\,(J=0)-1s2p\,(J=1)$	13.7510 ± 0.001	1832 ± 0.12	He-like
$1s^22s5d-1s^22s2p$	13.8073 ± 0.004	1846.8 ± 0.7	Be-like blend
CCD camera at 131 mm:			
$3l-2l'$	10.2362 ± 0.004	226.45 ± 0.04	H-like blend
$1s^24p-1s^22s$	11.5826 ± 0.001	629.21 ± 0.14	Li-like blend
$1s^25d-1s^22p$	11.6391 ± 0.001	645.9 ± 0.2	Li-like blend
$1s^22s5p\,(J=1)-1s^22s^2\,(J=0)$	12.4616 ± 0.001	882.3 ± 0.1	Be-like
$1s^24d-1s^22p$	12.9837 ± 0.004	1029.44 ± 0.06	Li-like blend
$1s3s-1s2p$	13.2805 ± 0.007	1112.23 ± 0.09	He-like blend
$1s3s\,(J=0)-1s2p\,(J=1)$	13.751 ± 0.001	1242.18 ± 0.11	He-like
$1s^22s5d-1s^22s2p$	13.8073 ± 0.004	1257.17 ± 0.26	Be-like blend
$1s^23p-1s^22s$	15.0107 ± 0.001	1578.04 ± 0.07	Li-like blend
CCD camera at 143 mm:			
$1s^22s5p\,(J=1)-1s^22s^2\,(J=0)$	12.4616 ± 0.001	65.28 ± 0.09	Be-like
$1s^24d-1s^22p$	12.9837 ± 0.004	211.97 ± 0.08	Li-like blend
$1s^23p-1s^22s$	15.0107 ± 0.002	766.1 ± 0.05	Li-like blend
$1s^22s4d-1s^22s2p$	15.1545 ± 0.001	802.65 ± 0.13	Be-like blend
$1s^23d-1s^22p$	17.302 ± 0.008	1353.91 ± 0.04	Li-like blend
$1s^23s-1s^22p$	18.4057 ± 0.005	1624.86 ± 0.03	Li-like blend
$1s^22s3d-1s^22s2p$	19.2906 ± 0.001	1836.01 ± 0.04	Be-like blend
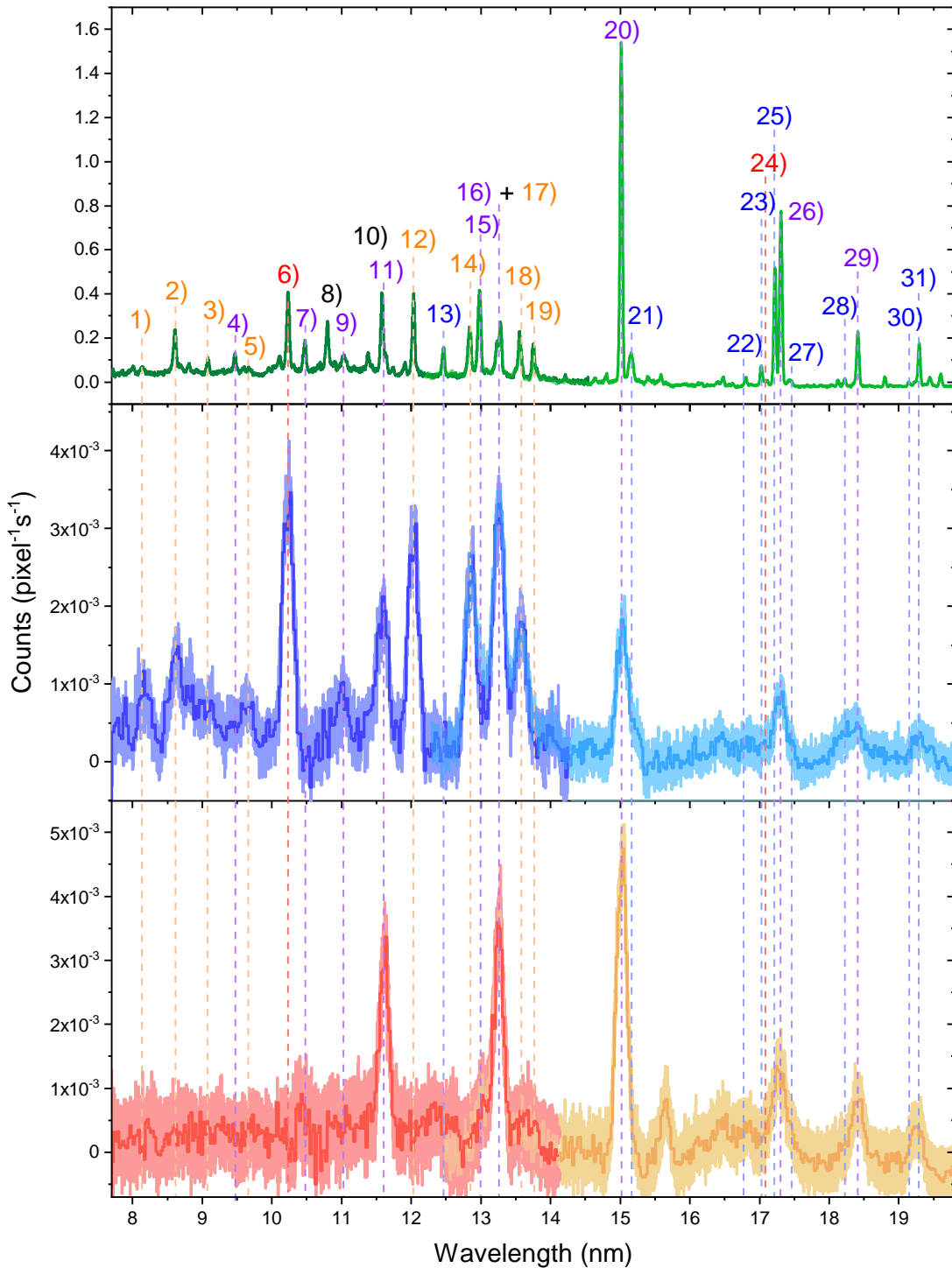
Figure 4.41: EUV spectra of highly charged oxygen in magnetic-trapping mode with initial electron-beam energy above the ionization threshold for fully ionized oxygen (**center**), the corresponding spectrum in the direct-excitation mode (**top**) and below the ionization threshold for production of hydrogen-like oxygen (**bottom**). Further details are described in the text.

EUV spectra in magnetic-trapping mode have been accordingly corrected for the spectral shift caused by the displacement of the ion cloud. The spectra presented in the center panel are arithmetic averages of 112 signal spectra in the MTM and 30 background spectra at the camera position of 124 mm (dark blue). For the camera position of 143 mm 37 signal images and four background images (light blue) were acquired. Analogously, 30 spectra in CX mode and four background images were acquired for the CX measurement below the ionization threshold for hydrogen-like oxygen in the bottom panel for a camera position of 124 mm (red). At 143 mm, 34 single CX spectra and four background measurements were acquired (orange). For the calculation of the uncertainty, a Poisson distribution can not be utilized because the CCD camera provides an arbitrary offset and thus the detected number of events does not correspond to real counts. The average number of detected events in the background measurements was in the order of 210 counts/pixel in 1800 s with an unknown intrinsic offset. The number of counts in the signal measurements was slightly higher by 0.4 counts/pixel. The uncertainty was calculated by determination of the standard deviation σ of the distribution of events in an arbitrary single background measurement. By subtraction of the averaged background from the averaged signal, the overall uncertainty is estimated according to

$$\text{err} = \sqrt{\left(\frac{\sigma}{\sqrt{N_{\text{sig}}}}\right)^2 + \left(\frac{\sigma}{\sqrt{N_{\text{BG}}}}\right)^2}, \tag{4.13}$$

where N_{sig} and N_{BG} are the number of single spectra of the signal and the background measurements, respectively. The error bars are plotted in shaded colors. Only two transitions of hydrogen-like oxygen could be identified. One spectral line is located at ~ 10.2 nm (line 6)), the other at ~ 17.1 nm (line 24)). In the magnetic trapping mode, only the strong 10.2 nm transition $3l$–$2l'$ is observed, which indicates that the $n = 6$ state is not populated by charge exchange. In the bottom panel, the spectrum below the threshold for production $I_{\text{P,H}}$ of hydrogen-like oxygen is illustrated in red. Therefore, only helium-like and beryllium-like transitions after capture can be observed.

In contrast to the CX measurements in the X-ray regime, where the electron-beam energies were set above and below the threshold of the fully-stripped projectile to extract the contribution of capture into the bare charge state, the lower bound of the beam energy in this measurement only allows for the production of helium-like oxygen. The ambition of the experiment was to investigate electron capture into the hydrogen-like state because only two transitions of capture into O^{8+} are expected. However, the reason for the choice of the energy above $I_{\text{P,Bare}}$ is a higher yield of hydrogen-like ions at higher beam energies and therefore higher count rates. The most intense transitions are $1s^2 4l - 1s^2 2l'$ and $1s^2 3l - 1s^2 3l'$. Transitions from higher states like $1s^2 5l - 1s^2 2l'$ are not present in

this spectrum, indicating that $n = 4$ is the highest excited principal quantum number state, which can be populated by charge exchange for this system. The spectral line at $\sim 15.6\,\text{nm}$ which was not present in the spectrum of the electron-beam on mode appears in magnetic-trapping mode. It can be speculated that the line could originate from a dipole-forbidden beryllium-like transition, but a proper assignment to a known transition can not be performed. Furthermore, the intensity ratio of line 20) to line 11) seems to be higher in the spectrum below the ionization threshold $I_{\text{P,H}}$ than above. An explanation could be a decreased yield of beryllium-like ions with higher electron-beam energies. Since a beryllium-like transition (line 21)) is in direct proximity of line 20) the overall apparent intensity of the 15 nm line could be increased in the spectrum with an initially lower electron-beam energy.

For the sake of completeness and illustration of possible electronic cascades in dependence of the populated level, a Grotrian diagram of the CX induced transitions of helium-like oxygen after electron capture is presented in figure 4.42 with the first electron in the ground state and the second electron in an excited state nl. The energy of the configurations on the ordinate is plotted as a function of the corresponding angular momentum l. Each panel shows an initial population of $n = 5$ with the corresponding angular momenta of $100\,\%$. All possible dipole-allowed transitions are color-coded by the branching ratio, where red arrows represent strong transitions with maximum $100\,\%$ probability and blue arrows comparably weak transitions in logarithmic scale. Triplet and singlet states are separated in this depiction.

A high population of $1s5d$ leads to an enhancement of the expected $1s4l \rightarrow 1s2l'$ transitions in the EUV range.

4.4.2.2 Comparison with charge exchange models

For comparison of the data to theoretical models, both CX spectra in figure 4.41 are normalized to an isolated lithium-like transition (line 11)) which is present in both spectra. Since no MCLZ calculations for CX of helium-like systems and lower charge states exist so far, and no transitions of helium-like oxygen after electron capture were detected above 14 nm, the spectra acquired at a camera position of 124 mm, covering a wavelength range of $8 - 14\,\text{nm}$ are compared to theory. After normalization, the spectrum below the ionization threshold $I_{\text{P,H}}$ is subtracted from the spectrum above $I_{\text{P,Bare}}$. The spectral lines which remain have an origin in initially fully ionized and hydrogen-like charge states of oxygen. The subtracted result is shown in the bottom panel of figure 4.43.

In the top panel, synthetic spectra of electron capture into fully ionized oxygen calculated employing the flexible atomic code (light blue) (chapter 2.3.4.5) and by an MCLZ approach using Kronos (chapter 2.3.4.4) for a collision energy of $20\,\text{eV/u}$ (orange) is shown. Capture

Table 4.4: Identified transitions of highly charged oxygen. The transition wavelengths are extracted from the NIST database. The values which are nor listed in the database are calculated from the theoretical energetic difference of the energy levels provided by NIST, are labeled with an asterisk. In the last three columns, the Einstein coefficients extracted from NIST are compared to calculations performed by FAC and to the values provided by the Kronos code. The Einstein coefficients of the hydrogenic system, calculated by Kronos, could not be extracted and are labeled by a dagger symbol.

Line	Transition	NIST wavelength (nm)	$A_{ki,\text{NIST}}$ $(10^{10}\,\text{s}^{-1})$	$A_{ki,\text{FAC}}$ $(10^{10}\,\text{s}^{-1})$	$A_{ki,\text{Kronos}}$ $(10^{10}\,\text{s}^{-1})$
1	$1s5p\,^3P - 1s2s\,^3S$	8.1914^*	*	1.10	1.23
2	$1s5l - 1s2l'$	8.6113 ± 0.009	8.55	8.46	3.63
3	$1s4p\,^3P - 1s2s\,^3S$	9.1078^*	*	2.23	2.38
4	$1s^28p - 1s^22s$	9.5082^*	*	–	–
5	$1s4d\,^3D - 1s2p\,^3P$	9.614 ± 0.004	18.22	15.79	5.32
6	$3l - 2l'$	10.24 ± 0.01	74.0	74.1	†
7	$1s^25p - 1s^22s$	10.4813^*	*	–	–
9	$1s^26l - 1s^22l'$	11.04 ± 0.03	–	–	–
11	$1s^24p - 1s^22s$	11.5826 ± 0.001	–	–	–
12	$1s3p\,^3P - 1s2s\,^3S$	12.033^*	*	5.18	5.32
13	$1s^22s5p\,^1P - 1s^22s^2\,^1S$	12.4616 ± 0.001	–	–	–
14	$1s3d - 1s2p$	12.8449 ± 0.005	53.5	48.11	16.12
15	$1s^24d - 1s^22p$	12.9837 ± 0.004	–	–	–
16	$1s^24s - 1s^22p$	13.227 ± 0.005	–	–	–
17	$1s3s - 1s2p$	13.2805 ± 0.007	2.51	2.14	2.26
18	$1s3d\,^1D - 1s2p\,^1S$	13.5820 ± 0.001	15.23	14.99	15.23
19	$1s3s\,^1S - 1s^22p\,^1P$	13.7510 ± 0.001	2.01	2.02	2.01
20	$1s^23p - 1s^22s$	15.0107 ± 0.002	–	–	–
21	$1s^22s4d - 1s^22s2p$	15.1545 ± 0.001	–	–	–
22	$1s^22p3p - 1s^22s2p$	16.799 ± 0.001	–	–	–
23	$1s^22s4d - 1s^22s2p$	17.022 ± 0.001	–	–	–
24	$6l - 3l'$	17.07 ± 0.01	4.35	4.36	†
25	$1s^22s3p - 1s^22s^2$	17.217 ± 0.001	–	–	–
26	$1s^23d - 1s^22p$	17.302 ± 0.008	–	–	–
27	$1s^22s4s\,^1S - 1s^22s2p\,^1P$	17.456 ± 0.001	–	–	–
28	$1s^22p3p\,^1S - 1s^22s2p\,^1P$	18.220 ± 0.001	–	–	–
29	$1s^23s - 1s^22p$	18.4057 ± 0.005	–	–	–
30	$1s^22s4p - 1s^22p^2$	19.15 ± 0.01	–	–	–
31	$1s^22s3d - 1s^22s2p$	19.2906 ± 0.001	–	–	–
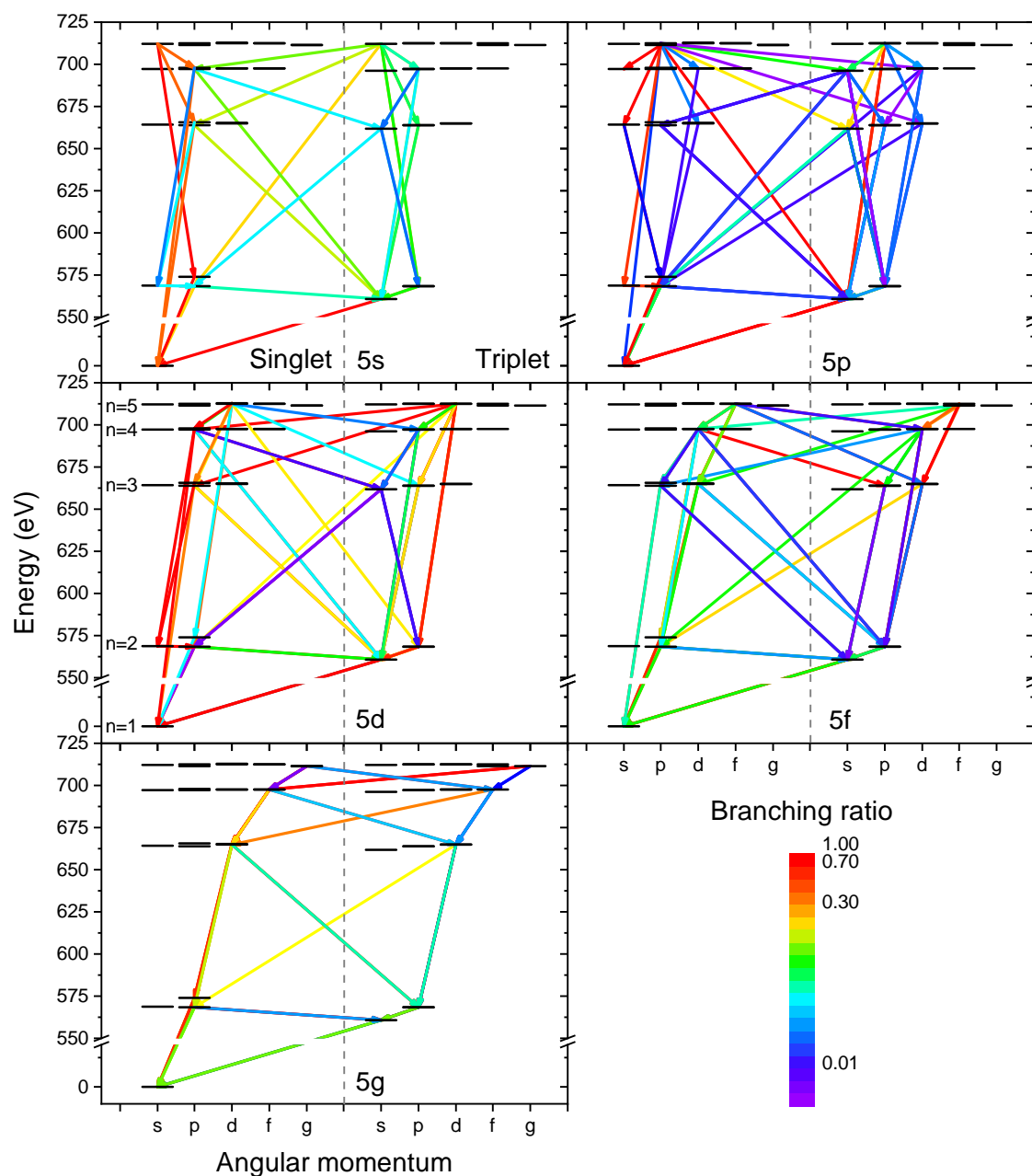
Figure 4.42: Grotrian diagram for transitions of helium-like oxygen with an initial population of 100% in different angular momentum states of $n = 5$, respectively. The energies of the levels are plotted on the ordinate as a function of the corresponding angular momentum on the abscissa. The branching ratios are color-coded, where red arrows indicate a transition with a probability of 100 % and violet less than 1 %. The singlet and triplet states are separated in this representation.

Figure 4.43: Comparison between synthetic CX spectra of O^{8+} and O^{7+} with H_2O obtained by the MCLZ approaches of Kronos and by FAC (**top panel**) and the experiment with the extracted contribution of CX between O^{8+} and O^{7+} with molecular oxygen (**bottom panel**). Additionally, the results of the reconstruction with the FAC cascade model for $n = 5$ are shown as a solid orange curve.

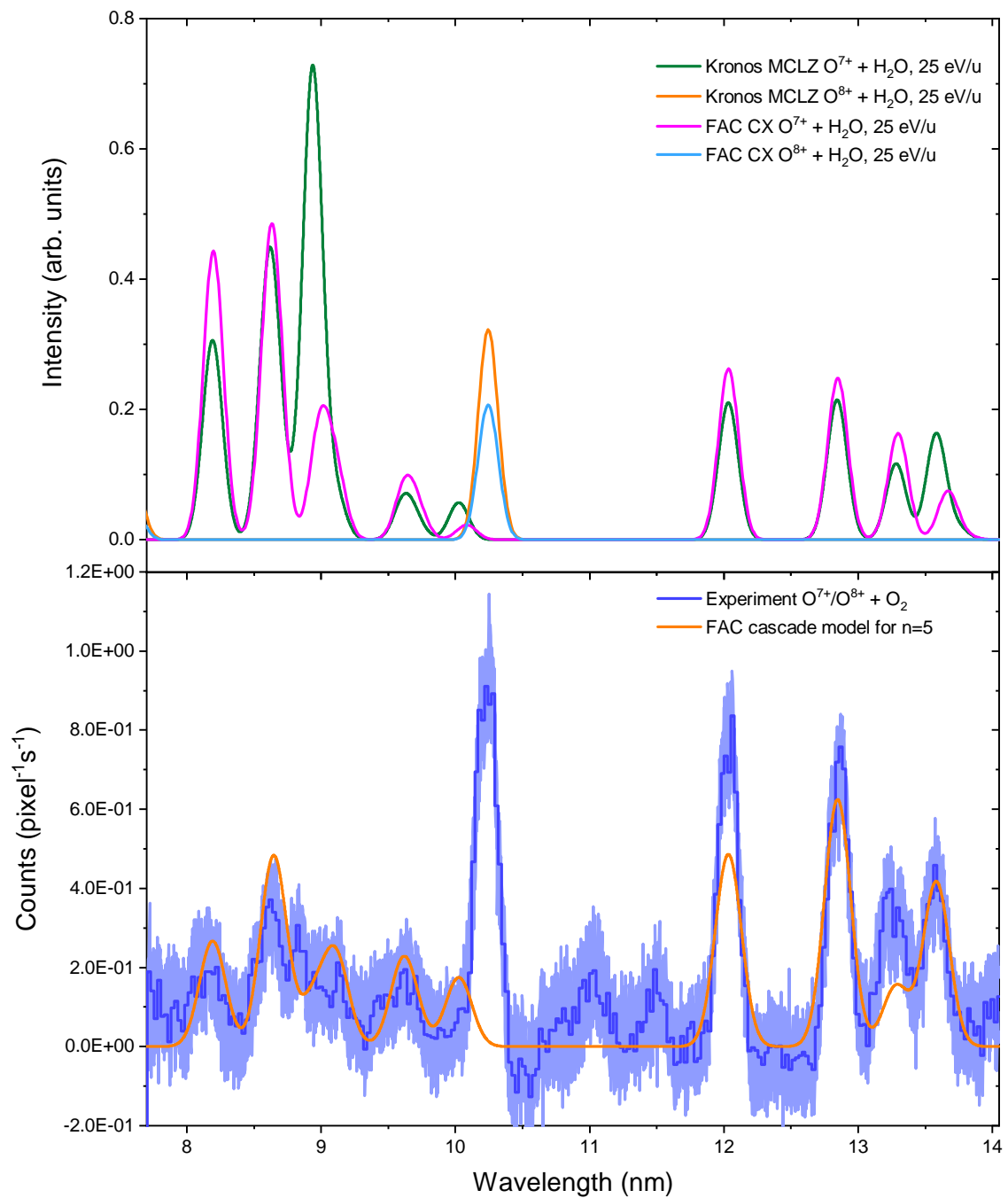into the hydrogenic state is depicted in green for the MCLZ approach and in magenta for the FAC calculation. The delta-function-like lines with their theoretical line positions and intensities are convolved with a Gaussian with a width corresponding to the experimental resolution. The choice of H_2O as a target for the Kronos calculation is based on a lack of data for O_2 in the intrinsic database of collisional cross-sections. Since H_2O has the smallest difference in the ionization potential of the targets available with $I_{P,H_2O} = 12.65\,\mathrm{eV}$ [157] to O_2 ($I_{P,O_2} = 12.0697\,\mathrm{eV}$ [164]), it is a valid approach to compare both targets.

To remark is a slight discrepancy between both models. For modeling of the cascade spectra Kronos utilizes the energy levels of helium-like oxygen from the NIST database whereas FAC performs an ab-initio calculation of those energy levels. Some of the calculated levels have a slight deviation in the order of $1\,\mathrm{eV}$ from the NIST values, which affects the transition energies. Since the calibration of the spectrometer is based on theoretically and experimentally determined transition wavelengths from five different references from the NIST database and the residuals of the calibration fit are smaller than $5 \times 10^{-3}\,\mathrm{nm}$, the transition energies provided by Kronos seem more confidable than the values from FAC. Both models predict an increased intensity of transitions $1snl - 1s2l'$ with $n \geq 4$ compared to the experiment.

Furthermore, the MCLZ approach of Kronos predicts electron capture almost into one single principal quantum number state $n = 5$. In the bottom panel of figure 4.44, the n-resolved single-electron capture cross-section into the hydrogenic charge state of oxygen is plotted as a function of the collision energy between O^{7+} and H_2O. At lower collision energies which are expected in an electron-beam ion trap, the probability of capture of an electron into $n = 5$ is three orders of magnitude higher than capture into higher or lower n-states.

For the application of the FAC cascade model described in section 2.3.4.5, the calculated transition rates provided by FAC are retained, but as a consequence of the discrepancy between the transition energies of FAC and Kronos, the energy levels from NIST are incorporated. Finally, the reconstruction of the angular momentum states with the CX fit model for $n = 5$ is overlayed in orange with the experimental data in the bottom panel. For lower wavelengths, a good agreement between the data and model can be noticed. For higher wavelengths, the intensities of the transitions $1s3p - 1s2s$ (line 12)) and $1s3s - 1s2p$ (line 17)) are underestimated by the fit of the cascade model. By inclusion of the principal quantum number states $n = 3, 4$ into the cascade model, the agreement between the CX fit model and the experiment improves as illustrated in figure 4.45. The hydrogen-like line at $\sim 10.2\,\mathrm{nm}$ is not included in the fit of the helium-like system. Since only one transition of capture into fully ionized oxygen is observed, it would be unsubstantial to extract any information about the distribution of angular momentum. Although both

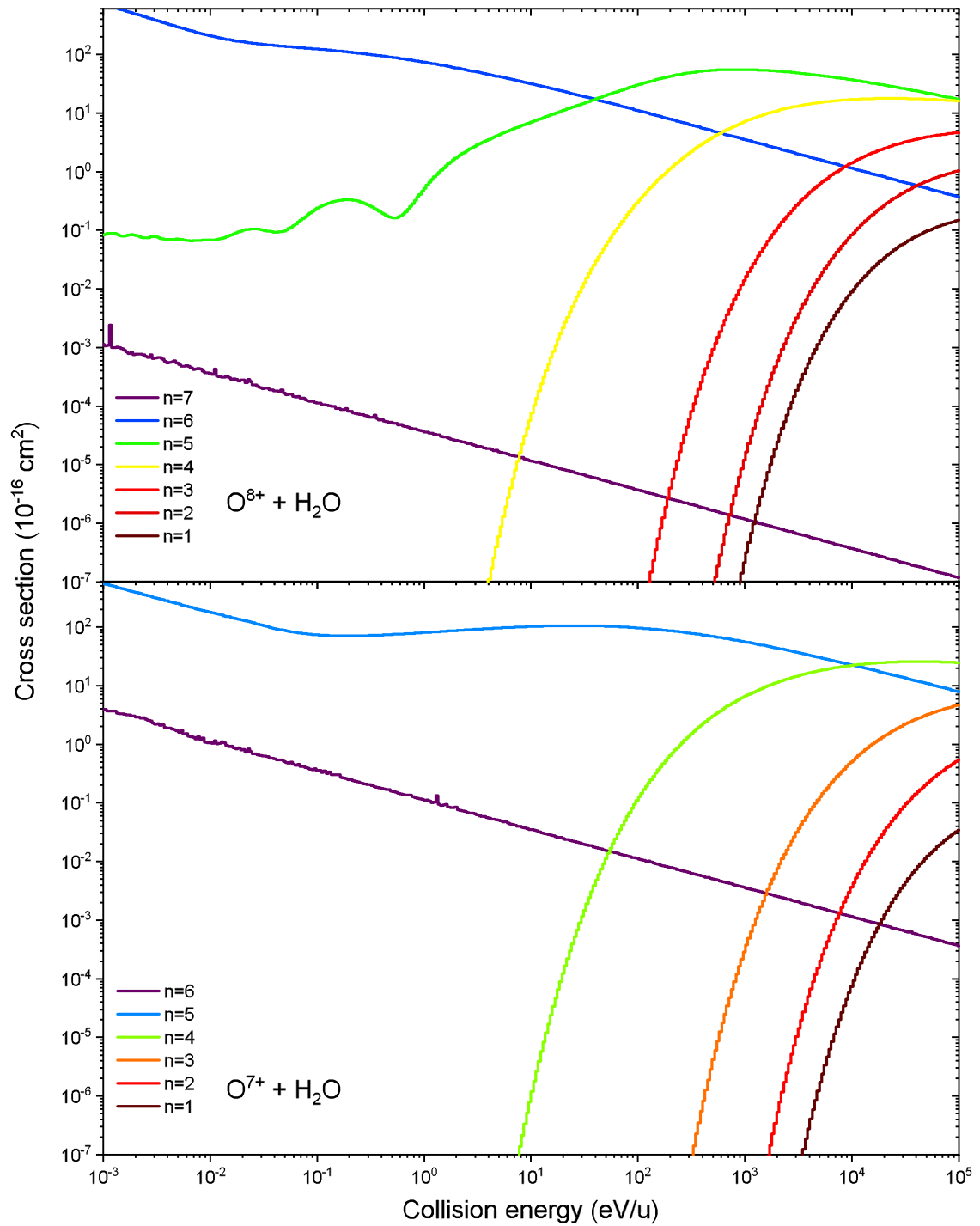**Figure 4.44:** Principal quantum number *n*-resolved single-electron cross-section of O^{8+} + H_2O (top panel) and O^{7+} + H_2O (bottom panel) as a function of the collision energy between projectile and target calculated with an MCLZ approach utilizing the Kronos code.
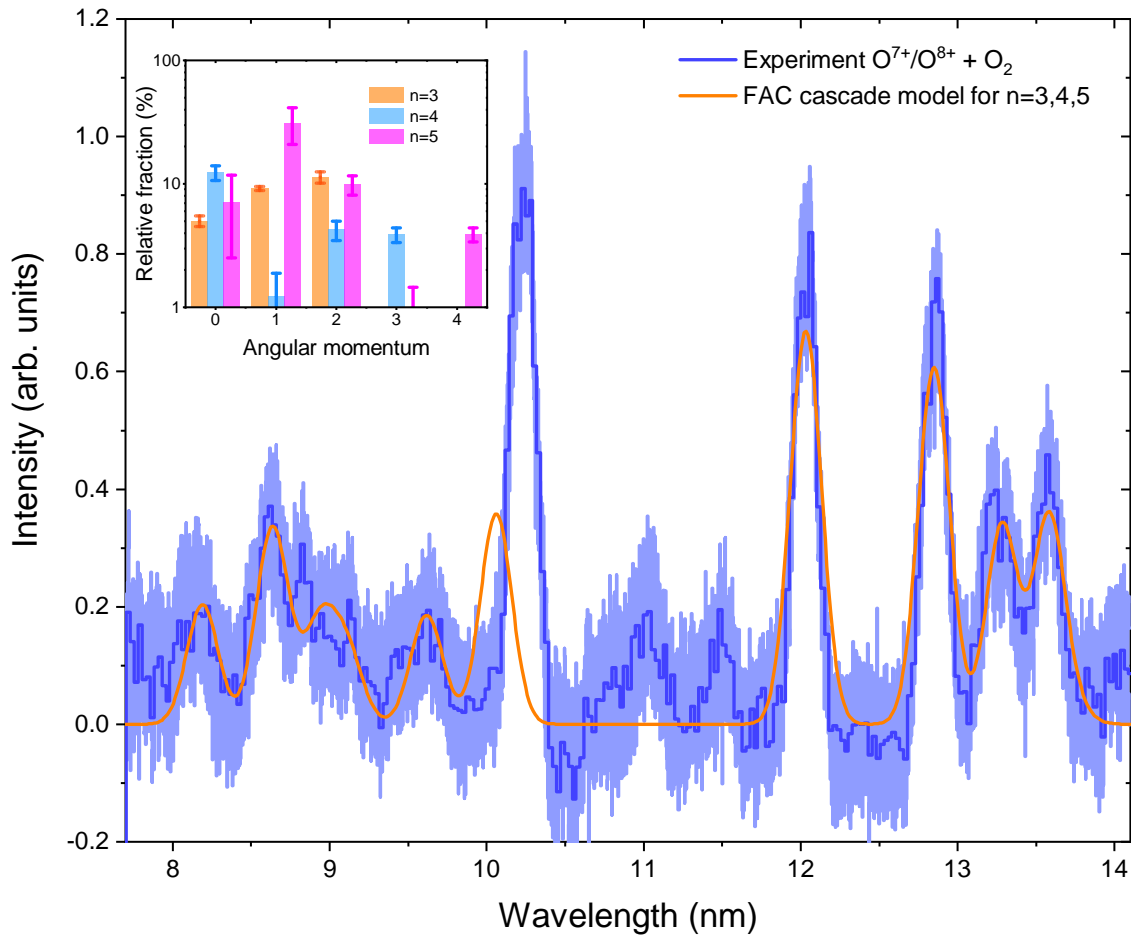
Figure 4.45: Charge exchange spectrum of O^{8+} and O^{7+} with molecular oxygen. The orange curve represents the reconstruction of the angular momentum distribution with the FAC cascade model by consideration of population of $n = 3, 4, 5$. The corresponding relative fractions of populated l-states are illustrated in the inset by orange, blue and magenta-colored bars, respectively.

models predict a comparably high population of $n = 6$ and a strong $6l - 3l'$ transition of the hydrogenic system at ~ 17.08 nm for lower collision energies (compare top panel of figure 4.44), no line is observed in the experiment which indicates that the $n = 6$ state is not populated by charge exchange in contradiction to the MCLZ approach. However, the classical-over-the-barrier method described in chapter 2.3.4.1 anticipates the highest principal quantum number state $n = 5$ in which the electron is captured. Unfortunately, the $5l - 3l'$ transition is outside of the investigated spectral range.

The reconstruction indicates an underestimation of the cross-section of the population of the $n = 3$ and $n = 4$ state by CX with the MCLZ approach. In table 4.4, the transition rates A_{ki} of the observed lines are listed. The values from NIST, FAC calculations, and

from the database of Kronos are compared in the last three columns. An underestimation of some transitions by a factor of three between FAC and Kronos is observed. In contrast, the agreement between NIST and FAC is satisfactory. The most considerable difference is in the order of 14 %. To remark is, that Kronos does not implement S-resolved transitions, whereas FAC provides transitions between different total angular momentum states of the initial level and the final level. This could explain the mismatch of both synthetic spectra, although a similar approach for the calculation is utilized. A second effect that is not included in both models is double-electron capture (DEC) and subsequent autoionization. This process has already been investigated by other groups [93, 59, 9, 10] with the conclusion that the cross-section of DEC is comparably high in the order of $1 \times 10^{-15}\,\mathrm{cm}^2$. DEC with autoionization leads to the same final charge state after electron capture as single-electron capture (SEC) but with an increased population of lower principal quantum number states n. For example, a double capture into $n = 5$ of an initially hydrogen-like system can occur, leading to the formation of a doubly-excited lithium-like system. The energy in the order of $\sim 45\,\mathrm{eV}$ of the transition of one electron from $n = 5$ to $n = 3$ can be transferred non-radiatively to the second electron. This energy is sufficient to ionize the latter electron with a binding energy of $\sim 35\,\mathrm{eV}$. The energy of $\sim 17\,\mathrm{eV}$ released by a $n = 5$ to $n = 4$ transition does not suffice to ionize the second electron. Also, a radiative channel of the doubly-excited state is possible where no autoionization occurs. Here the initially hydrogen-like system becomes a lithium-like system after capture leading to an increase of the intensity of lithium-like lines compared to SEC.

A direct comparison between the MCLZ approach for collisions between O^{7+} and H_2O at energies of 20 ev/u calculated by Kronos and the reconstruction of the distribution of angular momenta with the FAC cascade model is presented in figure 4.47 as an orange and a blue solid line, respectively. As outlined in figure 4.44, the most populated principal quantum number state is $n = 5$. The synthetic MCLZ charge exchange spectrum, convolved with the instrumental resolution in MTM serves as an input for the reconstruction for capture into $n = 5$ with the FAC cascade model. The relative l-population from the reconstruction is deduced from the coefficients of the spectral basis vectors described in chapter 2.3.4.5, whereas the l-distribution of the Kronos code is extracted from the MCLZ calculation presented in figure 4.46. The capture cross-section into triplet and singlet angular momentum states for $n = 5$ is plotted as a function of the collision energy between projectile and target.

The results for the relative fraction of different angular momenta are presented in the inset of the figure as orange bars for the MCLZ approach and as blue bars for the reconstruction method. Here the population of the singlet and triplet states for each angular momentum is summarized. In an ideal case, the reconstruction of the distribution with the cascade model should provide the same results for the relative fractions. Since the transition wavelengths
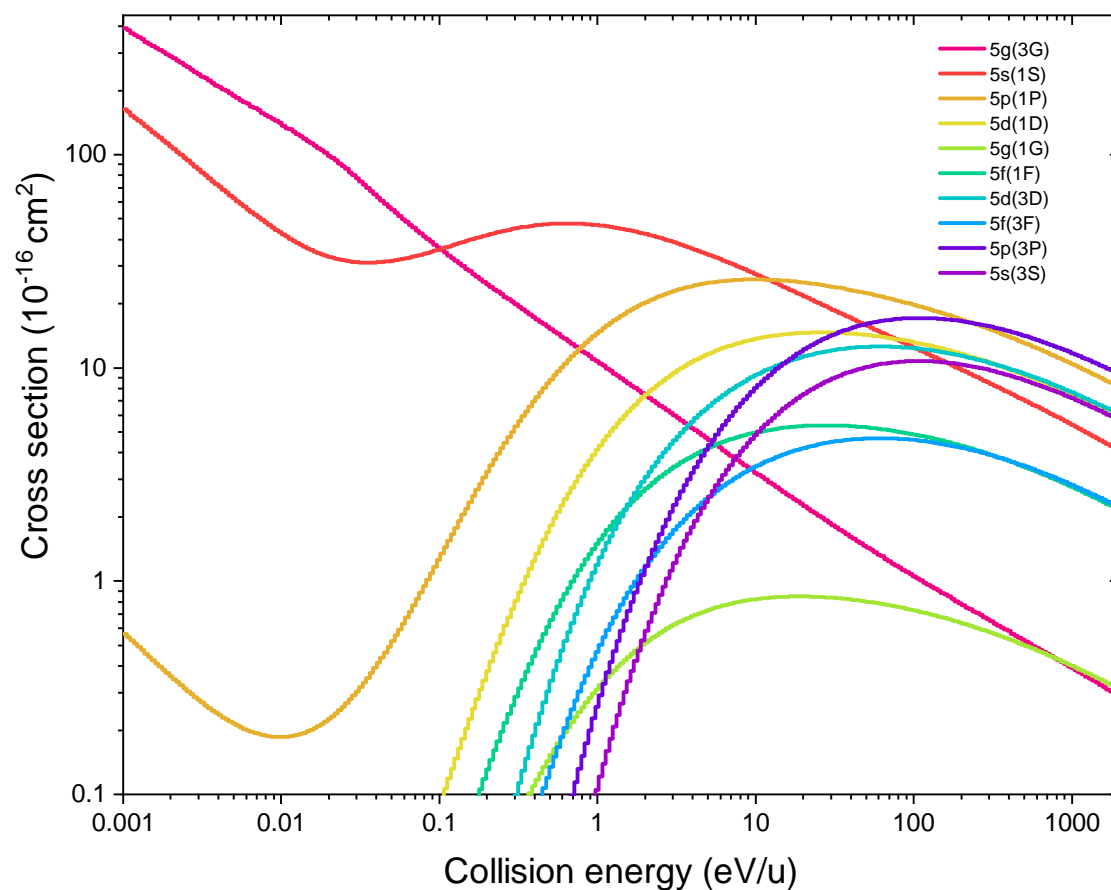
Figure 4.46: Charge exchange cross-sections for capture into different angular momentum states of $n = 5$ for interaction between O^{7+} and H_2O as a function of the relative collision energy, calculated by the MCLZ approach utilizing the Kronos code.
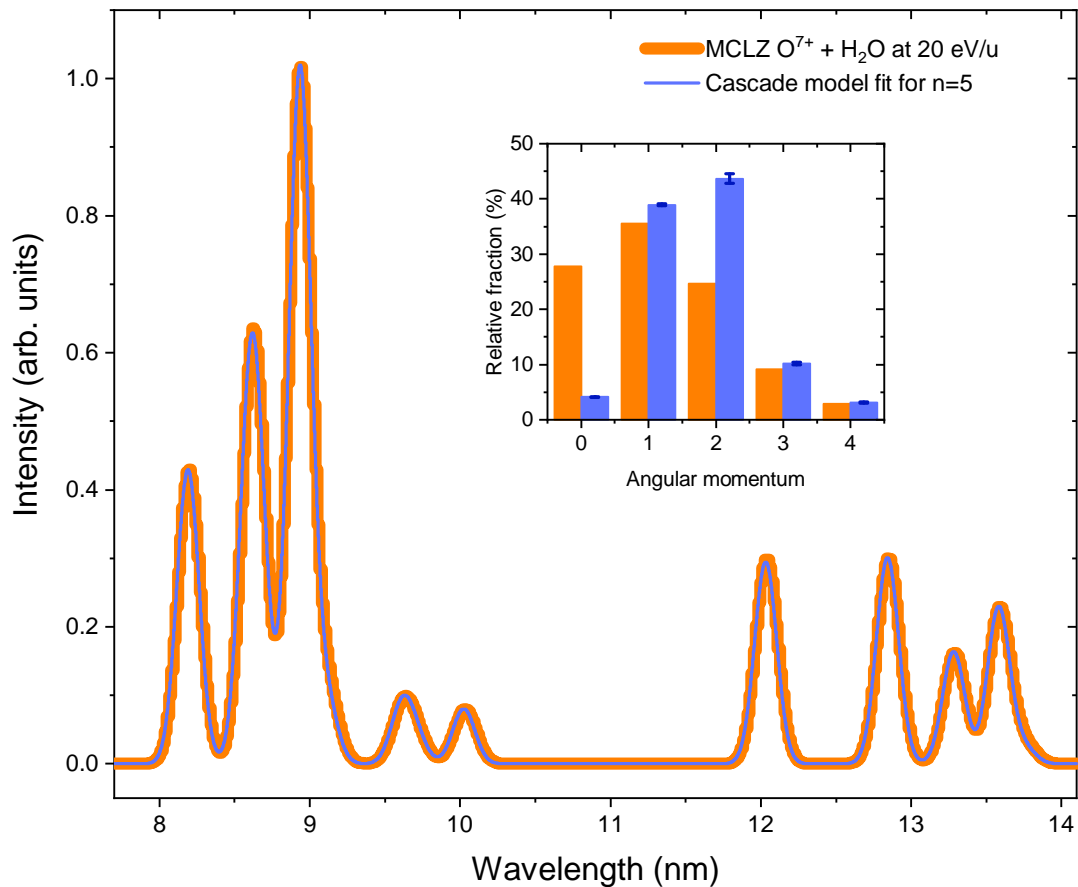
Figure 4.47: Synthetic CX spectrum of O^{7+} + H_2O at a collision energy of $20\,eV/u$, calculated with the MCLZ approach utilizing the Kronos code (solid orange curve) and the reconstruction of the angular momentum distribution by the FAC cascade model (solid blue curve) for single-electron capture into $n = 5$. The inset represents the relative fractions of angular momenta in the corresponding colors. The cross-sections for the l-state capture used by the MCLZ approach are extracted from figure 4.46.

are fixed, and the only fitting parameter for each spectral basis vector is the intensity, the number of degrees of freedom of the cascade model is five. The number of fitted transitions is higher by a factor of two, and thus the model is not overdetermined, leading to a reliable fit. The fact of the large discrepancy of the population of *s*- and *d*-states could originate from the mismatch of the transition rates of the FAC and the MCLZ calculation as outlined in table 4.4.

4.4.3 Charge exchange of argon in the EUV range

In earlier CX measurements of Ar^{17+} and Ar^{18+} with neutral argon as a donor, no lines were visible in MTM in the EUV range in contrast to the oxygen measurements. The spectral lines investigated within the framework of the oxygen EUV measurements, are exclusively transitions from *nl*-states into the *L*-shell. Transitions expected for highly ionized argon in this energy range are mostly from *nl*-states to $n = 4, 5$, which are less probable than the *L*-shell transitions, although the CX cross-sections increase with a higher charge of the projectile. In order to increase the photon yield of the argon transitions in this energy range, the EUV measurements have been carried out simultaneously to the X-ray measurements of Ar^{17+} and Ar^{18+} with a pulse of molecular hydrogen utilizing the pulsed gas injection system [13].

In figure 4.48, the EUV measurements are presented. In the top panel, spectral lines of highly charged oxygen during the electron-beam on mode, as presented in table 4.3 are used for calibration. In the middle panel, the spectrum of highly ionized argon was obtained during electron-beam on mode with an electron-beam energy of 8000 eV in order to produce fully ionized argon ions. Some spectral lines resulting from residual oxygen injected during previous measurements are indicated by vertical, dashed lines. The corresponding spectrum in MTM is presented in the bottom panel, according to the measurement scheme described in section 4.4.2 with an analogous estimation of the error bars. Since the pulsed injection system was not fully optimized hitherto, the gas inflow rate was higher than the pumping rate leading to a slow increase of the pressure in the trap and thus to unstable experimental conditions. Therefore, the number of acquired spectra, in total five, in magnetic trapping mode with pulsed injection were comparably low, causing an increase of the statistical uncertainty. The total length of the measurement cycle was 10 s with 6 s in the electron-beam on mode in order to efficiently produce Ar^{18+} with a current of 200 mA and an axial trapping potential of 800 V. The subcycle of the magnetic-trapping mode was 4 s whereas the EUV shutter was open for 3.5 s in order to exclude possible contributions from metastable states. The line positions were corrected for the displacement of the ion cloud, as discussed in section 4.4.2.

The dominant spectral line at 15 nm results from a lithium-like charge state of residual

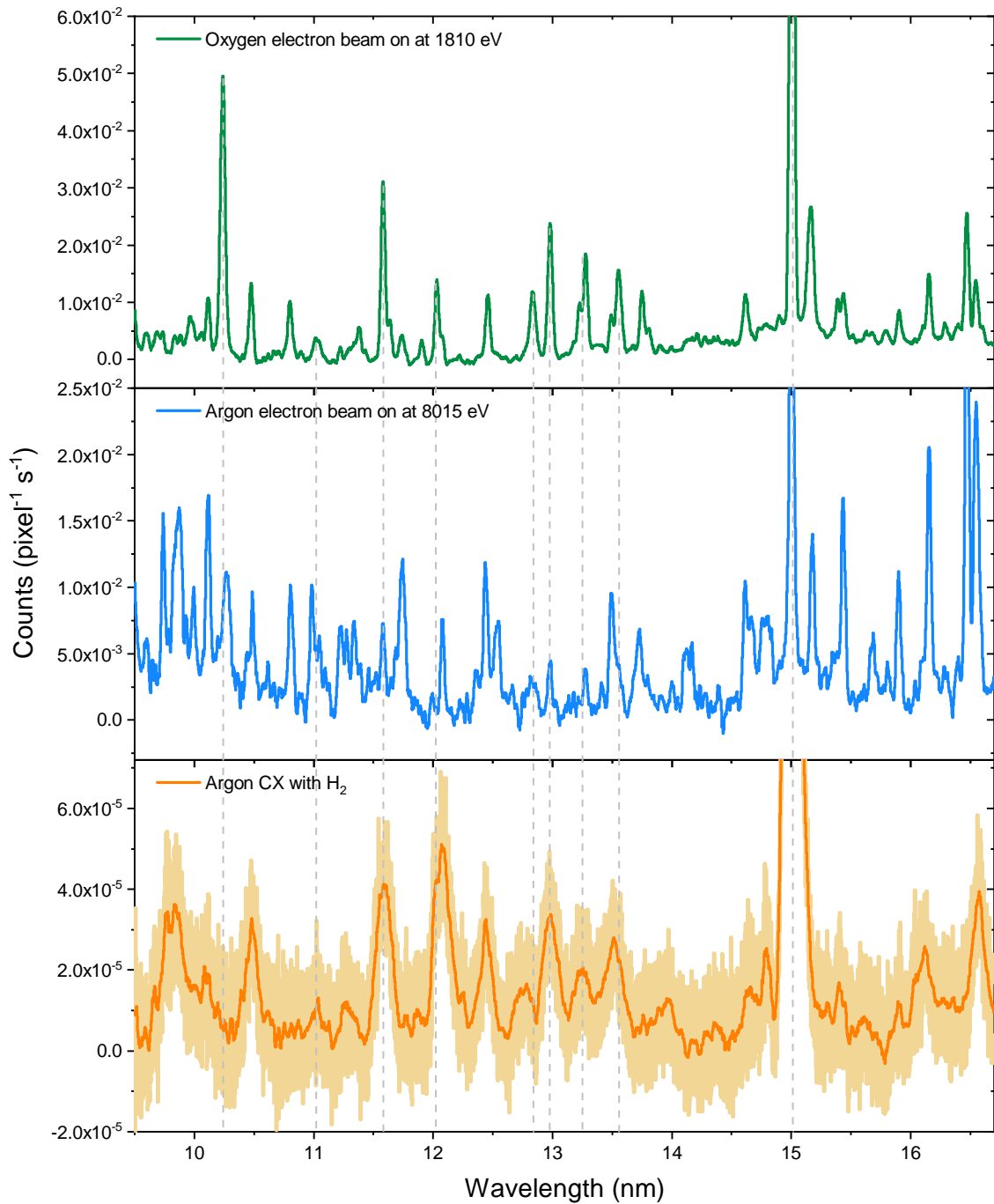**Figure 4.48: Top panel:** calibration spectrum of highly charged oxygen ions presented in table 4.3. **Center panel:** direct excitation of a mixture of highly charged argon and oxygen during the electron-beam on mode with a nominal beam energy of 8015 eV. **Bottom panel:** corresponding charge exchange spectrum in magnetic-trapping mode with pulsed H_2 injection as the donor species.

Table 4.5: Comparison between transition wavelengths of $1s5l - 1s4l'$ transitions of helium-like argon extracted from the energetic difference of levels provided by the NIST database and calculated directly by FAC.

Transition	NIST wavelength (nm)	FAC wavelength (nm)
$1s5p\,^3\mathrm{P}\,J = 2 - 1s4s\,^3\mathrm{S}\,J = 1$	13.5056	13.5176
$1s5d\,^3\mathrm{D}\,J = 3 - 1s4p\,^3\mathrm{P}\,J = 2$	13.7900	13.8011
$1s5d\,^1\mathrm{D}\,J = 2 - 1s4p\,^1\mathrm{P}\,J = 1$	14.0233	13.7584
$1s5s\,^3\mathrm{S}\,J = 1 - 1s4p\,^3\mathrm{P}\,J = 2$	14.1080	14.1087
$1s5s\,^1\mathrm{S}\,J = 0 - 1s4p\,^1\mathrm{P}\,J = 1$	14.1664	14.1752

oxygen, which was injected in a previous measurement. A cautious investigation of the CX spectrum in magnetic-trapping mode is illustrated in figure 4.49. In the top panel, synthetic collisional-radiative spectra calculated employing the Flexible Atomic Code for an electron-beam energy of 8015 eV is presented for hydrogen-like, helium-like, and lithium-like charge states of argon. The middle and the bottom panel shows the same spectra during electron-beam on mode and the corresponding magnetic-trapping mode as in figure 4.48. The gray areas represent spectral lines of highly charged oxygen identified in the previous section. Due to a lack of transitions of highly charged ions in the EUV range in standard wavelength catalogs, it is challenging to identify the spectral lines observed.

4.4.3.1 Helium-like argon

Theoretical energy levels are given in those databases for principal quantum numbers up to $n = 5$. Calculations performed by FAC provide transition energies between two excited states of argon ions containing more than one electron with comparably high energy levels in the order of $\sim 4000\,\mathrm{eV}$. Assuming a relative uncertainty of $0.01\,\%$ of the energy level calculations yields an uncertainty in the transition energy in the order of $1\,\mathrm{eV}$ which corresponds to a wavelength uncertainty of $\sim 0.2\,\mathrm{nm}$ which is larger than the width of an observed line. For instance, FAC calculations of a transition of helium-like argon from $1s5d\,^1\mathrm{D}\,J = 2$ to $1s4p\,^1\mathrm{P}\,J = 1$ yield a transition wavelength of $13.5176\,\mathrm{nm}$, whereas the NIST database provides $14.0233\,\mathrm{nm}$ extracted from the energy difference of both levels. A direct comparison between expected $1s5l - 1s4l'$ transitions up to $l = 2$ in the observed wavelength range is given in table 4.5.

Absolute energy levels higher than $1snl$ with $n > 5$ are not available in the NIST database, although $1snl - 1s5l'$ transitions with $n = 7, \ldots, 11$ are expected.
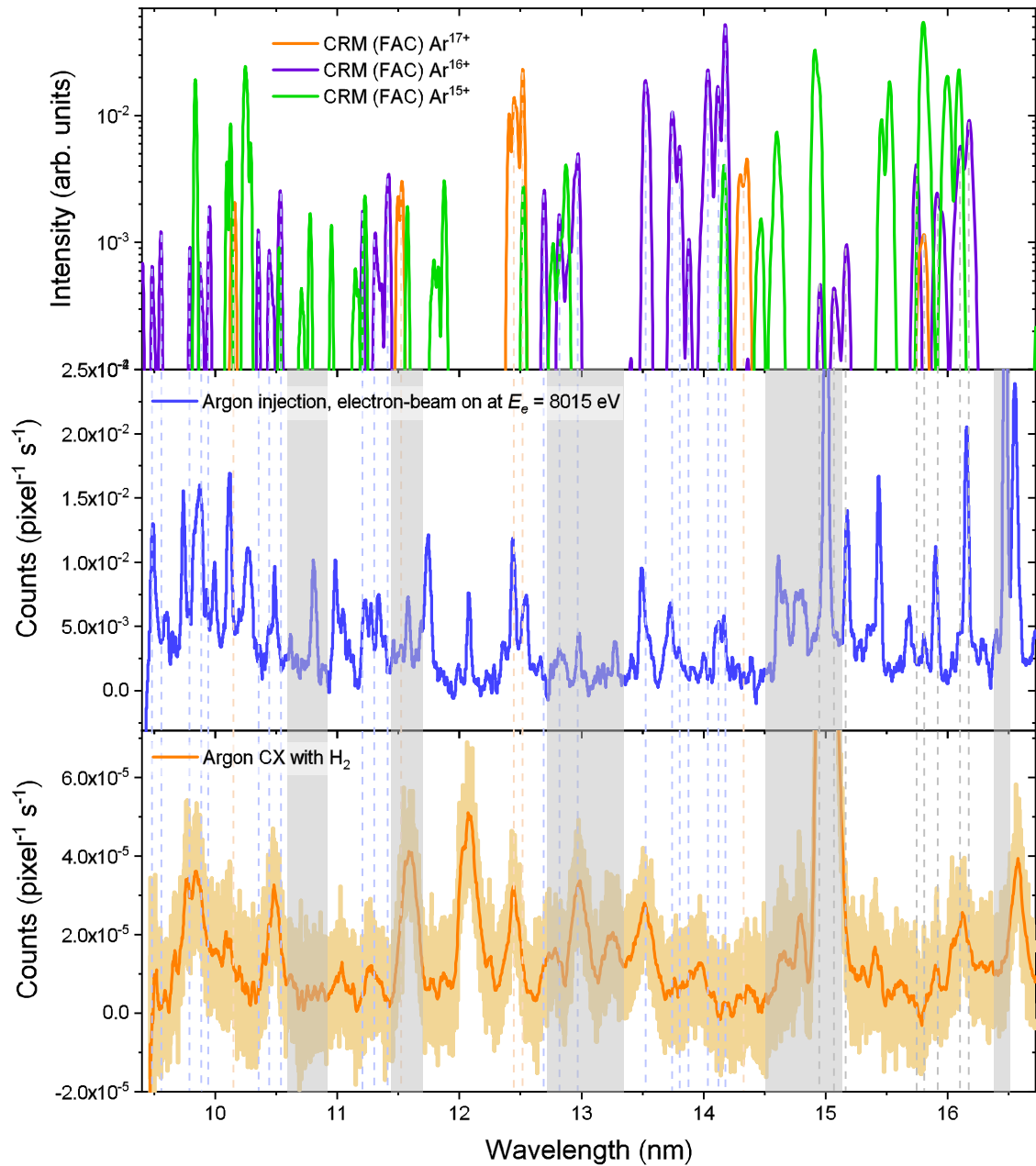
Figure 4.49: Top panel: collisional-radiative model for hydrogen-like, helium-like, and lithium-like transitions of argon ions with an electron-beam energy of 8015 eV. **Center panel:** direct excitation of highly charged argon from figure 4.48. **Bottom panel:** corresponding CX spectrum in MTM. The gray areas indicate transitions of highly charged oxygen investigated in section 4.4.2. Vertical dashed lines represent the transition wavelengths calculated with FAC in the top panel.

4.4.3.2 Hydrogen-like argon

For hydrogenic systems transitions from $n = 7, 8, 9 - n = 5$ and $n = 10 - n = 6$ are predicted in a wavelength range between $9\,\mathrm{nm}$ and $17\,\mathrm{nm}$. Transitions from higher states are not expected, since the highest populated level, according to MCLZ calculations, is $n = 10$ for the interaction of Ar^{18+} with H_2 (compare to figure 4.33). However, only the wavelength for the $5p\,J = 1/2 - 4s\,J = 1/2$ transition is identified in MTM to $\lambda = 12.445(1)\,\mathrm{nm}$. The value extracted from the NIST database is $\lambda_{\mathrm{NIST}} = 12.446\,152(10)\,\mathrm{nm}$, and the calculation performed with FAC yields $\lambda_{\mathrm{FAC}} = 12.4462\,\mathrm{nm}$, which is in a good agreement with the experimentally obtained transition wavelength. Nonetheless, according to the MCLZ calculation performed by the Kronos code, this transition is predicted to be the most intense. The predicted $n = 10 \to n = 6$ transition of hydrogen-like argon after capture at $\sim 15.7\,\mathrm{nm}$ was not observed, indicating that the $n = 10$ state is not populated by charge exchange for this collision.

In figure 4.50, the theoretical CX spectra for initially fully ionized and for hydrogen-like argon ions is compared to the experimentally obtained spectrum. In the top panel, the spectrum provided by the Kronos code for collisions of Ar^{18+} with molecular hydrogen at a collision energy of $10\,\mathrm{eV/u}$ and a low-energy l-distribution is illustrated as a solid green line. For comparison, a synthetic spectrum generated with FAC for the same collision with the same parameters is shown in orange. The corresponding transitions are labeled in green. Although the resulting ion after the reaction is hydrogenic, both codes yield diverging results, in particular, a difference in the transition wavelengths and moreover in intensity ratios can be observed. Cross-sections for CX of initially hydrogen-like argon are not available in the Kronos database. Instead, the charge exchange cross-section for collisions of Ar^{17+} is provided by the flexible atomic code CX model and illustrated in violet for collision with atomic hydrogen and blue for molecular hydrogen at a collision energy of $25\,\mathrm{eV/u}$, respectively.

In contrast to the predictions for the K-shell emission, significant differences in the line ratios are predicted for interaction with different neutral targets. However, no definite identification of spectral lines could be performed hitherto due to a lack of atomic transitions in standard databases and due to relatively high uncertainties in atomic structure calculations. An assignment of spectral lines would be highly speculative, and further analysis is not expressive and will not be performed within the frame of this work. Anyhow a first proof-of-principle measurement of charge exchange has been demonstrated for heavier elements in the EUV range where more cautious systematic investigations are crucial in order to identify the remaining transitions.
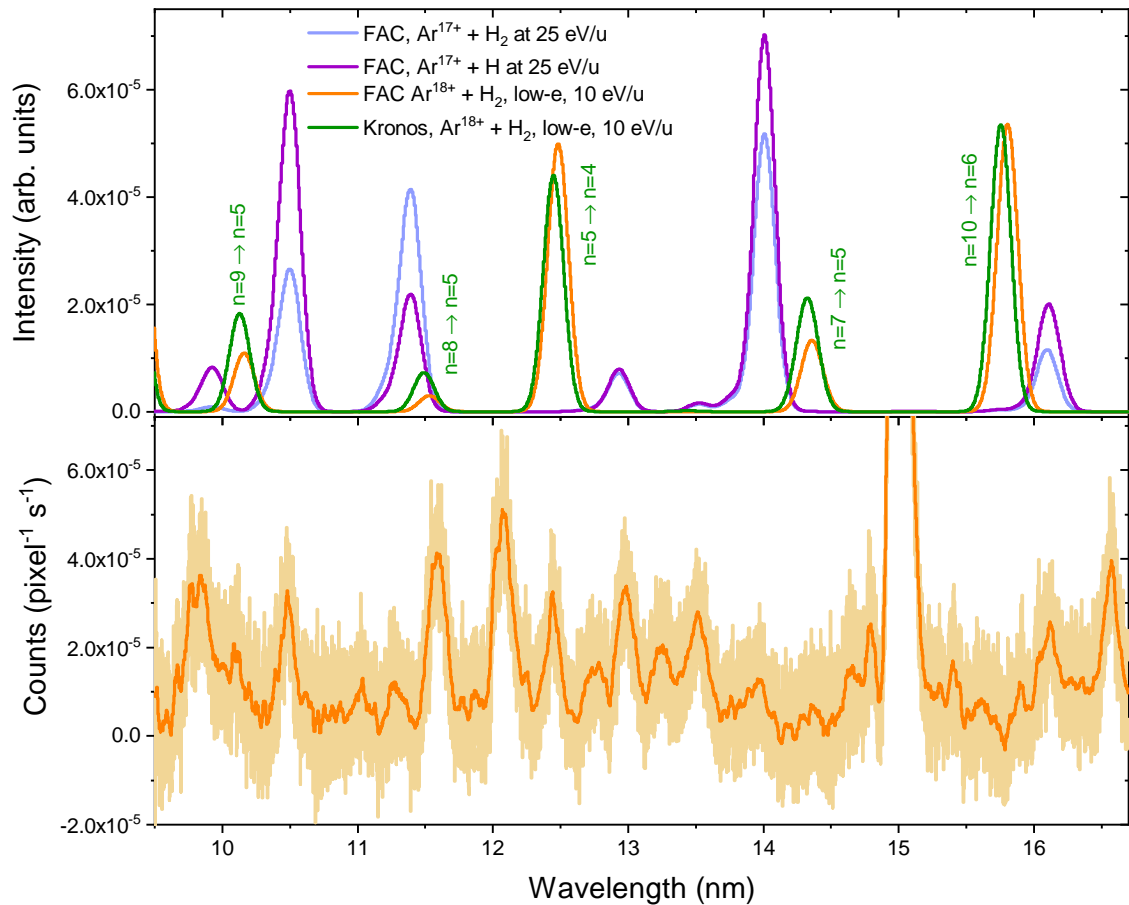
Figure 4.50: Top panel: Synthetic spectra for charge exchange between Ar^{18+} with molecular hydrogen in the EUV range, generated with Kronos and FAC. Calculation of Ar^{17+} with H and H_2 are performed with the FAC code. The cross-sections for this reaction are not available in the Kronos database. The hydrogenic transitions after electron capture are labeled correspondingly. **Bottom panel:** Experimental CX spectrum from figure 4.49.

5 Summary and outlook

In this work, a cryogenic electron beam ion trap for charge breeding of short-lived, rare isotopes was designed, assembled, characterized, and installed at the designated end station at the CANREB facility at TRIUMF in Vancouver, Canada. The compression of the electron-beam in the trap center was determined to $700\,\mathrm{A/cm^2}$ at a beam current of $64\,\mathrm{mA}$ and radius of $54\,\mathrm{\mu m}$ and extrapolated to $11\,000\,\mathrm{A/cm^2}$ at a maximum achieved electron-beam current of $1000\,\mathrm{mA}$, which is crucial in order to breed ions within a short time to high charge states. Furthermore, various studies were performed in order to investigate and characterize the properties of the electron beam, ion injection, ion extraction, and charge breeding of highly charged ions. The final commissioning of the EBIT as a charge breeder and integration into the CANREB facility will be completed in 2019.

Secondly, extensive investigation of the charge exchange process, where highly charged ions interact with neutral gas, was performed utilizing the FLASH-EBIT in Heidelberg, equipped with an extreme-ultraviolet spectrometer covering a wavelength range from $7\,\mathrm{nm}$ to $35\,\mathrm{nm}$, a vacuum-ultraviolet normal-incidence spectrometer for $35\,\mathrm{nm}$ to $150\,\mathrm{nm}$ and an X-ray detector for detection of higher energetic photons in an energy range of $350\,\mathrm{eV}$ to $30\,\mathrm{keV}$. The first proof-of-principle in-situ measurement of charge exchange in the EUV range in an electron-beam ion trap was presented. X-ray measurements were carried out for interaction of fully ionized and hydrogen-like argon with different target gases at different collision velocities.

Significant discrepancies between CX measurements of fully ionized argon interacting with neutral argon, compared to the results published by other groups [24, 32, 12, 11] using an EBIT were observed. Besides, a disagreement with prevailing theories of hydrogen-like systems after electron capture, like the multichannel Landau-Zener approach, as well as a disparity between theories among each other, were ascertained. These discrepancies were discussed extensively.

Furthermore, X-ray charge exchange measurements were performed with fully ionized sulfur as a projectile in order to provide a possible explanation for the observed emission-like line feature in galaxy clusters at $3.5\,\mathrm{keV}$ with a proposed origin in the decay of sterile neutrinos, which is a potential dark matter candidate. The capture of an electron from neutral gas into high Rydberg states and subsequent decay into the ground state leads to emission of an X-ray photon with an energy of $3.47(6)\,\mathrm{keV}$. Since hydrogen-like and fully

ionized sulfur is highly abundant in the interstellar medium, it can interact with atomic hydrogen and produce an emission line at this energy.

In addition, a comparison to various charge exchange models was performed. The theories are in a weak agreement with the experimental data, although the product ion after the reaction is a hydrogenic system. With the multichannel Landau-Zener approach, it is not possible to calculate the cross sections for electron capture into different angular momentum states, and thus, a distribution function has to be applied to the *n*-resolved cross-sections. In order to investigate capture into different *l*-states, a cascade model based on the flexible atomic code was developed, by reconstructing the experimental data. To extract conclusive information, the number of resolved lines has to be equal or larger than the number of the fit parameters, in particular, the number of allowed angular momenta, which is not given in most of the cases due to a poor spectral resolution of the detectors.

In the following, the results obtained from the measurements performed in this work will be discussed briefly.

X-ray charge exchange measurements of highly charged ions

In general, charge exchange measurements of fully ionized and hydrogen-like ions were performed by observation of *K*-shell X-rays with a silicon drift detector with a spectral resolution of FWHM $\approx 150\,\text{eV}$. The spectra were acquired by switching the electron beam on and off cyclically and simultaneously recording the X-ray spectrum as a function of the time within the cycle. During the beam-on mode, the ions were excited by electron impact. During the beam-off mode, the ions were magnetically confined, and only charge exchange led to emission of photons. The spectra were obtained for an initial electron-beam energy above the ionization threshold for the production of fully ionized ions. Here, initially entirely stripped and hydrogen-like systems emit *K*-shell X-rays. To extract the contribution of the initially bare system, a second spectrum slightly below this ionization threshold is acquired, normalized to a transition that is present in both spectra, and subtracted from the mixed spectrum.

Sulfur

Charge-exchange measurements were carried out with fully ionized and hydrogen-like sulfur interacting with molecular CS_2, according to the experimental technique described above. Systematic measurements with a variation of the injection pressure and electron-beam energy were performed. It has been demonstrated, that the observed unidentified emission line at $\sim 3.5\,\text{keV}$ in galaxy clusters with a proposed origin in the decay of sterile neutrinos, could be caused by charge exchange between fully ionized sulfur and atomic hydrogen, which

are both highly abundant in these astrophysical environments. A capture of an electron into a high Rydberg state of $n \geq 7$ in S^{16+} with subsequent decay into the ground state $n = 1$ produced an X-ray photon with an energy of $3.47(6)$ keV in this measurement. In the astrophysical modeling, performed in the publications of the proponents of dark matter decay, the included atomic data is lacking atomic transitions, in particular transitions from states $n \geq 5$. Since charge exchange is an efficient mechanism to populate this states, it should be included in the models in order to understand and interpret astrophysical spectra.

Furthermore, the data obtained during this work was compared to charge exchange models. The established distributions of angular momenta for capture into a specific principal quantum number n utilized by the multichannel Landau-Zener approach do not represent the experimental CX spectrum. The centroid of the high-energetic peak is overestimated to higher photon energies by the models. Only modification of the low-energy l-distribution, where the s-state is highly populated, could provide a good agreement with the experiment. This s-dominant capture is confirmed by the independent application of the Flexible-Atomic-Code cascade model in order to reconstruct the l-distribution. Almost 75 % of the electrons are captured into the $l = 0, n = 12$ state, according to the reconstruction results.

Argon

Accordingly, extensive studies of the interaction of the highly ionized species with neutral argon in the X-ray regime were carried out by variation of the axial trapping potential V_0 between 45 V and 1000 V in order to observe the change of the nl-population of the captured electron as a function of the collision energy, which is defined by V_0. No significant differences were observed, neither in the intensity ratios of the K-shell transitions nor in the hardness ratio, which is defined as the ratio of the integrated flux of $n \geq 3 \rightarrow n = 1$ transitions to the Lyman-α transition. Only a slightly increasing tendency of the hardness ratio with higher collision energies could be observed within the uncertainty range, contradicting the decreasing trend predicted by the classical-trajectory Monte-Carlo model, but in good accordance with the multichannel Landau-Zener approach. Furthermore, the significant discrepancy by a factor of two in the hardness ratio as a function of collision energy between various CX measurements of Ar^{18+} with neutral argon in EBITs and extraction measurements in gas cells is still an unresolved issue. The under- or overestimation of the collision energy is improbable since the slopes of the hardness ratio as a function of the collision energies are relatively flat with an absolute value of $\sim 4 \times 10^{-3}$ /eV in the extreme case of the CTMC model. Polarized emission induced by CX is also most unlikely since the predicted [74] and the measured degree of polarization [162] is in the order of ~ 0.05

for O^{5+} ions. Models or measurements for highly ionized argon ions are not available, so far. The influence on the hardness ratio by the magnetic field of the EBITs could also be excluded since no significant difference between measurements performed at $B = 6\,\text{T}$ and $B' = 3\,\text{T}$ was observed either in this experiment or in other experiments [11] with $B = 3\,\text{T}$ and $B' = 1\,\text{T}$. Another concern is the fact that the same measurement performed with similar experimental parameters in the same EBIT [24, 32] differed by $\sim 70\,\%$ in the hardness ratio. In conclusion, an unknown systematic effect causes the discrepancy between the charge exchange measurements, discussed above. This issue could not be resolved within the scope of this work.

Besides, no angular momentum distribution utilized by the MCLZ approach for collision with various neutral targets could represent the experimental spectrum. The most probable principal quantum number state is overestimated by the model. Only for CX of Ar^{18+} with neutral helium at high collision velocities in the order of $\sim 1000\,\text{eV/u}$, the center of the high-energetic peak is in agreement with the experiment, but the X-ray flux of $n \geq 3 \rightarrow n = 1$ is highly underestimated. However, this scenario is unrealistic, since the maximum applicable axial trapping potential is in the order of 3000 V, resulting in a maximum collision energy of $\sim 270\,\text{eV/u}$. Furthermore, the relative fraction of residual gas was estimated to $\sim 1\,\%$ for the measurement $Ar^{18+} + Ar$, and no significant effect of the residual gas, even if helium is the only contaminant, is expected.

Additionally, the interaction between Ar^{18+} and additional neutral targets, including molecular hydrogen, neon, and a mixture of neutral argon with residual gas, was studied. The hardness ratios with an axial trapping potential of $\sim 500\,\text{V}$ were determined to 0.54 ± 0.02, 0.75 ± 0.08, and 0.656 ± 0.001, respectively. No trivial scaling of the hardness ratio as a function of the ionization potential of the targets was observed, whereas the MCLZ approach predicts an increase with higher ionization energies.

For the injection of molecular hydrogen as a target, a dual injection system was installed and commissioned, consisting of a gas dosing valve for continuous projectile gas injection and a pulsed supersonic valve which provides gas pulses of a target gas with a duration of $\sim 60\,\mu\text{s}$. Since the pulsed system was not correctly adjusted in these measurements, the residual gas pressure in the magnet chamber increased steadily, leading to deteriorated trapping conditions.

Oxygen

Analogously, the charge exchange process of fully ionized and hydrogen-like oxygen with neutral O_2 was investigated in the X-ray domain. Oxygen is a low-Z ion, where the energetic difference between the Lyman-α transition at 653 eV and the highest expected Rydberg transition from $n = 5$ to the ground state at $\sim 836\,\text{eV}$ is comparably small, only

two lines, in particular, Lyman-α and Lyman-β could be resolved with the silicon drift detector. Since the actual energy-dependent quantum efficiency of the detector is not known and varies by two orders of magnitude in this energy range, quantitative analysis in terms of line ratios could not be performed conclusively.

EUV charge exchange measurements

Oxygen

To bypass the issue of low spectral resolution present in the X-ray domain, the investigated spectral domain was extended to longer wavelengths of 7 nm to 20 nm, where a larger number of spectral lines can be observed. In this work, a first proof-of-principle in-situ charge exchange measurement in an electron beam ion trap, utilizing a high-resolution grazing-incidence EUV spectrometer equipped with a mechanical shutter, was demonstrated. Here the spectra during the electron-beam on mode and the magnetic trapping mode of highly charged oxygen were separated. The spectral resolution was improved by a factor of two compared to other publications [36] where the oxygen ions were impinged onto a gas cell. One spectral line resulting from an $n = 3 \rightarrow n = 2$ transition of initially fully-ionized oxygen following charge exchange with molecular oxygen was observed at 10.24 nm. The $n = 6 \rightarrow n = 3$ transition at ~ 17.1 nm was not observed, indicating that the $n = 6$ state is not populated by charge exchange, contradicting the MCLZ theory, which predicts a population of $n = 5$ and $n = 6$ at the typical collision energies in an EBIT. In contrast, the classical over-the-barrier model anticipates the population of $n = 5$.

For single-electron capture into the initially hydrogen-like oxygen, the predicted state with a population of $\geq 99.9\,\%$ by MCLZ is $1s5l$. In magnetic-trapping mode $1s5l - 1s2l'$, $1s4l - 1s2l'$, and $1s3l - 1s2l'$ transitions were identified. Transitions from higher excited states are outside of the investigated spectral range. However, a direct comparison to synthetic spectra obtained from MCLZ calculations and with the FAC cascade model indicates, that the population of $n = 3$ is underestimated by theory. This suggests that either the assumption of capture into $n = 5$, exclusively, is not correct, or that double-electron capture with subsequent autoionization, leading to an increased population of $n = 3$, is underestimated. For more expressive assertions, further systematic investigations are required.

Argon

Analogously, charge-exchange measurements in the EUV range in highly charged argon interacting with molecular hydrogen were carried out. Only one transition from initially fully ionized argon, in particular, the $5p\,(J = 1/2) - 4s\,(J = 1/2)$ transition, has been identified in the magnetic-trapping mode to $\lambda = 12.445(1)$ nm. Due to a lack of atomic

transitions in standard wavelength catalogs, it was not possible to identify most of the electronic transitions. Calculations of transitions between excited states are not reliable with an uncertainty in the order of $\sim 0.2\,\mathrm{nm}$ in order to identify the spectral lines assuredly. Furthermore, the CX spectrum contains signatures from residual oxygen from previous measurements. The remaining unidentified spectral lines could also originate from other charge states. For further analysis, it is crucial to identify all transitions in a systematic study. A combination of the measurements in the EUV range and simultaneously in the X-ray range could serve in future experiments as a basis for the extraction of the relative nl-population.

Comparison with charge exchange models

As demonstrated in various charge exchange measurements, in particular, observation of K-shell X-rays [24, 32, 12, 11, 110, 109], the intensity ratios of spectral lines are strongly dependent on the initial population of the angular momentum states of the captured electrons. Thus, detailed knowledge of this distribution is crucial in order to understand the nature of the charge-exchange process.

All measurements presented in this thesis were compared to different charge-exchange models, in particular, the multichannel Landau-Zener method. For capture into an initially fully ionized system, the nl-states in which the electron is captured, are degenerate. Thus, established distributions of angular momenta have to be multiplied to the total n-resolved cross-section. Dependent on the collision energy, different l-distributions are applicable. However, this approach is not always valid and does not necessarily represent the actual relative population. As demonstrated in the X-ray measurements of fully-stripped sulfur, the electron is captured preferably into $l = 0$. This has been confirmed by a modified low-energy distribution applied with the MCLZ approach, and by the cascade model for the reconstruction of the l-population.

Nevertheless, the developed FAC reconstruction model has to be utilized cautiously. If the number of free parameters exceeds the number of spectral features, which is the case for the X-ray measurements due to a comparably low spectral resolution of the SDD, the extracted information of the l-distribution is possibly not conclusive. At least a tendency of the most probable l-states can be extracted. Besides, the different X-ray and EUV spectra could not be represented by the MCLZ approach with the established l-state distributions. Furthermore, different collisional-energy dependent l-distributions had to be applied to receive at least a qualitative agreement of the ratio between higher Rydberg transitions n to the ground state $n = 1$ and Lyman-α, although the trapping conditions, in particular, the collision energy, were kept relatively constant. This indicates that the l-distribution is not exclusively defined by the collision energy. According to the MCLZ approach, only

the n-resolved cross sections depend on the collision energy. The choice of the neutral target in the MCLZ calculation does not affect the theoretical shape of the spectrum, in contradiction to the present measurements and the measurements performed with a microcalorimeter [109, 110]. Only the most probable principal quantum number n in which the electron is captured, according to the model, is affected.

Furthermore, only a few neutral targets and highly ionized projectiles are available in the Kronos database, reducing the possible combinations in order to benchmark the theory with experimental data. Also, the cross-sections for the most probable n-states are not well represented by the MCLZ approach, as demonstrated in the EUV CX measurements with O^{8+} colliding with O_2. According to the theory, the $n = 5$ and $n = 6$ states should be populated almost equally at the given collision energies. The $n = 6$ to $n = 3$ transition was not observed in the experiment, implying that the population of $n = 6$ can be considered as negligible. Information on the $n = 5$ population can not be provided, because the $n = 5$ to $n = 3$ transition is outside of the low-energetic and the $n = 5$ to $n = 2$ transition outside of the high-energetic investigated spectral range. For further comparisons the measurement has to be studied systematically, covering a broader wavelength range.

Additionally, independent MCLZ approaches utilized by different codes were compared in this work. Although all models are based on the same numerical approach and the resulting system after electron transfer is hydrogenic, significant discrepancies in the synthetic K-shell spectra were observed for equal parameters and l-distributions. The disagreement is even more drastic for helium-like systems after electron capture, as demonstrated in the chapter about oxygen and argon charge exchange in the EUV range. One contribution of this discrepancy can be explained by different approaches of the implementation of the energy levels of the final states and the corresponding transition rates. The values utilized by the Kronos MCLZ model are extracted from the NIST database. In the case of missing data, in particular, for highly excited states, the values are extrapolated by scaling relations. To remark is, that not all possible transitions are implemented in the Kronos code. Only l-resolved and not J-resolved transitions are considered, which reduces the number of possible, allowed transitions. By contrast, the levels and rates implemented in the FAC model are based on ab-initio calculations. Since the transitions expected in the EUV range are between two excited states, the relative uncertainty of the transition wavelength becomes comparably large, which makes a reconstruction of the l-state distribution challenging, although the absolute uncertainty of the energy levels is in the order of less than $1\,\mathrm{eV}$ for helium-like system.

Moreover, the hardness ratio has been investigated, which is commonly used to provide qualitative information on the collision energy. According to MCLZ, the hardness ratio should increase with higher collision velocities. By contrast, the classical-trajectory Monte-Carlo method predicts a decrease for the same reaction. Although the projectile is a

one-electron system after the collision, the two well-established theories predict contradicting results. A comparison with an approach describing the system as a quasi-molecule during the collision would be profitable. Models like the quantum-mechanical molecular-orbital close-coupling (QMOCC) require fewer approximations and assumptions than MCLZ, but unfortunately, such calculations are only present for relatively light projectiles, so far. However, a single quantity like an intensity ratio, in particular, the hardness ratio, should be utilized cautiously since it was introduced historically by the community of X-ray astronomy as an auxiliary quantity due to a limited spectral resolution [136].

Conclusion

In this work, it has been shown, that a recently observed emission line at 3.5 keV in galaxy clusters with a proposed origin in dark matter decay, most likely originates from charge exchange of fully ionized sulfur with neutral gas. High-energetic states are populated efficiently, leading to emission of X-ray photons with comparably high energy. These transitions are mostly missing in standard wavelength catalogs and databases. This effect is usually ignored in astrophysical modeling resulting in misidentification of spectral lines and misinterpretation of astrophysical spectra. In order to understand and interpret these spectra, the charge-exchange process has to be included in the modeling procedure. For reliable modeling, a well-understood theory of charge exchange is required, in particular, the population of angular momenta of the captured electron since the intensities of high-energetic transitions are highly sensitive to this l-distributions. In order to benchmark those theories, laboratory charge-exchange measurements are crucial. Electron beam ion traps are suitable devices for production and trapping of ions for spectroscopic investigations. However, with the argon CX measurements performed in this work, it has been shown that similar measurements in various EBITs provided different results, which indicate unidentified systematics.

Furthermore, the commonly used theoretical l-state distributions for capture into initially bare ions in CX models, like the MCLZ approach, are not reliable, and the spectral resolution of the X-ray detectors in the investigated range of K-shell transitions is insufficient to extract conclusive information. This issue can be bypassed by investigation of a spectral range with more spectral lines, like the L-shell or M-shell transitions in the extreme-ultraviolet domain. For this purpose, charge-exchange measurements of highly charged oxygen and argon ions were performed inside an electron beam ion trap by utilization of an extreme-ultraviolet spectrometer. For the argon CX measurements, only a few lines could be identified due to a lack of atomic data and high uncertainties of theoretical transition energies. For the oxygen measurements, a discrepancy between the theoretical and experimentally obtained n-state population has been observed. Since more than one n-state was populated, contradicting

the theory, the number of fit parameters for the reconstruction of the l-state distribution exceeded the number of observed spectral lines. To obtain conclusive information about this distribution, simultaneous measurements in the EUV and X-ray domain by the use of a high-resolution X-ray detector are required in future experiments.

Finally, a tabulated overview of the charge-exchange measurements performed in this work is given in table 5.1, where the projectile ion, the target species, the investigated spectral domain, and brief comments are given.

Outlook

Various studies have been performed in this work in order to investigate the charge-exchange process. The obtained spectra could not be adequately represented by charge-exchange models, in particular, due to a lack of knowledge of the initial distribution of angular momentum states for single-electron capture. To investigate this process cautiously and to obtain quantitative results for the l-distribution, extensive systematic measurements by utilization of high-resolution detectors, such as microcalorimeters are crucial in the future. Furthermore, simultaneous measurements in different wavelength ranges in-situ and in extraction experiments with controlled conditions of the ion charge state and collision energy would provide profitable results to resolve the still existing discrepancy.

Finally, to demonstrate that a reconstruction of the distribution of angular momenta is possible, at least for hydrogenic projectiles after electron transfer, a synthetic spectrum, mimicking an expected charge-exchange spectrum, as expected for microcalorimeter measurements, is presented in figure 5.1 with the corresponding reconstruction results. The synthetic CX spectrum of fully ionized argon with an overlayed artificial noise is generated with FAC, convolved with a Gaussian with a width of FWHM $= 4.7$ eV corresponding to the spectral resolution of a microcalorimeter is represented by an orange curve. Thereby, the coefficients of the spectral basis vectors, described in chapter 2.3.4.5 for capture into different angular momentum states of $n = 9$, are multiplied with the corresponding fraction of the low-energy distribution, shown as orange bars in the inset of the figure. For the reconstruction of the l-state distribution, only the blue-shaded regions of the K-shell X-rays observed in the experiment and the investigated EUV range between 8 nm and 25 nm are considered as an input. The reconstruction results show a good agreement of the initial and the reconstructed l-state distribution. Furthermore, this approach enables the prediction of the relative intensities of the L- and M-shell transitions between 200 eV and 1100 eV. These results suggest the reliability of the developed cascade model for hydrogenic systems in order to extract information about the initial distribution of angular momenta of the transferred electron. To obtain such conclusive results in real experiments, simultaneous investigations of charge exchange in the X-ray range with a microcalorimeter

Table 5.1: Overview of the CX measurements performed in this work.

| Projectile	Target	Spectral range	Hardness ratio		Comments
			Exp.	Theo.	
S^{15+}	CS_2	$2-4\,\text{keV}$	0.130(4)	0.148	MCLZ, H target
S^{16+}	CS_2	$2-4\,\text{keV}$	0.72(1)	0.792	Exp.: s-dominant capture, MCLZ low-e, H target
Ar^{17+}	Ar + res. gas	$3-5\,\text{keV}$	0.137(1)	0.171	MCLZ, H_2 target
Ar^{17+}	H_2	$3-5\,\text{keV}$	0.140(3)	0.171	MCLZ, H_2 target
Ar^{18+}	Ar + res. gas	$3-5\,\text{keV}$	0.656(1)	–	High $\text{Ly}_\alpha/\text{Ly}_{n\geq6\rightarrow1}$ ratio
Ar^{18+}	H_2	$3-5\,\text{keV}$	0.54(2)	0.779	low-e distribution (MCLZ)
Ar^{18+}	H_2	$9-17\,\text{nm}$	–	–	One H-like line identified at 12.445(1) nm (5p − 4s) predicted (MCLZ) $n = 10 \rightarrow n = 6$ not visible
Ar^{18+}	Ne	$3-5\,\text{keV}$	0.75(8)	0.87(1)	low-e distribution (MCLZ), interpolated
Ar^{18+}	Ar	$3-5\,\text{keV}$	0.804(30)	0.790(5)	low-e distribution (MCLZ), interpolated
O^{7+}	O_2	$0.5-1\,\text{keV}$	–	–	Insufficient spectral resolution
O^{8+}	O_2	$0.5-1\,\text{keV}$	–	–	Insufficient spectral resolution
O^{7+}	O_2	$8-20\,\text{nm}$	–	–	Capture into $n = 3, 4, 5$
O^{8+}	O_2	$8-20\,\text{nm}$	–	–	MCLZ: $n = 5$ H-like line at 10.2 nm ($n = 3 \rightarrow n = 2$) MCLZ: $n = 5, 6$
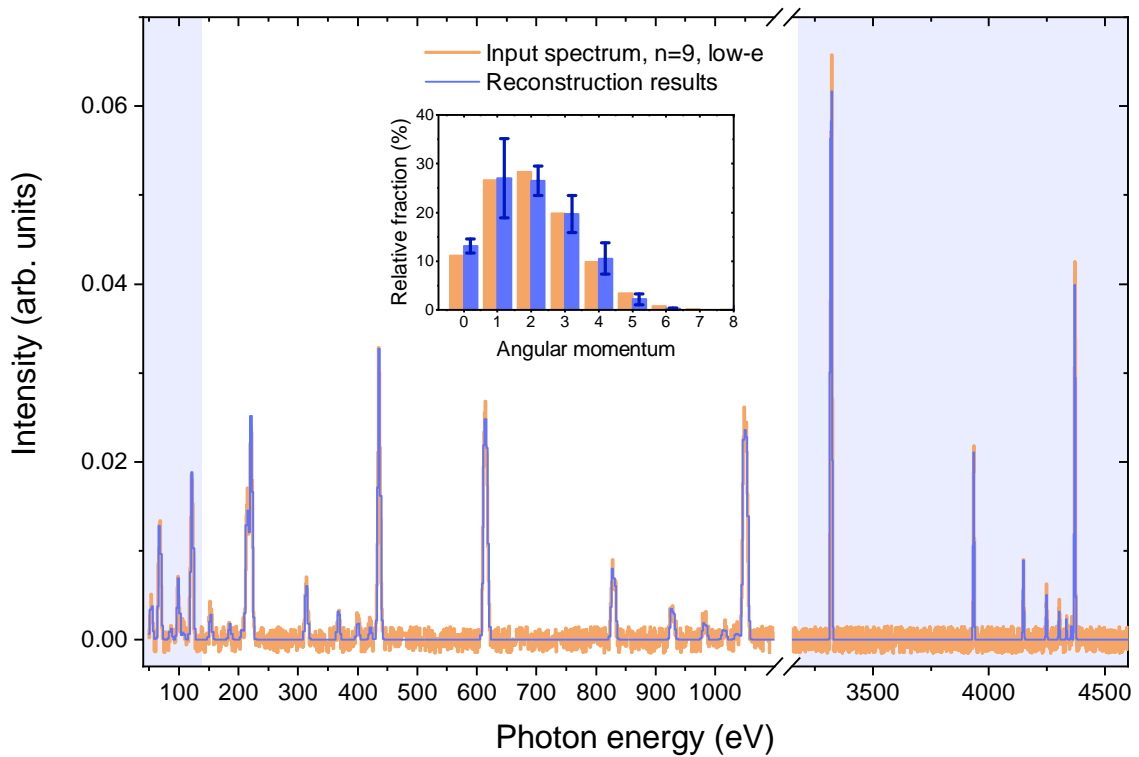
Figure 5.1: A synthetic CX spectrum of Ar^{18+}, which is expected in simultaneous EUV measurements with a grating spectrometer and X-ray measurements with a microcalorimeter is plotted in orange with the corresponding relative fraction of angular momenta of the captured electrons. The blue curve represents the reconstruction results by consideration of the blue-shaded regions, only.

and the EUV range are required in future measurements. Additionally, it has been shown, that it is possible to investigate charge exchange in the VUV domain with the 3-meter normal-incidence spectrometer in the zeroth-order diffraction. In future experiments a scheme will be developed, which allows for CX measurements in the the $\sim 30\,\text{nm} - 200\,\text{nm}$ range, which is of great interest for the astrophysical community, in particular for possible charge-exchange induced transitions at the interface between hot and cold galactic matter [84]. These experiments are crucial to benchmark the theories, which are utilized for astrophysical modeling. Improvements from the experimental side, as well as from the theoretical side, are neccessary in order to understand and interpret astrophysical spectra obtained by future space missions, like Athena or XRISM.

6 Abbreviations and symbols

Abbreviations

ADC	Analog-to-digital converter
AFG	Arbitrary function generator
ARIEL	Advanced Rare IsotopE Laboratory
CANREB	Canadian rare isotope facility with electron beam ion source
CCD	Charge-coupled device
COB	Classical over-the-barrier
CTMC	Classical trajectory Monte-Carlo
CX	Charge exchange
DEC	Double-electron capture
DR	Dielectronic recombination
DT	Drift tube
EBIS	Electron beam ion source
EBIT	Electron beam ion trap
eLINAC	Electron linear accelerator
EUVE	Extreme Ultraviolet Explorer
FAC	Flexible atomic code
HV	High voltage
EUV	Extreme ultraviolet
HCI	Highly charged ion
HRI	High Resolution Imager
HV	High voltage
LZ	Landau-Zener
LIS	Laser ion source
MCDF	Multi-configuration Dirac-Fock

MCHF	Multi-configuration Hartree-Fock
MCLZ	Multichannel Landau-Zener
MCP	Microchannel plate
MOS	Metal oxide semi-conductor
MPA	Multi-parameter data acquisition
MTM	Magnetic-trapping mode
OFHC	Oxygen-free high thermal conductivity
PEEK	Polyether ether ketone
PHA	Pulse height analyzer
PTFE	Polytetrafluoroethylene
QMOCC	Quantum Mechanical Molecular-Orbital Close-Coupling
RF	Radio frequency
RMBPT	Relativistic Many-Body Perturbation Theory
ROSAT	Röntgen Satellite
RR	Radiative recombination
SDD	Silicon drift detector
SEC	Single-electron capture
SNR	Supernova Remnant
SVA	Sampling voltage analyzer
TDC	Time-to-digital converter
TMP	Turbomolecular pump
TOF	Time-of-flight
TRIUMF	Orig.: TRI University Meson Facility
UHV	Ultra-high vacuum
ULF	Unidentified line feature
VUV	Vacuum ultraviolet
WFC	Wide Field Camera

Symbols

Angular momentum	L
Atomic mass unit	$u = 1.660539040(20) \times 10^{-27}\,\mathrm{kg}$
Bohr radius	$a_0 \approx 0.52917721067(12) \times 10^{-10}\,\mathrm{m}$
Boltzmann constant	$k_\mathrm{B} \approx 1.38064852(79) \times 10^{-23}\,\mathrm{J/K}$
Dirac matrix	$\vec{\alpha}$
Electric current	I
Electric field	$\vec{E}$
Electron mass	$m_\mathrm{e} = 9.10938356(11) \times 10^{-31}\,\mathrm{kg}$
Electrostatic potential	V, Φ
Elementary charge	$e = 1.6021766208(98) \times 10^{-19}\,\mathrm{C}$
Energy	E
Fine-structure constant	$\alpha = e^2/\left(4\pi\epsilon_0\hbar c\right) \approx 0.0072973525664(17)$
Frequency	ν
Hamilton operator	$\widehat{\mathrm{H}}$
Imaginary number	$\mathrm{i} = \sqrt{-1}$
Kinetic energy	E_kin
Magnetic field	$\vec{B}$
Momentum	p
Nuclear charge	Z
Orbital quantum number	l
Pauli matrix	σ_i
Permittivity of free space	$\epsilon_0 = {}^1\!/\!_{\mu_0 c_0^2} \approx 8.8541878176 \times 10^{-12}\,\mathrm{A\,s/(V\,m)}$
Planck constant	$h = 6.626070150(81) \times 10^{-34}\,\mathrm{J\,s}$
Proton mass	$m_\mathrm{P} \approx 1.672621898(21) \times 10^{-27}\,\mathrm{kg}$
Reduced Planck constant	$\hbar = h/2\pi$
Rydberg energy	$R_y = 1/2\,\alpha^2 m_e c^2 \approx 13.605693009(84)\,\mathrm{eV}$
Speed of light in vacuum	$c_0 = 299\,792\,458\,\mathrm{m/s}$
Spin	$\vec{S}$
Spin quantum number	s

Total angular momentum	$\vec{J}$
Total $\vec{J}$ quantum number	j
Vacuum permeability	$\mu_0 = 4\pi \times 10^{-7}\,\text{H/m}$
Voltage	U
Wavelength	λ

7 Bibliography

References

[1] accessed on 04.04.2019. URL: https://heasarc.gsfc.nasa.gov/docs/rosat/hyakutake_caption.html (cit. on p. 11).

[2] accessed on 24.10.2018. URL: http://henke.lbl.gov/optical_constants/filter2.html (cit. on p. 69).

[3] accessed on 09.05.2019. URL: https://heasarc.gsfc.nasa.gov/docs/xrism/about/ (cit. on p. 126).

[4] accessed on 13.05.2019. URL: http://www.med.harvard.edu/jpnm/physics/refs/xrayemis.html (cit. on p. 129).

[5] K. Abrahamsson, G. Andler, L. Bagge, E. Beebe, P. Carlé, H. Danared, S. Egnell, K. Ehrnstén, M. Engström, C.J. Herrlander, J. Hilke, J. Jeansson, A. Källberg, S. Leontein, L. Liljeby, A. Nilsson, A. Paal, K.-G. Rensfelt, U. Rosengård, A. Simonsson, A. Soltan, J. Starker, M.af Ugglas, and A. Filevich. "CRYRING — a synchrotron, cooler and storage ring". *Nuclear Instruments and Methods in Physics Research Section B: Beam Interactions with Materials and Atoms* 79.1 (1993), pp. 269–272. DOI: https://doi.org/10.1016/0168-583X(93)95341-2 (cit. on p. 45).

[6] V. A. Abramov, F. F. Baryshnikov, and V. S. Lisitsa. "Charge transfer between hydrogen atoms and the nuclei of multicharged ions with allowance for the degeneracy of the final states". *Sov. Phys. JETP* 3 (1978), p. 47 (cit. on pp. 38, 117).

[7] R Abrines and I. C. Percival. "Classical theory of charge transfer and ionization of hydrogen atoms by protons". *Proceedings of the Physical Society* 88 (1966), pp. 861–872. DOI: https://doi.org/10.1088/0370-1328/88/4/306 (cit. on p. 33).

[8] F. A. Aharonian and et al. "Hitomi Constraints on the 3.5 keV Line in the Perseus Galaxy Cluster". *The Astrophysical Journal Letters* 837.1 (2017), p. L15. DOI: https://doi.org/10.3847/2041-8213/aa61fa (cit. on pp. 106, 124, 125).

[9] R. Ali, P. Beiersdorfer, C. L. Harris, and P. A. Neill. "Charge-exchange x-ray spectra: Evidence for significant contributions from radiative decays of doubly excited states". *Phys. Rev. A* 93 (1 2016), p. 012711. DOI: https://doi.org/10.1103/PhysRevA.93.012711 (cit. on pp. 26, 173).

[10] R. Ali, P. A. Neill, P. Beiersdorfer, C. L. Harris, M. J. Raković, J. G. Wang, D. R. Schultz, and P. C. Stancil. "On the Significance of the Contribution of Multiple-Electron Capture Processes to Cometary X-Ray Emission". *The Astrophysical Journal* 629.2 (2005), pp. L125–L128. DOI: https://doi.org/10.1086/447768 (cit. on pp. 26, 173).

[11] F. I. Allen, C. Biedermann, R. Radtke, G. Fussmann, and S. Fritzsche. "Energy dependence of angular momentum capture states in charge exchange collisions between slow highly charged argon ions and argon neutrals". *Phys. Rev. A* 78 (3 Sept. 2008), p. 032705. DOI: https://doi.org/10.1103/PhysRevA.78.032705 (cit. on pp. 126, 183, 186, 188).

[12] Frances Allen. "Electron Capture by Highly Charged Ions from Surfaces and Gases". PhD thesis. Humboldt-Universität zu Berlin, 2008 (cit. on pp. 151, 152, 154, 183, 188).

[13] Daniel Altmann. "Inbetriebnahme eines gepulsten Gasinjektionssystems für Ladungsaustauschmessungen von O^{8+} und $O^{7}+$ mit H_2 in einer Elektronenstrahl-Ionenfalle". Bachelor thesis. Ruprecht-Karls-Universität Heidelberg, 2019 (cit. on pp. 147, 176).

[14] K. Altwegg, H. Balsiger, and J. Geiss. "Composition of the Volatile Material in Halley's Coma from In Situ Measurements". *Space Science Reviews* 90.1 (1999), pp. 3–18. DOI: https://doi.org/10.1023/A:1005256607402 (cit. on p. 9).

[15] "An unexpectedly low oscillator strength as the origin of the Fe xvii emission problem". *Nature* 492 (2012), pp. 225–228. DOI: https://doi.org/10.1038/nature11627 (cit. on p. 14).

[16] M. E. Anderson, E. Churazov, and J. N. Bregman. "Non-detection of X-ray emission from sterile neutrinos in stacked galaxy spectra". *Monthly Notices of the Royal Astronomical Society* 452.4 (2015), pp. 3905–3923. DOI: https://doi.org/10.1093/mnras/stv1559 (cit. on p. 106).

[17] H. A.Rowland. "XXIX. On concave gratings for optical purposes". *The London, Edinburgh, and Dublin Philosophical Magazine and Journal of Science* 16.99 (1883), pp. 197–210. DOI: https://doi.org/10.1080/14786448308627419 (cit. on p. 71).

[18]   X. Barcons, D. Barret, A. Decourchelle, J. W. den Herder, A. C. Fabian, H. Matsumoto, D. Lumb, K. Nandra, L. Piro, R. K. Smith, and R. Willingale. "Athena: ESA's X-ray observatory for the late 2020s". *Astronomische Nachrichten* 338.2-3 (2017), pp. 153–158. DOI: https://doi.org/10.1002/asna.201713323 (cit. on p. 126).

[19]   T. M. Baumann. "Entwicklung eines Gitterspektrometers zur Untersuchung vakuumultravioletter Strahlung von hochgeladenen Ionen" (2008) (cit. on pp. 68, 72, 162).

[20]   T. M. Baumann. "Spektroskopische Untersuchungen resonanter Rekombinationsprozesse an hochgeladenem Silizium in einer Elektronenstrahl-Ionenfalle". Dissertation. Ruprecht-Karls-Universität Heidelberg, 2012 (cit. on pp. 49, 72, 74).

[21]   P. Beiersdorfer, M. Bitter, M. Marion, and R. E. Olson. "Charge-exchange-produced K-shell x-ray emission from Ar^{16+} in a tokamak plasma with neutral-beam injection". *Phys. Rev. A* 72 (3 Sept. 2005), p. 032725. DOI: https://doi.org/10.1103/PhysRevA.72.032725 (cit. on p. 126).

[22]   P. Beiersdorfer, K. R. Boyce, G. V. Brown, H. Chen, S. M. Kahn, R. L. Kelley, M. May, R. E. Olson, F. S. Porter, C. K. Stahle, and W. A. Tillotson. "Laboratory Simulation of Charge Exchange-Produced X-ray Emission from Comets". *Science* 300 (2003), pp. 1558–1560. DOI: https://doi.org/10.1126/science.1084373 (cit. on pp. 11, 12, 108, 157).

[23]   P. Beiersdorfer, C. M. Lisse, R. E. Olson, G. V. Brown, and H. Chen. "X-Ray Velocimetry of Solar Wind Ion Impact on Comets". *The Astrophysical Journal* 549.1 (2001), pp. L147–L150. DOI: https://doi.org/10.1086/319143 (cit. on p. 151).

[24]   P. Beiersdorfer, R. E. Olson, G. V. Brown, H. Chen, C. L. Harris, P. A. Neill, L. Schweikhard, S. B. Utter, and K. Widmann. "X-Ray Emission Following Low-Energy Charge Exchange Collisions of Highly Charged Ions". *Phys. Rev. Lett.* 85 (24 2000), pp. 5090–5093. DOI: https://doi.org/10.1103/PhysRevLett.85.5090 (cit. on pp. 126, 151–154, 183, 186, 188).

[25]   P. Beiersdorfer, L. Schweikhard, P. Liebisch, and G. V. Brown. "X-Ray Signature of Charge Exchange in the Spectra of L-Shell Iron Ions". *The Astrophysical Journal* 672.1 (2008), pp. 726–732. DOI: https://doi.org/10.1086/522617 (cit. on p. 139).

[26]   Peter Beiersdorfer. "Laboratory X-Ray Astrophysics". *Annual Review of Astronomy and Astrophysics* 41.1 (2003), pp. 343–390. DOI: https://doi.org/10.1146/annurev.astro.41.011802.094825 (cit. on pp. 14, 107, 151).

[27] C. Beilmann, Z. Harman, P. H. Mokler, S. Bernitt, C. H. Keitel, J. Ullrich, and J. R. Crespo López-Urrutia. "Major role of multielectronic K-L intershell resonant recombination processes in Li- to O-like ions of Ar, Fe, and Kr". *Phys. Rev. A* 88 (6 2013), p. 062706. DOI: https://doi.org/10.1103/PhysRevA.88.062706 (cit. on p. 25).

[28] C. Beilmann, P. H. Mokler, S. Bernitt, C. H. Keitel, J. Ullrich, J. R. Crespo López-Urrutia, and Z. Harman. "Prominent Higher-Order Contributions to Electronic Recombination". *Phys. Rev. Lett.* 107 (14 2011), p. 143201. DOI: https://doi.org/10.1103/PhysRevLett.107.143201 (cit. on p. 25).

[29] C. Beilmann, O. Postavaru, L. H. Arntzen, R. Ginzel, C. H. Keitel, V. Mäckel, P. H. Mokler, M. C. Simon, H. Tawara, I. I. Tupitsyn, J. Ullrich, J. R. Crespo López-Urrutia, and Z. Harman. "Intershell trielectronic recombination with K-shell excitation in Kr^{30+}". *Phys. Rev. A* 80 (5 2009), p. 050702. DOI: https://doi.org/10.1103/PhysRevA.80.050702 (cit. on p. 25).

[30] Christian Beilmann. "Über die Stärke mehrelektronischer Resonanzen bei der Photorekombination und -ionisation". Dissertation. Ruprecht-Karls-Universität Heidelberg, 2012 (cit. on p. 25).

[31] S. Bernitt. "Resonante Anregung astrophysikalischer Röntgen-Übergänge in hochgeladenen Eisenionen mit dem Freie-Elektronen-Laser LCLS". Dissertation. Ruprecht-Karls-Universität Heidelberg, 2013 (cit. on p. 70).

[32] Gabriele L. Betancourt-Martinez, Peter Beiersdorfer, Gregory V. Brown, Richard L. Kelley, Caroline A. Kilbourne, Dimitra Koutroumpa, Maurice A. Leutenegger, and F. Scott Porter. "Observation of highly disparate K-shell x-ray spectra produced by charge exchange with bare mid-Z ions". *Phys. Rev. A* 90 (5 2014), p. 052723. DOI: https://doi.org/10.1103/PhysRevA.90.052723 (cit. on pp. 115, 122, 126, 139, 151, 152, 154, 183, 186, 188).

[33] M. A. Blessenohl. In preparation. Dissertation. Ruprecht-Karls-Universität Heidelberg, 2019 (cit. on pp. 95, 96).

[34] M. A. Blessenohl, S. Dobrodey, C. Warnecke, M. K. Rosner, L. Graham, S. Paul, T. M. Baumann, Z. Hockenbery, R. Hubele, T. Pfeifer, F. Ames, J. Dilling, and J. R. Crespo López-Urrutia. "An electron beam ion trap and source for reacceleration of rare-isotope ion beams at TRIUMF". *Review of Scientific Instruments* 89.5 (2018), p. 052401. DOI: https://doi.org/10.1063/1.5021045 (cit. on pp. 49, 50, 52, 62, 64, 80, 82–84, 86, 87, 89–91).

[35] K. Bockasten and K. B. Johansson. "The Spectrum of O V". *Ark. Fys. (Stockholm)* 38 (1968), pp. 563–584 (cit. on pp. 161, 163).

[36] D. Bodewits. "Cometary X-rays: solar wind charge exchange in cometary atmospheres". PhD thesis. Rijksuniversiteit Groningen, 2007 (cit. on pp. 12, 27, 187).

[37] N. Bohr. "On the Constitution of Atoms and Molecules". *Philosophical Magazine* 26 (1913), pp. 1–25 (cit. on p. 17).

[38] A. Boyarsky, J. Franse, D. Iakubovskyi, and O. Ruchayskiy. "Checking the Dark Matter Origin of a 3.53 keV Line with the Milky Way Center". *Phys. Rev. Lett.* 115 (16 2015), p. 161301. DOI: https://doi.org/10.1103/PhysRevLett.115.161301 (cit. on pp. 106, 122).

[39] A. Boyarsky, O. Ruchayskiy, D. Iakubovskyi, and J. Franse. "Unidentified Line in X-Ray Spectra of the Andromeda Galaxy and Perseus Galaxy Cluster". *Phys. Rev. Lett.* 113 (25 2014), p. 251301. DOI: https://doi.org/10.1103/PhysRevLett.113.251301 (cit. on pp. 13, 106, 122, 123).

[40] Branduardi-Raymont, G., Bhardwaj, A., Elsner, R. F., Gladstone, G. R., Ramsay, G., Rodriguez, P., Soria, R., Waite, J. H., Jr, and Cravens, T. E. "A study of Jupiter's aurorae with XMM-Newton". *A&A* 463.2 (2007), pp. 761–774. DOI: https://doi.org/10.1051/0004-6361:20066406 (cit. on p. 13).

[41] U. G. Briel, B. Aschenbach, G. Hasinger, H. Hippmann, E. Pfeffermann, P. Predehl, J. H. M. M. Schmitt, O. Schwentker, W. Voges, and U. Zimmermann. *ROSAT User's Handbook*. accessed on 05.04.2019. 1996. URL: https://heasarc.gsfc.nasa.gov/docs/rosat/ruh/handbook/handbook.html (cit. on p. 10).

[42] E. Bulbul, M. Markevitch, A. Foster, R. K. Smith, M. Loewenstein, and S. W. Randall. "Detection of an Unidentified Emission Line in the Stacked X-Ray Spectrum of Galaxy Clusters". *The Astrophysical Journal* 789.1 (2014), p. 13. DOI: https://doi.org/10.1088/0004-637X/789/1/13 (cit. on pp. 13, 106, 122–125).

[43] J Burgdörfer, R Morgenstern, and A Niehaus. "Angular momentum of captured electrons: The classical over-barrier model and its limitations". *Nuclear Instruments and Methods in Physics Research Section B: Beam Interactions with Materials and Atoms* 23 (1-2 1987), pp. 120–122. DOI: https://doi.org/10.1016/0168-583X(87)90426-5 (cit. on pp. 29, 33).

[44] S. E. Butler and A. Dalgarno. "Charge transfer of multiply charged ions with hydrogen and helium Landau-Zener calculations". *The Astrophysical Journal* 241 (1980), pp. 838–843. DOI: https://doi.org/10.1086/158395 (cit. on p. 34).

[45] Natalie Mary Cann and Ajit J. Thakkar. "Oscillator strengths for S-P and P-D transitions in heliumlike ions". *Phys. Rev. A* 46 (9 1992), pp. 5397–5405. DOI: https://doi.org/10.1103/PhysRevA.46.5397 (cit. on pp. 161, 163).

[46] Francis F. Chen. *Introduction to Plasma Physics and Controlled Fusion*. Springer International Publishing AG Switzerland, 2016. DOI: https://doi.org/10.1007/978-3-319-22309-4 (cit. on p. 102).

[47] C. D. Child. "Discharge From Hot CaO". *Phys. Rev. (Series I)* 32 (5 May 1911), pp. 492–511. DOI: https://doi.org/10.1103/PhysRevSeriesI.32.492 (cit. on p. 80).

[48] M. Cicoli, J. P. Conlon, M. C. D. Marsh, and M. Rummel. "3.55 keV photon line and its morphology from a 3.55 keV axionlike particle line". *Phys. Rev. D* 90 (2 2014), p. 023540. DOI: https://doi.org/10.1103/PhysRevD.90.023540 (cit. on p. 106).

[49] T. E. Cravens. "Comet Hyakutake x-ray source: Charge transfer of solar wind heavy ions". *Geophysical Research Letters* 24.1 (1997), pp. 105–108. DOI: https://doi.org/10.1029/96GL03780 (cit. on p. 11).

[50] J. R. Crespo López-Urrutia, P. Beiersdorfer, D. W. Savin, and K. Widmann. "Precision measurement of the lifetime of the $1s2s^3S_1$ metastable level in heliumlike O^{6+}". *Phys. Rev. A* 58 (1 1998), pp. 238–241. DOI: https://doi.org/10.1103/PhysRevA.58.238 (cit. on pp. 129, 157, 159).

[51] J. R. Crespo López-Urrutia, P. Beiersdorfer, and K. Widmann. "Lifetime of the $1s2s\,^3S_1$ metastable level in He-like S^{14+} measured with an electron beam ion trap". *Phys. Rev. A* 74 (1 2006), p. 012507. DOI: https://doi.org/10.1103/PhysRevA.74.012507 (cit. on p. 111).

[52] J. R. Crespo López-Urrutia, M. C. Simon, C. Beilmann, J. Rudolph, R. Steinbrügge, S. Eberle, M. Schwarz, T. M. Baumann, B. L. Schmitt, F. Brunner, R. Ginzel, R. Klawitter, K. Kubićek, S. W. Epp, P. H. Mokler, V. Mäckel, J. Ullrich, G. V. Brown, A. Graf, M. Leutenegger, P. Beiersdorfer, E. Behar, R. Follath, G. Reichardt, and O. Schwarzkopf. "Photoionizing trapped highly charged ions with synchrotron radiation". *AIP Conference Proceedings* 1438.1 (2012), pp. 80–85. DOI: https://doi.org/10.1063/1.4707859 (cit. on p. 45).

[53] Renata S. Cumbee. "Highly-Charged Ion Collisions with Atoms: Applications to X-ray Emission in the Universe". Dissertation. The University of Georgia, 2016 (cit. on pp. 14, 35, 151).

[54] F. J. Currell. "Trapping highly charged ions: fundamentals and applications". The physics of electron beam ion traps (2001). Ed. by J. Gillaspy (cit. on p. 103).

[55] F. Currell and G. Fussmann. "Physics of electron beam ion traps and sources". *IEEE Transactions on Plasma Science* 33.6 (2005), pp. 1763–1777. DOI: https://doi.org/10.1109/TPS.2005.860072 (cit. on pp. 34, 48, 142, 153).

[56] H. Danared, A. Källberg, and A. Simonsson. "CRYRING at the LSR at FLAIR". *Hyperfine Interactions* 194.1 (Aug. 27, 2009), p. 129. DOI: https://doi.org/10.1007/s10751-009-0040-7 (cit. on p. 45).

[57] Dennerl, K., Lisse, C. M., Bhardwaj, A., Burwitz, V., Englhauser, J., Gunell, H., Holmström, M., Jansen, F., Kharchenko, V., and Rodríguez-Pascual, P. M. "First observation of Mars with XMM-Newton - High resolution X-ray spectroscopy with RGS". *A&A* 451.2 (2006), pp. 709–722. DOI: https://doi.org/10.1051/0004-6361:20054253 (cit. on p. 13).

[58] C. Dessert, N. L. Rodd, and B. R. Safdi. "Evidence against the decaying dark matter interpretation of the 3.5 keV line from blank sky observations". *arXiv e-prints*, arXiv:1812.06976 (Dec. 2018), arXiv:1812.06976. arXiv: 1812.06976 [astro-ph.CO] (cit. on p. 107).

[59] N. Djurić, S. J. Smith, J. Simcic, and A. Chutjian. "Absolute Single and Multiple Charge Exchange Cross Sections for Highly Charged C, N, and O Ions Colliding with CH4". *The Astrophysical Journal* 679.2 (2008), pp. 1661–1664. DOI: https://doi.org/10.1086/587782 (cit. on p. 173).

[60] S. Dobrodey. "Untersuchung von K-LL-Resonanzen dielektronischer Rekombination und simultaner Innerschalen-Vakuum-Ultraviolett Übergänge in hochgeladenem Eisen mit einer Elektronenstrahl-Ionenfalle". Master thesis. Ruprecht-Karls-Universität Heidelberg, 2014 (cit. on pp. 47, 67).

[61] E. D. Donets, V. I. Ilyushchenko, and V. A. Alpert. "Ultrahigh vacuum electron beam source of highly stripped ions". *Premiere Conference Internationale sur les Sources d'Ions* (1970) (cit. on p. 45).

[62] G. W. F. Drake. "Theory of Relativistic Magnetic Dipole Transitions: Lifetime of the Metastable 2^3S State of the Heliumlike Ions". *Phys. Rev. A* 3 (3 1971), pp. 908–915. DOI: https://doi.org/10.1103/PhysRevA.3.908 (cit. on p. 157).

[63] S. W. Epp. "Röntgen-Laserspektroskopie hochgeladener Ionen in einer EBIT am Freie-Elektronen-Laser FLASH". Dissertation. Ruprecht-Karls-Universität Heidelberg, 2007 (cit. on pp. 49, 63, 107).

[64] S. W. Epp, J. R. Crespo López-Urrutia, G. Brenner, V. Mäckel, P. H. Mokler, R. Treusch, M. Kuhlmann, M. V. Yurkov, J. Feldhaus, J. R. Schneider, M. Wellhöfer, M. Martins, W. Wurth, and J. Ullrich. "Soft X-Ray Laser Spectroscopy on Trapped Highly Charged Ions at FLASH". *Phys. Rev. Lett.* 98 (18 2007), p. 183001. DOI: https://doi.org/10.1088/0953-4075/43/19/194008 (cit. on p. 49).

[65]   Tosi F., Capria M. T., Capaccioni F., Filacchione G., Erard S., and et al. "THERMAL
       MAPS AND PROPERTIES OF COMET 67P AS DERIVED FROM ROSETTA/VIR-
       TIS DATA". *46th Lunar and Planetary Science Conference (2015)* (2015) (cit. on
       p. 10).

[66]   Taotao Fang and Claude R. Canizares. "Probing Cosmology with the X-Ray Forest".
       The Astrophysical Journal 539.2 (2000), pp. 532–539. DOI: https://doi.org/10.
       1086/309270 (cit. on p. 10).

[67]   L. M. Field, Karl Spangenberg, and Robert Helm. "Control of electron-beam
       dispersion at high vacuum by ions". *Electrical communication* (1947), pp. 108–121
       (cit. on p. 45).

[68]   I. Fischer, A. Lochschmidt, A. Strobel, G. Niedner-Schatteburg, K. Müller-Dethlefs,
       and V. E. Bondybey. "The non-resonant two-photon zero kinetic energy photoelec-
       tron spectrum of CS2". *Chemical Physics Letters* 202.6 (1993), pp. 542–548. DOI:
       https://doi.org/10.1016/0009-2614(93)90045-3 (cit. on p. 118).

[70]   A. R. Foster, L. Ji, R. K. Smith, and N. S. Brickhouse. "Updated Atomic Data
       and Calculations for X-Ray Spectroscopy". *The Astrophysical Journal* 756.2 (2012),
       p. 128. DOI: https://doi.org/10.1088/0004-637X/756/2/128 (cit. on pp. 106,
       122).

[71]   M Frankel, P Beiersdorfer, G V Brown, J Clementson, M F Gu, and L Schweikhard.
       "X-ray signatures of charge exchange in L-shell iron and sulfur". *Journal of Physics:
       Conference Series* 163 (2009), p. 012051. DOI: https://doi.org/10.1088/1742-
       6596/163/1/012051 (cit. on p. 139).

[72]   Bernhard Franzke. "The heavy ion storage and cooler ring project ESR at GSI".
       *Nuclear Instruments and Methods in Physics Research Section B: Beam Interactions
       with Materials and Atoms* 24-25 (1987), pp. 18–25. DOI: https://doi.org/10.
       1016/0168-583X(87)90583-0 (cit. on p. 45).

[73]   Ryuichi Fujimoto, Kazuhisa Mitsuda, Dan McCammon, Yoh Takei, Michael Bauer,
       Yoshitaka Ishisaki, F. Scott Porter, Hiroya Yamaguchi, Kiyoshi Hayashida, and
       Noriko Y. Yamasaki. "Evidence for Solar-Wind Charge-Exchange X-Ray Emission
       from the Earth's Magnetosheath". *Publications of the Astronomical Society of Japan*
       59.sp1 (2007), S133–S140. DOI: https://doi.org/10.1093/pasj/59.sp1.S133
       (cit. on p. 13).

[74]   M. Gacesa, H.-R. Müller, R. Côté, and V. Kharchenko. "POLARIZATION OF
       THE CHARGE-EXCHANGE X-RAYS INDUCED IN THE HELIOSPHERE". *The
       Astrophysical Journal* 732.2 (Apr. 2011), p. L21. DOI: https://doi.org/10.1088/
       2041-8205/732/2/l21 (cit. on p. 185).

[75] Amy C. Gall, Adam R. Foster, Roshani Silwal, Joan M. Dreiling, Alexander Borovik, Ethan Kilgore, Marco Ajello, John D. Gillaspy, Yuri Ralchenko, and Endre Takács. "EBIT Observation of Ar Dielectronic Recombination Lines near the Unknown Faint X-Ray Feature Found in the Stacked Spectrum of Galaxy Clusters". *The Astrophysical Journal* 872.2 (2019), p. 194. DOI: https://doi.org/10.3847/1538-4357/ab0177 (cit. on p. 107).

[76] E. Gatti and P. Rehak. "Semiconductor drift chamber — An application of a novel charge transport scheme". *Nuclear Instruments and Methods in Physics Research* 225.3 (1984), pp. 608–614. DOI: https://doi.org/10.1016/0167-5087(84)90113-3 (cit. on p. 66).

[77] A. Gewering-Peine, D. Horns, and J.H.M.M. Schmitt. "A sensitive search for unknown spectral emission lines in the diffuse X-ray background with XMM-Newton". *Journal of Cosmology and Astroparticle Physics* 2017.06 (2017), p. 036. DOI: https://doi.org/10.1088/1475-7516/2017/06/036 (cit. on p. 106).

[78] R. Ginzel, S. G. Higgins, P. Mrowcynski, P. Northway, M. C. Simon, H. Tawara, J. R. Crespo López-Urrutia, J. Ullrich, G. Kowarik, R. Ritter, W. Meissl, C. Vasko, C. Gösselsberger, A. S. El-Said, and F. Aumayr. "A deceleration system at the Heidelberg EBIT providing very slow highly charged ions for surface nanostructuring". *Nuclear Instruments and Methods in Physics Research Section B: Beam Interactions with Materials and Atoms* 268.19 (2010), pp. 2972–2976. DOI: https://doi.org/10.1016/j.nimb.2010.05.020 (cit. on pp. 60, 126).

[79] FAST ComTec GmbH. *MPA-3 Multiparameter Data Acquisition System user manual.* manual. Version 2.11. 2014 (cit. on p. 95).

[80] KETEK GmbH. *AXAS-M Analytical X-Ray Acquisition System-Modular User's Manual.* Manual. 2013 (cit. on pp. 66, 68).

[81] T. I. Gombosi, K. Lorencz, and J. R. Jokipii. "Combined first- and second-order Fermi acceleration in cometary environments". *Journal of Geophysical Research: Space Physics* 94.A11 (1989), pp. 15011–15023. DOI: https://doi.org/10.1029/JA094iA11p15011 (cit. on p. 11).

[82] T. I. Gombosi, M. Neugebauer, A. D. Johnstone, A. J. Coates, and D. E. Huddleston. "Comparison of observed and calculated implanted ion distributions outside comet Halley's bow shock". *Journal of Geophysical Research: Space Physics* 96.A6 (1991), pp. 9467–9477. DOI: https://doi.org/10.1029/90JA02750 (cit. on p. 11).

[83] Gu, L., Kaastra, J., Raassen, A. J. J., Mullen, P. D., Cumbee, R. S., Lyons, D., and Stancil, P. C. "A novel scenario for the possible X-ray line feature at 3.5 keV - Charge exchange with bare sulfur ions". *A&A* 584 (2015), p. L11. DOI:

https://doi.org/10.1051/0004-6361/201527634 (cit. on pp. 13, 14, 107, 115, 126).

[85]   M. F. Gu. "The flexible atomic code". *Canadian Journal of Physics* 86 (2008), pp. 675–689. DOI: https://doi.org/10.1139/P07-197 (cit. on pp. 21, 39, 108).

[86]   D. Habs, W. Baumann, J. Berger, P. Blatt, A. Faulstich, P. Krause, G. Kilgus, R. Neumann, W. Petrich, R. Stokstad, D. Schwalm, E. Szmola, K. Welti, A. Wolf, S. Zwickler, E. Jaeschke, D. Krämer, G. Bisoffi, M. Blum, A. Friedrich, C. Geyer, M. Grieser, H.W. Heyng, B. Holzer, R. Ihde, M. Jung, K. Matl, W. Ott, B. Povh, R. Repnow, M. Steck, E. Steffens, D. Dutta, T. Kühl, D. Marx, S. Schröder, M. Gerhard, R. Grieser, G. Huber, R. Klein, M. Krieg, N. Schmidt, R. Schuch, J.F. Babb, L. Spruch, W. Arnold, and A. Noda. "First experiments with the heidelberg test storage ring TSR". *Nuclear Instruments and Methods in Physics Research Section B: Beam Interactions with Materials and Atoms* 43.3 (1989), pp. 390–410. DOI: https://doi.org/10.1016/0168-583X(89)90383-2 (cit. on p. 45).

[87]   D. R. Hartree. "The Wave Mechanics of an Atom with a Non-Coulomb Central Field. Part I. Theory and Methods". *Mathematical Proceedings of the Cambridge Philosophical Society* 24.1 (1928), pp. 89–110. DOI: https://doi.org/10.1017/S0305004100011919 (cit. on p. 20).

[88]   A. Hermann, K. v. Meyenn, and V. F. Weisskopf, eds. *Wolfgang Pauli.* Wissenschaftlicher Briefwechsel mit Bohr, Einstein, Heisenberg u.a. Vol. 1. Springer-Verlag New York Inc., 1979 (cit. on p. 9).

[89]   G. Herrmann. "Optical Theory of Thermal Velocity Effects in Cylindrical Electron Beams". *Journal of Applied Physics* 29 (1958). DOI: https://doi.org/10.1063/1.1723053 (cit. on pp. 48, 52).

[90]   A Hibbert. "Transitions in O V". *Journal of Physics B: Atomic and Molecular Physics* 13.9 (1980), pp. 1721–1730. DOI: https://doi.org/10.1088/0022-3700/13/9/007 (cit. on pp. 161, 163).

[91]   S. Higgins. "Implementation of a deceleration beamline for the investigation of charge exchange processes using highly charged ions". Master thesis. Imperial Collage London, 2009 (cit. on p. 126).

[92]   S. Horiuchi, P. J. Humphrey, J. Oñorbe, K. N. Abazajian, M. Kaplinghat, and S. Garrison-Kimmel. "Sterile neutrino dark matter bounds from galaxies of the Local Group". *Phys. Rev. D* 89 (2 2014), p. 025017. DOI: https://doi.org/10.1103/PhysRevD.89.025017 (cit. on p. 106).

[93] K. Ishii, A. Itoh, and K. Okuno. "Electron-capture cross sections of multiply charged slow ions of carbon, nitrogen, and oxygen in He". *Phys. Rev. A* 70 (4 2004), p. 042716. DOI: https://doi.org/10.1103/PhysRevA.70.042716 (cit. on pp. 26, 173).

[94] R. K. Janev. "Excited States Created in Charge Transfer Collisions Between Atoms and Highly Charged Ions". *Physica Scripta* 1983.T3 (1983), p. 208. DOI: https://doi.org/10.1088/0031-8949/1983/T3/041 (cit. on p. 36).

[95] R.K. Janev and Hannspeter Winter. "State-selective electron capture in atom-highly charged ion collisions". *Physics Reports* 117.5 (1985), pp. 265–387. ISSN: 0370-1573. DOI: https://doi.org/10.1016/0370-1573(85)90118-8 (cit. on pp. 26, 34, 36–38, 117).

[96] Tesla Jeltema and Stefano Profumo. "Deep XMM observations of Draco rule out at the 99 per cent confidence level a dark matter decay origin for the 3.5 keV line". *Monthly Notices of the Royal Astronomical Society* 458.4 (2016), pp. 3592–3596. DOI: https://doi.org/10.1093/mnras/stw578 (cit. on p. 106).

[97] W.R. Johnson, D.R. Plante, and J. Sapirstein. "Relativistic Calculations of Transition Amplitudes in the Helium Isoelectronic Sequence". Advances In Atomic, Molecular, and Optical Physics 35 (1995), pp. 255–329. ISSN: 1049-250X. DOI: https://doi.org/10.1016/S1049-250X(08)60165-2 (cit. on p. 157).

[98] J. S. Kaastra, R. Mewe, and H. Nieuwenhuijzen. "SPEX: a new code for spectral analysis of X & UV spectra." *11th Colloquium on UV and X-ray Spectroscopy of Astrophysical and Laboratory Plasmas* (1996), pp. 411–414 (cit. on p. 115).

[99] Satoru Katsuda, Hiroshi Tsunemi, Koji Mori, Hiroyuki Uchida, Hiroko Kosugi, Masashi Kimura, Hiroshi Nakajima, Satoru Takakura, Robert Petre, John W. Hewitt, and Hiroya Yamaguchi. "POSSIBLE CHARGE-EXCHANGE X-RAY EMISSION IN THE CYGNUS LOOP DETECTED WITHSUZAKU". *The Astrophysical Journal* 730.1 (2011), p. 24. DOI: https://doi.org/10.1088/0004-637x/730/1/24 (cit. on p. 13).

[100] Young Soon Kim and R. H. Pratt. "Direct radiative recombination of electrons with atomic ions: Cross sections and rate coefficients". *Phys. Rev. A* 27 (6 1983), pp. 2913–2924. DOI: https://doi.org/10.1103/PhysRevA.27.2913 (cit. on p. 24).

[101] Koutroumpa, D., Modolo, R., Chanteur, G., Chaufray, J.-Y., Kharchenko, V., and Lallement, R. "Solar wind charge exchange X-ray emission from Mars - Model and data comparison". *A&A* 545 (2012), A153. DOI: https://doi.org/10.1051/0004-6361/201219720 (cit. on p. 13).

[102] V. A. Krasnopolsky, J. B. Greenwood, and P. C. Stancil. "X-ray and extreme ultraviolet emissions from comets". *Space Science Reviews* 113.3 (2004), pp. 271–373. DOI: https://doi.org/10.1007/s11214-005-6263-2 (cit. on pp. 11, 117).

[103] Vladimir A. Krasnopolsky and Michael J. Mumma. "Spectroscopy of Comet Hyakutake at 80–700 A: First Detection of Solar Wind Charge Transfer Emissions". *The Astrophysical Journal* 549.1 (2001), pp. 629–634. DOI: https://doi.org/10.1086/319064 (cit. on p. 11).

[104] V. A. Krupin, S. N. Tugarinov, A. G. Barsukov, A. Yu. Dnestrovskij, L. A. Klyuchnikov, K. V. Korobov, S. A. Krasnyanskii, N. N. Naumenko, A. R. Nemets, A. V. Sushkov, and G. N. Tilinin. "Charge-exchange recombination spectroscopy of the plasma ion temperature at the T-10 tokamak". *Plasma Physics Reports* 39.8 (Aug. 1, 2013), pp. 632–643. ISSN: 1562-6938. DOI: https://doi.org/10.1134/S1063780X13070040 (cit. on p. 126).

[105] Willis E. Lamb and Robert C. Retherford. "Fine Structure of the Hydrogen Atom by a Microwave Method". *Phys. Rev.* 72 (3 1947), pp. 241–243. DOI: https://doi.org/10.1103/PhysRev.72.241 (cit. on p. 19).

[106] Lamy, P. L., Toth, I., Groussin, O., Jorda, L., Kelley, M. S., and Stansberry, J. A. "Spitzer Space Telescope observations of the nucleus of comet 67P/Churyumov-Gerasimenko*". *A&A* 489.2 (2008), pp. 777–785. DOI: https://doi.org/10.1051/0004-6361:200809514 (cit. on p. 9).

[107] L. D. Landau. "To the theory of energy transmission in collissions. II". *Phys. Zs. Sowjet* 2 (1932), p. 46 (cit. on pp. 13, 34).

[108] A. Lapierre, M. Brodeur, T. Brunner, S. Ettenauer, A.T. Gallant, V. Simon, M. Good, M. W. Froese, J. R. Crespo López-Urrutia, P. Delheij, S. W. Epp, R. Ringle, S. Schwarz, J. Ullrich, and J. Dilling. "The TITAN EBIT charge breeder for mass measurements on highly charged short-lived isotopes—First online operation". *Nuclear Instruments and Methods in Physics Research Section A: Accelerators, Spectrometers, Detectors and Associated Equipment* 624.1 (2010), pp. 54–64. DOI: https://doi.org/10.1016/j.nima.2010.09.030 (cit. on p. 58).

[109] M. A. Leutenegger, P. Beiersdorfer, G. V. Brown, R. L. Kelley, C. A. Kilbourne, and F. S. Porter. "Measurement of Anomalously Strong Emission from the $1s-9p$ Transition in the Spectrum of H-Like Phosphorus Following Charge Exchange with Molecular Hydrogen". *Phys. Rev. Lett.* 105 (6 2010), p. 063201. DOI: https://doi.org/10.1103/PhysRevLett.105.063201 (cit. on pp. 108, 126, 151, 154, 156, 188, 189).

[110] Maurice A Leutenegger, Gabriele L Betancourt-Martinez, Peter Beiersdorfer, Gregory V Brown, Richard L Kelley, Caroline A Kilbourne, and F Scott Porter. "Charge exchange measurements with an x-ray calorimeter at an electron beam ion trap". *Physica Scripta* T156 (2013), p. 014006. DOI: https://doi.org/10.1088/0031-8949/2013/t156/014006 (cit. on pp. 151, 156, 188, 189).

[111] M. A. Levine, R. E. Marrs, J. R. Henderson, D. A. Knapp, and M. B. Schneider. "The Electron Beam Ion Trap: A New Instrument for Atomic Physics Measurements". *Physica Scripta* 1988.T22 (1988), p. 157. DOI: https://doi.org/10.1088/0031-8949/1988/T22/024 (cit. on p. 46).

[112] M.A. Levine, R.E. Marrs, J.N. Bardsley, P. Beiersdorfer, C.L. Bennett, M.H. Chen, T. Cowan, D. Dietrich, J.R. Henderson, D.A. Knapp, A. Osterheld, B.M. Penetrante, M.B. Schneider, and J.H. Scofield. "The use of an electron beam ion trap in the study of highly charged ions". *Nuclear Instruments and Methods in Physics Research Section B: Beam Interactions with Materials and Atoms* 43.3 (1989), pp. 431–440. DOI: https://doi.org/10.1016/0168-583X(89)90386-8 (cit. on p. 46).

[113] William Lichten. "Resonant Charge Exchange in Atomic Collisions". *Phys. Rev.* 131 (1 1963), pp. 229–238. DOI: https://doi.org/10.1103/PhysRev.131.229 (cit. on p. 34).

[114] C. M. Lisse, D. J. Christian, K. Dennerl, K. J. Meech, R. Petre, H. A. Weaver, and S. J. Wolk. "Charge Exchange-Induced X-Ray Emission from Comet C/1999 S4 (LINEAR)". *Science* 292.5520 (2001), pp. 1343–1348. DOI: https://doi.org/10.1126/science.292.5520.1343 (cit. on p. 11).

[115] C. M. Lisse, K. Dennerl, J. Englhauser, M. Harden, F. E. Marshall, M. J. Mumma, R. Petre, J. P. Pye, M. J. Ricketts, J. Schmitt, J. Trümper, and R. G. West. "Discovery of X-ray and Extreme Ultraviolet Emission from Comet C/Hyakutake 1996 B2". *Science* 274.5285 (1996), pp. 205–209. DOI: https://doi.org/10.1126/science.274.5285.205 (cit. on pp. 10, 11).

[116] W. Lotz. "An Empirical Formula for the Electron-Impact Ionization Cross-Section". *Zeitschrift für Physik* 206 (1967), pp. 205–211. DOI: https://doi.org/10.1007/BF01325928 (cit. on p. 23).

[117] *Low Energy Germanium Detector.* C49322. accessed on 16.04.2019. Nov. 2016 (cit. on p. 67).

[118] D. Malyshev, A. Neronov, and D. Eckert. "Constraints on 3.55 keV line emission from stacked observations of dwarf spheroidal galaxies". *Phys. Rev. D* 90 (10 Nov. 2014), p. 103506. DOI: https://doi.org/10.1103/PhysRevD.90.103506 (cit. on p. 106).

[119]   R. E. Marrs, M. A. Levine, D. A. Knapp, and J. R. Henderson. "Measurement of electron-impact–excitation cross sections for very highly charged ions". *Phys. Rev. Lett.* 60 (17 Apr. 1988), pp. 1715–1718. DOI: https://doi.org/10.1103/PhysRevLett.60.1715 (cit. on p. 46).

[120]   Kazuhisa Mitsuda, Mark Bautz, Hajime Inoue, Richard L. Kelley, Katsuji Koyama, and et al. "The X-Ray Observatory Suzaku". *Publications of the Astronomical Society of Japan* 59.sp1 (Jan. 2007), S1–S7. ISSN: 0004-6264. DOI: https://doi.org/10.1093/pasj/59.sp1.S1 (cit. on pp. 10, 106).

[121]   Peter J. Mohr, Günter Plunien, and Gerhard Soff. "QED corrections in heavy atoms". *Physics Reports* 293.5 (1998), pp. 227–369. DOI: https://doi.org/10.1016/S0370-1573(97)00046-X (cit. on p. 21).

[122]   W. Mróz, J. Wol/owski, E. Woryna, B. Králiková, J. Krása, L. Láska, K. Mašek, J. Skála, K. Rohlena, O. B. Shamaev, B. Yu. Sharkov, H. Haseroth, K. L. Langbein, and T. R. Sherwood. "Laser plasma as a source of highly ionized ions". *Review of Scientific Instruments* 65.4 (1994), pp. 1272–1274. DOI: https://doi.org/10.1063/1.1145031 (cit. on p. 45).

[123]   P. D. Mullen, R. S. Cumbee, D. Lyons, and P. C. Stancil. "Charge Exchange-induced X-Ray Emission of Fe xxv and Fe xxvi via a Streamlined Model". *The Astrophysical Journal Supplement Series* 224.2 (2016), p. 31. DOI: https://doi.org/10.3847/0067-0049/224/2/31 (cit. on pp. 34, 118).

[124]   P. D. Mullen, D. Lyons, R. S. Cumbee, and P. C. Stancil. *Kronos*. Feb. 2017 (cit. on pp. 38, 146, 149).

[125]   M. J. Mumma, V. A. Krasnopolsky, and M. J. Abbott. "Soft X-Rays From Four Comets Observed With". *The Astrophysical Journal* 491.2 (Dec. 1997), pp. L125–L128. DOI: https://doi.org/10.1086/311071 (cit. on pp. 10, 11).

[126]   R. F. Mushotzky, S. S. Holt, E. A. Boldt, P. J. Serlemitsos, and B. W. Smith. "Observation of the core of the Perseus cluster with the Einstein solid state spectrometer - Cooling gas and elemental abundances". *The Astrophysical Journal* 244 (1981), pp. L47–L51. DOI: https://doi.org/10.1086/183477 (cit. on pp. 13, 107).

[127]   J. Needham. *Science and Civilization in China*. Mathematics and the Sciences of the Heavens and the Earth. Vol. 3. 1959. ISBN: 0521058015 (cit. on p. 9).

[128]   M. Neugebauer. "Spacecraft observations of the interaction of active comets with the solar wind". *Reviews of Geophysics* 28.2 (1990), pp. 231–252. DOI: https://doi.org/10.1029/RG028i002p00231 (cit. on p. 10).

[129] A Niehaus. "A classical model for multiple-electron capture in slow collisions of highly charged ions with atoms". *Journal of Physics B: Atomic and Molecular Physics* 19.18 (1986), p. 2925. DOI: https://doi.org/10.1088/0022-3700/19/18/021 (cit. on p. 33).

[130] J. L. Nolte, P. C. Stancil, H. P. Liebermann, R. J. Buenker, Y. Hui, and D. R. Schultz. "Final-state-resolved charge exchange in C^{5+} collisions with H". *Journal of Physics B: Atomic, Molecular and Optical Physics* 45.24 (2012), p. 245202. DOI: https://doi.org/10.1088/0953-4075/45/24/245202 (cit. on p. 118).

[131] T.G. Northrop, C.M. Lisse, M.J. Mumma, and M.D. Desch. "A Possible Source of the X-Rays from Comet Hyakutake". *Icarus* 127.1 (1997), pp. 246–250. DOI: https://doi.org/10.1006/icar.1997.5694 (cit. on p. 11).

[132] R. E. Olson and A. Salop. "Charge-transfer and impact-ionization cross sections for fully and partially stripped positive ions colliding with atomic hydrogen". *Phys. Rev. A* 16 (2 1977), pp. 531–541. DOI: https://doi.org/10.1103/PhysRevA.16.531 (cit. on p. 33).

[133] R. E. Olson and A. Salop. "Electron transfer between multicharged ions and neutral species". *Phys. Rev. A* 14 (1976), pp. 579–585. DOI: https://doi.org/10.1103/PhysRevA.14.579 (cit. on p. 34).

[134] Alan Owens, A. N. Parmar, T. Oosterbroek, A. Orr, L. A. Antonelli, F. Fiore, R. Schulz, G. P. Tozzi, M. C. Maccarone, and L. Piro. "Evidence for Dust-related X-Ray Emission from Comet C/1995 O1 (Hale-Bopp)". *The Astrophysical Journal* 493.1 (1998), pp. L47–L51. DOI: https://doi.org/10.1086/311119 (cit. on p. 11).

[135] F. Pajot, D. Barret, T. Lam-Trong, J.-W. den Herder, L. Piro, M. Cappi, J. Huovelin, R. Kelley, J. M. Mas-Hesse, K. Mitsuda, S. Paltani, G. Rauw, A. Rozanska, J. Wilms, M. Barbera, F. Douchin, H. Geoffray, R. den Hartog, C. Kilbourne, M. Le Du, C. Macculi, J.-M. Mesnager, and P. Peille. "The Athena X-ray Integral Field Unit (X-IFU)". *Journal of Low Temperature Physics* 193.5 (2018), pp. 901–907. DOI: https://doi.org/10.1007/s10909-018-1904-5 (cit. on p. 126).

[137] G Peach, H E Saraph, and M J Seaton. "Atomic data for opacity calculations. IX. The lithium isoelectronic sequence". *Journal of Physics B: Atomic, Molecular and Optical Physics* 21.22 (1988), pp. 3669–3683. DOI: https://doi.org/10.1088/0953-4075/21/22/006 (cit. on pp. 161, 163).

[138] R. A. Phaneuf, F. W. Meyer, and R. H. McKnight. "Single-electron capture by multiply charged ions of carbon, nitrogen, and oxygen in atomic and molecular hydrogen". *Phys. Rev. A* 17 (2 Feb. 1978), pp. 534–545. DOI: https://doi.org/10.1103/PhysRevA.17.534 (cit. on p. 11).

[139]   J. R. Pierce. "Rectilinear Electron Flow in Beams". *Journal of Applied Physics* 11 (1940). DOI: https://doi.org/10.1063/1.1712815 (cit. on p. 52).

[140]   H. van Regemorter. "Rate of Collisional Excitation in Stellar Atmospheres". *Astrophysical Journal* 136 (1962), pp. 906–915. DOI: https://doi.org/10.1086/147445 (cit. on p. 22).

[141]   N. Rohringer and R. London. "Atomic inner-shell x-ray laser pumped by an x-ray free-electron laser". *Phys. Rev. A* 80 (1 July 2009), p. 013809. DOI: https://doi.org/10.1103/PhysRevA.80.013809 (cit. on p. 45).

[142]   Hiroshi Ryufuku, Ken Sasaki, and Tsutomu Watanabe. "Oscillatory behavior of charge transfer cross sections as a function of the charge of projectiles in low-energy collisions". *Phys. Rev. A* 21 (3 1980), pp. 745–750. DOI: https://doi.org/10.1103/PhysRevA.21.745 (cit. on pp. 13, 27).

[143]   Tobias Schlummer. "Charge exchange recombination in X-ray spectra of He-like argon measured at the tokamak TEXTOR". PhD thesis. Heinrich-Heine-Universität Düsseldorf, 2014 (cit. on p. 126).

[144]   E. Schrödinger. "Quantisierung als Eigenwertproblem I und II". *Annalen der Physik* 79 (4 1926), pp. 361–376, 489–527 (cit. on p. 17).

[145]   E. Schrödinger. "Quantisierung als Eigenwertproblem III". *Annalen der Physik* 80 (4 1926), pp. 437–490 (cit. on p. 17).

[146]   E. Schrödinger. "Quantisierung als Eigenwertproblem III". *Annalen der Physik* 81 (4 1926), pp. 109–139 (cit. on p. 17).

[147]   David Seargent. *The Greatest Comets in History.* 2009. DOI: https://doi.org/10.1007/978-0-387-09513-4 (cit. on p. 9).

[148]   Chintan Shah, Pedro Amaro, Rene Steinbrügge, Christian Beilmann, Sven Bernitt, Stephan Fritzsche, Andrey Surzhykov, José R. Crespo López-Urrutia, and Stanislav Tashenov. "Strong higher-order resonant contributions to x-ray line polarization in hot plasmas". *Phys. Rev. E* 93 (6 2016), p. 061201. DOI: https://doi.org/10.1103/PhysRevE.93.061201 (cit. on p. 108).

[149]   Chintan Shah, Stepan Dobrodey, Sven Bernitt, René Steinbrügge, José R. Crespo López-Urrutia, Liyi Gu, and Jelle Kaastra. "Laboratory Measurements Compellingly Support a Charge-exchange Mechanism for the 'Dark Matter' 3.5 keV X-Ray Line". *The Astrophysical Journal* 833.1 (2016), p. 52. DOI: https://doi.org/10.3847/1538-4357/833/1/52 (cit. on pp. 13, 107).

[150] Chintan Shah, Holger Jörg, Sven Bernitt, Stepan Dobrodey, René Steinbrügge, Christian Beilmann, Pedro Amaro, Zhimin Hu, Sebastian Weber, Stephan Fritzsche, Andrey Surzhykov, José R. Crespo López-Urrutia, and Stanislav Tashenov. "Polarization measurement of dielectronic recombination transitions in highly charged krypton ions". *Phys. Rev. A* 92 (4 2015), p. 042702. DOI: `https://doi.org/10.1103/PhysRevA.92.042702` (cit. on p. 108).

[151] G. Sikler. "Massenspektroskopie kurzlebiger Sr- und Sn-Isotope und Aufbau der SHIPTRAP-Penningfallen". Dissertation. Ruprecht-Karls-Universität Heidelberg, 2003 (cit. on p. 60).

[152] M. C. Simon. "Photoionisation hochgeladener Ionen durch weiche Röntgenstrahlung in einer Elektronenstrahl-Ionenfalle". Dissertation. Ruprecht-Karls-Universität Heidelberg, 2010 (cit. on pp. 60, 61).

[153] M. C. Simon, J. R. Crespo López-Urrutia, C. Beilmann, M. Schwarz, Z. Harman, S. W. Epp, B. L. Schmitt, T. M. Baumann, E. Behar, S. Bernitt, R. Follath, R. Ginzel, C. H. Keitel, R. Klawitter, K. Kubi ček, V. Mäckel, P. H. Mokler, G. Reichardt, O. Schwarzkopf, and J. Ullrich. "Resonant and Near-Threshold Photoionization Cross Sections of Fe^{14+}". *Phys. Rev. Lett.* 105 (18 Oct. 2010), p. 183001. DOI: `https://doi.org/10.1103/PhysRevLett.105.183001` (cit. on pp. 45, 88).

[154] M. C. Simon, M. Schwarz, S. W. Epp, C. Beilmann, B. L. Schmitt, Z. Harman, T. M. Baumann, P. H. Mokler, S. Bernitt, R. Ginzel, S. G. Higgins, C. H. Keitel, R. Klawitter, K. Kubiček, V. Mäckel, J. Ullrich, and J. R. Crespo López-Urrutia. "Photoionization of N 3 + and Ar 8 + in an electron beam ion trap by synchrotron radiation". *Journal of Physics B: Atomic, Molecular and Optical Physics* 43.6 (2010), p. 065003. DOI: `https://doi.org/10.1088/0953-4075/43/6/065003` (cit. on pp. 45, 88).

[155] M. C. Simon, M. Schwarz, B. L. Schmitt, C. Beilmann, S. W. Epp, T. M. Baumann, K. Kubicek, R. Ginzel, S. G. Higgins, R. Klawitter, V. Mäckel, S. Bernitt, P. H. Mokler, J. Ullrich, and J. R. Crespo López-Urrutia. "Photoionization of ions in arbitrary charge states by synchrotron radiation in an electron beam ion trap". *Journal of Physics: Conference Series* 194.1 (2009), p. 012009. DOI: `https://doi.org/10.1088/1742-6596/194/1/012009` (cit. on p. 88).

[156] Randall K. Smith, Nancy S. Brickhouse, Duane A. Liedahl, and John C. Raymond. "Collisional Plasma Models with APEC/APED: Emission-Line Diagnostics of Hydrogen-like and Helium-like Ions". *The Astrophysical Journal* 556.2 (2001), pp. L91–L95. DOI: `https://doi.org/10.1086/322992` (cit. on p. 122).

[157] Keith B. Snow and Timothy F. Thomas. "Mass spectrum, ionization potential, and appearance potentials for fragment ions of sulfuric acid vapor". *International Journal of Mass Spectrometry and Ion Processes* 96.1 (1990), pp. 49–68. DOI: https://doi.org/10.1016/0168-1176(90)80041-Z (cit. on p. 170).

[158] R. Stensgaard. "ASTRID - The Aarhus Storage Ring". *Physica Scripta* 1988.T22 (1988), p. 315. DOI: https://doi.org/10.1088/0031-8949/1988/T22/051 (cit. on p. 45).

[159] F. Richard Stephenson and Kevin K. C. Yau. "Astronomical Records in the CH'UN-CH'IU Chronicle". *Journal for the History of Astronomy* 23.1 (1992), pp. 31–51. DOI: https://doi.org/10.1177/002182869202300103 (cit. on p. 9).

[160] Strüder, L. and et al. "The European Photon Imaging Camera on XMM-Newton: The pn-CCD camera". *Astronomy&Astrophysics* 365.1 (2001), pp. L18–L26. DOI: https://doi.org/10.1051/0004-6361:20000066 (cit. on pp. 108, 122).

[161] T. Tamura, R. Iizuka, Y. Maeda, K. Mitsuda, and N. Y. Yamasaki. "An X-ray spectroscopic search for dark matter in the Perseus cluster with Suzaku". *Publications of the Astronomical Society of Japan* 67.2 (2015), p. 23. DOI: https://doi.org/10.1093/pasj/psu156 (cit. on p. 106).

[162] H Tanuma, T Hayakawa, C Verzani, H Kano, H Watanabe, B D DePaola, and N Kobayashi. "Polarization spectroscopy of O5+(1s23p) states produced in the collisions of O6+with He and H2". *Journal of Physics B: Atomic, Molecular and Optical Physics* 33.22 (Nov. 2000), pp. 5091–5098. DOI: https://doi.org/10.1088/0953-4075/33/22/310 (cit. on p. 185).

[163] K. Taulbjerg. "Reaction windows for electron capture by highly charged ions". *Journal of Physics B: Atomic and Molecular Physics* 19.10 (1986), p. L367. DOI: https://doi.org/10.1088/0022-3700/19/10/007 (cit. on p. 34).

[164] Russell G. Tonkyn, Jerry W. Winniczek, and Michael G. White. "Rotationally resolved photoionization of O2+ near threshold". *Chemical Physics Letters* 164.2 (1989), pp. 137–142. DOI: https://doi.org/10.1016/0009-2614(89)85005-5 (cit. on p. 170).

[165] F. Torretti, R. Schupp, D. Kurilovich, A. Bayerle, J. Scheers, W. Ubachs, R. Hoekstra, and O. O. Versolato. "Short-wavelength out-of-band EUV emission from Sn laser-produced plasma". *Journal of Physics B: Atomic, Molecular and Optical Physics* 51.4 (2018), p. 045005. DOI: https://doi.org/10.1088/1361-6455/aaa593 (cit. on p. 45).

[166] E. Träbert. "Lifetime Measurements of Highly Charged Ions". *Physica Scripta* T100.1 (2002), p. 88. DOI: https://doi.org/10.1238/physica.topical.100a00088 (cit. on p. 129).

[167] M. Trinczek, A. Werdich, V. Mironov, P. Guo, A.J. González Martínez, J. Braun, J.R. Crespo López-Urrutia, and J. Ullrich. "A laser ion source for an electron beam ion trap". *Nuclear Instruments and Methods in Physics Research Section B: Beam Interactions with Materials and Atoms* 251.1 (2006), pp. 289–296. ISSN: 0168-583X. DOI: https://doi.org/10.1016/j.nimb.2006.06.013 (cit. on p. 75).

[168] J A Tully, M J Seaton, and K A Berrington. "Atomic data for opacity calculations. XIV. The beryllium sequence". *Journal of Physics B: Atomic, Molecular and Optical Physics* 23.21 (1990), pp. 3811–3837. DOI: https://doi.org/10.1088/0953-4075/23/21/016 (cit. on pp. 161, 163).

[169] Turner, M. J. L. and et al. "The European Photon Imaging Camera on XMM-Newton: The MOS cameras". *Astronomy&Astrophysics* 365.1 (2001), pp. L27–L35. DOI: https://doi.org/10.1051/0004-6361:20000087 (cit. on pp. 108, 122, 124).

[170] O. Urban, N. Werner, S. W. Allen, A. Simionescu, J. S. Kaastra, and L. E. Strigari. "A Suzaku search for dark matter emission lines in the X-ray brightest galaxy clusters". *Monthly Notices of the Royal Astronomical Society* 451.3 (2015), pp. 2447–2461. DOI: https://doi.org/10.1093/mnras/stv1142 (cit. on pp. 13, 106, 122, 123).

[171] J.H Waite, D Grodent, B.M Mauk, T Majeed, G.R Gladstone, S.J Bolton, J.T Clarke, J.-C Gérard, W.S Lewis, L.M Trafton, R.J Walker, A.P Ingersoll, and J.E.P Connerney. "Multispectral observations of Jupiter's aurora". *Advances in Space Research* 26.10 (2000). Planetary Ionospheres and Magnetospheres, pp. 1453–1475. DOI: https://doi.org/10.1016/S0273-1177(00)00089-2 (cit. on p. 13).

[172] R.S. Walling and J.C. Weisheit. "Bound-state excitation in ion-ion collisions". *Physics Reports* 162.1 (1988), pp. 1–43. DOI: https://doi.org/10.1016/0370-1573(88)90079-8 (cit. on p. 23).

[173] B J Wargelin, P Beiersdorfer, and G V Brown. "EBIT charge-exchange measurements and astrophysical applications". *Canadian Journal of Physics* 86.1 (2008), pp. 151–169. DOI: https://doi.org/10.1139/p07-125 (cit. on p. 26).

[174] B. J. Wargelin, M. Markevitch, M. Juda, V. Kharchenko, R. Edgar, and A. Dalgarno. "ChandraObservations of the "Dark" Moon and Geocoronal Solar Wind Charge Transfer". *The Astrophysical Journal* 607.1 (2004), pp. 596–610. DOI: https://doi.org/10.1086/383410 (cit. on p. 13).

[175]   C. Warnecke. "The CANREB Electron Beam Ion Source: Assembly, Characterisation and first Tests". Bachelor thesis. Ruprecht-Karls-Universität Heidelberg, 2017 (cit. on pp. 80, 82).

[176]   A. A. Werdich. "Konstruktion und Aufbau einer Laser-Ionenquelle für die Freiburger Elektronenstrahl-Ionenfalle". Diploma thesis. Albert-Ludwigs-Universität, 2000 (cit. on pp. 75, 76).

[177]   E. Wigner and J. von Neumann. "Uber merkwürdige diskrete Eigenwerte. Uber das Verhalten von Eigenwerten bei adiabatischen Prozessen". *Physikalische Zeitschrift* 30 (1929), pp. 467–470 (cit. on p. 34).

[178]   *XMM-Newton Users Handbook.* Issue 2.16. ESA: XMM-Newton SOC. 2018 (cit. on pp. 10, 108, 122).

[179]   C. Zener. "Non-adiabatic crossing of energy levels". *Proceedings of the Royal Society of London A: Mathematical, Physical and Engineering Sciences* 137.833 (1932), pp. 696–702. DOI: https://doi.org/10.1098/rspa.1932.0165 (cit. on pp. 13, 34).

[180]   Y H Zhang, Yu A Litvinov, T Uesaka, and H S Xu. "Storage ring mass spectrometry for nuclear structure and astrophysics research". *Physica Scripta* 91.7 (June 2016), p. 073002. DOI: https://doi.org/10.1088/0031-8949/91/7/073002 (cit. on p. 14).

List of publications

[1] M. A. Blessenohl, **S. Dobrodey**, C. Warnecke, M. K. Rosner, L. Graham, S. Paul, T. M. Baumann, Z. Hockenbery, R. Hubele, T. Pfeifer, F. Ames, J. Dilling, and J. R. Crespo López-Urrutia. "An electron beam ion trap and source for re-acceleration of rare-isotope ion beams at TRIUMF". *Review of Scientific Instruments* 89.5 (2018), p. 052401. DOI: https://doi.org/10.1063/1.5021045.

[2] G. Brenner, S. Bernitt, **S. Dobrodey**, R. Steinbrügge, M. A. Blessenohl, A. Cieluch, Z. Hockenbery, S. Kühn, J. Nauta, M. A. Sanchez, S. W. Epp, and J. R. Crespo López-Urrutia. "High-precision laser spectroscopy of the fine-structure transition $2s^2S_{1/2} - 2p^2P_{3/2}$ at 136 eV in lithiumlike Kr^{33+} using a free-electron laser". *Phys. Rev. A* (2019). **In peer-review process (date: 01.08.2019)**.

[3] L. Mercadier, A. Benediktovitch, C. Weninger, M. A. Blessenohl, S. Bernitt, H. Bekker, **Dobrodey, S.**, A. Sanchez-Gonzalez, B. Erk, C. Bomme, R. Boll, Z. Yin, V. P. Majety, R. Steinbrügge, M. A. Khalal, F. Penent, J. Palaudoux, P. Lablanquie, A. Rudenko, D. Rolles, J. R. Crespo López-Urrutia, and N. Rohringer. "Evidence of Extreme Ultraviolet Superfluorescence in Xenon". *Phys. Rev. Lett.* 123 (2 July 2019), p. 023201. DOI: https://doi.org/10.1103/PhysRevLett.123.023201.

[4] Chintan Shah, Holger Jörg, Sven Bernitt, **Dobrodey, Stepan**, René Steinbrügge, Christian Beilmann, Pedro Amaro, Zhimin Hu, Sebastian Weber, Stephan Fritzsche, Andrey Surzhykov, José R. Crespo López-Urrutia, and Stanislav Tashenov. "Polarization measurement of dielectronic recombination transitions in highly charged krypton ions". *Phys. Rev. A* 92 (4 Oct. 2015), p. 042702. DOI: https://doi.org/10.1103/PhysRevA.92.042702.

[5] Chintan Shah, **Stepan Dobrodey**, Sven Bernitt, René Steinbrügge, José R. Crespo López-Urrutia, Liyi Gu, and Jelle Kaastra. "Laboratory Measurements Compellingly Support a Charge-exchange Mechanism for the 'Dark Matter' 3.5 keV X-Ray Line". *The Astrophysical Journal* 833.1 (2016), p. 52. DOI: https://doi.org/10.3847/1538-4357/833/1/52.

[6] F. Torretti, A. Windberger, A. Ryabtsev, **Dobrodey, S.**, H. Bekker, W. Ubachs, R. Hoekstra, E. V. Kahl, J. C. Berengut, J. R. Crespo López-Urrutia, and O. O. Versolato. "Optical spectroscopy of complex open-4d-shell ions $Sn^{7+} - Sn^{10+}$". *Phys. Rev. A* 95 (4 Apr. 2017), p. 042503. DOI: https://doi.org/10.1103/PhysRevA.95.042503.

[7] A. Windberger, F. Torretti, A. Borschevsky, A. Ryabtsev, **Dobrodey, S.**, H. Bekker, E. Eliav, U. Kaldor, W. Ubachs, R. Hoekstra, J. R. Crespo López-Urrutia, and O. O. Versolato. "Analysis of the fine structure of $Sn^{11+} - Sn^{14+}$ ions by optical

spectroscopy in an electron-beam ion trap". *Phys. Rev. A* 94 (1 July 2016), p. 012506. DOI: https://doi.org/10.1103/PhysRevA.94.012506.

In this work, reference [1] has been utilized in the chapter about the setup and characterization of the CANREB-EBIS with a more detailed description. Reference [5] has been consulted in the chapter about the charge exchange measurements of highly ionized sulfur with additional information about the experiment and space missions.

Acknowledgments